



**HAL**  
open science

# Dynamics and Structure close to the Glass and Jamming transitions ; Experiments and Simulations

Raphaël Candelier

► **To cite this version:**

Raphaël Candelier. Dynamics and Structure close to the Glass and Jamming transitions ; Experiments and Simulations. Data Analysis, Statistics and Probability [physics.data-an]. Université Pierre et Marie Curie - Paris VI, 2009. English. NNT: . tel-00440848v1

**HAL Id: tel-00440848**

**<https://theses.hal.science/tel-00440848v1>**

Submitted on 12 Dec 2009 (v1), last revised 13 Jan 2010 (v2)

**HAL** is a multi-disciplinary open access archive for the deposit and dissemination of scientific research documents, whether they are published or not. The documents may come from teaching and research institutions in France or abroad, or from public or private research centers.

L'archive ouverte pluridisciplinaire **HAL**, est destinée au dépôt et à la diffusion de documents scientifiques de niveau recherche, publiés ou non, émanant des établissements d'enseignement et de recherche français ou étrangers, des laboratoires publics ou privés.

THÈSE DE DOCTORAT  
DE L'UNIVERSITÉ PIERRE ET MARIE CURIE

Spécialité : PHYSIQUE

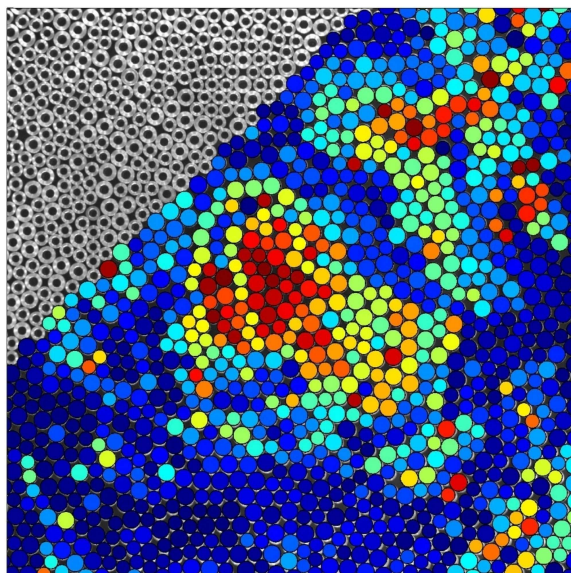
*École doctorale 389 : La physique de la particule à la matière condensée*

présentée par  
Raphaël CANDELIER

pour obtenir le grade de  
DOCTEUR DE L'UNIVERSITÉ PIERRE ET MARIE CURIE



**Dynamics and Structure**  
**close to the Glass and Jamming transitions**  
Experiments and Simulations



Thèse soutenue le 9 novembre 2009 devant le jury composé de :

M. Olivier DAUCHOT	Directeur de thèse
M. Ludovic BERTHIER	Rapporteur
M. Pedro Miguel REIS	Rapporteur
Mme. Leticia CUGLIANDOLO	Examinatrice
M. Martin VAN HECKE	Examineur
M. Gilles TARJUS	Examineur

Université Pierre & Marie Curie - Paris 6  
Accueil, inscription des doctorants et base de données  
Esc G, 2ème étage  
15 rue de l'école de médecine  
75270-PARIS CEDEX 06

Tél. Secrétariat : 01 42 34 68 35  
Fax : 01 42 34 68 40  
Tél. étudiants de A à EL : 01 42 34 69 54  
Tél. étudiants de EM à ME : 01 42 34 68 41  
Tél. étudiants de MF à Z : 01 42 34 68 51  
E-mail : [scolarite.doctorat@upmc.fr](mailto:scolarite.doctorat@upmc.fr)



*A Tiphaine,  
pour son Amour.*

## Abstract

The glass transition is the dramatic dynamical slowdown one observes when cooling down a liquid or densifying a set of particles into an amorphous state. In this thesis we explore two distinct situations related to this phenomenology, mostly in the case of granular materials.

In a first part we study the strongly non-linear response of an assembly of frictional grains under vibration when they are very densely packed. To this aim we pull a probe particle – an “intruder” – through the media and follow the dynamics of the particles around. We evidence the presence of two transitions : the first one is analogous to a fluidisation transition, as shown by the evolution from a continuous to a highly intermittent motion and by the appearance of a yield stress in the response; the second one is identified as the jamming transition that occurs in several systems. We show that the reorganizations induced by the intruder display critical signatures at the transition, as previously shown by the study of the same system without drag, leading to interesting connections with recent simulations in athermal and frictionless particles systems.

In a second part, we study the relations between the very short term dynamics – essentially made of vibrations of the particles around their equilibrium positions – and the long time scale dynamics where dynamical heterogeneities are responsible for the slowdown of the structural relaxations on approach to the glass transition. The dynamics of the metastable states is analyzed in two experimental granular systems (grains under cyclic shear or in a fluidized bed) as well as in simulations of repulsive particles. We show the dominant role of quasi-instantaneous cooperative displacements to build the large intermittent decorrelation patterns that one observes on longer time scales through a facilitation mechanism. Facilitation becomes less and less efficient when the packing fraction increases, leading to increasingly separated and concentrated dynamical events in space and time. The vibrational dynamics leading to the cooperative motion are also investigated, and we show that the latter are essentially driven by the structure, coarse grained at a mesoscopic scale.

**Keywords** : glass transition, jamming transition, out-of-equilibrium systems, granular materials, criticality, dynamical susceptibility.

## Résumé court

La transition vitreuse se caractérise par un ralentissement dramatique de la dynamique, soit lorsqu'on refroidit un liquide soit lorsque l'on compactifie une assemblée de particules dans un état amorphe. Dans cette thèse nous explorons deux situations distinctes liées à cette phénoménologie, principalement dans le cas de matériaux granulaires.

Dans une première partie nous étudions la réponse fortement non-linéaire d'un système de particules frottantes vibrées à très haute densité soumis à une contrainte locale. Pour cela nous tirons une particule "intrus" à force constante dans le milieu en suivant le mouvement des particules alentour. Nous mettons en évidence deux transitions distinctes : la première est l'analogue d'une transition de fluidification et se manifeste par le passage d'un mouvement continu de l'intrus à un mouvement fortement intermittent ainsi que par l'apparition d'une contrainte seuil dans la réponse ; la deuxième est identifiée à la transition de blocage qui intervient de manière générique dans de nombreux systèmes. Nous montrons que les réorganisations induites par l'intrus ont un comportement critique à la transition, venant conforter le caractère critique de la transition de blocage mis en évidence en l'absence d'intrus, et établissant d'intéressantes connections avec des simulations récentes de systèmes athermiques de particules non-frottantes.

Dans une deuxième partie nous étudions les relations entre la dynamique à très court terme – essentiellement vibratoire – et à plus longue échelle de temps, où de fortes hétérogénéités dynamiques sont responsables du ralentissement des relaxations structurales à l'approche de la transition vitreuse. La dynamique des états métastables est analysée dans plusieurs systèmes granulaires (cellule de cisaillement cyclique et lit fluidisé) ainsi que dans une simulation d'un liquide de Lennard-Jones répulsif ; nous mettons en évidence le rôle de mouvements coopératifs quasi-instantanés qui construisent à long terme par un mécanisme de facilitation de larges motifs de décorrélation intermittents. Ce mécanisme de facilitation diminue lorsque le matériau se densifie, menant à des événements dynamiques de plus en plus séparés et concentrés dans l'espace et le temps. La dynamique vibratoire aboutissant aux mouvements coopératifs est elle aussi étudiée, et nous montrons que ces derniers sont déterminés pour une large part par la structure du matériau à un niveau mésoscopique.

**Mots clés** : transition vitreuse, transition de blocage, systèmes hors-équilibre, matériaux granulaires, criticalité, susceptibilité dynamique.

## Preamble

Rome, January 2006, at nightfall . Above Termini station a strange ballet takes place : thousands (millions ?) of starlings fly in from the countryside to their roosting site. Before settling into trees for the night, they spend roughly 20 minutes doing incredible aerial displays. “It’s a truly amazing sight !” say the tourists on the ground. “It’s a pain !” say the managers of the cafés on the *Piazza dei Cinquecento*. “It’s time !” say the experimentalists of the INFM.

Inspired by the aerial displays, a group of scientists led by theoretical physicists in Rome set up *StarFlag*, a multidisciplinary, multinational collaboration to study the birds’ flocking behavior. The main aim was to determine the fundamental laws of collective behavior and self-organization of animal aggregations in 3D. In addition to the physicists, theoretical biologists, biologists and economists were also part of the ballet.

I have spend roughly one year in the Rome team. This experience was extraordinary for me in many regards ; every evening during 3 months I was on the roof of the *Museo Nazionale Romano*, feeling the delicious sensation of being a part of the ballet. I’ve learnt a lot on experimental issues and human relations. This collective work led to two publications [1, 2]. As I was just funded for just one year, I have started the present thesis just after this “pre-doctoral” position. Obviously, grains do not have the same flavour than birds : the beauty of their organization is hidden. But if one keeps looking at it, at the end of the day their dance appears as fascinating.



Figure 1: The Rome team. **Left** A. Cavagna, the project’s deputy coordinator. **Middle** The stars, the starlings. **Right** From left to right : I. Giardina, J.-P. Bouchaud (visitor), V. Zdravkovic and M. Ballerini.

## Remerciements

*Une thèse, c'est comme une raclette : ça se partage.*

– Proverbe GITan

L'écriture des remerciements est un exercice difficile. D'une part parce que de très nombreuses personnes ont contribué à l'aboutissement de ce travail, et d'autre part parce qu'il faut remercier chacun à son juste apport.

Mes premières pensées vont à anne-Marie Cazabat, ex-directrice de l'Ecole Doctorale 389 : là où d'autres m'ont littéralement claqué la porte au nez à cause de mon parcours légèrement "atypique", elle m'a accueilli et soutenu avec un entrain qui m'a beaucoup touché. Ce travail n'a pu être financé que grâce à sa confiance et ses efforts bienveillants.

Je tiens ensuite à remercier Jean-Philippe Bouchaud pour m'avoir soutenu dans mon premier projet de thèse et pour m'avoir trouvé un *pré-doc* d'un an à Rome. Expérience riche en émerveillement, scientifiquement et humainement, pour laquelle je dois remercier Andréa Cavagna et Irene Giardina pour leur accueil et leur courage dans ce projet difficile. De cette expérience je garde un léger accent serbe qui ressort parfois quand je parle anglais et que je dois à Vladimir Zdravkovic, un compagnon généreux et attentionné. Je tiens aussi à remercier Jean-Philippe pour sa remarquable disponibilité et son expertise d'excellence tout au long des trois ans que j'ai passé au sein du GIT.

Mes meilleures pensées vont naturellement à Olivier "Le chef" Dauchot, qui en plus d'être "au top" scientifiquement jouit d'un positivisme hors norme. La relation de confiance mutuelle, à la fois conviviale et travailleuse que nous avons construit ensemble au cours de ces trois années est pour moi un modèle, que j'espère pouvoir retrouver à l'avenir. La légende dit que Pierre-Gilles de Genes appelait ses étudiants ses "trois mousquetaires" ; Olivier pour sa part nous appelle ses "zozos" (Julien Deseigne ayant été sacré *zozo premier*, j'en déduis donc que je suis *zozo zéro*). Cette dénomination est peut être moins romanesque, mais elle traduit une forme de complicité rare et un humour certain.

Le Groupe Instabilités et Turbulence est une joyeuse *oligarchie*, que je remercie chaleureusement pour son accueil. Tout expérimentateur sain d'esprit sait combien son travail repose sur celui des techniciens, et il faut dire que le GIT est fort bien loti avec le travail de grande qualité de Vincent Padilla (toujours la pêche et la banane à la fraise) et de Cécile Gasquet (qui accouchera peut-être un jour d'un petit pingouin, sait-on jamais ?). Ajoutons que ce sont tous les deux à la fois de très bons techniciens pour la science mais aussi pour la vie de groupe. Vient ensuite mon collègue de bureau : si je devais remercier Sébastien au mètre, il me faudrait écrire de très nombreuses lignes ; je ne citerai donc que son incroyable patience, son enthousiasme inoxydable, son humour décapant et sa grande capacité d'écoute.

J'ai eu la chance et le plaisir de passer les deux dernières années de ma thèse en compagnie de Julien Deseigne. J'ai partagé avec ce penseur décomplexé de nombreux transports, et son amitié a sans doute été une des plus belles découvertes de ma thèse. Puisses-tu réussir à faire parler tes moutons, et venir à bout de tes nombreux projets. Je ne saurais aussi que trop remercier Guillaume Marty et Frédéric Lechenault, mes deux prédécesseurs, pour le travail très important qu'il ont fourni sur les expériences (ils sont en quelque sorte les grand-parents de ce bébé), Emmanuelle Gouillart pour notre duo "Le geek, c'est chic", Marco Bonetti pour ses conseils et sa gentillesse, Elisabeth Bouchaud et Carolina Brito pour leur bonne humeur rayonnante, et enfin bien sûr Arnaud Chiffaudel, Bérengère Dubrulle et François Daviaud pour leurs conseils toujours très précieux et leur capacité à animer le GIT au quotidien. Je n'oublie pas non plus de remercier mes thésards acolytes Romain Monchaux et Gilles Collette, Pierre-Philippe Cortet pour nos quelques discussions du café, ainsi que les stagiaires de Master que j'ai eu le plaisir d'encadrer : François Paradis, Ahmed Khelladi, Baudouin Saint-Yves et Corentin Coulais. Certains commencent en ce moment-même une thèse au GIT, et je leur souhaite de prendre autant de plaisir dans ce groupe que j'y ai pris, ainsi que la réussite scientifique qui sera, j'en suis certain, totale.

Clairement, je n'aurais pas pu réaliser toutes les expériences et simulations présentées dans ce travail tout seul. De nombreuses collaborations fructueuses ont été établies, et je tiens à les mentionner ici. Tout d'abord je dois énormément à Giulio Biroli, un théoricien hors norme (puisqu'il s'intéresse aux expériences) et dont la patience et la disponibilité m'ont beaucoup touché. Je voudrais remercier sincèrement aussi toutes les personnes qui ont contribué à produire et analyser les données : Asaph Widmer-Cooper, Peter Harrowell, David Reichamn, Jonathan Kummerfeld, Adam Abate, Douglas Durian et Matthieu Renouf.

Je remercie vivement les membres du jury qui ont apporté un regard critique et constructif à ce travail, et spécialement les deux rapporteurs dont les remarques et les conseils ont amélioré la qualité du manuscrit.

Je dois enfin beaucoup à mon entourage : à Tiphaine, dont l'amour est le meilleur des soutiens et qui m'a offert un excellent pot de thèse, à mon père et ma soeur, et tous les véritables amis qui ont un jour partagé ma passion des sciences : Raymond, Matei, Isabelle, Sophie et Renaud.

Voici donc mon premier résultat : bien plus qu'un simple apprentissage scientifique, la thèse est une expérience humaine unique et forte<sup>1</sup>. J'y ai beaucoup appris sur moi et sur les autres. Pour conclure j'aimerai donc citer le très sage Léonard Nimoy<sup>2</sup> :

*Plus on partage, plus on possède. Voilà le miracle.*

---

<sup>1</sup>Ce résultat a sans doute déjà été démontré, mais *il ne sert à rien d'être le premier à montrer quelque chose, il vaut mieux être le dernier à le redécouvrir.* (G. Parisi).

<sup>2</sup>Léonard Nimoy est devenu célèbre en interprétant M. Spoke dans Star Trek.

# Contents

<b>1</b>	<b>Introduction</b>	<b>5</b>
1.1	The Glass transition . . . . .	7
1.1.1	Phenomenological Definition . . . . .	7
1.1.2	The glass transition is more than “just cool” . . . . .	10
1.1.3	Glass formers: a huge family . . . . .	11
1.1.4	The structural mystery . . . . .	13
1.1.5	Toward a dynamical transition . . . . .	15
1.1.6	Dynamical heterogeneities . . . . .	19
1.2	The Jamming transition . . . . .	21
1.2.1	What is jamming? . . . . .	21
1.2.2	The acquisition of rigidity . . . . .	23
1.2.3	Criticality and diverging lengthscale . . . . .	24
1.2.4	The role of friction . . . . .	27
1.3	Jamming versus Glass . . . . .	31
1.3.1	Where is point J? . . . . .	31
1.3.2	The hard spheres case . . . . .	32
1.3.3	The soft spheres case . . . . .	34
1.3.4	Conclusion, and a few questions . . . . .	37
1.4	This work . . . . .	38
<b>2</b>	<b>Systems</b>	<b>39</b>
2.1	Experiments and simulations . . . . .	40
2.1.1	The vibrating experiment . . . . .	40
2.1.2	The shearing experiment . . . . .	49
2.1.3	The fluidized bed experiment . . . . .	54
2.1.4	Softly interacting particles liquid simulation . . . . .	56
2.1.5	Vertically vibrated monodisperse grains . . . . .	59
2.2	Data processing and analysis . . . . .	61
2.2.1	Image processing . . . . .	61
2.2.2	Tracking . . . . .	65
2.2.3	Databases . . . . .	67
2.2.4	Data analysis: the Granulobox . . . . .	69
2.3	Tables . . . . .	70

<b>3</b>	<b>Let's jam!</b>	<b>73</b>
3.1	Dynamics at the jamming transition . . . . .	74
3.1.1	State of the art . . . . .	74
3.1.2	Further studies on the statistics of the displacements .	80
3.2	The journey of an intruder . . . . .	84
3.2.1	State of the art . . . . .	84
3.2.2	Introducing our intruder . . . . .	89
3.2.3	Results and discussion . . . . .	91
3.3	Toward jamming . . . . .	105
3.3.1	Aging . . . . .	105
3.3.2	The "parachutist" protocol . . . . .	106
3.4	Discussion and perspectives . . . . .	110
<b>4</b>	<b>Through the cooling glass</b>	<b>113</b>
4.1	State of the art . . . . .	115
4.1.1	The granulo-utopia . . . . .	115
4.1.2	A glassy dynamics . . . . .	115
4.1.3	Dynamical heterogeneities . . . . .	119
4.2	The building blocks of dyn. heterogeneities . . . . .	121
4.2.1	More on cage Jumps . . . . .	121
4.2.2	Results . . . . .	126
4.3	The fate of facilitation . . . . .	131
4.4	And what about real liquids? . . . . .	141
4.4.1	Relaxation originates from soft modes . . . . .	141
4.4.2	Structure-induced dynamical correlations in supercooled liquids . . . . .	142
4.5	A few other ideas . . . . .	149
4.5.1	Anatomy of a cycle . . . . .	149
4.5.2	A few other ideas that did not really worked, and why	155
4.5.3	What would a crystal think of all this? . . . . .	162
4.6	Discussion and perspectives . . . . .	166
<b>A</b>	<b>Letter on the intruder</b>	<b>173</b>
<b>B</b>	<b>Recipes</b>	<b>179</b>
B.1	Geometrical recipes . . . . .	179
B.1.1	Laguerre tessellation . . . . .	179
B.1.2	Region Of Interest . . . . .	181
B.1.3	Distance to affinity . . . . .	182
B.1.4	Clustering . . . . .	185
B.2	Dynamical recipes . . . . .	186
B.2.1	Density relaxation statistics . . . . .	186

## *How to read this thesis ?*

Here is a list of tips for an efficient reading :

- All space units are expressed in diameters of small grains. Every time we speak of a “grain diameter”, the reader should understand a *small* grain diameter.
- The packing fractions are all expressed as the surface of the grains divided by the total surface :

$$\phi = \frac{S_{small} + S_{large}}{S_{total}}$$

**Technical content / side result** This box indicates to the reader that it is a technical point or a side result that can be skipped in a first reading.

Here is a list of the recurrent abbreviations :

- **Pdf** stands for *probability density function*.
- **cPdf** stands for *cumulated probability density function*.
- **DH** stands for *dynamical heterogeneities*.
- **CJ** stands for *cage jump*.
- **ROI** stands for *Region Of Interest*.
- **MSD** and **RMSD** stands for *Mean Square Displacement* and *Root Mean Square Displacement*.



# Chapter 1

## Introduction

### Contents

---

<b>1.1</b>	<b>The Glass transition . . . . .</b>	<b>7</b>
<b>1.2</b>	<b>The Jamming transition . . . . .</b>	<b>21</b>
<b>1.3</b>	<b>Jamming versus Glass . . . . .</b>	<b>31</b>
<b>1.4</b>	<b>This work . . . . .</b>	<b>38</b>

---

*Atoms of unlike nature come together to form a skanda, or compound atom.  
All the objects in the world are various types of compound atoms only,  
while the world itself is a much bigger aggregate of atoms and skandas.*  
– Jain Philosophy

India, VI<sup>th</sup> century BCE. The ancient Jainism philosophy claims that matter is composed of elementary entities able to combine and form complex objects. A century later, in Greece, Leucippus and his student Democritus introduced the term *atom*. Both conceptions were purely philosophical, and have been relayed in the XIII<sup>th</sup> century by corpuscularianism, based on alchemists' experiments. Since that time, one of the most fascinating challenges for chemists and physicists has been to understand how these elementary particles structure matter. A related question is how this inner structure influences the mesoscopic and macroscopic properties of the materials.

In 1611, Kepler hypothesized that the symmetry of snow flakes arose from an hexagonal packing of water molecules. In 1895, Von Laue realized the first X-ray diffraction experiment, revealing for the first time the inner structure of crystals. Then, during the XX<sup>th</sup> century several macroscopic properties of crystals (optical and mechanical properties, electronic and thermal conductivity, etc) have been linked to their microscopically ordered structure. The transition from liquid to crystalline solid – during which the appearance of a regular order liberates an amount of latent heat – became one of the archetypal first order phase transitions. To now, a wide knowledge has been accumulated on both the formation of crystalline order and its consequences on the macroscopic properties of matter. As

Cahn has argued [3], it is generally the ability to make a strong link between microscopic structure and physical properties that essentially defines an established field of material science.

But matter is far from being always ordered, and amorphous solids are ubiquitous in nature. One can cite some volcanic rocks (*e.g.* granite), meteorites (*e.g.* moldavite), or the eukaryotic seaweeds that synthesize a silica cell wall (*e.g.* diatoms) and produce the most important part of silica glass on earth. Amorphous matter is also omnipresent in our daily life: plastics are made of entangled molecules of polymers, window glasses are built out of randomly arranged silica molecules (see fig. 1.1), and sand piles are assemblies of disordered grains.

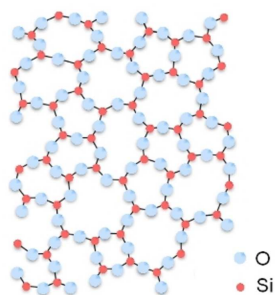


Figure 1.1: 2D representation of the amorphous structure of glassy silica ( $\text{SiO}_2$ ). No long range order is present.

Several practical applications of amorphous matter can be cited: a laser can melt and solidify the recording layer of a rewritable CD into an amorphous or a crystalline state, making areas appear like the pits and lands of a prerecorded CD. Hydrogels – *i.e.* water trapped in an amorphous polymer network – are currently used as scaffolds in tissue engineering and have the ability to sense changes of pH, temperature, or the concentration of a metabolite (*e.g.* modern contact lenses). Radioactive wastes are embedded in glasses with extremely low diffusion coefficients to ensure their confinement

and insulation. Bulk metallic glasses have been recently shown to combine strength, ductility and toughness. Even the cotton candy of our childhood was an amorphous solid!

However, in comparison, the understanding of the macroscopic properties of amorphous solids and the way they form – often called the *glass transition* for liquids and *jamming transition* for assemblies of particles<sup>1</sup> – is far from achieved. According to Anderson in 1995, “*The deepest and most interesting unsolved problem in solid state theory is probably the nature of glass and the glass transition.*” [4]. Maybe the most intriguing feature of such systems is that their ability to flow dramatically changes during the glass transition, while there is no obvious evolution in their inner structure. It may be the first time in solid state physics that such a disconnection appears.

In this introductory chapter, the reader will find a state of the art on both the glass and jamming transitions. First, we will recall the phenomenology of glass-former systems and their thermodynamic and dynamic characterizations. Second, the jamming transition will be presented and a brief review of the recent literature will enable us to underline the crucial role of the

<sup>1</sup>More precise definitions will be given in the following.

force network in the acquisition of rigidity and, following recent studies, to find point  $J$ . Then we will make an attempt to clarify the similarities and dissimilarities between those two transitions and to draw some phase diagrams. Finally, a brief presentation of the contents of this manuscript will conclude this chapter.

## 1.1 The Glass transition

### 1.1.1 Phenomenological Definition

When one cools down a liquid, a transition to a solid state happens. At school the students learn about the transition to the crystalline solid state, a well established first order phase transition, during which a latent heat appears due to the emergence of a regular order at the microscopic level. But there exists several cases for which this transition can be avoided and no such latent heat jump is observed [5] as the liquid goes toward the solid state. This is the case for liquids cooled fast enough (“quenched”), or for materials that simply cannot arrive in a regularly ordered state because of microscopic constraints (*e.g.* steric constraints in polymers).

These behaviors are illustrated on fig. 1.2, in a diagram where the specific volume is plotted against the temperature  $T$ . Starting from a liquid state, as the temperature decreases the system can usually freeze at the melting point  $T_m$  through a first order phase transition and becomes a crystal, which is the state minimizing the free energy. If the liquid is quenched fast enough it can remain in a metastable state beyond the melting point, a state called *supercooled* liquid. The supercool branch is just an extrapolation of the liquid branch. Then, at some point called  $T_g$ , a change of slope in the specific volume versus temperature curve occurs – generically called the *glass transition* – and the evolution with the temperature becomes very close to that of the crystal.

**It’s just a question of time** Note that the change of slope from the supercooled branch to the glass branch is smooth, and that  $T_g$  is more like a small interval rather than a sharp value. Actually, the transition occurring at  $T_g$  is due to the cross-over between two time scales: the cooling rate  $1/T \cdot dT/dt$ , usually fixed, and the structural relaxation time  $\tau_\alpha$  which grows as the temperature decreases. As long as the structural relaxation time is small enough, the particles can rearrange themselves and “adapt” their inner structure to the cooling: the system remains in a supercooled state. However, as soon as the relaxation time becomes large enough, *i.e.* such that the structure cannot relax on the typical cooling rate timescale, the supercooled branch is left and the system falls out of equilibrium. Hence in the so-reached glassy states the structure is frozen.

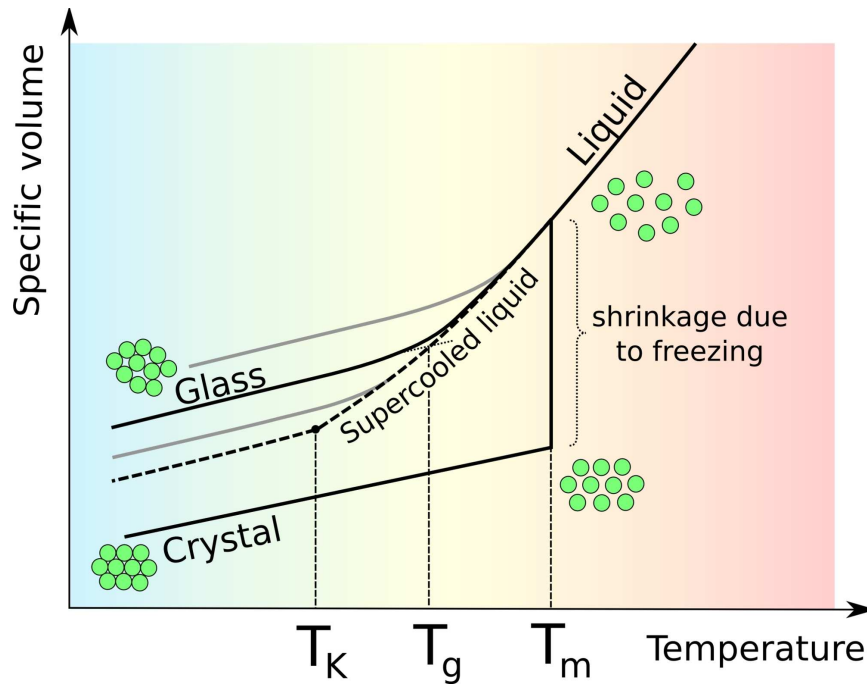


Figure 1.2: How to become a solid: at  $T_m$ , if the liquid has the time to reach its equilibrium position it becomes a crystal. If the liquid is quenched, the metastable branch continues the liquid branch and leads ultimately to a glass, at  $T_g$ . Several glass branches are possible, depending on the cooling rate. An ideal glass transition may eventually exist at  $T_K$ , corresponding to an infinitely slow cooling.

**The large viscosity limit** Empirically,  $T_g$  is defined as the temperature below which the macroscopic viscosity reaches a certain value, such that it is “reasonable”<sup>2</sup> to consider that the material is solid. This value has been fixed at  $10^{12}$  Pa.s, or equivalently  $10^{13}$  Poises. One can deduce a typical relaxation time scale  $\tau_\alpha$  from the viscosity  $\eta$  with Maxwell’s relation  $\tau_\alpha = \eta/G_\infty$ , where  $G_\infty$  stands for the instantaneous elastic shear modulus.

To give an idea of what is  $10^{12}$  Pa.s and how to reach it, a few examples can be given. The Thomas Parnell’s *pitch drop experiment* is a nice example of very viscous fluid flow (see box below). Note that the pitch viscosity is around  $10^8$  Pa.s, and it has been estimated that a drop of glassy pitch, *i.e.*  $10^4$  more viscous, would take more than  $10^6$  years to form.

Another striking example is water: the viscosity of water at ambient temperature is around  $10^{-2}$  Pa.s, so to form a water glass one would need to increase the viscosity by a factor  $10^{14}$ . This could be only achieved by

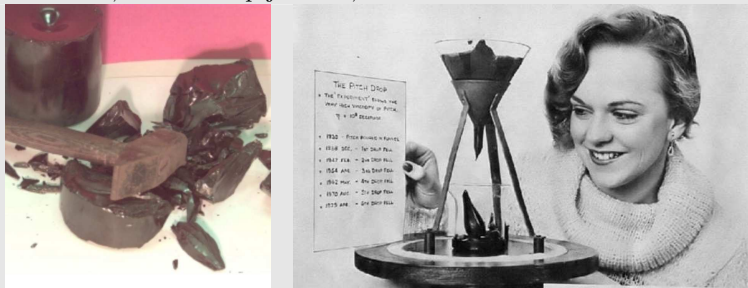
<sup>2</sup>As stressed out in [6], “it is hard to define the word ‘reasonable’ in any reasonable manner”.

cooling the water prodigiously quickly, namely with a cooling rate of the order of  $10^6$  K/s. It is therefore rare to find glassy water, but several other materials are easier to "glassify", like window glasses where cooling rates of a few  $10^{-2}$  K/s are sufficient to avoid crystallization [7].

### The Pitch drop experiment

Though at room temperature pitch appears to be a solid and can be shattered by a hammer (see left figure below), it is in fact a very high-viscosity liquid. Pr. Thomas Parnell started in 1927 the following experiment at the University of Queensland: he heated a sample of pitch and poured it into a sealed funnel. Then, he waited. In 1930, when he felt the pitch was settled enough, he cut the bottom of the funnel, freeing the pitch to begin its mind-bogglingly slow downward escape.

Pr. Parnell lived long enough to record only two drips - the first in 1938, eight years after the opening of the funnel - and the second, nine years later in 1947. On the right picture below, the 6<sup>th</sup> drop just felt, in 1979.



As of 2009 – 79 years after the experiment was begun – the pitch has dripped only eight times. Curiously, as it only drips every 8 to 9 years, no one has ever actually seen a drop fall. A webcam was setup in 2000, but due to technical problems it missed the drip. The last drip was in 2000, so the pitch is due to drop any day now. One can try their luck, and patience, at [mms://drop.physics.uq.edu.au/PitchDropLive](http://mms://drop.physics.uq.edu.au/PitchDropLive). This experiment is listed as the longest running lab experiment by Guinness World Records, and Pr. Parnell received the IgNobel prize posthumously in 2005.

**Several branches, and the ideal glass transition** Fig. 1.2 illustrates the fact that the liquid can fall out of equilibrium at very different temperatures. As predicted by the previous timescale argument, the location of  $T_g$  strongly depends on the cooling rate: the lower the cooling rate, the later the system will become a glass.

A hotly debated question is the existence of a thermodynamic glass transition (also called *ideal glass transition*) on the metastable branch, usually denoted  $T_K$ <sup>3</sup>. This ideal glass transition would occur in the limit of the in-

<sup>3</sup>The ideal glass transition is called the "Kauzmann" transition as a reference to the early interpretations of Kauzmann [8]: he hypothesized that some kind of phase transition should happen as the entropy of the liquid become lower than the entropy of the crystal. We know now that the entropy of the liquid is lower than the crystal's at the freezing / melting transition [9].

finitely slow cooling rate, and would be therefore the densest reachable point on the metastable branch. One can immediately see that two big experimental problems raise when exploring the very slow cooling rate limit: (i) the experimental time diverges and (ii) crystallization is increasingly hardly avoided.

Some support for the ideal glass transition can be given by the predictions of mean field models and Mode Coupling Theory altogether with recent numerical [10] and experimental data [11]. However, this is still an open discussion, and we will not debate whether or not such a thermodynamical transition exists. Our concerns are numerical and experimental, and in practice the systems always fall in a glassy state at some point: the ideal glass state *can not* be observed. Let us hypothesize that it exists, without great consequence on any of the following considerations.

### 1.1.2 The glass transition is more than “just cool”

In addition to the large number of decades involved in the growth of the relaxation timescale of supercooled liquids, the temperature dependence of this growth is of noticeable importance. When plotting the log of the viscosity as a function of the reduced temperature  $T_g/T$  for several materials, one gets an “Angell” [12] plot (see fig. 1.3) in which two types of glasses appear: *strong* glass formers form straight lines while *fragile* glass formers draw convex curves.

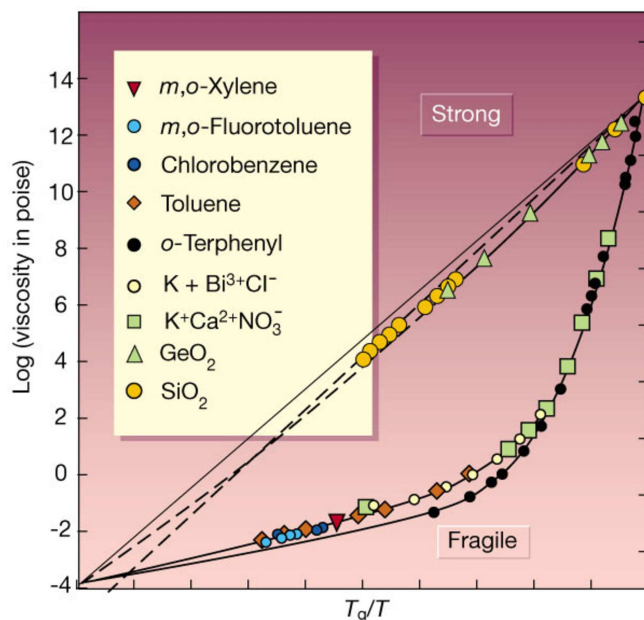


Figure 1.3: “Angell” plot of the viscosity as a function of the reduced temperature  $T_g/T$  for a few glass formers approaching the glass transition. Strong glass formers have a logarithmically increasing viscosity, while fragile glass formers display a convex evolution. From Debenedetti and Stillinger [13].

Strong glasses correspond to an Arrhenius behavior, for which one can extract an effective activation energy. This suggests a simple relaxation mechanism with energy barriers crossed by activation. Silica, and therefore

our window’s glass, falls in this category. The relaxation of fragile glasses is different: their convex curvature implies that the energy barriers become higher as the temperature decreases. This behavior – often called “super-Arrhenius” – suggests that increasingly more particles have to be mobilized to pass the energy barriers, hence hinting that the formation of fragile glasses is an intrinsically collective phenomenon. The glass transition is therefore more than the slowdown one would expect if the material was “just cooled”.

This is supported by the fact that the viscosity – and equivalently the typical relaxation time – are well-fitted by the Vogel-Fulcher-Tamman (VFT) law:

$$\tau_\alpha = \tau_0 \cdot \exp\left(\frac{DT_0}{T - T_0}\right) \quad (1.1)$$

The parameter  $D$  enables to tune the fragility, a higher  $D$  meaning a less fragile glass. A divergence of the relaxation time is expected at  $T_0$ , and therefore a phase transition of some kind. However, several other laws can fit these curves as well, like the Bässler law:

$$\tau_\alpha = \tau_0 \cdot \exp\left(K \left[\frac{T^*}{T}\right]^2\right) \quad (1.2)$$

which leads to a divergence only at  $T = 0$ .

Actually, even if the viscosity increases by several orders of magnitude, the evolution of its logarithm is modest and one cannot unambiguously determine the underlying law by fitting experimental [14] or numerical [6] data. As a consequence, the existence of an underlying true phase transition remains an active matter of debate.

### 1.1.3 Glass formers: a huge family

There is a large family of systems displaying such a slow relaxation. Beyond molecular glasses, the glass-formers family includes colloidal particles and emulsions, for which the microscopic diffusion timescale is of the order of the millisecond (instead of the picosecond for real liquids). The dynamics of these mesoscopic particles is decoupled from the temperature, but glassy states can be reached by compression: for instance Cheng *et al.* [15] have observed a tremendous slowdown of the relaxation timescales in a colloidal hard sphere dispersion and found a nice fit with a VFT-law in density.

One step further, a whole set of completely *athermal* systems, like the macroscopic beads of granular systems, exhibits the same phenomenology when they are packed. A concrete example is the following: D’Anna and Gremaud [16] have studied the slowdown of a granular system made of millimetric glass beads, subject either to a continuous vertical sine vibration or to taps<sup>4</sup>. An accelerometer measures the reduced acceleration  $\Gamma = a\omega^2/g$ ,

---

<sup>4</sup>The explored range of frequencies  $f_s$  goes from 50 to 371 Hz, and taps consists of

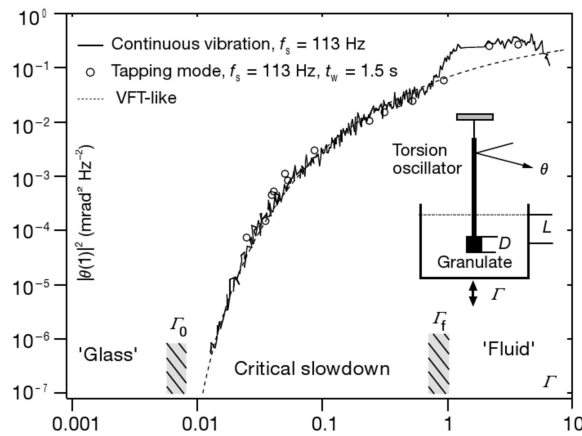


Figure 1.4: Power spectrum level at 1 Hz,  $|\theta(1)|^2$ , versus  $\Gamma$  obtained from continuous vibration spectra (—) or from tapping spectra ( $\circ$ ). The dotted line is obtained according to a VFT-like form. Adapted from D’Anna and Gremaud [16].

and a torsion oscillator whose rotating probe is immersed in the granular material measures the “granular noise” given by the power spectrum level at 1 Hz,  $|\theta(1)|^2$ . The oscillator performs a brownian-like motion, and the angular deflection  $\theta$  is optically detected. The authors measure a  $1/f^2$  noise and use the Wiener-Khintchine theorem to assert that the noise intensity at a given frequency is proportional to the diffusion coefficient. In fig. 1.4, the noise intensity at 1 Hz is represented as a function of the reduced acceleration  $\Gamma$ : the dramatic slowdown – characteristic of glass-formers – is strikingly similar to those observed in thermal liquids, both for the vibrating and the tapping procedures. The data are obtained by decreasing  $\Gamma$ , but equivalent measures are recorded if  $\Gamma$  is increased. Also, no difference is seen if the points are collected at a rate two orders of magnitude smaller. Moreover, a VFT-like law of the form  $|\theta(1)|^2 = A \cdot \exp(B \cdot [\Gamma - \Gamma_0]^p)$  fits well the data.

Hence for athermal systems alternative diagrams similar to 1.2 can be drawn, and in particular fig. 1.5-like diagrams where the control parameter is the packing fraction  $\phi$ .

In this diagram,  $\phi_F$  and  $\phi_M$  represent the freezing (liquidus) and melting (solidus) points and  $\phi_{OCP}$  is the *Ordered Close Packing*.  $\phi_K$  is the ideal transition (if any) and  $\phi_{GCP}$  the corresponding “close packing” quantity, the *Glass Close Packing*. Several “glassy” branches are possible starting from the metastable branch.

Immediately, several questions arise: can vibration be considered as an effective temperature? Or is there an intensive parameter associated with free volume that could be considered as an effective temperature? To what extent is this “thermalization” akin to the classical thermodynamic temperature? Can one build a thermodynamic description of granular packings? Some general results for dynamical systems [17] suggest that, in the stationary states, their properties could be well described by the ensemble average

---

single cycles of a  $f_s$  sine wave separated by lags  $t_w$ . The reduced acceleration  $\Gamma$  varies between 0.003 and 6.

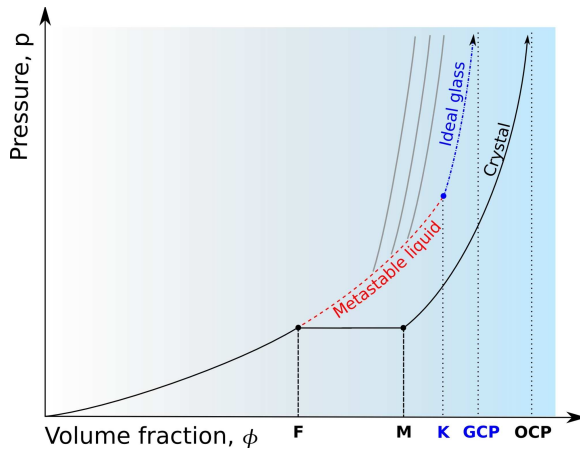


Figure 1.5: Schematic phase diagram for 3D hard spheres, in case of the presence of an ideal glass transition, as a function of the packing fraction  $\phi$ . Adapted from Parisi and Zamponi [9].

of a certain measure. Several propositions have been made for this measure; the first one, proposed by Edwards [18], only take into account microscopic volumes, neglecting the energy or the force network. Other approaches include a description of the force distribution in the material [19].

These are still hotly debated issues. Here, we just want to emphasize that the phenomenology of the slowing down of real liquids when temperature is lowered and assemblies of particles when density is increased are strikingly similar, and that all the following observations in this introduction chapter stand for both thermal and athermal systems. So from now on we will consider indiscriminately thermal and athermal glass formers, with respective transition-relevant parameters the temperature  $T$  and the packing fraction  $\phi$ . Phenomenological support for this analogy had been given in Marty's thesis [20], and we will see in 4.4.2 that the correspondence may be even deeper, since we show that the same microscopic mechanisms are at play.

#### 1.1.4 The structural mystery

*Two things threaten the world: order and disorder.*

– Paul Valéry

The fact that meso and macroscopic particles display a glassy behavior has a great practical importance, because it is much simpler to observe them in experiments. Instead of using a microscope to locate the molecules, one can simply increase the size of the systems up to a macroscopic scale and use standard digital photography to track the particles; one can still treat large enough systems, with several thousands of particles. This way, several structural and dynamical quantities can be directly and quite precisely computed, and compared to theoretical predictions.

The ability to compute structural quantities in these systems confirmed a crucial point, already suggested in light scattering experiments on real liq-

uids and in simulations [21]: structure does not seem to evolve as the system fall out of equilibrium and as the dynamics tremendously slows down. An overview of the different quantities proposed in the literature, and why we believe that they fail to achieve a general description of the glass transition is given in 4.5.2.

**An article of faith.** A number of recent investigations have considered the connection between dynamics and structure, by means of topological approaches (*e.g.* [22]), potential energy (*e.g.* [23]), or free volume (*e.g.* [24]) for instance. While most of them have reported some correlation, none has established a correlation of sufficient strength to indicate a causal link, *i.e.* that the dynamics was determined by the selected aspect of the local structure. Ediger remarked in [25] that: “*At present, it is an article of faith that something in the structure is responsible for dynamics that can vary by orders of magnitude from one region of the sample to another at  $T_g$ .*”

Given the extensive literature on this topic, we will not enter into a detailed description of all the attempts to characterize the relation between dynamics and structure at the glass transition; a brief summary of the ones we have tried or checked (and why they failed), will be given in 4.5.2. Note that a recent technique, based on the use of the isoconfigurational ensemble [21, 26], showed that the localized low-frequency normal modes of a configuration in a supercooled liquid are causally correlated to the irreversible structural reorganization of the particles within this configuration. This point surely deserves further investigations, and we will illustrate in 4.4.2 that we have been able (*i*) to reproduce this result in a close but different system and (*ii*) to be more specific on the correspondence between some non-local<sup>5</sup> structural properties and the dynamics of the particles.

**On the susceptibility of a true phase transition.** One argument against a true phase transition is that the evolution of the structure is at odds with the classical phase transition scenario. Consider for instance a system close to its liquid-gas critical point; the order parameter is the density  $\rho(\vec{r})$  and the transition is associated with the divergence of the spatial density fluctuations at the critical point, generating the famous critical opalescence [27]. Density fluctuations  $\delta\rho(\vec{r}) = \rho(\vec{r}) - \langle\rho\rangle$  grow because large correlated domains arise; the latter are usually probed with the spatial correlation function:

$$G(\vec{r}) = \int \langle \delta\rho(\vec{u}) \cdot \delta\rho(\vec{u} + \vec{r}) \rangle d\vec{u} \quad (1.3)$$

---

<sup>5</sup>Though the soft modes in [26] are “localized” and the structural properties “non-local”, we are talking of the same objects. They are larger than one single grain but smaller than the whole system; so they are *localized* or *not*, depending on the viewpoint.

At this point there are two parallel ways to probe the correlation length: the first one is to compute the susceptibility:

$$\chi = \int G(\vec{r}) d\vec{r} \quad (1.4)$$

that will naturally increase with the correlations, and diverge when  $T$  approaches the critical temperature  $T_c$  like  $\chi \propto |T - T_c|^{-\nu(2-\eta)}$ . The second method is to consider the radial behavior of this correlation function  $G(r) \propto r^{2-d-\eta} e^{-r/\xi}$  and to extract the correlation length  $\xi$ . In particular  $\xi$  diverges like  $|T - T_c|^{-\nu}$  at the critical point. Moreover, the typical fluctuation time  $\tau$  will also diverge, and is linked to  $\xi$  with the following relation:

$$\tau \propto \xi^z \quad (1.5)$$

where  $z$  is called the dynamical exponent.

In glass formers, though the slowdown of the dynamics could be interpreted as a critical divergence of the fluctuation time, such spatial correlations of the density field do not seem to have any special behavior in the vicinity of  $T_g$ .

As a conclusion, several purely structural observables have been investigated, but none of them have been able – so far – to explain by itself the tremendous slowdown of the dynamics.

### 1.1.5 Toward a dynamical transition

However, physical intuition associated with several clues – for instance the super-Arrhenius behavior and the VFT fit – suggests that the slowing down is accompanied with a growing lengthscale. To get out of this seemingly paradoxical situation, several authors [28, 29, 30] have proposed the idea that this length scale is not structural, but *dynamical*. The underlying idea is that as individual moves become more difficult when the liquid cools down, the particles have to collaborate in increasingly larger aggregates to rearrange. Such collective rearrangements do not correspond to the structural heterogeneity as in the classical view presented in 1.1.4, but rather to the heterogeneity of the dynamics itself.

**Intermediate scattering function.** A first measure that captures the heterogeneous nature of the relaxation field is the self part of the intermediate scattering functions:

$$F_s(\vec{k}, \tau, T) \equiv \left\langle \frac{1}{N} \sum_{j=1}^N e^{i\vec{k} \cdot \vec{r}_j(\tau)} e^{-i\vec{k} \cdot \vec{r}_j(0)} \right\rangle = \left\langle \frac{1}{N} \sum_{j=1}^N e^{i\vec{k} \cdot [\vec{r}_j(\tau) - \vec{r}_j(0)]} \right\rangle \quad (1.6)$$

where  $\vec{r}_j(\tau)$  is the position of particle  $j$  at a lag time  $\tau$ . This is indeed an appropriate quantity to study the relaxation of a system composed of

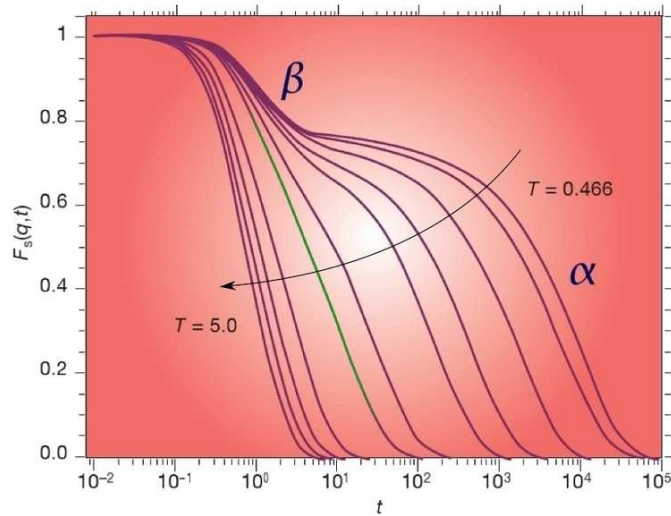


Figure 1.6: Evolution of the self-intermediate scattering function in a supercooled Lennard–Jones mixture. Temperatures are expressed in reduced units of  $T/T_g$  and are from left to right: 5, 4, 3, 2, 1 (green), 0.8, 0.6, 0.55, 0.5, 0.475, and 0.466. Note the two-step relaxation behavior upon decreasing  $T$ . Adapted from Debenedetti and Stillinger[13].

$N$  tracked particles, since this is the Fourier transform of the Van Hove function [31], *i.e.* the probability to find a particle at time  $t$  at a distance between  $r$  and  $r + dr$  from its initial position.  $F_s(t)$  is a measure of the time needed so that a particle has lost the “memory” of its initial position, or conversely have moved more than  $1/\|\vec{k}\|$ . As this quantity is accessible with light and neutron scattering techniques, it has been widely measured.

At high temperature this function is exponential, while for lower values of  $T$  a two-step relaxation appears: a rapid relaxation first, usually called  *$\beta$ -relaxation*, followed by a plateau and then a second relaxation, slower and well-fitted by stretched exponentials, usually called  *$\alpha$ -relaxation*. The latter corresponds to the structural relaxation of the liquid<sup>6</sup>. The usual interpretation of this behavior is the following: at very short time the particles have a ballistic regime and decorrelate easily, but very soon they are blocked by their neighbors and cannot diffuse freely, leading to a plateau at intermediate time scales during which the structure little evolve. At last, the  $\alpha$ -relaxation traduces the fact that some sets of particles can still move albeit collectively, hence decorrelating the structure on the very long timescales.

<sup>6</sup>Several other quantities probe the same phenomena, eventually on wider temperature intervals, for instance the dielectric susceptibility. See [32] for a review and interesting openings on the measurement of the dynamical susceptibility.

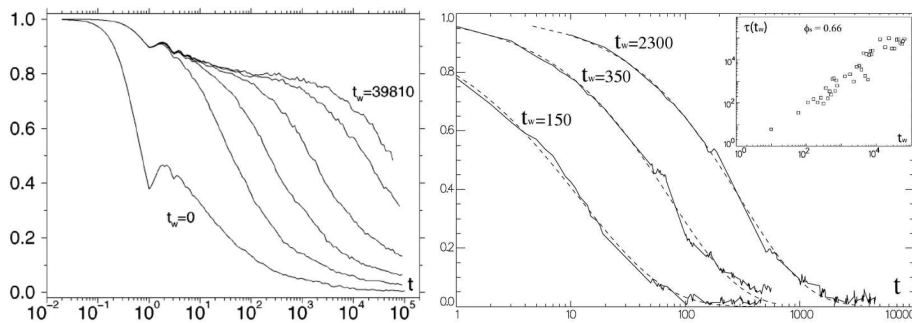


Figure 1.7: **Left**  $F_s(\vec{q}, t_w, \tau, T)$  for several values of  $t_w$  in a Lennard-Jones liquid. From Kob and Barrat [36]. **Right** Same dependence in the granular system of Kabla and Debrégeas [37]. **Inset** Characteristic relaxation time  $\tau(t_w)$  as a function of the packing fraction.

**Cages.** This interpretation is coherent with a well known feature of the dynamics of the particles called the *cage effect*. In all glass-formers on approach to the glass transition (*e.g.* [33, 34, 35]) the trajectory of every single particle evolves from Brownian motion in the liquid phase to a “caged” behavior, namely the fact that a particle remains trapped in some regions of space for long times, vibrating around a quasi-equilibrium position (see fig. 4.1). At some – seemingly unpredictable – times, the particles displace their equilibrium positions during a “cage escape”, or “jump”. As the system approaches the glass transition, the cage time becomes longer and longer, justifying the growth of the plateau in the intermediate scattering function. Cage jumps will be at the basis of our analysis in chapter 4.

**Ageing.** A system at equilibrium is time-invariant; when a supercooled liquid falls out of equilibrium and become a glass, this property is lost. The structure factor – as defined in eq.(1.6) – acquires a fourth parameter  $t_w$ , the “age” of the system, and becomes:

$$F_s(\vec{q}, t_w, \tau, T) = \left\langle \frac{1}{N} \sum_{j=1}^N e^{i\vec{q} \cdot [r_j^*(t_w + \tau) - r_j^*(t_w)]} \right\rangle \quad (1.7)$$

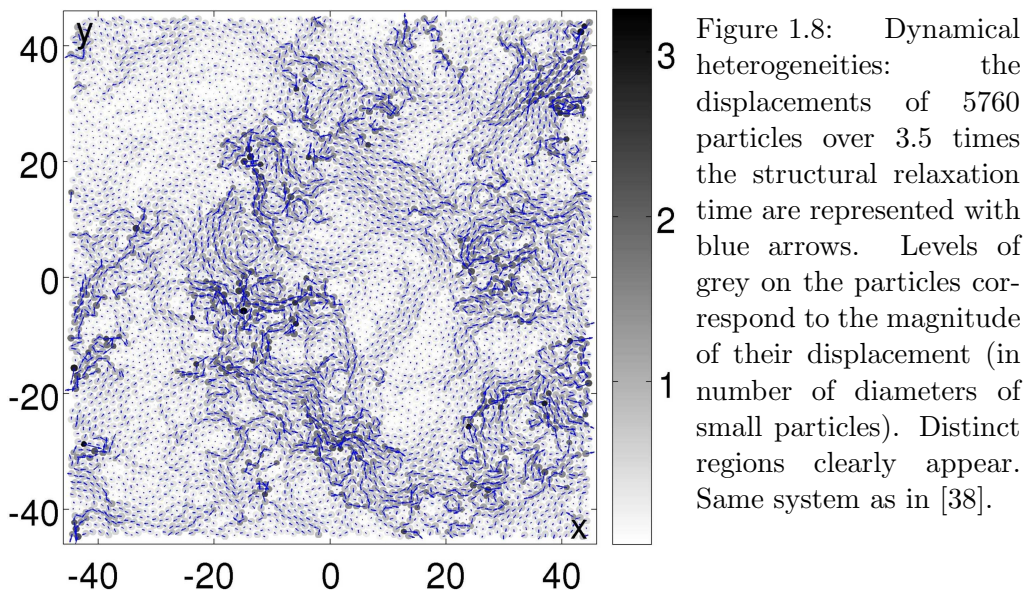
In a simulated Lennard-Jones liquid close to the glass transition, one can indeed observe that the structural relaxation clearly depends on the age of the system [36] (see fig. 1.7-left). Kabla and Debrégeas [37] have also observed the same phenomenon in a tapped granular system: they prepare the system in a compact state by applying large amplitude taps, and when the packing is dense enough,  $t_w$  is set to 0 and the experiment can start; the pile is then gently tapped in order to create some movements without varying the packing fraction. They analyze the structural relaxation with

multispeckle diffraction and observe that the typical decay time grows with the age of the system (fig. 1.7-right and inset).

In our analysis of the dynamics close to the glass transition (chapter 4), we will let this observation aside and focus on the supercooled states, *i.e.* when the system is still at equilibrium. For our study of the jammed states in chapter 3, we will perform our measurements in very dense states but in a reversible regime where no aging occur; the issue of aging will however be briefly addressed in 3.3.1.

**Heterogeneous relaxation.** The stretched exponential behavior of the  $\alpha$ -relaxation can be explained in 2 different manners: (*i*) the relaxation is locally exponential but the typical time scale varies from place to place, such that the average of all these contributions is a stretched exponential, or (*ii*) the relaxation is a locally complex and already non-exponential. Several experimental and theoretical works (see [25] for a review) suggest that both scenarios are at play, but the essential conclusion is that the dynamics close to the glass transition is heterogeneous in space. As supercooled liquids are ergodic, the dynamics is also heterogeneous in time, meaning that fast regions become slow after some time, and vice-versa.

All this suggests that some collective reorganizations appear in supercooled liquids close to the glass transition, forming the spatial heterogeneities. On what time scale do they typically appear? What is their typical size? How do these time and length scales evolve with the proximity to glassiness? During the last decade, the study of dynamical heterogeneities greatly helped to answer these questions.



### 1.1.6 Dynamical heterogeneities

Several simulations of liquids, in which the position of each particle is known at each time, have confirmed the existence of a heterogeneous dynamics. For instance, the displacements of the particles in a simulated binary softly interacting particles liquid [38] are represented on fig. 1.8. Clearly, distinct regions appear.

When one now follows a single particle, the square displacement probed over a time  $t$  shows large “jumps” separated by long plateaus, during which the particles essentially vibrate around the same equilibrium position (see fig. 1.9a). When one coarsegrains on a specific region of space, or equivalently if one looks at a system with few particles, the same behavior is observed and the structure relaxes by “earthquakes” or “cracks” (see fig. 1.9b). When one now takes several particles from different random regions of a large system, the jumps seem to happen at random and cannot be predicted from the average relaxation (fig. 1.9c).

Hence the structural relaxation shows strong fluctuations when probed on a sufficiently large length scale. Theoreticians intuited that the typical time and length scales of the dynamical relaxation should be contained in these fluctuations, and found that the four point correlation functions is a useful tool to describe these fluctuations. Indeed, in the case of a classical second order phase transition the order parameter is a structural quantity (*e.g.* the density  $\rho$ ), while in the case of the glass transition it is the temporal correlations themselves that are close to zero in the liquid phase and finite in the glass state (see [6] for a review). The equivalent of an order parameter would be the dynamical quantity  $C_\rho(\tau) = \langle \delta\rho(\tau)\delta\rho(0) \rangle$  in the limit  $\tau \rightarrow \infty$ .

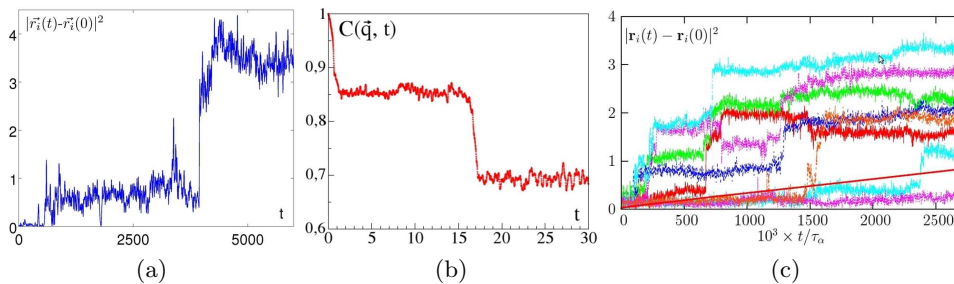


Figure 1.9: **(a)** and **(c)** Square displacement of individual particles of softly interacting particle liquids, respectively issued from the dataset of [38] and from Berthier and Biroli [6]. In (c), the average value is shown as the full red line. **(b)** Self scattering function  $C(\vec{q}, t) \equiv \langle \exp[jq(r_i(t) - r_i(0))] \rangle_i$  versus time, where  $i$  is an average on all particles,  $r_i(t)$  is the position of particle  $i$  at time  $t$  and  $\|\vec{q}\| = 2\pi/\sigma_1$  in a system of  $N = 256$  bidisperse hard spheres (from Brito and Wyart [39]), at  $\phi = 0.837$ . Note the plateaus of  $C(\vec{q}, t)$ , and the drops, called “earthquakes”.

The 2 points correlation function  $G(\vec{r})$  of relation (1.3) is then replaced by the 4 points (2 in time, 2 in space) correlation function:

$$G_4(\vec{r}, \tau) \equiv \int \langle \delta h_\rho(\vec{u}, \tau) \cdot \delta h_\rho(\vec{u} + \vec{r}, \tau) \rangle_t d\vec{u} \quad (1.8)$$

where  $h_\rho(\vec{r}, \tau) = \delta\rho(\vec{r}, \tau)\delta\rho(\vec{r}, 0)$  is the local temporal correlation, and  $\delta h_\rho = h_\rho - \langle h_\rho \rangle$ . The susceptibility  $\chi$  defined in relation (1.4) becomes the dynamical susceptibility  $\chi_4(\tau)$ :

$$\chi_4 \equiv \int G_4(\vec{r}, \tau) d\vec{r} \quad (1.9)$$

and can be evaluated with the following relation:

$$\chi_4(\tau) \sim \langle [H(\tau) - \langle H(\tau) \rangle]^2 \rangle \quad (1.10)$$

where  $H(\tau) = \int h_\rho(\vec{r}, \tau) d\vec{r}$ .

The general behavior of  $\chi_4(\tau)$  is always as follows [40, 41]: it first increases, peaks at an intermediate time scale, and then decreases. Fig. 1.10-left shows examples of this peak for several temperatures. It measures the typical size of the decorrelation domains, which grows as the system goes glassy. Note that the magnitude of the peak depends on the length scale at which the motion is probed, as illustrated on fig. 1.10-right, and that there exists at a given temperature – or packing fraction – a length scale for which the peak amplitude of the  $\chi_4$  is maximal. The dependence of the  $\chi_4$  on the parameters is explicitly detailed in appendix B.2.

Moreover, a characteristic length can be extracted from the decay of  $G_4(r)$ , usually called  $\xi_4$ . It has been suggested that the increase of  $\chi_4^{max}$  as

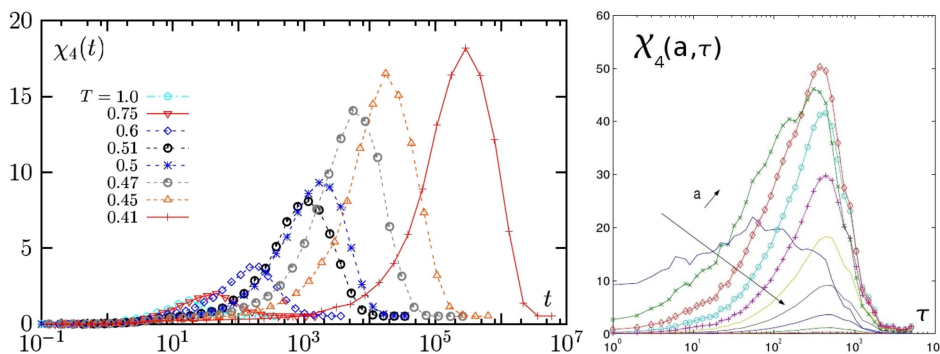


Figure 1.10: **Left** Time dependence of  $\chi_4(t)$  in a Lennard-Jones supercooled liquid. From Berthier and Biroli [6].  $\chi_4^{max}$  shifts to larger times and larger values when  $T$  is decreased, revealing the growing length scale of dynamic heterogeneity. **Right** Time dependence of  $\chi_4(t)$  in a granular system for different values of the probing length scale  $a$ . From Dauchot *et al.* [40].

the temperature diminishes corresponds to an increase of  $\xi_4$  [42, 43]. This result is particularly relevant with respect to the numerous theories of the glass transition invoking or involving growing areas of dynamical correlations. As a consequence, finding a growing lengthscale associated to the growing timescale is a strong argument in favor of a critical transition, and remains an important *casus belli*. However, critical or not, this transition is of a different kind of the usually known phase transitions since it is a *dynamical* transition, that occurs without clear structural signature.

## 1.2 The Jamming transition

*The rule is, jam tomorrow and jam yesterday - but never jam today.*

– Lewis Carroll, *Through the looking glass, and what Alice found there* (1871)

### 1.2.1 What is jamming?

To illustrate what jamming is, an entertaining example is the “rickshaw jam” game<sup>7</sup> (see fig. 1.11), in which one has to move a rickshaw out of a parking where many other vehicles are blocking the way. The vehicles can be displaced along their axis until they are themselves blocked by other vehicles. As intuition – and daily experience – would predict, two behaviors can be observed as the amount of free space between the vehicles is reduced: (i)

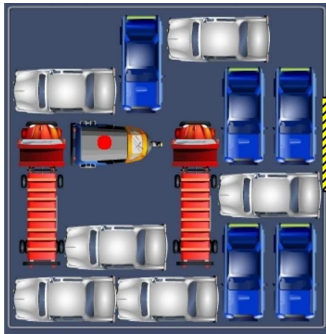


Figure 1.11: The *rickshaw jam* game. Translate vehicles in order to move the rickshaw (marked with a red dot) to the door on the right.

(ii) it becomes harder and harder to move, even for a very few steps. The time needed to browse a given distance grows and the number of vehicles to move grows as well<sup>8</sup>; this is the challenging point of the game. (ii) At some point the assembly of vehicles will jam, *i.e.* the only possible movement is the global translation. If

one pushes a single car, all the cars will move as a whole, except the rattlers. In this simple system, macroscopic rigidity arises from entanglement.

More generally, one specificity of assemblies of macroscopic particles is that – contrary to real liquids – one can study their properties as a function of the packing fraction even at zero temperature. For instance, one can make hard spheres inflate and observe that the overlap pressure is zero until a certain packing fraction, at which it diverges [44]. Similarly, a set of particles with finite-range repulsive interactions confined in a quasi-statically volume-decreasing box will build up a pressure at a sharply-defined density [45]. This

<sup>7</sup>Available at <http://www.freeonlinegames.com/racing-games/rickshaw-jam.html>

<sup>8</sup>Note that here the particles move asynchronously, and “time” is expressed in number of moves, like in a Monte Carlo simulation.

effect is called the *jamming transition*. If one wants to define jamming in a protocol-independent manner<sup>9</sup>, the best definition is that an amorphous system jams when it develops a yield stress [46]<sup>10</sup>. Interestingly, at non-zero temperature jamming occurs together with a sharp slowdown of the dynamics and eventually dynamical arrest<sup>11</sup>.

Actually, a wide class of systems – thermal or not – jams. Granular systems jam at several occasions: avalanches at the surface of a sand pile naturally stop when the slope becomes lower than a precise angle [48, 49], or grains in a hopper may stop flowing if some force chains establish between the boundaries of the funnel, giving the grains the ability to sustain the weight of the whole pile. Some other (better controlled) protocols of jamming of hard spheres, with or without friction, will be presented below.

Colloids are another usual playground to study jamming. Recently, a

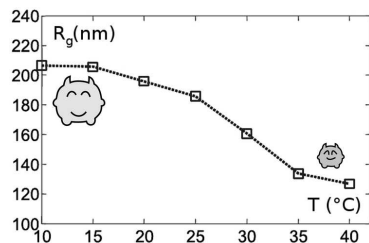


Figure 1.12: Radius of gyration  $R_g$  of thermosensitive PNIPAM microgel particles as a function of  $T$ . Adapted from Purnomo *et al.* [50].

large number of colloidal studies have been focusing on thermosensitive microgel particles, called PNIPAM (for poly-N-isopropylacrylamide) [50]. One can indeed make them substantially grow or shrink by tuning the temperature on an easily accessible temperature panel, as illustrated on fig. 1.12. Thanks to this useful property, these systems acquired rapidly the status of model experiments for jamming: they are the ideal experimental counterpart of the numerous previous numerical studies in

which particles grow.

Several other examples in the field of condensed matter can be mentioned. In emulsions, two regimes can be identified: at low droplet concentrations the mechanical response of the system is driven by the liquid matrix while at high concentration the mechanical properties are totally different [51]. Sheared foams display a yield stress above which they flow and below which they do not [52]. One can also cite the case of toothpaste [53], entangled polymers [54], amongst others (see [55] for a review).

Interestingly, the scope of jamming extends far beyond condensed matter physics. For instance, equivalent problems are encountered in protein folding [56] and, of course, traffic jams [57, 58]. The basic idea is that a growing number of constraints makes the system jam, or block, very rapidly. These questions are formally addressed in studies of constraint satisfaction problems and optimization under constraint problems [59, 60].

Coming back to assemblies of particles, jamming is often associated with

<sup>9</sup>See [9] for a review of the protocols leading to a jamming transition.

<sup>10</sup>This transition is sometimes called the rigidity transition. For a discussion, see [47].

<sup>11</sup>Once again, the slowdown is sharper than what one would expect with a simple Arrhenius model of fixed energy barriers.

the appearance of mechanical rigidity. Here we will present the theoretical framework ruling the acquisition of rigidity in a purely elastic model, as well as simulations and experiments with and without friction, which suggest the existence of a critical point.

### 1.2.2 The acquisition of rigidity

Maxwell [61] defined the rigidity of a solid with the following reasoning: consider a system made of  $N$  particles in a  $d$ -dimension space, linked by  $N_c$  perfect springs with equal stiffness  $k$ . If the displacement of particle  $i$  is  $\delta\vec{R}_i$ , the energy variation of a global displacement can be written as:

$$\delta E = \frac{k}{2} \sum_{\langle ij \rangle} \left[ \left( \delta\vec{R}_j - \delta\vec{R}_i \right) \cdot \vec{n}_{ij} \right]^2 \quad (1.11)$$

where the sum is on all couples  $\langle ij \rangle$  of particles in contact and  $\vec{n}_{ij}$  is the unitary vector going from  $i$  to  $j$ . One can also express this relation in an algebraic form:

$$\delta E = \langle \delta\mathbf{R} | \mathcal{M} | \delta\mathbf{R} \rangle \quad (1.12)$$

where  $|\delta\mathbf{R}\rangle$  is a  $d \times N$  vector representing the displacement of all particles, and  $\mathcal{M}$  is called the *dynamical matrix*. Its eigenvectors  $\mathcal{U}_k$  are the vibrating modes of the system and their eigenvalues  $\lambda_k$  are their squared frequency:  $\forall k, \lambda_k = \omega_k^2$  (see [62, 63] for details).

Such an elastic system is rigid if and only if there is no zero frequency mode, except of course the trivial global translation modes. Starting from a high number of constraints – *i.e.* a high number of link  $N_c$  – one can remove the contacts until at least a zero frequency mode, also called *soft mode*, appears (see fig. 1.13).

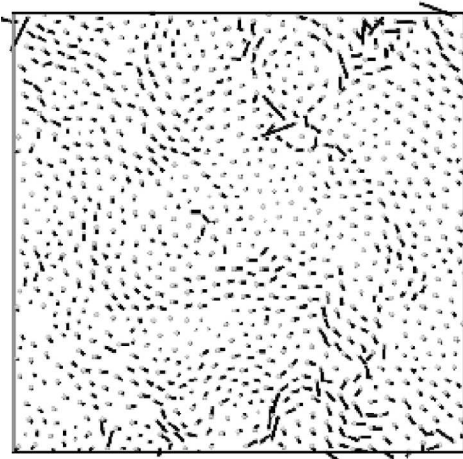


Figure 1.13: A soft mode for a 2D system of  $N \simeq 1000$  particles with periodic boundary conditions. Relative displacements are represented with black lines. Starting from an isostatic configuration, 20 contacts along the vertical borders (in grey) have been removed. The soft modes have then been computed and the mode pictured is an arbitrary linear combination of these modes. From Wyart [64].

As all terms in eq.(1.11) are positive, the soft mode verifies:

$$\forall \langle ij \rangle, (\delta\vec{R}_j - \delta\vec{R}_i) \cdot \vec{n}_{ij} = 0 \quad (1.13)$$

Interestingly, this is a purely geometrical relation, independent of the potential between the particles. Maxwell noticed that the number of independent constraints  $N_c$  should be greater or equal than the number of degrees of freedom  $N_d = N.d$  so that no solution can be found. It is therefore the necessary and sufficient condition of a rigid system. If one defines the average coordination  $z \equiv 2N_c/N$ , the number of constraints is  $N_c = Nz/2$  and this condition can be rewritten:

$$z \geq 2d \equiv z_{iso}^0 \quad (1.14)$$

Importantly, this is a global criterion since soft modes represent the displacement of the whole assembly of particles.

If  $z$  is strictly greater than  $2d$  the system is called *hyperstatic*, if it is strictly lower the system is *hypostatic*, and if it is exactly  $2d$  the system is *isostatic*, or *marginally rigid*. As we will see in the following, this is the case on jamming if the rattlers<sup>12</sup> are excluded. One can directly measure the distance to isostaticity (*i.e.* the distance to rigidity) by computing the average coordination excess  $\delta z_0 = z - z_{iso}^0$ .

Starting from Maxwell's and Alexander's [65] works, Wyart has predicted the divergence of a characteristic length scale  $l^*$  associated to the lowest frequency modes close to the rigidity transition [64].  $l^*$  is typically the size of the largest sub-systems having soft modes, and scales as:

$$l^* \propto \delta z_0^{-1}. \quad (1.15)$$

In addition, this theory makes predictions on the critical exponents of several measurable quantities. In the case of a harmonic interaction potential, one would expect the pressure  $p$  scaling as  $\phi - \phi_c$ , the average excess of coordination  $\delta z_0$  as  $p^{1/2}$ , the shear modulus  $G_\infty$  as  $\delta z_0$  and the elastic bulk modulus  $K$  to be constant.

### 1.2.3 Criticality and diverging lengthscale

This theory echoes previous numerical studies by O'Hern *et al.* [45], in which  $2D$  and  $3D$  systems made up of particles interacting with finite range repulsive potentials jam in a disordered state at *zero temperature* and *zero applied stress*. They found two major results:

- The distribution of  $\phi_c$  values becomes narrower as the system size increases, so that all configurations jam at the same packing fraction in the thermodynamic limit. For a given protocol in the thermodynamic limit, there is a unique jamming threshold  $\phi_c$  at which particles can no longer avoid each other, and the bulk and shear moduli simultaneously

---

<sup>12</sup>Rattlers are particles that are free to move in a cavity formed by their neighboring particles. They have a lack of contact on an entire semicircle.

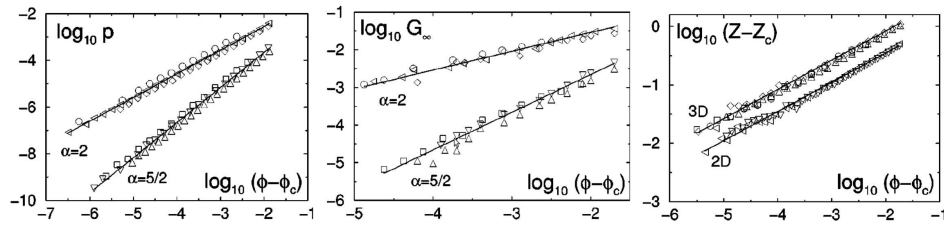


Figure 1.14: Pressure  $p$  (left), static shear modulus  $G_\infty$  (middle) and average excess number of contacts per particle  $\delta z_0 = z - z_{iso}^0$  (right) for 3D monodisperse ( $\circ$ ), 3D bidisperse ( $\diamond$ ), and 2D bidisperse ( $\triangleleft$ ) systems with harmonic repulsions ( $\alpha = 2$ ) and for 3D monodisperse ( $\square$ ), 3D bidisperse ( $\triangle$ ), and 2D bidisperse ( $\nabla$ ) systems with Hertzian repulsions ( $\alpha = 5/2$ ).  $N = 1024$  ( $N = 512$ ) particles were respectively used for the 2D (3D) systems. From O’Hern *et al.* [45].

become finite. This defines *point J*, the jamming threshold occurring at zero temperature and zero applied stress.

It has been proposed to assimilate point *J* with random close packing ( $\phi_{RCP} \sim 0.64$  in 3D). However the precise value of point *J* has been found to depend on the details of the protocol [66], and the concept of random close packing itself seems ill-defined.

- Point *J* has reminiscent properties of a critical point. For instance, as point *J* is approached from higher packing fractions power-law scalings are found for the vanishing of the pressure, shear modulus, and the average coordination excess, as shown in fig. 1.14. The authors underline the fact that the exponents depend on the interparticle potential, as predicted by Wyart’s theory. Finally, the values found for the exponents in these numerical simulations are coherent with the exponents derived from Wyart’s analysis.

This work also suggests the existence of a length scale that diverges at point *J*. Shortly after, Ellenbroek *et al.* [46, 67] have strengthened this view by studying 2D packings of frictionless Hertzian spheres<sup>13</sup> confined in a box with a known force acting at the boundaries. They make the system approach jamming from above, reducing the pressure at the boundaries, and they observe that the heterogeneity of the response to either a global shear stress or a local load are increasingly heterogeneous as the pressure is close to zero (see fig. 1.15).

Ellenbroek *et al.* noticed that the response to a global forcing becomes increasingly non-affine near point *J*, and attributed this effect to the proximity of soft modes. Indeed, as suggested by Wyart’s theory and measured

<sup>13</sup>Hertzian repulsion takes the elastic deformation of the contact into account, such that contact forces scale like the overlap between the neighboring particles to the power 3/2.

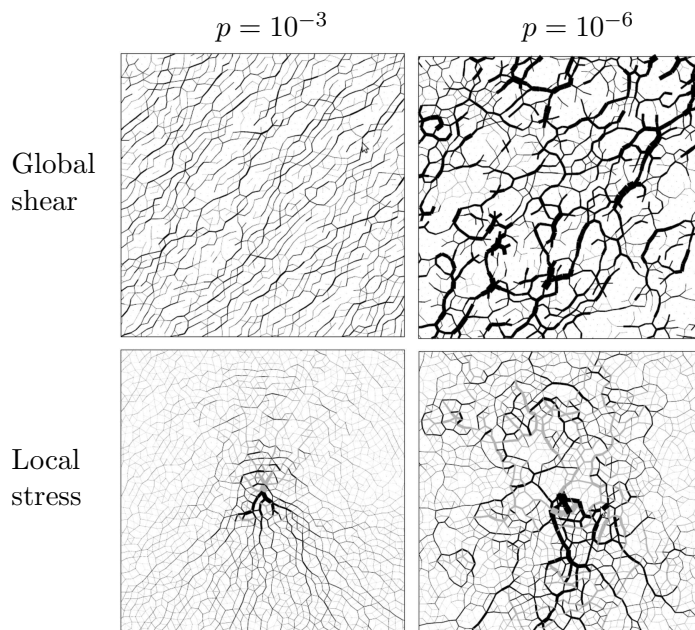


Figure 1.15: **Top** Responses to a global shear, with only the compressed contacts drawn. **Bottom** Responses to an in-plane external force on a single particle. Black (grey) lines indicate an increase (decrease) in contact force, the thickness corresponds to the magnitude of the change. Left images are at  $p = 10^{-3}$  while right ones are at  $p = 10^{-6}$ . From Ellenbroek *et al.* [46].

by Ellenbroek *et al.* a large excess of soft modes heaps the density of states  $D(\omega)$  close to point  $J$ . Ultimately, at point  $J$ , the density of states is a constant all the way down to zero frequency (see fig. 1.16).

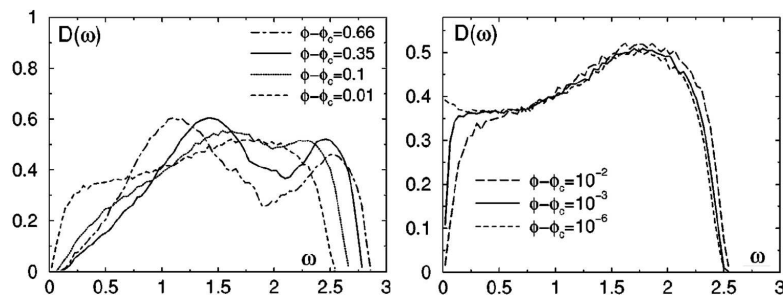


Figure 1.16: Density of states  $D(\omega)$  as a function of  $\omega$  for a 3D ( $N = 1024$ ) system with harmonic repulsions at packing fractions (**left**) far from  $\phi_c$  and (**right**) close to  $\phi_c$ . One can see an excess of low-frequency modes as the packing fraction approaches  $\phi_c$ . From O'Hern *et al.* [45].

### 1.2.4 The role of friction

Experimental studies of macroscopic hard spheres – like granular materials – often add another challenging difficulty, namely the presence of dry friction. Frictional forces amongst grains usually behave within Coulomb’s model: no motion happens as long as the tangential force  $f_t$  remains below the threshold value  $\mu f_n$ , where  $f_n$  is the normal force and  $\mu$  the static friction coefficient, but sliding occurs as soon as the tangential force  $f_t$  reaches the threshold value. For an immobile contact with a given value of  $F_n$ , this directly leads to a degeneracy of the possible tangential force:  $f_t \in [-\mu f_n, \mu f_n]$ . As a consequence in an experiment one cannot determine the force network, even with a perfect precision on the positions.

Moreover, friction is usually hysteretic because the dynamical friction coefficient is often smaller than the static friction coefficient. This causes the evolution of a granular system to depend on its history. In particular, for a given configuration and a given force network, the system can be flowing or not, depending on its history.

**In theory.** Despite these complications, one can take friction into account in the previous theoretical framework. The forces applying on each pair of grains in contact have to be added to the description: for each contact  $\langle ij \rangle$  there is a normal component  $f_n^{ij}$  and a tangential component  $f_t^{ij}$ . The system is at rest when all forces and torques equilibrate on each particle:

$$\forall i, \sum_j f_n^{ij} \cdot \vec{n}_{ij} + f_t^{ij} \cdot \vec{n}_{ij}^\perp = \vec{0} \quad (1.16)$$

$$\forall i, \sum_j f_t^{ij} \cdot \vec{n}_{ij}^\perp = \vec{0} \quad (1.17)$$

The counting argument is now the following: there are  $dNz/2$  contact force components constrained by  $dN$  force equations and  $d(d-1)N/2$  torque balance equations, *i.e.*  $d(d+1)N/2$  constraints. The rigidity criterion is:

$$z \geq d + 1 \equiv z_{iso}^\mu \quad (1.18)$$

Note that this rigidity criterion is looser than in the frictionless case as soon as  $d > 1$ . Hence, in  $2D$ , depending on the history of the packing the rigidity transition can occur anywhere in the range  $3 < z < 4$ . The point where the pressure appears/vanishes is located at an average coordination number which is most of the time greater than the isostatic value  $z_{iso}^\mu = 3$ , and is different for each configuration. What selects the contact number of a frictional packing at  $J$  is not well understood. Still, simulations for disks in  $2D$  show that in practice  $z_J(\mu) = z^\mu(p=0)$  is a decreasing function of  $\mu$ , ranging from 4 at small  $\mu$  to 3 for large  $\mu$  [68, 69, 70] (see for instance fig. 1.18-right in the limit  $p \rightarrow 0$ ). The elastic moduli  $G_\infty$  and  $K$  keep the same scaling, respectively in  $\delta z_0$  and constant.

**In the lab.** In parallel, Majmudar *et al.* [71] have experimentally studied the behavior of an assembly of photoelastic grains in a confinement cell made of 4 position-controlled mobile walls. Photoelasticity is indeed a useful property to locate experimentally the contacts sustaining a finite strain. They found the predicted scalings, namely  $\delta z_0 \propto \delta\phi^{1/2}$  and  $p \propto \delta\phi^\psi$  with  $\psi = 1.1$ , as depicted on fig. 1.17:

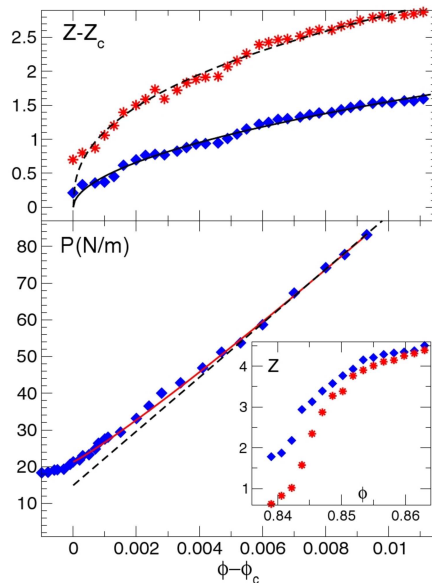


Figure 1.17: Average contact number and pressure at the jamming transition. **Top** and **bottom** panels show  $\delta z_{iso}^0$  and  $p$  vs  $\phi - \phi_c$ , respectively, with rattlers included (red stars) or excluded (blue diamonds). Dashed and full curves in the top panel give power-law fits  $(\phi - \phi_c)^\beta$  with  $\beta = 0.495$  and  $0.561$  for the case with and without rattlers. Full curve in the lower panel gives the fit  $(\phi - \phi_c)^\psi$  with  $\psi = 1.1$ . The dashed line shows a linear law for comparison. **Inset**  $z$  vs  $\phi$  for a larger range in  $\phi$ . From Majmudar *et al.* [71].

However, as the authors honestly remark “*These fits depend on the choice of  $\phi_c$ , which has some ambiguity due to the rounding; the data allow a range from around 0.840 to 0.843. In fact,  $\phi_c$  can be determined in several ways: the point where  $z$  reaches 3, the point where  $p$  begins to rise above the background, etc*”. This points out the difficulty to locate the rigidity transition in experimental systems.

**In silico.** Somfai *et al.* [70] have studied numerically the behavior of a frictional system made of 1000 polydisperse  $2D$  disks interacting via a  $3D$  Hertz-Midlin potential and Coulomb friction. The packings were prepared by cooling while slowly inflating the particle radii in the presence of a linear damping force, until the required pressure is obtained. Once a packing was made, the additional damping force was switched off. Coulomb friction plays a crucial role in this preparation protocol, and the main role of the static friction coefficient  $\mu$  is to tune the average coordination number.

Two main results can be drawn (see fig. 1.18): first, both the low-frequency cross-over  $\omega^*$  in the density of states below which the continuum scaling  $\propto \omega^{d-1}$  is recovered and the ratio  $G/K$  (with  $K$  roughly constant) scale with  $\delta z_0$ , regardless of the presence of friction. Second, the average

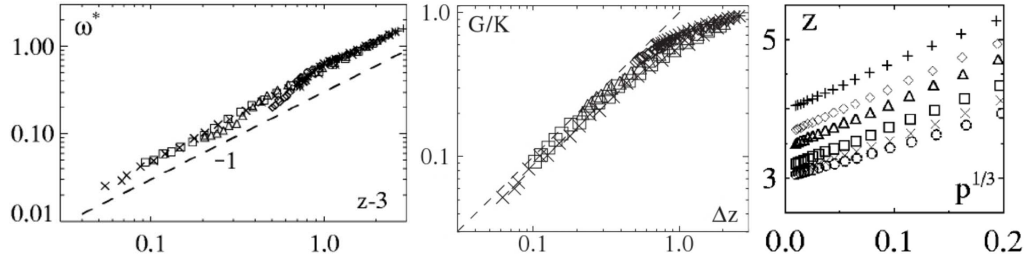


Figure 1.18: **Left**  $\omega^*(\delta z)$ . **Middle** Ratio  $G/K$  as a function of  $\delta z_0$ . **Right** Average coordination  $z$  as a function of  $p^{1/3}$  for various  $\mu$ : 0(+), 0.1(◇), 0.2(Δ), 0.5(□), 1(×) and 10(o). From Somfai *et al.* [70].

coordination number is a complex function of  $\mu$  and  $p$ , but the value  $z_J^\mu$  obtained when  $p \rightarrow 0$  varies as expected between 3 and 4 and the excess of coordination  $\delta z^\mu(p) = z(\mu, p) - z_J^\mu$  scales as  $p^{1/3}$ .

Van Hecke *et al.* [72, 73] have also taken into account the fully mobilized contacts to modify the counting argument: let  $m = |f_t|/\mu f_n$  be the *mobilization* of a contact, such that the contacts at the Coulomb threshold *i.e.* for which  $m = 1$ , are called “fully mobilized contacts”. Van Hecke *et al.* noticed that, for gently prepared packings, the probability density of normalized tangential ( $f_t/\mu$ ) vs normal ( $f_n$ ) forces exhibits a singularity for small  $\mu$ , which

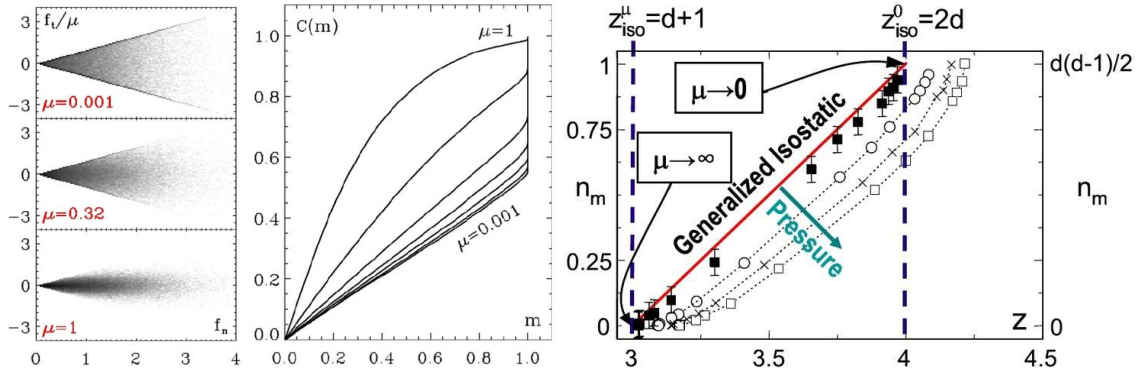


Figure 1.19: **Left** Scatter plots of  $f_t/\mu$  versus  $f_n$  for three packings at  $\mu = 0.001, 0.32,$  and  $1$ . All forces are normalized so that  $\langle f_n \rangle = 1$ .  $p = 2 \times 10^{-5}$ . **Middle** Cumulative distribution of the mobilization  $C_m$  for several  $\mu$ : it exhibits a clear jump near  $m = 1$  at small  $\mu$ .  $p = 2 \times 10^{-5}$ . **Right** Number of fully mobilized forces per particle  $n_m$  as a function of the contact number  $z$ . The data points are obtained in  $2D$ , for  $p \sim 5 \times 10^{-5}$  (□),  $p \sim 2 \times 10^{-5}$  (×) and  $p \sim 5 \times 10^{-6}$  (○). The limit  $p = 0$  (■) is estimated. The red solid line indicates the maximum of  $n_m$ , and such packings are marginal, while below this line one finds hyperstatic stable packings. Adapted from Shundyak *et al.* [72] and van Hecke [55].

rapidly diminishes for larger  $\mu$ , as can be seen in fig. 1.19-left by the excess of values appearing at the boundaries of the Coulomb cone and in fig. 1.19-middle by the jump of the cumulated distribution  $C(m) = \int_0^m P(m') dm'$  at  $m = 1$ .

Since at fully mobilized contacts tangential and normal forces are related, this leads to additional constraints in the counting argument: introducing  $n_m$  as the number of fully mobilized contacts per particle, the  $N.n_m$  additional mobilization constraints make the  $d(d+1)N/2$  rotational and translational degrees of freedom need to be constrained by  $dNz/2 - N.n_m$  independent force components for a packing to be stable, instead of  $dNz/2$ . This lead these authors to propose the generalized isostaticity criterion:

$$z \geq (d+1) + \frac{2n_m}{d} = z_{iso}^\mu + \frac{2n_m}{d} \equiv \delta z^m \quad (1.19)$$

The authors emphasize that, for a surprisingly large range of friction coefficients, gently prepared packings tend to be marginal at jamming (in the  $p \rightarrow 0$  limit), *i.e.* to lie close to the generalized isostaticity line one can see in fig. 1.19-right.

In addition, Henkes *et al.* [73] have shown that the generalized isostaticity can be successfully extended to the dynamical case: they compute the density of states (DOS) of frictional sphere packings while taking into account the fact that contacts at the mobilization threshold ( $m = 1$ ) slip with constant  $f_t$  during small amplitude vibrations, and recover the low-frequency plateau for a very wide range of  $\mu$ . This plateau indeed disappears very quickly as  $\mu$  increases if the fully mobilized contacts are treated as elastic, like the other contacts. The difference between these two situations is illustrated in fig. 1.20.

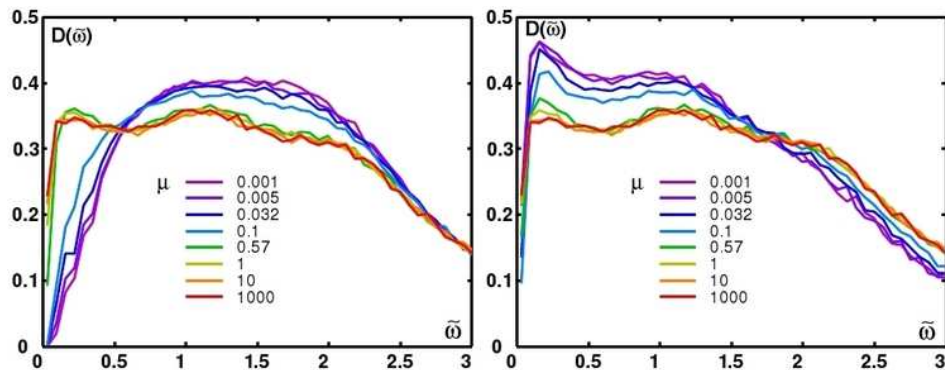


Figure 1.20: DOS while approaching the line of generalized isostaticity ( $p = 1.41 \times 10^{-6}$ ) for a wide range of  $\mu$ , with fully mobilized contacts treated as non-slipping (**left**) or slipping (**right**). From Henkes *et al.* [73].

**In conclusion.** As a conclusion, we can say that a great effort has been made recently to extend the results obtained for frictionless spheres, especially at zero stress and zero temperature where criticality is observed, to the frictional case. The generalized isostaticity criterion appears to be the relevant criterion to avoid the jump of  $z_{iso}^\mu$  when friction becomes finite, and also to describe the dynamics of frictionless and frictional soft spheres in an unified view.

More generally, one would like now to extend the concept of jamming as a function of the packing fraction to non-zero temperature systems and non-zero stress systems, for hard and soft particles, with or without friction. Given these five axis, can one draw a coherent phase diagram? This is a mighty task, not yet achieved, but this is what we are going to address in the next section.

## 1.3 Jamming versus Glass

We have overviewed so far both the glass and jamming transitions, and we have seen that the glass transition is defined from a purely *dynamical* point of view, while – *a contrario* – the jamming transition is often defined from a *mechanical* point of view. Moreover, we have seen that the glass transition is likely to be a *dynamical* transition without clear structural signature, while at the well-defined jamming point the transition is purely *structural*<sup>14</sup>. From this viewpoint, the transitions are different.

On the other hand, the glass and jamming transitions have several common points: the values of  $\phi_G$  and  $\phi_J$  given in the literature are often very close, and several phenomena such as the super-Arrhenius slowdown and dynamical heterogeneities have been reported in both cases<sup>15</sup>. So the question that naturally emerges is whether these two phenomena can be unified in a single paradigm, or not.

### 1.3.1 Where is point J?

Following Cates *et al.* [74], Liu and Nagel [75] laid the foundations of a unification attempt with the following remark: several systems – including foams, granular matter and colloids – have the property to stop flowing, or reversely start to flow, depending on the applied strain. Similarly, a glass former has the property to start/stop flowing according to the temperature. They propose that all glass formers could belong to a common class of systems, for which they propose a phase diagram with three axis: temperature  $T$ , strain  $\Sigma$  and inverse density  $1/\phi$  (see fig. 1.21).

---

<sup>14</sup>The term *structural* used here encompass both the position of the particles and the force network, *i.e.* all the static characterizations of the packing.

<sup>15</sup>However some care should be taken. Both phenomena have been historically associated for along time, and in addition the terminology may change from place to place.

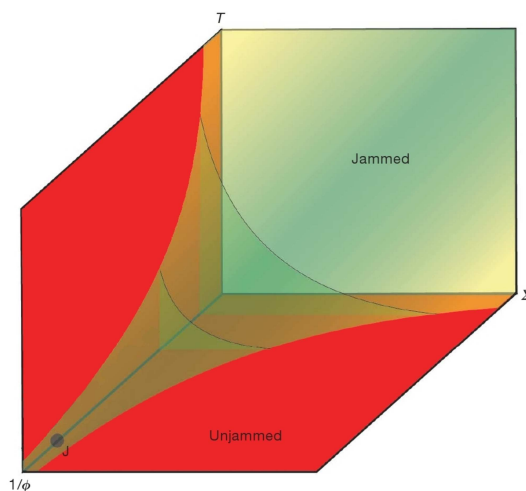


Figure 1.21: A possible phase diagram for glassiness and jamming. The blocked region, near the origin, is enclosed by the green surface. The lines in the planes are purely speculative. Adapted from Zhang *et al.* [76].

In this diagram, thermal glassy systems are in the temperature/density plane while athermal systems are in the strain/density plane. The “not flowing” or “blocked” state is a common property of all systems in the appropriate region of the 3D phase diagram. This plot has been improved since its first proposal [75], especially with the position of point  $J$  on the density axis: since the critical nature of point  $J$  at zero temperature and zero applied strain may be the only well-established feature of jamming, it is important to have it on the diagram as a reference point. Note that this diagram does not take into account the softness of the particles or the static friction coefficient for instance.

A remark that can be made is that if point  $J$  is a true critical point, critical scalings should appear when it is approached from all directions, and in particular in the temperature/density plane where usual glasses lie. However, such scalings have not been unambiguously observed yet.

In spite of this unification attempt, great care has to be taken not to confuse the two transitions: similar consequences may not arise from the same cause, and one cannot unambiguously claim for a one and unique transition without clear evidences. Let us examine now a few studies that clearly establish both *phenomenological* and *conceptual* differences.

### 1.3.2 The hard spheres case

An incredible amount of work has been done in the past few years, and – at least on the hard sphere case – a great effort has been put into drawing phase diagrams gathering several features of the glass transition and jamming. This is what we present here, inspired by a recent paper by Parisi and Zamponi [9].

Let us focus on the diagram of fig. 1.22, which is a zoom on the metastable supercooled liquid and glassy branches. The glass transition is the moment

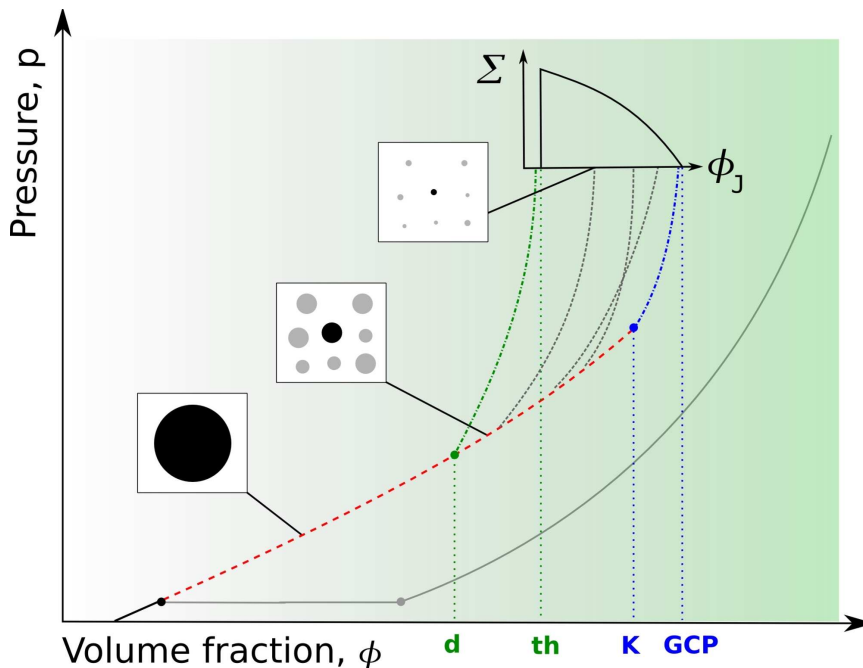


Figure 1.22: Schematic mean field phase diagram for 3D hard spheres. The solid black and gray lines represent the liquid/solid transition at equilibrium. The metastable liquid is made of one single state below  $\phi_d$  while above it is the superposition of many states. If the system is stuck in one of these states and compressed, it follows one of the glass branches. At  $\phi_K$  the system reaches the densest possible state for a metastable liquid, and if further compressed enters the ideal glass state. The pressure of the later diverges at  $\phi_{GCP}$ , while it diverges at  $\phi_{th}$  if the transition is at  $\phi_d$ . In the inset, the complexity (*i.e.* the logarithm of the number of metastable states) is plotted as a function of the jamming density  $\phi_J$ . Adapted from Parisi and Zamponi [9].

when the system leaves the metastable branch, and jamming occurs when the pressure diverges, thus at a slightly higher packing fraction. Both phenomena are therefore distinct and conceptually very different.

The very first remark one can make on this diagram is the existence of  $\phi_d$ . In the mean-field view, below a certain density  $\phi_d$  the metastable liquid is made of a single state, while above  $\phi_d$  many metastable states are superposed to form the liquid.

Second, when the system lays between  $\phi_d$  and  $\phi_K$  and is compressed too fast, it enters a glassy branch where its structure is frozen. The transition is signalled by a change of slope *i.e.* a jump in the compressibility. One can explain this change by a simple timescale argument: in the dense liquid phase the particles vibrate very rapidly around their equilibrium positions ( $\beta$ -relaxation) while on a much larger timescale some collective reorganizations

happen, leading to structural relaxation ( $\alpha$ -relaxation). If the density is changed by an amount  $\Delta\phi$ , the pressure is directly changed by an amount  $\Delta p_0$ . Then, a two timescales relaxation process happen: first on the short time scale the average size of the cages will decrease and the pressure will relax to a value  $\Delta p_1 < \Delta p_0$ , and second the structural relaxation will induce another relaxation of the pressure and lead to a value  $\Delta p_\infty < \Delta p_1$ . The point is that in the glass phase the time scale of later relaxation diverges, the pressure cannot relax further than  $\Delta p_1$  and the compressibility is smaller.

Then, several glass branches are possible. As depicted on fig. 1.22, there is no reason for these branches to be parallel and we have voluntarily represented two branches crossing each other. In addition, the existence of many glass branches implies the existence of many jamming points. As Parisi and Zamponi wrote: “to each configuration of the liquid at a given density  $\phi \in [\phi_d, \phi_K]$  one can associate a jammed configuration at a density  $\phi_J(\phi)$ , obtained by compressing this configuration fast enough to avoid structural relaxation. A “glass state” can be roughly thought as a set of configurations leading to the same jammed configuration after a fast compression.”

Finally, the number of glassy states  $\mathcal{N}$  corresponding to each jamming density  $\phi_J$  grows exponentially with the size of the system and a function  $\Sigma(\phi_J)$  called *complexity* [9]:

$$\mathcal{N}(\phi_J) = e^{N \cdot \Sigma(\phi_J)} \quad (1.20)$$

The complexity function  $\Sigma(\phi_J)$  has the shape reported in the inset of fig. 1.22: it starts at  $\phi_{th}$  – the jamming packing fraction when the glass transition is at  $\phi_d$  – and vanishes at  $\phi_{GCP}$  – the jamming packing fraction when the glass transition is at  $\phi_K$ .

Note that the results presented here stand for 3D systems; in 2D, some authors argue that the situation may be slightly different [77, 78]. Let us now present very recent results of simulations on soft spheres.

### 1.3.3 The soft spheres case

Berthier and Witten [10, 79] have conducted extensive simulations on compressible repulsive 3D spheres at several temperatures and packing fractions, and report that the dynamics at equilibrium obey critical scaling in the vicinity of a critical point at  $T = 0$  and  $\phi_0 = 0.635 \pm 0.005$ , that the authors call *point G* (see fig. 1.23). They highlight the fact that this point is different from the jamming point, whatever one considers the point  $J$  at  $\phi_J \simeq 0.648$  found in [45] or the point  $J^*$  at  $\phi_J^* = 0.662$  found in [10], maybe with a better controlled annealing protocol.

Importantly, by approaching point  $G$  with several different paths, Berthier and Witten can evaluate accurately the value of  $\phi_0$  by determining the fol-

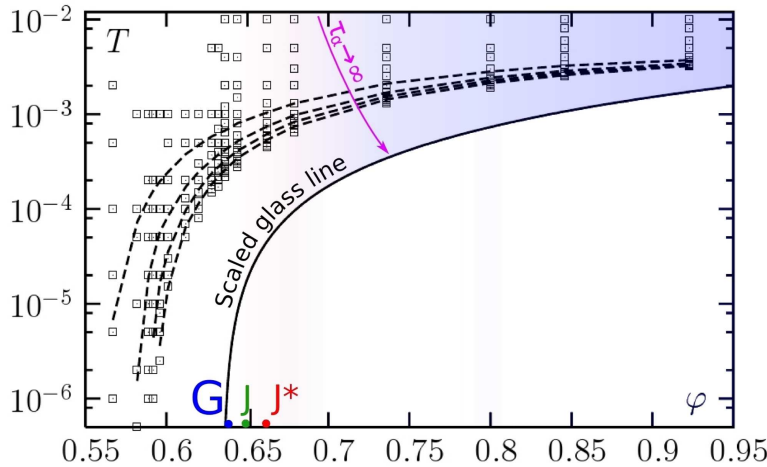


Figure 1.23:  $T$  vs  $\phi$  phase diagram with investigated state points ( $\square$ ). Four isorelaxation time (dashed) lines are displayed, showing  $\tau_\alpha$  from  $10^1$  to  $10^4$ . Scaling permits accurate determination of the glass point  $G$  at  $T = 0$  and  $\phi_0 = 0.635$ . The glass transition (full) line is obtained assuming a specific form of the scaling function. The jamming point  $\phi_J^* = 0.662$  is in red, while  $\phi_J = 0.648$  determined in [45] is shown in green. The bluer region on the right side correspond to more fragile glasses. Adapted from Berthier and Witten [10].

lowing functional form of the dynamics:

$$\tau_\alpha(\phi, T) \simeq \exp \left[ \frac{A}{|\phi_0 - \phi|^\delta} F_\pm \left( \frac{|\phi_0 - \phi|^{2/\mu}}{T} \right) \right] \quad (1.21)$$

where  $\delta \approx 2$ ,  $\mu \approx 1.3$  and the scaling functions  $F_\pm$  applies to densities above / below  $\phi_0$ . This scaling form is interesting for several reasons:

- The divergence of the scaling function  $F_+(x)$  implies that the dependence of  $\tau_\alpha$  becomes steeper with increasing temperature, *i.e.* that the glass is more fragile. So, as depicted by the shading off on fig. 1.23, the higher the packing fraction, the more fragile the glass. This provides a nice explanation for fragility without invoking a change in the chemical composition of the material for instance.
- It determines accurately the scaled glass line and point  $G$ , depicted in fig. 1.23. This provides strong support for the existence of an ideal glass transition.
- It justifies the following relation between packing fraction and temperature:

$$\phi_{eff}(\phi, T) \simeq \phi - a.T^{\mu/2} \quad (1.22)$$

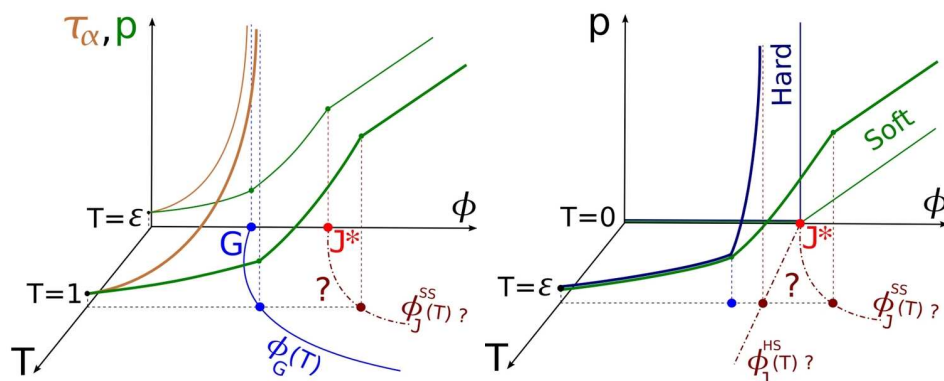


Figure 1.24: **Left** A possible sketch for repulsive soft spheres. The evolution of the pressure  $p$  (green) and the relaxation time  $\tau_\alpha$  (brown) are depicted at  $T = \epsilon$  (thin) and  $T \gg \epsilon$  (strong). **Right** A sketch to compare the evolution of systems made of hard (dark blue) and soft (green) spheres, at  $T = 0$  (thin) and  $T = \epsilon$  (strong). On both diagrams, the curves  $\phi_J(T)$  for hard and soft spheres are speculative.

where  $a > 0$  is a numerical prefactor.

The last-mentioned point is of crucial interest since it links packing fraction and temperature into a unified framework.

This enables us to draw the synthetic diagram of fig. 1.24-left, which is somehow an extension of the diagram in fig. 1.22, but for soft spheres. One can recognize the scaled glass line  $\phi_G(T)$  (in blue), which is somehow an extension of the  $K$  point previously mentioned. Considering only the “ideal” case, the relaxation time  $\tau_\alpha$  (in brown) diverges around point  $G$  when the temperature is close to zero ( $T = \epsilon$ ) and at  $\phi_G(T)$  when the temperature is greater. When one considers the pressure  $p$  (in green), it grows as the packing fraction increases, with a change of compressibility at  $\phi_G(T)$ . For  $T = 0$ , point  $J^*$  is the moment where the pressure becomes finite; the diagram suggests the existence of a  $\phi_J^{SS}(T)$  curve for  $T$  finite, corresponding to the packing fractions at which the soft particles start to permanently interpenetrate. At this point, another change of compressibility happens<sup>16</sup>.

One can also draw a comparison between the evolution of  $p$  for compressed hard and soft spheres while the temperature is kept constant. This is schemed in fig. 1.24-right. At  $T = 0$ , below point  $J^*$  (red dot) the pressure remains null, while at point  $J^*$  the pressure either diverges immediately in the case of purely incompressible spheres, either becomes finite for softer particles. In this latter case, the pressure continues to grow as the packing densifies. At a finite temperature, but still very close to 0 ( $\epsilon = 0^+$ ), a second

<sup>16</sup>Note that the changes of compressibility depicted in fig. 1.24 may not be realistic. It is possible that the branch above  $\phi_J(T)$  has a higher compressibility than below  $\phi_J(T)$ .

point of interest appear below jamming: this is the point where the system loses its ergodicity and enters a glassy branch (blue dot). The compressibility changes but in different manners in the hard and soft cases: with hard spheres the pressure dramatically increases and diverges at  $\phi_J^{HS}(T)$  while with soft spheres the pressure increases more gently, until a second change of compressibility at  $\phi_J^{SS}(T)$ . Note that the  $\phi_J(T)$  curves are purely speculative. We have drawn  $\phi_J^{HS}(T)$  straight, because in the case of hard spheres the  $2D$  diagram  $p/T$  as a function of  $\phi$  is temperature-invariant, but the presence and shape of  $\phi_J^{HS}(T)$  for instance is not established yet.

### 1.3.4 Conclusion, and a few questions

To conclude, we can say that the glass transition and the jamming transition are distinct phenomena in systems at non-zero temperature, both for hard and soft spheres. In particular, the glass transition is a purely dynamical phenomenon, while jamming relates to the force network.

At the end of this introduction, several open issues remain. Here are the few questions that we will address in the sequel:

- **Jamming.** Is jamming a critical phenomenon? Does it manifest itself at finite temperature, shear or stress? What are its experimental signatures in the dynamics of thermal / vibrated particles, or in the response to a perturbation?
- **Glass.** What are the mechanisms responsible for the slow relaxation in glass formers? How do the widely observed dynamical heterogeneities build up? What is the role – if any – of the structure?

## 1.4 This work

In this work, we will primarily focus on granular materials, *i.e.* systems made of athermal, hard and frictional particles. In addition, the data stemming from a simulation of repulsive softly interacting particles will be also analyzed. This manuscript is composed as follows: after a long but necessary description of the systems and the associated protocols, the results are divided into two (almost independent) parts.

In the first part, we characterize the signatures of the jamming transition for a  $2D$  granular assembly under vibration and with friction. Bridging the gap between the idealized situation at zero temperature and zero strain depicted in [45] and the systems with more complex interactions – like granular media – is a challenge that needs to be raised. In particular, a reminiscence of the critical nature of point  $J$  has been previously measured in [80, 81]. The analysis of the dynamical heterogeneities – in a system where structure does not evolve – revealed a peak of the timescale at which the heterogeneities are maximal and which is associated with the presence of super-diffusivity. In addition, a clear divergence of the lengthscale driving the dynamical correlation function has been shown to exhibit a critical behavior upon jamming. Here we will investigate the highly non-linear response of an intruder dragged through the very same media. Our study confirms these early results through the response of the system: a peak of intermittency is found on jamming, altogether with a critical divergence of the time and length scales of the reorganizations in the media. This work is a first step to reconcile firstly the indicators of criticality, secondly the micro and macro-rheological measurements, and thirdly the evolution of microscopic structural quantities.

In the second part, we concentrate on the supercooled state dynamics and the appearance of the dramatic slowdown. Both cage jumps and dynamical heterogeneities have been shown (*i*) to be commonly observed in all types of supercooled systems and (*ii*) to be related to the late  $\alpha$ -relaxation of the structure factor. We will therefore investigate the mechanisms relating cage jumps to dynamical heterogeneities in several systems: the cyclic shear experiment set up by Marty [20, 82] during his thesis, the monolayer fluidized bed experiment set up by Abate *et al.* [83, 84] in which the packing fraction is tunable, and finally a simulation of repulsive softly interacting particles. From this, we try to elucidate the relative contributions of cooperative motion associated to “local softness” and the facilitation mechanisms leading to large collective reorganization.

Finally, a brief conclusive chapter will summarize and discuss our main results, with respect to the pressing questions in the scope of supercooled liquids. Some new questions will be raised, and an attempt of roadmap for future experiments will be given. At the end of the manuscript, a few appendices will quench the thirsty readers.

# Chapter 2

# Systems

## Contents

---

<b>2.1</b>	<b>Experiments and simulations</b>	<b>40</b>
<b>2.2</b>	<b>Data processing and analysis</b>	<b>61</b>
<b>2.3</b>	<b>Tables</b>	<b>70</b>

---

As underlined in the introduction, one can find a dramatic dynamical slowing down in a huge panel of systems: real liquids of course, but also simulations of liquids, colloids, emulsions, foams, grains etc. Performing a meta-analysis on several systems spanning the whole family of glass formers from soft, thermal, frictionless particles to hard, athermal grains is a challenge that needs to be addressed in order to reveal the general features of such systems. This is also a task to be performed when the number of experimental results and theoretical concepts increases, as it has been the case in the last decades.

We do not pretend to have benchmarked the whole set of glassy systems, neither to have performed a meta-analysis sufficient to draw all the conclusions of the scenarios of the glass and jamming transitions. However, we have started to gather data from several systems, to analyze them with the same statistical tools, and to compare them. In chapter 3, we compare the dynamical behavior of grains at the onset of jamming to the structural and dynamical response of the same system to an external stress. In chapter 4, we propose a scenario for the appearance of dynamical heterogeneities in an experiment of cyclicly sheared grains and then investigate how it extends to a fluidized bed of grains and to a simulation of a frictionless, softly interacting particles liquid.

We would like to emphasize here the benefits of sharing experimental data amongst different research teams to create valuable scientific collaboration. Our hope is that the collaborations set up during these three years will carry on and continue to develop.

One aim of this chapter is to introduce each of these systems. In a first part, the reader will find for each data set some technical details, precise

descriptions of the protocols and concise explanations of the experimental choices, as well as references to the corresponding publications. Another aim of this chapter is to explain the generic tools that we have built up to treat and analyze the data. This is the second part of this chapter. The last pages are devoted to a summary – in table format – of the systems’ peculiarities according to different aspects, a “lifebuoy” to help the reader to navigate with us into this pool of data.

As an appetizer, the following table summarizes in what chapter(s) each system is studied:

System	Chapter(s)
The vibrating experiment	3.1, B.2
The intruder in the vibrating experiment	3.2
The cyclic shear experiment	4.1, 4.2
The fluidized bed experiment	4.3
The glass former simulation	4.4
The shearing experiment’s simulation	4.5.1
The monodisperse experiment	4.5.3

Table 2.1: Summary of the systems used in each chapter.

## 2.1 Experiments and simulations

### 2.1.1 The vibrating experiment

#### Setup

The vibrating experiment has been set up by Frederic Lechenault during his thesis. Many people contributed to the realization, including Olivier Dauchot, Vincent Padilla and Cécile Gasquet. This system is an archetype of collaborative work: during this thesis, I have, *technically speaking*, only realized a single experimental run: the aging protocol, shortly presented in 3.3.1. All the other data acquisitions have been realized by Lechenault and Master trainees: Lilly Bertereche, François Paradis and Baudoin Saint-Yves. My main contributions have been first to transfer the data acquired by Lechenault into databases and perform a few complementary calculations to his work<sup>1</sup>, and second to treat and analyze all the following experimental acquisitions, in particular when an intruder is dragged through the sample.

Since this experimental apparatus has already been described in detail in Lechenault’s thesis [47], let us just cover here its principal characteristics. Different views of the experimental setup are shown in fig. 2.1, and a schematic diagram is presented in fig. 2.2.

---

<sup>1</sup>The main results of Lechenault will be presented in 3.1.1 while the recent studies start in 3.1.2.



Figure 2.1: The experimental setup of the vibrating experiment. **Top left:** General view. One can see ① the counterweighting box full of lead, ② the lighting system, ③ the camera position and ④ the fixations of the experimental apparatus through the wall. **Top right:** View of ① the piston, ② the force sensor and ③ the translation platen. **Middle left:** View of ① the rotating device supporting the rod, ② the belt and ③ the trigger sensor. **Middle right:** View of ① the motor, ② the horizontality adjusting wheels, ③ the confinement cell and ④ the moving bottom plate. **Bottom** View of ① the rotating device stirring ② the rod. ③ The bottom plate oscillates at 10Hz with a 1cm amplitude.

The experimental system consists of 8250 grains with diameters 4 mm and 5 mm covering an equal surface (3670 big and 4580 smalls) lays out on a glass plate. On each grain, a hole along the axis of the cylinder makes the tracking through image analysis easier. The glass plate can oscillate

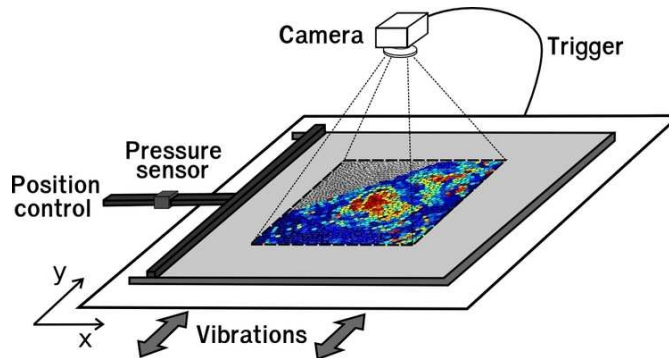


Figure 2.2: Scheme of the vibrating experiment.

horizontally in the  $y$ -direction, at a frequency of 10 Hz and with a amplitude of  $1 \text{ cm}^2$ . The grains are mixed altogether and confined in a  $2D$  cell, fixed in the laboratory frame. The important feature to keep in mind is that the boundaries are fixed, while the bottom plate oscillates and injects the energy.

The total surface of the cell can be finely tuned by the means of a piston linked to a position controller. This controller allows very precise steps of the piston's position in the  $x$ -direction (*i.e.* perpendicular to the vibration), down to micrometric precision. We can therefore tune the packing fraction with increments of the order of  $\delta\phi = 5.10^{-3}$ .

On this piston, a force sensor is installed to measure the pressure at the boundaries. The dimensionless normal force  $P$  is be defined as follows:

$$P = \frac{F_{piston}}{Mg}$$

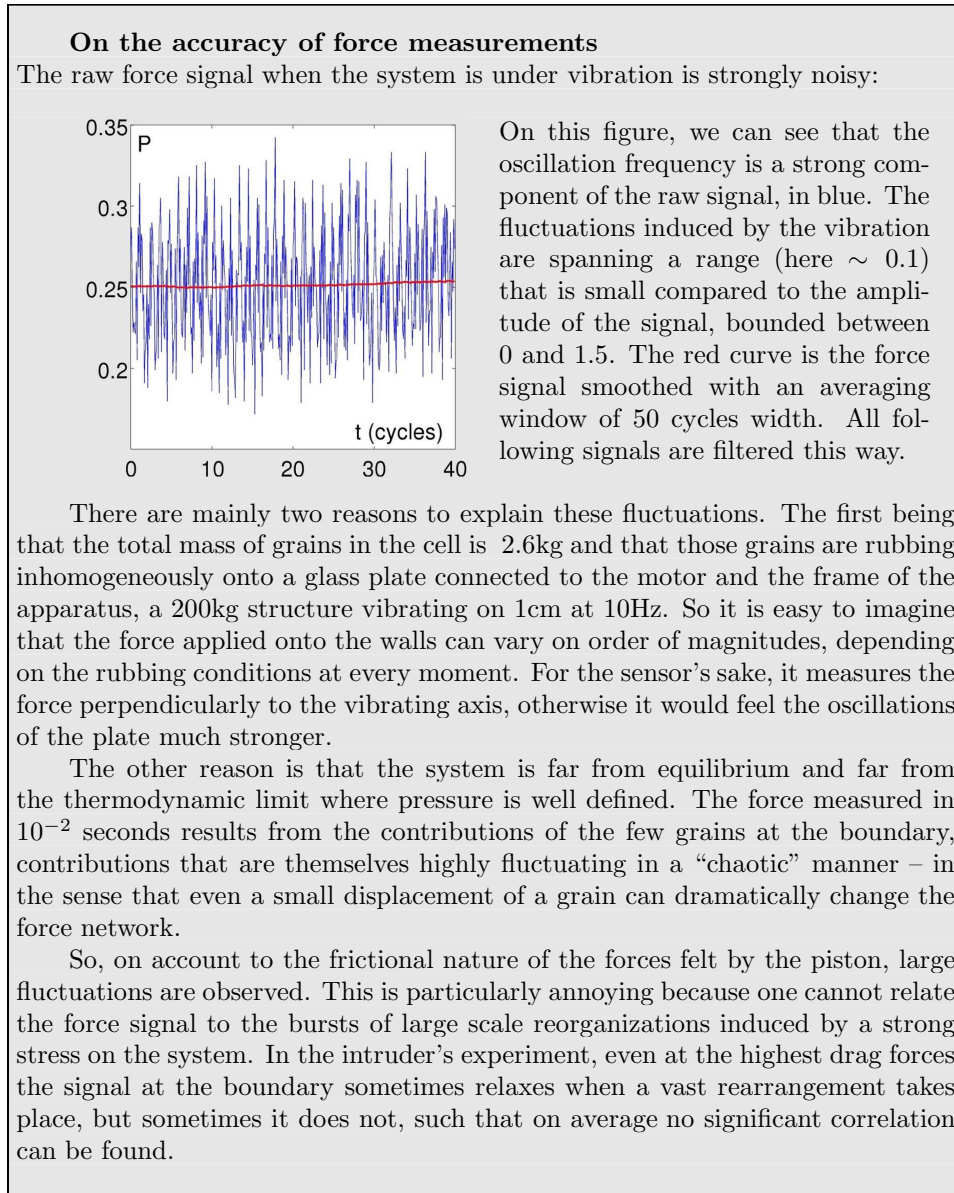
where  $F_{piston}$  is the force measured by the force sensor,  $M$  the total mass of the grains in the cell and  $g$  the gravity acceleration constant. As the static friction coefficient between the grains and the bottom plate is of the order of 0.5, a pressure of 0.5 is sufficient to make the whole assembly of grains slip.

Though this quantity is dimensionless, we will call it the *pressure* for convenience. To be rigorous, the term *pressure* cannot be employed here since (i) the system will be kept far for a thermodynamic equilibrium in all the experiments and (ii) the number of collisions per unit of time may be too small to properly define a kinetic pressure. This is nevertheless a macroscopic measurement of the packing's state, and moreover it should capture the appearance of mechanical rigidity as we will see in the "protocol" paragraph. However, this force sensor is *not* able to catch the reorganization

---

<sup>2</sup>Note that these parameters are fixed once and for all in this thesis.

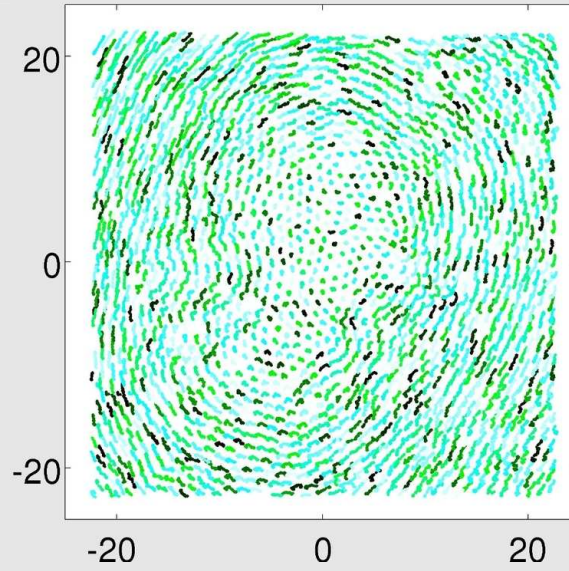
events in the system, even in the case of the intruder where they have both a large scale and a large amplitude.



Pictures are taken in the central region of the cell with a camera triggered by the oscillations of the plate. The resulting stroboscoped motion of the grains enables us to eliminate the oscillatory motion, and to compare directly the looser states where the grains are carried away by the bottom plate and the jammed states where they are rather fixed in the laboratory frame.

### Convection

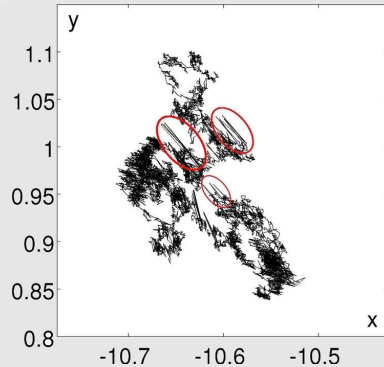
When the packing fraction is too low, some convection regimes are observed. These movements last on time scales that depend on the packing fraction but are typically sufficiently long not to be seen with the eye. For instance, here are the trajectories of the grains in 10,000 oscillations at  $\phi = 0.8382$ :



These kind of global, solid rotation of the assembly of grains are going either clockwise or counterclockwise in different realizations – the sense of rotation can even change during the same run – like a dynamical instability. Convection is a general phenomenon observed in loose packings, whatever the energy injection. See 4.3 for another example in a fluidized bed of grains. We systematically discard all the data showing convection from our analyzes, except for [85] (see page 137, and the corresponding discussion in 4.3).

### Rattlers

Sometimes, a void is created around a particle. Because of the strong energy



injection in the bulk, this particle immediately takes advantage of the free space to bounce on its neighbors and extensively explore this "cage". The friction being inhomogeneous, those particles never come back to the same position from one cycle to another. The stroboscopic trajectory of a rattling particle is shown in the adjacent plot.

Note that this particle is *sometimes* a rattler (red ellipses), and *sometimes* not. Rattling is a spatially and temporally intermittent characteristic. As a cons-

equence, the global displacement's statistic is biased by those few highly moving particles in a matrix of quasi-blocked grains.

Following Lechenault's studies, we discard from all the following analysis all the particle - times which have an instantaneous displacement larger than  $10^{-2}$ . This is an efficient filter, since the typical instantaneous displacement is of the order of  $10^{-3}$  with a standard deviation also of the order of  $10^{-3}$ , for all the studied packing fractions.

However, the rattlers are real events of the system. Their number and frequency evolve significantly with the packing fraction so their statistics could contain some physical information.

## Protocols

Several variations have been performed starting from the first protocol proposed by Lechenault. Let us present first his original protocol, then its mutations – principally the intruder protocol – and finally discuss the general features one can learn about jamming from these different protocols prior to (almost) any data analysis.

**Unjamming an assembly of grains** The original protocol of the experiment is described in Lechenault's thesis [47] and in recent publications [80] so let us briefly recall it: starting from a loose state of the system, several steps of increasing packing fractions are firstly performed. When the lateral wall moves, the force measured on the piston rapidly increases and then slowly decreases. We let the system evolve until the measured force does not significantly diminish anymore, and perform another position increment. In this way, we can reach highly packed states up to  $\phi = 0.845$ . At each step the system is aging as evidenced by the force relaxation (see fig. 2.3-left), until the densest states where relaxations are no longer observed in the experimental time.

We then decrease stepwise the packing fraction. The force at the boundaries simply decreases and immediately finds a stationary value. This is easy to understand: when the packing fraction increases the number of constraints increases as well – thus forcing the system to evolve – whereas in the decreasing steps the system just feels a small scaling, each particle having a little bit more space to move, and the system is not forced to evolve. A plot of the measured pressure during the protocol is shown in fig. 2.3-left.

Another important feature of the decreasing steps is that the system is in a *reversible* state, *i.e.* one can apply the reverse packing fraction increase and the pressure will return to its previous value without neither a peak at short times nor a slow relaxation (see fig. 2.3-right). This sounds reasonable since the constraints induced by the reverse increasing step had been previously removed in the decreasing step. For these reasons, we have

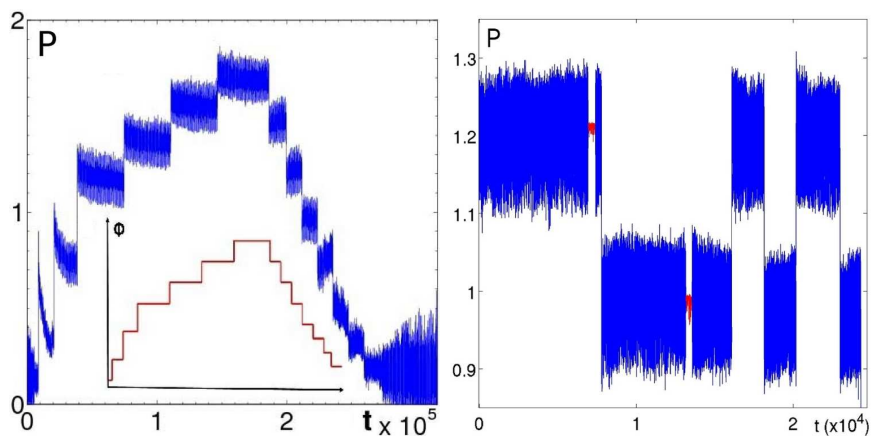


Figure 2.3: **Left** Protocol of the vibrating experiment. The red signal in the inset is the position of the piston and the blue signal is the pressure (measured force reduced by the total weight of grains in the cell). When the packing fraction increases stepwise, the force increases strongly and then relaxes, while not when the packing fraction decreases. The total duration of this protocol lasts from 10 to 15 hours. **Right** Reversibility and static pressure. After a decreasing step, the opposite increasing step is reversible. The red points are measured when the vibration is stopped, defining the *static* pressure. From Lechenault's thesis [47].

been working essentially in the descending steps where stationarity can be hypothesized, at least more than in the ascending steps.

We therefore study the *unjamming* transition. Several macroscopic clues of unjamming are given to the experimentalist when the system unjams, the first being the sound produced by the apparatus. From relatively silent in the jammed states, the apparatus becomes extremely noisy as in the looser states the grains hit the walls of the confinement cell, in an intermittent coupled regime. The force fluctuations are also stronger in these noisy looser states, as shown in figure 2.4.

Second, when they are jammed the grains are almost fixed in the laboratory frame, while they are much more carried out by the bottom plate in the unjammed states.

The last macroscopic evidence of unjamming is given by the force sensor. We define the *dynamic* pressure as the force signal observed when the bottom plate is oscillating and the *static* pressure as the force measured when the oscillations are stopped (see fig. 3.1, page 75). When the packing fraction decreases, at a certain value the static pressure vanishes while the dynamic pressure remains finite. At this point, the system is losing its rigidity and is not able to stock energy in a static manner. We identify this packing fraction as the *unjamming* transition described in the introduction, and call

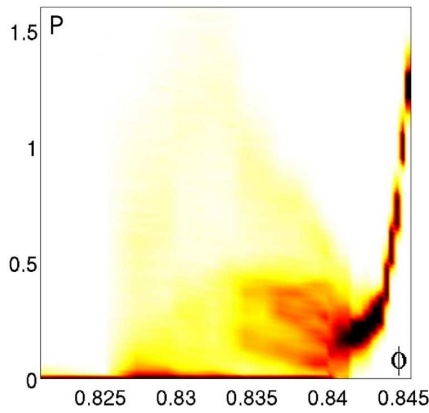


Figure 2.4: Force distributions. At each packing fraction, *i.e.* for each vertical line, the Pdf of the pressure is showed in color code. The average value decreases with the packing fraction, while the fluctuations strongly increase below unjamming, at  $\phi_J \simeq 0.842$ .

it  $\phi_J$ .

We typically acquire images during 20 minutes (10,000 oscillations) at each decreasing step, and record the force signal at 100 Hz. The main results obtained with this system in previous studies will be described in 3.1. Let us now present briefly some other protocols that have been realized during my thesis. All the technical features presented so far will be the same: the grains, the camera, the lighting system and the acquisition chain remain unchanged.

**The intruder protocols** In this protocol, the system is modified such that a probe particle – the “intruder” – can be dragged. The intruder itself is a cylinder with the same height than the others grains and which diameter

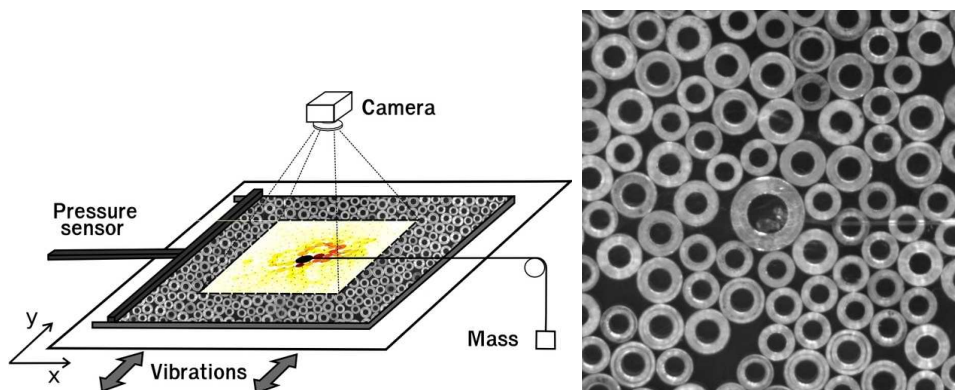


Figure 2.5: **Left:** Scheme of the vibrating experiment with an intruder. **Right:** Zoom on the intruder (the big particle in the center). The fishing wire is visible on the right side.

is twice the diameter of a small grain<sup>3</sup>. The intruder is pierced such that a fishing wire can be tied up to it. The knot is inside the intruder and two trenches on the side and the top of the intruder maintain the wire. The fishing wire is tighten between the top of the other grains and the Plexiglas plate, and does not disturb the dynamics of the other grains.

In all the data presented here, we have been dragging the intruder along the  $x$ -direction – *i.e.* perpendicular to the vibrations – with a constant force. In practice, this is easily done by hanging a mass via a pulley, as depicted in fig. 2.5.

A detailed analysis of the data collected with the intruder’s protocols will be done in 3.2.

**The aging protocol** In this protocol, we study the dynamics of the grains while the packing fraction is stepwise increased. At each step the pressure at the wall sharply increases first, and then relaxes extremely slowly. We have acquired both the pressure signal and the images in order to observe the evolution of the grains’ dynamics as the average force network amplitude decreases.

Unfortunately, we have not observed a clear evolution of the dynamics with a single but already long ( $\sim 70,000$  cycles) run. A brief analysis of the results will be done in 3.3.1.

**The parachutist protocol** The idea is to bring the system at an already high packing fraction and then to “parachute” it somewhere randomly in the possible phase space. We do this in the following way: we stop the vibration and stir the grains while the packing fraction remains constant. During this manual stir the pressure at the wall strongly increases. We then start to shake again and acquire the pressure’s relaxation as well as the images from the camera.

The analysis of the images during these relaxations have not been performed yet, but an analysis of the first results on the pressure relaxation will be done in 3.3.2. It gives interesting insights on the configurational energy landscape and on the way our system evolves into it.

**Discussion on the different protocols** Four different protocols have been realized, and some new other ones are in preparation for the incoming years. A few general remarks can be extracted from all these manners to probe the same system close to jamming:

---

<sup>3</sup>There was no particular reason to choose a bigger grain, apart from the fact that intruders are often bigger grains in the literature. In our case, this size difference turned out to pose some difficulties because it is a possible reason for the shift in the value of  $\phi_J$  observed in all the intruder’s runs. New experiments should be done with an intruder indiscernible from the other particles to avoid this effect.

First, though the energy injection is strongly anisotropic the motion of the grains themselves is isotropic. For instance only very few differences have been observed by Lechenault in the root mean square displacements along both directions, at all time scales. Of course, this is no longer true close to the intruder in movement.

Second, the precise value of the jamming transition can slightly vary from one run to another, simply because the configurations are different. Indeed, there is no reason *a priori* that the system acquires the ability to sustain stress at the very same packing fraction for each configuration. The values we find for  $\phi_J$  in different runs are summed up in table 2.2:

Experiment		$\phi_J$
Without intruder	Lechenault's thesis	0.8419
	Aging protocol	0.8424
	The parachutist protocol	$\sim 0.85$ <sup>1</sup>
With intruder	Drag $F_1 = 0.029$	0.8369
	Drag $F_2 = 0.064$	0.8383
	Drag $F_3 = 0.113$	0.8379
	Variable drag	0.8388

Table 2.2: Values of  $\phi_J$  for different experimental runs.

The lower values for the intruder's experiments may be due to extra polydispersity induced by the intruder. To check this, one should perform a run where the intruder has the size of the other grains, and verify that the variations of  $\phi_J$  are smaller.

Though it is not possible to define an absolute value of  $\phi_J$ , the distance to jamming in every configuration seems to be the relevant parameter to compare the phenomenology in different runs. For this reason we will often use the reduced packing fraction  $\epsilon = (\phi - \phi_J)/\phi_J$  instead of  $\phi$ .

### 2.1.2 The shearing experiment

The cyclic shear experiment has been set up by Guillaume Marty during his thesis [20]. Many people contributed to the realization, including Olivier Dauchot, Louis Marié, Vincent Padilla and Cécile Gasquet. During my thesis, we have changed the camera, the lighting, we have added a torque sensor and realized a major update of the control and acquisition programs, and we have performed a run over 10,000 cycles.

---

<sup>1</sup>The value found in the parachutist protocol is an estimation based on the fit described in 3.3.2 (p. 108), since jammed states seems *not* to be reachable in this protocol.

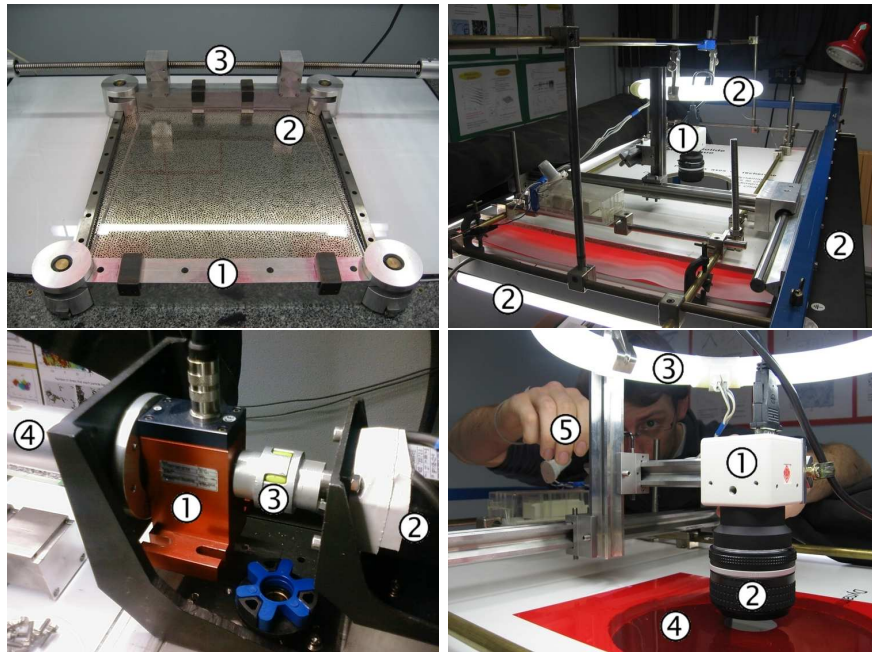


Figure 2.6: The experimental setup of the cyclic shear experiment. **Top left:** General view. One can see ① the shearing cell, the bottom bar being fixed to the marble and the upper bar being carried away by the screw, ② a trapezoidal Plexiglas plate on top of the grains and ③ the screw. **Top right:** Top View. One can see ① the camera and ② the neon lights. **Bottom left:** The torque sensor. The different elements are ① the torque sensor, ② the motor, ③ the connection between the motor and the sensor and ④ the connection between the sensor and the screw. **Bottom right** View of ① the camera and ② the objective, ③ the circular neon around the camera, ④ a light filter to avoid direct reflects of the circular neons on the top of the grains, and ⑤ the hand of the experimentalist.

**Setup** Different views of the experimental setup are shown in fig. 2.6. The experimental system consists of 8350 grains in equal proportions (4175 big and 4175 smalls) laying out on a glass plate fixed to an horizontal marble. The grains are mixed altogether and confined in a  $2D$  shearing cell. The shearing cell has a fixed bar, and the opposite bar is carried away by a 1 m long screw that converts the rotation of a motor into translation. The lateral bars are attached to the fixed bar but they can slide into the moving bar in order to adjust their length during the shear. In its rectangular position, the cell is a square of 50x50cm. Due to the shear geometry, the total area in the cell remains constant during the cycles.



Figure 2.7: One grain to rule them all.

The polydispersity due to factory production has been measured by Marty on a set of 500 particles: the measured standard deviation on the diameters is  $\sim 5 \mu\text{m}$ . For a monodisperse set of grains, this creates a polydispersity:

$$\Delta_{factory} = \sqrt{\langle d_i^2 \rangle - \langle d_i \rangle^2} / \langle d_i \rangle \simeq 10^{-3}$$

which is roughly 10 times below the polydispersity induced by bidispersity. On every grain, a hole along the axis of the cylinder makes the grains detection easier.

#### Motor

We have been using a 400 W continuous current *Fenwick*, model *SGMAH-04AAF41D*.

#### Camera

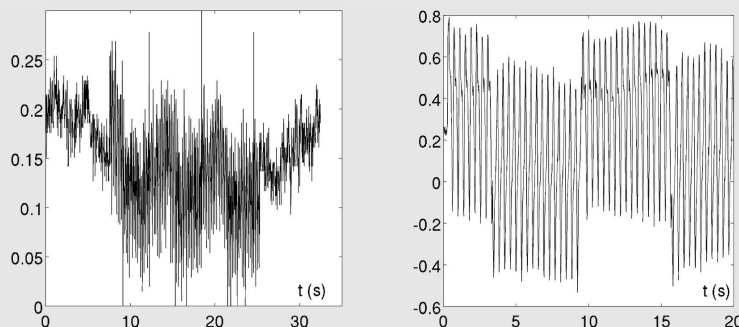
The camera is a Redlake *MegaPlus II* with a 2048x2048 CCD allowing 8 bytes images in grey levels up to a framerate of 5 Hz, which is fast enough for this experiment. The opening time is 65 ms. The camera is linked to a controller linked to the computer via firewire. The *IMAQ for 1394 cameras* driver software connects to the *IMAQ* libraries in *Labview*.

#### Torque acquisition

The torque sensor is a *KISTLER 0170MS* "Mini-smart", version *RAU*. It can measure torques up to 20 N.m with maximum axial and radial forces of 150 N.

The maximal torque that the motor can support is 1.27 N.m, and typical values of the torque during the cyclic shear are around 0.25 N.m.

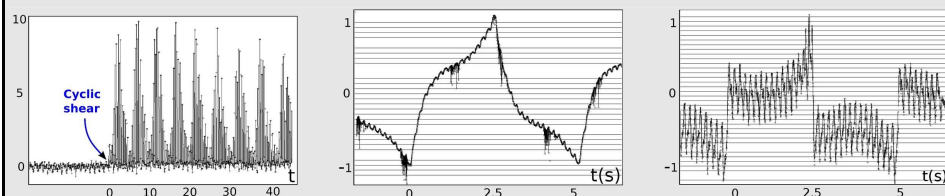
The torque sensor measures the deformation of a cylinder that connects the motor to the screw. It is very sensitive to the unwanted radial forces, in particular when the axis of the sensor is slightly misaligned. An important issue has been to filter the noise arising from different sources:



The above curves show the signal (in Volts -  $1 \text{ V} \equiv 0.025 \text{ N.m}$ ) obtained from the sensor when it is only linked to the motor (left) and when it is linked to the screw, the cell being detached from the screw (right). Even when it does not carry out the screw, some noise arise from the amplification system. However, the amplitude of this noise is small compared to the signal obtained when the screw is added, and much smaller than with the cell full of grains. The screw itself pre-

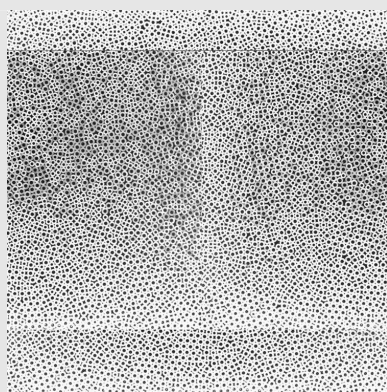
sents some radial asymmetry: the right signal contains the typical rotation frequency of the motor (4 Hz) and the frequency of the cycle (0.2 Hz).

When acquiring with the cell full of grains, the unfiltered signal is extremely noisy (see the left figure below; unitary on the vertical axes are arbitrary):



We have therefore added a low-pass filter. When the cutting frequency is too low (*e.g.* 1 Hz, middle figure) one gets the tendency of the signal but the accuracy is lost on the rapid moments where the rotation changes direction. On the contrary, when the cutting frequency is too high (*e.g.* 67 Hz, right figure) the signal is strongly influenced by the frequency of the motor. Finally, we have set the cutting frequency at an intermediate value of 5 Hz.

**Known issues with the setup.** The major source of bugs in this experimental setup comes from the electromagnetic noise generated by the control variator of the motor. When one looks at the signal caught by an antenna in the room when the variator is switched on, one sees a peak of 10V every 20 $\mu$ s. This strong electromagnetic noise can perturb the commands that controls the motor: it can lead to *dramatic* effects during the experiment if the motor never receives the command to rotate the other way round, for instance. The acquired images can also be strongly affected by the electromagnetic noise; see the picture below for instance, where several areas have been inverted.



There are a few solutions. First one has to plug the variator onto a different energy source than the rest of the system, unless the computers and the camera will be perturbed. A new electric table has been installed in order to receive the variator, but it did not solved completely the problems. Using gained wires or wrapping cylindrical magnets around the sensitive wires is another solution. Faraday cages have also been added around the camera and the variator.

**Protocol: general features** We apply cyclic shear, with a constant shear rate of  $1^\circ.s^{-1}$  up to a  $5^\circ$  angle. The whole cycle (back and forth) frequency is  $\sim 0.1$  Hz. The image acquisition is stroboscoped to this frequency, *i.e.* we

take picture only when the shearing cell comes back to its initial, rectangular position<sup>4</sup>.

The camera takes pictures in the bulk of the cell only, avoiding boundary effect; the acquisition field is a square that contains roughly 4100 particles. The movement of the grains during the shear is not filmed, the shear playing the role of the energy injection: from one cycle to another, the grains have typically moved of  $10^{-2}$ , which is very small compared to the displacement of the grains close to the upper moving wall in the laboratory frame, of the order of  $\sim 10$ . Remarkably, the displacements statistics in the acquisition zone is perfectly homogeneous and isotropic, despite the strong heterogeneity imposed by the external driving.

Corté *et al.* [86] and Menon and Ramaswamy [87] have recently studied assemblies of particles under cyclic shear and evidenced that below a critical strain amplitude the particles simply retrace their trajectories back under the periodic drive. However, when the strain amplitude exceeds some concentration-dependent critical value, the particles no longer return periodically to the same positions but exhibit small random displacements. Our system is clearly above this threshold since (i) the packing is very dense and (ii) we experimentally observe small displacements from one cycle to another, and eventually sometimes large scale reorganizations (as we shall see in 4.2).

Note that in this shear geometry, the total area inside the cell remains constant. A crucial limitation of this setup is that we can not vary the packing fraction. One could imagine to introduce a piston on the upper bar so that the surface of the cell can be tuned during the experiment, or simply add or remove grains from the packing. However this would not allow us to explore looser packings and probably only a few denser packings since the system “selects” its packing fraction. Indeed, if one tries to run the experiment with too few grains, the shear will create a void close to the lateral bars and the system will naturally increase its packing fraction – by reducing the total surface occupied by the grains – up to a certain value, apparently constant<sup>5</sup>  $\phi_{shear} \simeq 0.84$ . If ones wants to bring the system above  $\phi_{shear}$ , the pressure during the shear will increase dramatically and the system will break. Actually, the system “breaks” by simply ejecting some grains out of the horizontal monolayer.

**Preparation protocol** To prepare our system, we put a mixture of bidisperse grains at a low packing fraction,  $\phi \sim 0.80$ . We add a few grains, make 200 cycles, add some grains again, make another 200 cycles, etc. until no

---

<sup>4</sup>The shear stops for 500 ms before each picture, to avoid blur. A longer exposition time makes it possible to have good lighting conditions on a broader area, hence a broader acquisition field.

<sup>5</sup>We have no argument to say that  $\phi_{shear}$  is a precise value instead of an interval. But if it is a interval, it is very narrow.

free space is left in the cell. At this point, we “parachute” the system somewhere randomly in the phase space by stirring the grains. If we record the torque signal for a few thousands cycles after the system has been brought in this state, we get the signal reported in fig. 2.8.

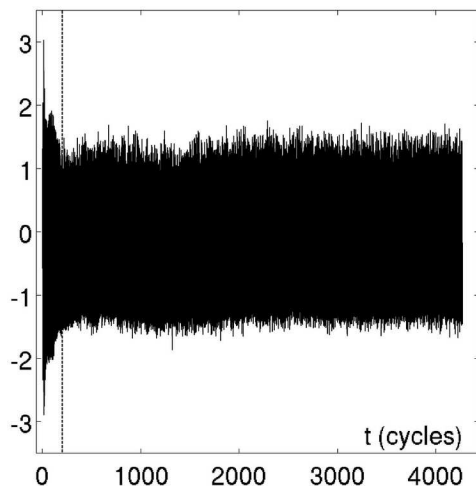


Figure 2.8: Torque signal over 4,500 cycles after the system have been parachuted in a random configuration, at  $\phi_{shear}$ . One sees a first rapid decay in roughly 200 cycles, and then that the torque remains stationary. Units on the vertical axis are arbitrary.

In the very first cycles the torque is quite high. This may be due to the constraints generated while stirring the grains. It takes roughly 200 cycles for the typical value of the torque during one cycle to decrease and to reach a stationary value. During these first cycles the system explores its local phase space, reduces the constraints and reaches a local minimum of configurational energy, minimizing by the way the torque needed to shear the system.

We run the experiment once the torque signal has relaxed. It is remarkable that the torque measured at the original position (*i.e.* when the cell is a square) is constant for a long time. We have recorded this signal during a 25,000 cycles acquisition ( $\sim 35$  hours) without images and the torque at the original position never changed (at the level of the experimental precision): this indicates that there are no profound, large amplitude reorganizations amongst the grains, even on very long time scales. This indicates also that the system is not trying to optimize some configurational energy, but rather stays in a stationary state.

### 2.1.3 The fluidized bed experiment

A major limitation of the cyclic shear experiment is that the packing fraction is fixed. Abate and Durian have measured several dynamical and structural quantities in assemblies of bidisperse grains for several packing fractions, and published several papers with different sets of data stemming from the same experimental apparatus [83, 84, 88]. They have kindly accepted to share some of their data with us. The data we have analyzed corresponds to

that used in [84], but with 3 additional denser packing fractions ( $\phi = 0.780$ , 0.791 and 0.802).

**Setup** This system consists of a bidisperse mixture of steel beads of diameters  $d_s = 3.18$  mm and  $d_l = 3.97$  mm, with respective masses of 0.130 and 0.266 g, confined to a circular region of diameter 17.7 cm. These beads roll on a circular horizontal sieve, which is 17.70 cm in diameter and has a 100  $\mu\text{m}$  mesh size.

The packing fraction – equal to the fraction of projected area occupied by the entire collection of beads – is varied from  $\phi = 0.597$  to 0.802 by changing the total number of beads from 1,470 to 1,975. The motion of the beads is excited by a vertical upflow of air through the mesh at fixed superficial speed of 545  $\text{cm}\cdot\text{s}^{-1}$  for the lower area fractions, and 500  $\text{cm}\cdot\text{s}^{-1}$  for the highest three packing fractions<sup>6</sup> (see fig. 2.9). The uniformity of the airflow is achieved by mounting the sieve atop a  $45 \times 45 \times 122$   $\text{cm}^3$  windbox,

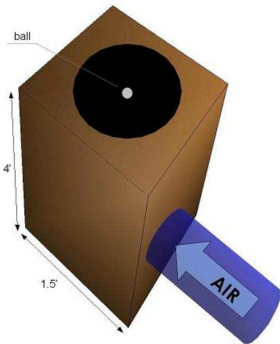


Figure 2.9: The fluidized bed experiment setup.

for which Abate and coworkers have measured the airspeeds manually with a hot-wire anemometer. This is a device consisting of a rod with a wire on the tip, connected to a voltmeter. The wire is placed in the air flow and the airspeed is measured within an accuracy of 10  $\text{cm}\cdot\text{s}^{-1}$ . The airspeed has been measured at different locations to check for uniformity. The air flow is uniform to  $\pm 10$   $\text{cm}\cdot\text{s}^{-1}$  across the cell.

The air speed is large enough to drive stochastic bead motion by turbulence ( $Re \approx 10^4$ ), but is small enough so that the beads maintain contact with the sieve and roll without slipping.

Images are captured at a frame rate of 120 Hz. In what follows we will set the unit of time to 1/120 second, *i.e.* 8.33 ms. The duration of the experimental runs is 15 minutes, *i.e.* 10,800 frames.

#### Technical details

The system of beads is illuminated by six 100 W incandescent bulbs, arrayed in a 30.5 cm diameter ring located 90 cm above the sieve. Specularly reflected light from the very top of each bead is imaged by a digital CCD camera, *Pulnix 6710*, placed at the center of the illumination ring. The sensing element consists of a  $644 \times 484$  array of  $10 \times 10$   $\mu\text{m}$  square pixels, 8 bits deep.

<sup>6</sup>Though the speed flow slightly differs, no abrupt change in the dynamics has been observed.

### 2.1.4 Softly interacting particles liquid simulation

All the systems presented so far belong to the family of granular materials *i.e.* athermal particles interacting with a hard sphere potential, and with friction. Being athermal and highly dissipative, these systems need to be driven by a permanent energy injection, and are therefore by definition “out-of-equilibrium” systems.

To extract some general features of the dynamics of supercooled systems, one has to consider systems that are closer to real liquids. As mentioned in the introduction, the dynamics of the particles in real liquids is however very difficult to probe because of the small time and length scales, and always indirectly. A convenient alternative is to run a simulation of a model liquid with a well-known interaction potential. This gives access not only to the very precise positions of the particles, but also to the whole interaction network. Another extremely precious feature, impossible to realize in experimental systems, is that one can perform isoconfigurational samplings, *i.e.* running several evolutions of the same initial configuration with randomized moments [21].

**Models and algorithms** The simulations have been done by Asaph Widmer-Cooper in the *Computer Science and Engineering* program of UC Berkeley. A precise description of the algorithms is given in his thesis [21], but let us recall here the main features. We consider a two-dimensional glass-forming liquid consisting of an equimolar binary mixture of particles interacting via purely repulsive potentials of the form:

$$u_{ab}(r) = \epsilon \left[ \frac{\sigma_{ab}}{r} \right]^{12} \quad (2.1)$$

where  $\sigma_{ab}$  rules the interaction between particles of types  $a$  and  $b$ . All units will be reduced so that  $\sigma_{11} = \epsilon = m = 1.0$ , where  $m$  is the mass of both types of particle. The reduced unit of time is given by  $\tau = \sigma_{11} \sqrt{m/\epsilon}$ . A total of  $N$  particles are enclosed in a square box with periodic boundary conditions. The molecular dynamics simulations were carried out at constant number of particles, volume and temperature (therefore called “NVT” simulations) using the Nosé-Poincaré-Andersen (NPA) algorithm developed by Laird *et al.* [89, 90].

The structural, dynamic and thermodynamic properties of this model glass-forming liquid have been characterized by Perera and Harrowell [91, 22]. All configurations investigated were equilibrated configurations taken from the study in [22] and re-equilibrated with the NPA Hamiltonian. While the supercooled liquid state is strictly metastable, we will refer to such configurations as “equilibrated”.

**Additive or non-additive?** We have made a few trials before choosing the parameters of the system. Our first attempt was to use some well-known, already published data. In this regard, the data in [26] was appealing, but two things were unsatisfactory: first there are only  $N = 1024$  particles, which is too few to clearly avoid size effects in the computation of the four point correlation functions, and second there are some small crystalline clusters. So we have decided to realize new simulations, with the following organization: Widmer-Cooper ran the simulations and computed the Debye-Waller maps at several instants, the Saclay group (Candelier, Dauchot and Biroli) did the analysis of the dynamics (cage jumps and dynamical heterogeneities) and Kummerfeld and Reichman computed the soft modes in a few configurations.

To quantify microcrystallization further, we have plotted on figure 2.10 middle-left an instantaneous map of the percentage of neighbors of the same kind, *i.e.* large or small. The red areas correspond to crystalline domains containing regular hexagons of large particles. These microcrystallites have an influence on the dynamics: when one averages the dynamical correlation  $Q_{p,t}^*$  over time<sup>7</sup>, it appears that the crystalline zones are far less decorrelated than the truly amorphous zones (see fig. 2.10-top left). This heterogeneity in the structure itself trivially leads to a spatial heterogeneity in the relaxation process, but the temporal intermittency may be limited since the microcrystallite evolves modestly during the simulation time. The heterogeneities have a different nature than in completely amorphous glass formers, where they are both spatial and temporal.

Perera and Harrowell have studied the influence of the temperature on microsegregation in  $NPT$  simulations<sup>8</sup> [22]. They find that the tendency to microsegregate increases when the temperature goes below  $T = 0.5$ <sup>9</sup>, without a clear demixing of the two species of particles. Since the system in [26] is at  $T = 0.4$ , it may microsegregate in some areas.

In order to avoid microsegregation, we could simply use higher temperatures, but in this case we could not explore the vicinity of the glass transition. So we have used a *non-additive* system instead. This means that given the interactions between small particles  $\sigma_{11} = 1.0$  and between large particles  $\sigma_{22} = 1.4$ , instead of having an additive rule for the cross-species interactions, namely  $\sigma_{12} = \frac{\sigma_{11} + \sigma_{22}}{2} = 1.2$ , we have taken  $\sigma_{12} = 1.1$ . Indeed, a smaller value of  $\sigma_{11}$  increases the attraction between small and large particles and can compensate the energy gain of mono-crystalline cluster forming at low temperature. Note also that the temperature in the non-additive system is  $T = 0.45$  instead of 0.4 in the additive one.

In the non-additive system, three observations can be made on the struc-

---

<sup>7</sup>See B.2 for a precise definition of  $Q_{p,t}^*$ .

<sup>8</sup>In  $NPT$  simulation, the constant parameters are the number of articles  $N$ , the pressure  $P$  and the temperature  $T$ .

<sup>9</sup>The reduced units of temperature are  $k_B/\varepsilon$ , where  $\varepsilon = 1$ .

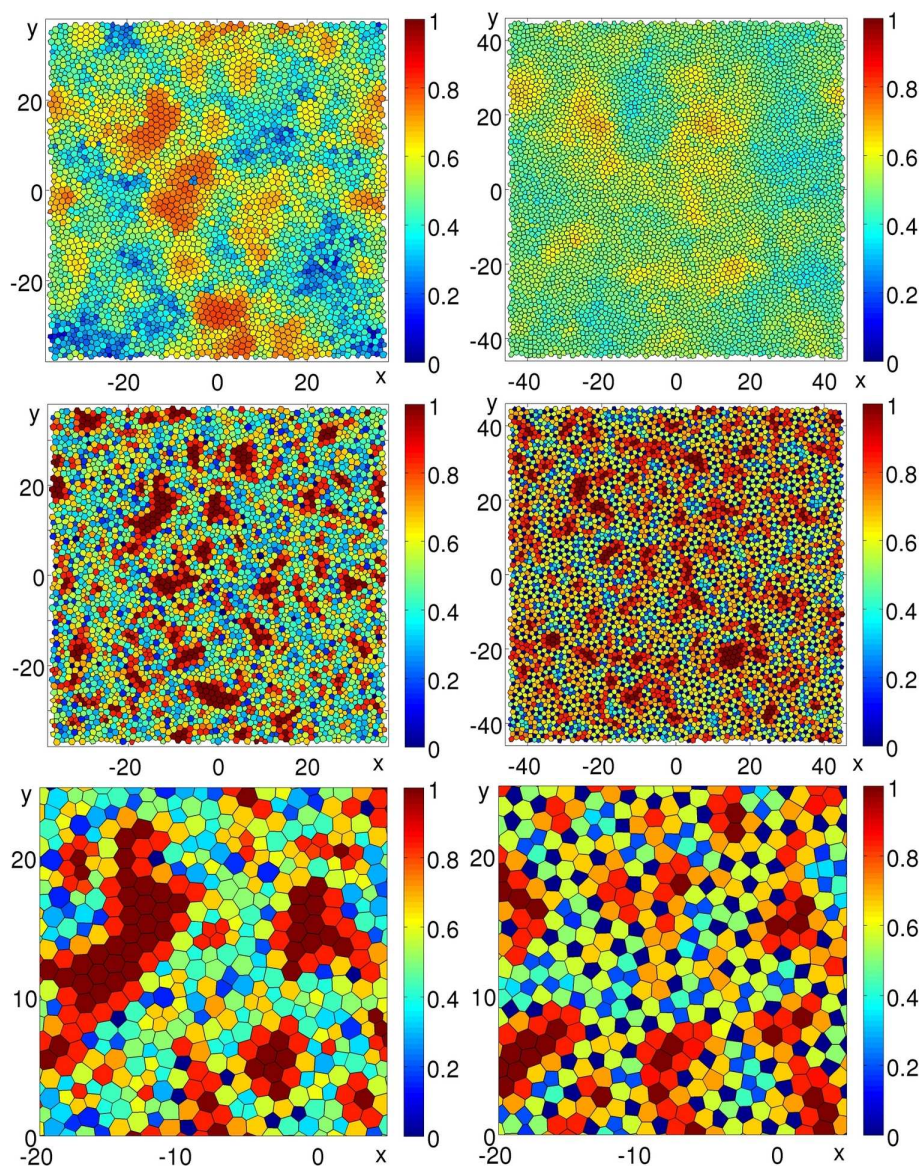


Figure 2.10: Micro-crystallization and average dynamics. **Top** Average decorrelation maps.  $Q_{p,t}(\tau^*)$  is averaged over  $t$  for each particle.  $\tau^* = 850$  for the large additive system at  $T = 0.4$  (left) and 600 for the large non-additive system at  $T = 0.45$  (right). **Middle** Percentage of nearest neighbors of the same kind. Note that the large micro-crystallites (red areas) present in the large additive system (left) are much smaller in the large non-additive system (right).  $t = 1$ . **Bottom** Same as above, zoomed. Note the difference in crystalline order: crystallites for the additive system and crystal alloy for the non-additive system.

ture and the dynamics:

- There are still clusters of the same kind, but they are considerably smaller than in the additive case (see fig. 2.10 middle-right).
- The averaged relaxation on a long time scale is much more homogeneous in space (compare fig. 2.10 top-left and right). We believe that this is a direct consequence of the disparition of crystalline clusters.
- A new kind of “order” appears however, closer to a crystal of a binary alloy. The mesh of this binary crystal is made of small particles with pentagon-shaped Voronoï cells surrounded by large particles with heptagon-shaped cells.

Fortunately, this new kind of order restores a spatially homogeneous relaxation on time scales of the order of the simulation time. We will consider in the following that it does not disturb the dynamics.

**Methods** Widmer-Cooper has run 5 configurations with  $N = 1440$  particles and one configuration with  $N = 5760$  particles, each of them having 190,000 time steps separated by  $0.07\tau_0$ , where  $\tau_0$  is the typical time for 10 collisions. In the following, we will concentrate only on the large system where  $N = 5760$ .

In addition to this configuration with a large number of particles, Widmer-Cooper has run several isoconfigurations at different instants. To generate these isoconfigurational ensembles of runs at a given temperature  $T$ , he starts with a configuration that has been equilibrated at  $T$  and for each isoconfiguration he randomly assigns the initial particle momenta from the appropriate Maxwell-Boltzmann distribution.

This liquid of soft particles played an important role in the understanding of the results presented in chapter 4. In particular, it allows us to compute the soft modes and the Debye-Waller maps probing the local energy landscape, and to compare them to the dynamics of the configurations on long time scales.

### 2.1.5 Vertically vibrated monodisperse grains

In all the systems presented so far, bidisperse grains have been used to avoid crystallization. Indeed, the time scale on which the grains could separate into distinct crystalline phases is considerably higher than the experimental times. However, it could be interesting to test our data analysis toolkit onto a set of monodisperse beads. First, this would provide a sanity check of our methods in a system where the transition from liquid to solid is well known and with a clear signature in the structure. Then, Reis *et al.* [92, 93] have studied such a system of monodisperse beads, and even though

their monodisperse system is known not to exhibit a glass transition, they observe many of the precursors usually associated with glassy dynamics. They have kindly accepted to share their data with us in order to push further the comparison with glassy systems, namely by computing the four point correlation functions.

The experimental apparatus is adapted from a geometry introduced by Olafsen and Urbach [94]. Energy is injected into a collection of stainless steel spheres through sinusoidal vertical vibration with frequency  $f$  and dimensionless acceleration  $\Gamma = A(2\pi f^2/g)$ , where  $A$  is the amplitude of vibration and  $g$  the gravitational acceleration. The forcing parameters are fixed at  $f = 50$  Hz and  $\Gamma = 4$ .

The spheres have a diameter  $d = 1.191$  mm and are confined in a fixed volume gap set by a horizontal stainless steel annulus of 101.6 mm inner diameter, sandwiched between two glass plates (see fig. 2.11-left). The thickness of this annulus is  $1.6d$ , thus constraining the system to be quasi-2D. The top glass plate is optically flat, but the bottom plate is roughened by sandblasting generating random structures from 50 to  $500\mu\text{m}$ . Upon vibration, the rough plate homogeneously randomizes the trajectories of the particles. The dynamics is recorded with high speed photography at 840 Hz and the particle trajectories are tracked in a  $15 \times 15$  mm<sup>2</sup> central region.

The system is horizontal to minimize gravity-induced effects such as

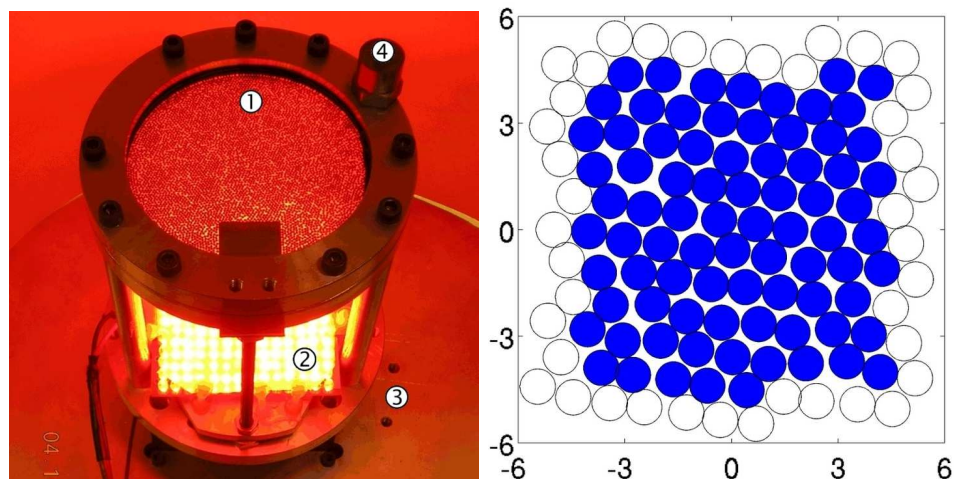


Figure 2.11: The monodisperse experiment. **Left** Artistic view of the experimental setup. One can see ① the confinement cell, ② the lighting system, ③ the vibration device and ④ the acceleration sensor. **Right** Typical acquisition area. There are 81 particles in this frame, which is the maximum for these data. The white particles are not in the ROI since they are too close to the border of the acquisition field.

rolling and compaction. The total number of particles is varied in the fixed volume cell over a wide range, from a single particle to an hexagonally packed crystal. A total of 54 packing fractions have been explored.

These data will be shortly analyzed in 4.5.3. Note however that the small size of the acquisition window limits the analysis of the spatial correlations and constraints the range of comparison with glass forming systems.

## 2.2 Data processing and analysis

This large number of systems represents an enormous amount of data. Since they have several origins their initial format was different. It was therefore crucial to develop a common framework both able to deal with a large amount of data and flexible enough so that new data can be easily inserted. In this section, we explain the basis of this framework in 4 points: Image processing, particle tracking<sup>10</sup>, databases and data analysis.

### 2.2.1 Image processing

In all our experiments, the raw data are images: one has to perform some image processing to extract the particles' positions and sizes. To this aim, we have chosen the *LabView* suite, a performant package of data acquisition and analysis tools. Thanks to its image processing dedicated tool, *Vision Assistant*, which have a simple but powerful graphical interface, a lot of time can be saved during the development phase. Moreover the treatment itself is efficient since the Labview routines are well optimized.

Here are typical raw pictures taken from different experimental setups:

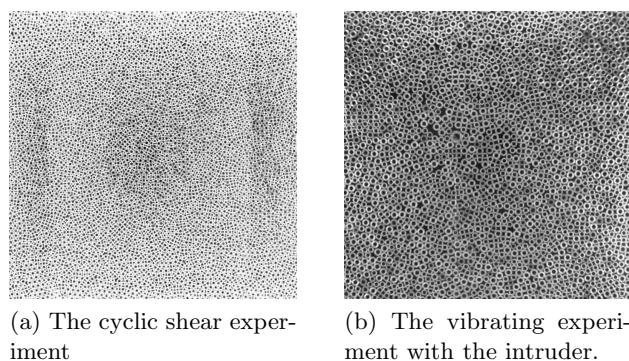


Figure 2.12: Typical raw images from the different experimental systems

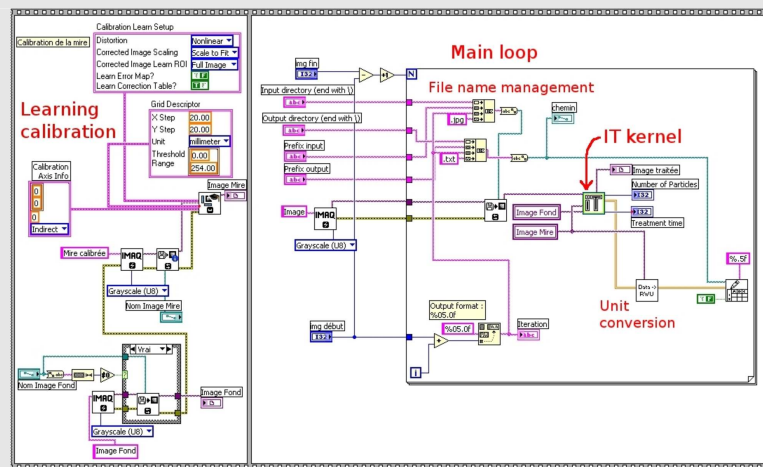
---

<sup>10</sup>Often, image treatment and tracking are merged in an entangled set of programs. This can have some interest, for instance one could imagine to decrease the number of false positive detections in the image treatment by focusing only in the regions where a particle is likely to be. However, the complexity of the programs strongly increase, and many spurious results can emerge from this retroaction loop. In general, this is not a good practice and it should be avoided unless there is no other possibility.

One immediately notices strong differences between those pictures, mainly due to the lighting conditions. As a result the image treatment framework have to be separated into two parts: a specific part that treats only the particular features of each system, namely the conversion from an image to an array of positions and sizes, and a generic part that deals with all the operations that are redundant in each system.

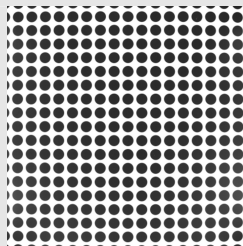
### The program

Here is a sketch of the global image treatment program:



The specific operations are treated in a special kernel, here *IT.vi*. This program takes an image buffer filled with the image to treat for input and returns an array of positions and sizes, in pixels. The generic operations made by the kernel program are the following:

- Compensate image distortions. The objectives of the cameras always induce a small distortion, more pronounced at the boundaries. For instance, in the cyclic shear experiment the camera induce a “fat cushion” alteration: the lines become concave curves with a deformation that goes up to 7 pixels. By learning the deformation from a regular mire picture, the program can apply a reverse, non-linear operation to the images and produce an undistorted image. Here is a typical mire image and an undistorted background image (note the small black zones at the boundaries):



- Remove a background. This is optional, but it can be very useful to compensate non-homogeneous lighting conditions. It can give spectacular results, especially with lighting conditions that fluctuate on a time scale much longer than the acquisition period, but much smaller than the experimental time.
- Make a loop to treat all the images of a run at once.
- Convert pixel units in “real world units”, *i.e.* millimeters or directly in our adimensionalized unit, the diameter of small particles.
- Save the output arrays of positions and sizes to files.

A sequence of typical operations is shown in fig. 2.13, performed onto the images of the vibrating experiment:

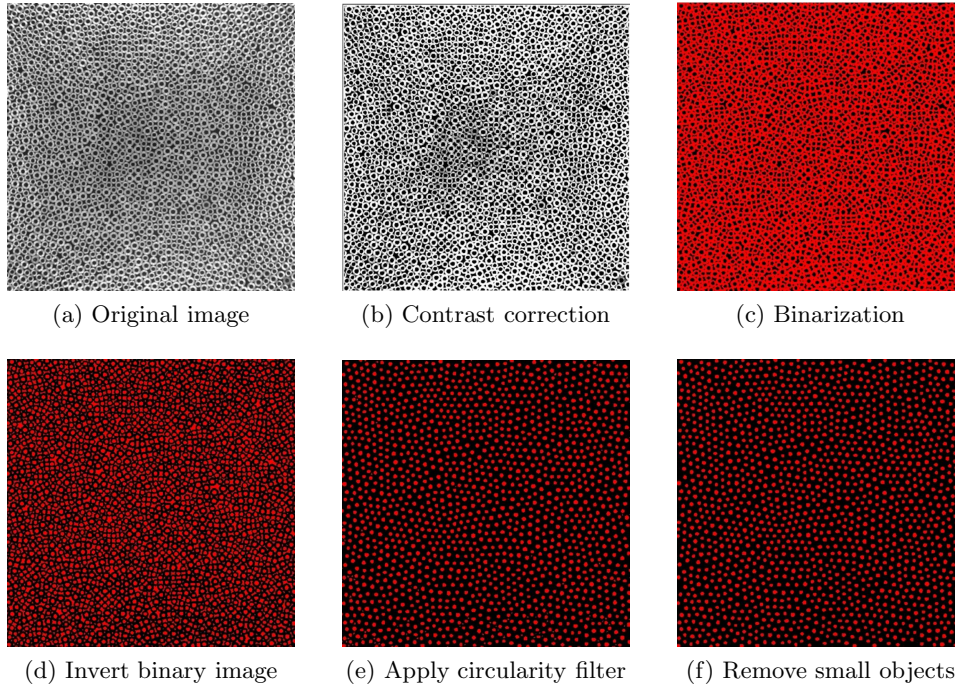


Figure 2.13: Main steps of the image treatment. Though these operations are generic, they have to be finely tuned to every case.

Depending on the homogeneity of the lighting and a few other parameters, the number of necessary operations can vary from 5 up to 20 in the most difficult cases.

An interesting issue is error handling. A distinction has to be made between false positive and missing particles. On one hand, false positive are interstitial spaces that have enough pixels to pass over the small size particle filter. They have little importance as long as their number is not too large:

their presence fluctuates a lot in time such that they can easily be removed during the tracking.

On the other hand, missing particles are clearly the worst error, since it will not be possible to recover the particle's position unless inferring it from its neighborhood.

### Retrieving algorithm

Retrieve a particle that has been lost during image treatment may sound an odd idea at first sight. However, in dense states, the position of a particle is highly constrained by the position of its first neighbors, so it is possible to guess the position with a high accuracy.

To determine quickly and locally the first neighbors, one can use the following algorithm: take the interpolation of the position of the particle at times  $t - 1$  and  $t + 1$  as the origin of space, and consider the set of particles inside a disk of radius 2, in which all the nearest neighbors will stand, but not only. The position of each of these particles can be expressed in polar coordinates  $(r, \theta)$ . The convex hull of the set of points with coordinates  $(1/r, \theta)$  finds the nearest neighbors.

Once the first neighbors have been determined without errors, a simple minimization algorithm taking the radius of the particles into account will find the most probable position of the missing particle.

A benchmark study revealed that this method locates the missing particles with the same precision than for the other ones. We have used this method for a small amount of particle-times (in a ratio depending on the experiment, often 0 and maximally  $3.5 * 10^{-5}$ ) and the retrieved particles are labelled with a special marker in the databases, so that it is still possible to discard them *a posteriori*.

However this method still has some limitations: as soon as two or more adjacent particles are missing, the constraints imposed by the neighbors' positions are often not enough. In addition, it is not possible to retrieve particles at the boundary of the acquisition field.

In the cyclic shear experiment and the vibrating experiment, the image treatment algorithm locates the holes inside the cylinders instead of the grains themselves. Other techniques have been used by Abate and Durian and by Reis *et al.* : in the fluidized bed experiment the particles are spherical and the reflect on the top of the steel balls is used (this reflect is due to of the lighting apparatus above the experiment) while in the monodisperse experiment, the particles are shadowing the light source that diffuse from below and appear in black on the CCD. *In fine*, the positions of the particles are extracted from these disk-shaped sets of pixels, by determining their center of mass. The precision on the position of the particles is of the order of  $10^{-3}$  diameters of small grains in the cyclic shear experiment and the fluidized bed experiment, and  $5.10^{-4}$  in the vibrating experiment<sup>11</sup>.

<sup>11</sup>We could improve the precision on the positions by using the various grey scales in the

The precision on the particles' sizes is the intrinsic polydispersity of the particles, estimated at  $10^{-5}$  for the grains used in the cyclic shear experiment and the vibrating experiment; the precision on their area, in pixels, is enough to discriminate perfectly between big and small particles.

An important remark is that it is not possible to determine the contact network from experimental images. As a result a whole range of crucial information carried by the force network is not accessible to experimental measurements.

### 2.2.2 Tracking

Once the positions and sizes of the particles have been determined, the tracking process can be employed. The great advantage of investigating dense matter states is that they are usually very slowly evolving: this is a decisive issue for the tracking.

Indeed, the key criterion is the following: it is only possible to track the particles that stay in their Voronoï cells between two successive images. If the particles are moving too fast compared to the acquisition rate and their relative distances, the distances between a particle at time  $t$  and  $t + 1$  can be larger than the distance to another particle at  $t + 1$  that have moved close to the position at  $t$ . In this case mismatches are not only possible, their number sharply increases.

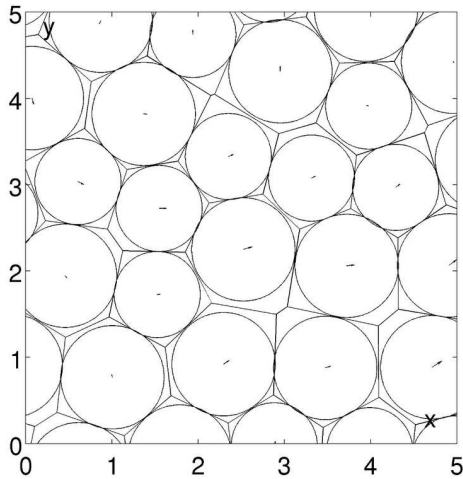


Figure 2.14: Amplitude of the displacements in a single time step compared to the size of Voronoï cells (in the cyclic shear experiment).

To be precise, global affine transformations of the grain positions (translation, rotation, shear and more rarely scaling) can induce large displacements but does not disturb the tracking if they are correctly removed. So it may be possible to track highly moving particles if they are embedded in a global current, at a certain coarsegrained scale. So the precise criterion for tracking ability is the following: one can only track the particles for which the *relative movement to one another* (*i.e.* when the coarsegrained currents are removed) are smaller than their Voronoï cell sizes.

Since in most of our data the displacements in one single time step is very short ( $10^{-3}$  for the vibrating ex-

---

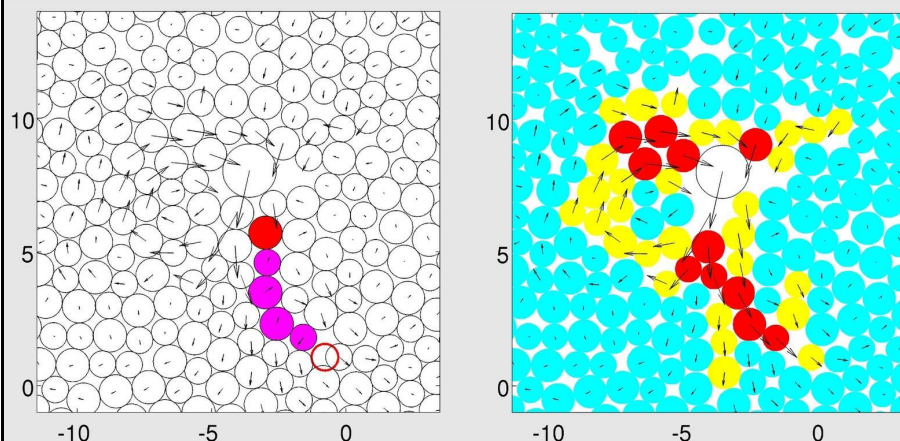
images instead of binarizing them. For instance we could use a direct correlation of the images to a reference single particle pattern.

periment and  $10^{-2}$  for the cyclic shear experiment, see fig. 2.14), tracking is an easy task and we do not need to take the coarsegrained flow into account.

This means that it is easy to have a 100% tracking if there is no particle loss during the image treatment for all the dense packings we are studying in this thesis.

### Tracking the intruder

There is a special case, however, namely when the intruder is evolving in a loose packing of grains. It can move up to several grains diameters in a single time step. The intruder being bigger than the other grains, it is easy to track, but tracking the surrounding grains becomes a far from obvious task. Here is a typical tracking problem (left) and the solution (right):



A chain of particles has been mismatched (in magenta), and there are two unmatched particles (in red), one at time  $t$  (plain) and one at time  $t + 1$  (contour). These two unmatched particles are clearly too far to be linkable.

The following algorithm has been employed to address this type of issues:

- Make a first match with a severe maximal distance criterion. Only the particles that are moving a few are matched, with eventually a few mismatches amongst the most mobile particles that fall on the top of another particle. This matches the cyan particles in the right picture.
- Compute the average flow around each particle, and consider now [the position of the particle at time  $t +$  the local current] as the position of each particle at time  $t$ .
- Make a second match with the same severe maximal distance. The average flow will create some new good matches and may destroy the wrong ones. In the right picture, the yellow particles are newly matched with success.
- Iterate this process by re-computing the average flow and re-match at every step. This algorithm rapidly converges to the good matching, here at the 3<sup>rd</sup> step the remaining red particles are matched with success.

### 2.2.3 Databases

Once we have the particle's positions and sizes, the experiments are at the same level than the output of the simulations (except that one cannot extract the forces from the potential, which is unknown). All those data are stored in an generic manner into databases on a separate server.

**Global architecture** The reader will find technical details on this architecture in a separate appendix<sup>12</sup>. As a brief introduction, the basic architecture is the following:

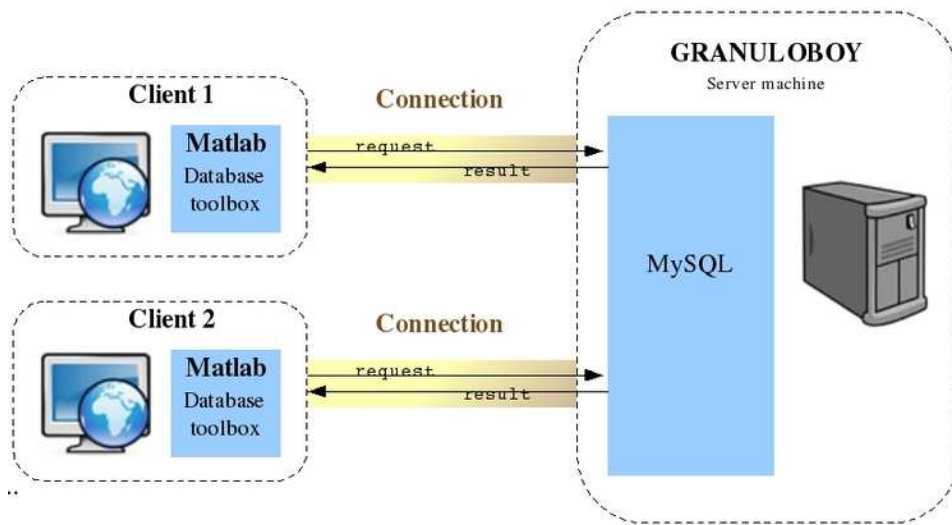


Figure 2.15: Scheme of the client-server interactions.

The server is a dedicated machine, located in a dedicated air-cooled room, with other servers. There is little difference between this server and a classical web server, except the low number of connections.

Users (or clients) have access to the server's data via the network: first, they have to establish a connection with the server program, then they can make requests, and finally they receive the result of the request. No computation is done on the server machine: all the calculus are done on the client machines. However, the server machine is not only a storage support, it has the crucial task to retrieve data. One of the major advantage of a database framework is that there is no opening/closing file time. By example, for the simplest repetitive action to find one particle's position through time for the cyclic shear experiment, it is 1000 times faster than scanning the files on a local hard drive.

<sup>12</sup> *Les bases de données pour les GITans* (french). Can be downloaded at: <http://iramis.cea.fr/spec/GIT/index.php?ici=toolbox>

Using a database framework provide several other advantages. First of all, backups are simple and can be automatically realized. Second, all the users can access exactly the same data, or one single user can access the same data from different client machines. This prevents the users from having multiple copies of the same data, eventually with separated evolutions.

**Databases, tables and particle-times** The data are stored in databases, that are collections of tables. Tables are arrays, the records being the rows of this array. The columns describe the attributes of each record. The unitary record is the particle-time (PT), *i.e.* a particle at a certain time. The attributes of a PT are two indexes of particle and time, its position, size, number of nearest neighbors, etc. There is no limitation for the number of possible attributes.

When counting in terms of PT, the amount of data can easily be estimated and compared. For instance, in the cyclic shear experiment where we follow roughly 4,000 particles in 10,000 time steps the number of PT is of the order of  $4 \cdot 10^7$ . The images for this run take 25 Go, while the raw PT take 1 Go. Table 2.16 summarizes the volumes for all the systems that have been inserted during the last 3 years.

	Systems	PT (in millions)
The cyclic shear experiment	Guillaume Marty's thesis	25
	Multiple angle exp.	75
	Data presented here	40
The vibrating experiment	Lechenault's thesis	230
	The intruder	60
The fluidized bed experiment	15 packing fractions	300
The monodisperse experiment	54 packing fractions	50
The glass former simulation	Additive, small systems	1025 <sup>13</sup>
	Additive, large system	82
	Non-additive, small systems	2740 <sup>13</sup>
	Non-additive, large system	109
The shearing experiment's simulation	2 packing fractions + 1 cycle	20
TOTAL		4755

Figure 2.16: Summary of the amount of data for the different systems. The shaded cells are not presented in this thesis.

To be complete, one has to add the content of the tables dealing with structural properties of the Laguerre tessellation containing neighborhood links and vertices information, which is roughly 3 times the volume of the raw PT data itself. All this represent  $\sim 1$ To of ASCII data. Though this amount of storage is common nowadays, it is however quite rare for purely ASCII data. If all these lines were printed into an encyclopedia, it would extend on a 20 kilometers shelf! This is only one order of magnitude below the famous Library of Congress for instance, which gathers 25 To of raw ASCII data.

### 2.2.4 Data analysis: the Granulobox

Dealing with this huge amount of data coming from several sources requires a dedicated framework. We have built up a complete *Matlab* toolbox, named the “Granulobox”. The *Core* part – the part that is generic to all users – contains  $\sim 100$  files, while the entire toolbox contains more than 1500 files. A rather complete manual of the Granulobox can be found in the *help files* of the toolbox.

Briefly, the principal asset of the Granulobox resides in the use of a special object, the *handler*. Basically, the handler is like a pointer on a special system, experiment and run: it is the key to access the data since it embeds the connexion to the database, but it is also the roadmap to navigate between several systems or several runs with changing parameters. It simply makes it easy to jump from one system to another. There are several consequences:

- The same pool of programs can analyze several data.
- The number of programs is an *intensive* quantity rather than an *extensive* one. One can then spend more time to make these few programs robust, instead of coding numerous specific programs.
- A new user can exploit this system at a smaller cost.
- Extensive cross-system studies become accessible.

Data treatment and analysis is an important part of the research work, and is too often neglected. This is nowadays one of the major basis of efficiency in research. There is even no need to be at the edge of technology, but it is crucial to use the right tool at the right time and place. One way to achieve this is to exchange information and ideas in order to construct a common framework. My hope is that the framework we have set up during

---

<sup>13</sup>It may be surprising that the small systems are much bigger in terms of PT than the big ones. This is due to the fact that for the small systems we have several configurations, and a frame rate 10 times higher.

this thesis will help my colleagues and followers, and that they will continue to make it evolve in the same spirit.

## 2.3 Tables

In this section, tables are presented that summarize the properties of the different systems.

**Code names** Here is a table of the code names of each system in the databases. These code names are used in a subsequent tables, and in the data storage and treatment architecture *in silico*. References of the corresponding papers and thesis are given.

System	Code name	Comments	Ref.
The vibrating experiment	dra_001	Lechenault's data	[47, 80, 81]
	dra_002	The aging protocol	
	dra_003	The parachutist protocol	
	dra_906	The intruder, one $F$ many $\phi$	[95, 96]
	dra_907	The intruder, many $F$ one $\phi$	[95, 96]
The cyclic shear experiment	gra_001	Guillaume Marty's thesis	[20, 82, 40]
	gra_002	Different angles ( $8^\circ \rightarrow 3^\circ \rightarrow 8^\circ$ )	[20]
	gra_003	Raphael's Candelier data	[35]
The shearing experiment's simulation	grs_001	1 cycle (decomposition)	
	grs_002	806 cycles at $\phi = 0.819$	
	grs_003	1140 cycles at $\phi = 0.830$	
The fluidized bed experiment	add_001	Original data (108,000 frames)	[84]
	add_002	Reduced data (10,800 frames)	[85]
The glass former simulation	hrs_001	Additive, small system	[26, 21]
	hrs_002	Additive, large system	
	hrs_003	Non-additive, small system	[21]
	hrs_004	Non-additive, large system	[38]
	hrs_005	Non-Additive, isoconfigurations in the large system	[38]
The monodisperse experiment	hor_001	Monodisperse, 54 packing fractions	[93]

Table 2.3: Table of code names.

**General information** Here is some general information on each system and on the corresponding particles. The columns are:

- $N_p$  The number of particles in the system, and  $N_{ROI}$  the average number of particles in the *ROI* at each time frame.
- $T$  The total number of time frames.
- $\sigma_l/\sigma_s$  The ratio of the diameters of large and small particles in experiments, or interaction parameter for the softly repulsive particles.
- $\Delta$  The intrinsic polydispersity of the sample. If  $\sigma_i$  is the diameter of particle  $i$  and  $\langle \cdot \rangle_p$  the average over particles,  $\Delta$  is given by the formula:

$$\Delta = \frac{\sqrt{\langle \sigma_i^2 \rangle_p - \langle \sigma_i \rangle_p^2}}{\langle \sigma_i \rangle_p}$$

- $\phi$  The packing fraction (surfacic fraction). The density  $d = N_p/S_{total}$  is given in [.] for softly repulsing particles in which  $\phi$  cannot be defined.

If there are several values, the total range is given and the number of values is in parenthesis.

System	$N_p$	$N_{ROI}$	T	$\sigma_l/\sigma_s$	$\Delta$	$\phi$ , [d]
add_002	1 470-1 975(15)	1 300	10 800	1.248	0.111	0.597-0.802 (15)
dra_001	8 250	1 350	10 000	1.25	0.111	0.8402-0.8457 (15)
dra_002	8 250	1 630	8 570-71 017 (8)	1.25	0.111	0.840-0.846(8)
dra_003	8 250	1 800	10 000	1.25	0.111	0.835-0.840(8)
dra_906	8 250	1 616	165-5 325 (15)	1.25	0.114	0.8306-0.8418 (15)
dra_907	8 250	/	50-32 766 (36)	1.25	0.114	0.8383-0.8399 (3)
gra_001	8 000	2 800	10 000	1.2	0.091	0.84
gra_002	8 000	2 800	10k $\rightarrow$ 5k $\rightarrow$ 10k	1.2	0.091	0.84
gra_003	8 350	3 785	10 000	1.2	0.091	0.84
grs_001	8 715	3 800	400	1.2	0.091	0.819
grs_002	8 715	3 800	806	1.2	0.091	0.819
grs_003	8 350	3 800	1 140	1.2	0.091	0.830
hor_001	4 146-5 607	38-78	8 192	/	0	0.570-0.770 (54)
hrs_001	1 024	1 024	200 857 (5)	1.4	0.167	[0.747]
hrs_002	4 096	4 096	20 085	1.4	0.167	[0.747]
hrs_003	1 440	1 440	190 000 (5)	1.4	0.082	[0.719]
hrs_004	5 760	5 760	19 000	1.4	0.082	[0.719]
hrs_005	5 760	5 760	1 500 (6)	1.4	0.082	[0.719]

Table 2.4: General informations and basic structural properties.



# Chapter 3

## Let's jam!

### Contents

---

<b>3.1</b>	<b>Dynamics at the jamming transition . . . . .</b>	<b>74</b>
<b>3.2</b>	<b>The journey of an intruder . . . . .</b>	<b>84</b>
<b>3.3</b>	<b>Toward jamming . . . . .</b>	<b>105</b>
<b>3.4</b>	<b>Discussion and perspectives . . . . .</b>	<b>110</b>

---

*We're jamming, jamming and I hope you like jamming too  
Ain't no rules, ain't vow, we can do it anyhow  
– Bob Marley and the Wailers, Jamming (1977)*

A wide range of athermal systems such as grains flowing onto a pile, colloids, gels or cars on a highway exhibits a sharp transition between a liquid-like flowing state to a solid-like arrested state, which usually occurs in a narrow range of density. One could be tempted to gather all these at-first-sight seemingly equivalent phenomenologies into the same concept of *Jamming* [75]. However, to now, the only unambiguous definition of jamming has been given for frictionless spheres at zero temperature [45] where “point  $J$ ” has been found to induce critical scalings above jamming. Even in this quite restrictive case, point  $J$  is strongly dependent on the protocol [66, 6]. Moreover, in practice, for thermal systems jamming can happen at several values, namely in a “ $J$ -interval” [9], depending on the history of the system and in particular on the out-of-equilibrium branch chosen by the system when entering the glassy state.

In this chapter, we consider a glassy granular system under mechanical driving and we discuss experimental evidences of a clear distinction between dynamical arrest and the onset of rigidity. The system, made of a horizontally vibrated monolayer of bidisperse grains, was first studied by Lechenault *et al.* [47, 80, 81] with the experimental setup described in 2.1.1; the authors have shown that the appearance of rigidity is accompanied by critical dynamical fluctuations. Four-point correlators exhibit a critical scaling in the sharp vicinity of the packing fraction  $\phi_J$  above which the pressure

in the absence of vibration becomes non-zero, and the associated correlation length scale is shown to soar significantly around this point.

In the present work we will study the non-linear response to a local perturbation in the same experimental apparatus, namely by pulling a probe through the media with a constant force. We will see that increasing dynamical fluctuations loom upon jamming, with a coherent set of critical exponents. This protocol also gives interesting connections with the force network and the reorganization patterns around the probe.

The chapter is organized as follows: in a first section we review the most important results obtained by Lechenault *et al.* [47, 80, 81] in 3.1.1, which we will complete with recent results obtained in the context of the present study in 3.1.2. Then we will introduce briefly the new experiment conducted in the same setup, the results of which can be found in a Letter (published in *Physical Review Letters*, see [95] or appendix A where one can find a full version at page 174) and in a longer paper: “Journey of an intruder through the fluidisation and jamming transitions of a dense granular media” submitted to *Physical Review E*, the latter being fully reported here. The chapter finishes with a few other studies aimed at exploring the dynamics of glassy states with other protocols. Finally, we will give an overall view of our understanding of jamming in the light of all the above observations.

## 3.1 Dynamics at the jamming transition

### 3.1.1 State of the art

Let us first present the dynamical properties of granular materials close to jamming by taking as a reference the experiment set up by Lechenault during his thesis. This is indeed now a well-known system in which several quantities have been already computed, and moreover this is the basis on which we have built our experiments. Most of the results presented in this section have been established by Lechenault *et al.* [80, 81, 47]; the first part of this section will be devoted to a brief review of these results. Some new developments will be presented afterwards.

The experimental setup – which has been presented in the “Systems” chapter (2.1.1) – consists of a bidisperse monolayer of disks horizontally vibrated in a fixed rectangular cell, with a mobile wall allowing precise surfacic fraction control.

**Protocol** Providing reproducible measurements and reaching a steady state analogous to those reported in [97] *i.e.* in which macroscopic observables are in one to one correspondence with the control parameter in a reversible and history independent manner requires a specific protocol. One first performs a series of compression steps to reach a highly jammed configuration (typically of the order of  $\phi = 0.846$ ) before stepwise decompressing

the system. At each step the pressure signal is acquired as a function of time both with and without vibration. In the compression phase, the pressure relaxes after each step but never reaches a stationary state. In the decompression phase however, stationary and reversible pressure signals are obtained. However, the structural relaxation time  $\tau_\alpha$  is much longer than our experimental time (10,000 cycles). Although the system is not fully equilibrated, it appears to be in partial equilibrium within the basin of configurations corresponding to a given structural arrangement of the grains.

The mean pressure in the decompression phase, its residual static part (when the vibration is switched off) and the kinetic part defined as their difference are shown as a function of the packing fraction in fig.3.1.

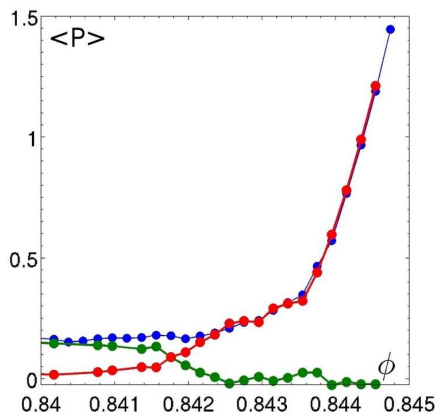


Figure 3.1: Dynamic *vs* static pressure as functions of the packing fraction. Blue points are the average values of the dynamic pressure while red points stand for the static pressure (see definition in the text). The difference between dynamic and static pressures is in green.

At high packing fractions, static internal stresses are important, and completely dominate the mean pressure. The grain assembly, in this regime, is rigidly locked to the frame. As the packing fraction is decreased, a kinetic contribution appears as the grains unlock from the side walls and start making a distinctive noise. Lechenault *et al.* identified these phenomena with the rigidity / jamming transition, and thereby obtained  $\phi_J$  within a  $5 \cdot 10^{-4}$  accuracy for each run, the precise value of  $\phi_J$  depending on the details of the protocol<sup>1</sup>. At lower packing fractions, the pressure is of purely kinetic origin: the grains slide on the sides and move along with the plate. In these loose states the static pressure is zero.

**Trajectories.** Fig. 3.2 shows the trajectories of a single grain during the whole experimental window ( $10^4$  vibration cycles) for packing fractions sitting on both sides of the transition. Clearly, the typical exploration of the particle is much larger for the lower packing fractions. Incipient caging dynamics emerges for the trajectories at large packing fractions: successive positions of the grain seem to stay confined around fixed positions for a long time and then hop around from one cage to another over longer time scales.

<sup>1</sup>See table 2.2 at page 49 for a comparison.

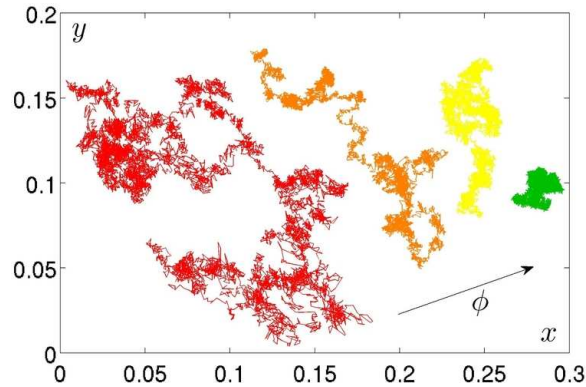
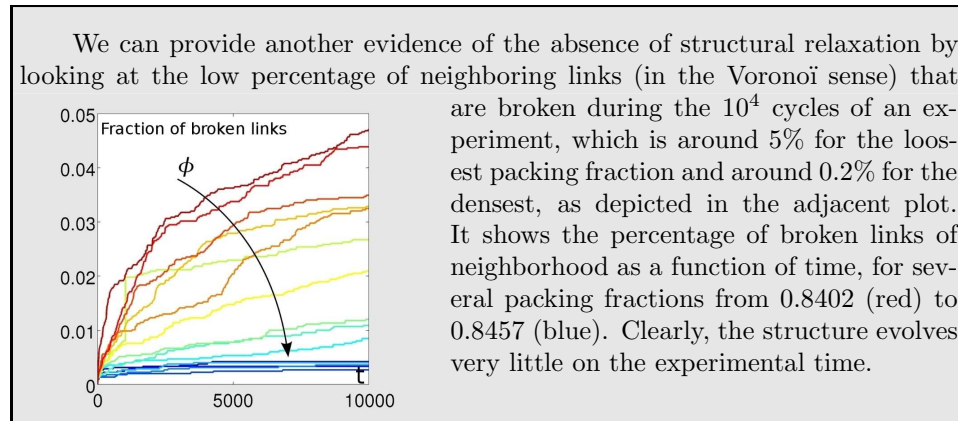


Figure 3.2: Typical trajectories of a grain during a 20 minute acquisition. The packing fractions are  $\phi = 0.8402$  (red),  $\phi = 0.8417$  (orange),  $\phi = 0.8422$  (yellow),  $\phi = 0.8430$  (green).  $\phi_J$  would stand between the orange and yellow trajectories.

The striking feature of these trajectories is the remarkably small amplitude of the motion. Even at the loosest packing fraction, the grains do not move much further than a fraction of diameter ( $d_{tot} \sim 0.2$ ) over the course of one experiment. Moreover, the cage hops are occurring on distances of the order of  $10^{-3}$  to  $10^{-2}$ . This is a strong indication that for all studied packing fractions, the structure of the system does not relax<sup>2</sup>.



We can provide another evidence of the absence of structural relaxation by looking at the low percentage of neighboring links (in the Voronoï sense) that are broken during the  $10^4$  cycles of an experiment, which is around 5% for the loosest packing fraction and around 0.2% for the densest, as depicted in the adjacent plot. It shows the percentage of broken links of neighborhood as a function of time, for several packing fractions from 0.8402 (red) to 0.8457 (blue). Clearly, the structure evolves very little on the experimental time.

Before describing the details of the displacements' statistics, one needs to clarify the meaning of the datasets over which one performs the computations. As a matter of fact, a finite fraction of the grains intermittently “rattles” during the whole run, from  $\sim 0.05$  at  $\phi = 0.8457$  to  $\sim 0.90$  at 0.8402. Let us pinpoint the rattling events as the instants at which a step larger than the cut-off length scale<sup>3</sup>  $d_r = 0.1$  is performed. It is hence nat-

<sup>2</sup>In particular, the “cages” observed here are *different* from those evidenced and discussed in chapter 4, since the amplitudes of the jumps are typically 100 times smaller. As a consequence the jumps evoked here *can not relax the structure*, while the jumps studied in chapter 4 can.

<sup>3</sup>The choice for this cut-off was motivated by the study of displacement statistics. One can see on fig. 3.3-left that when the rattling events are removed, the typical unitary

ural to perform temporal and spatial averages over the sets of *non-rattling* particle-times couples, which will be the rule in all the following analysis.

**Mean square displacement.** The mean square displacement for a given packing fraction  $\phi$  and a given lag  $\tau$  is defined as:

$$\sigma_\phi^2(\tau) = \langle \Delta x_{p,t}(\tau)^2 \rangle_{p,t} + \langle \Delta y_{p,t}(\tau)^2 \rangle_{p,t} = \sigma_x^2(\tau) + \sigma_y^2(\tau) \quad (3.1)$$

where  $\Delta x_{p,t}(\tau) = x_p(t+\tau) - x_p(t)$  and  $p$  stands for the particle indexes. The means square displacements along the  $x$  and  $y$  directions are roughly equal at all packing fractions and time lags. This means that the displacements are isotropic at all time scales, a remarkable feature given the very anisotropic forcing.

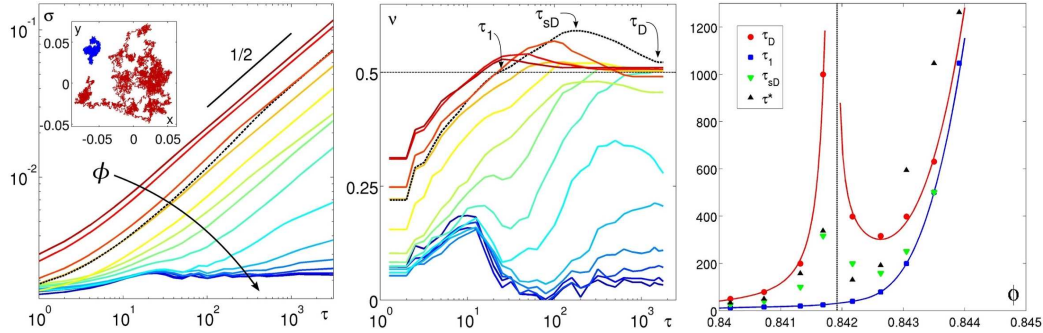


Figure 3.3: **Left** Root mean square displacement  $\sigma(\tau)$  as a function of  $\tau$  for all studied values of  $\phi$ , from 0.8402 (red) to 0.8457 (blue). The curve for the closest value to  $\phi_J = 0.8419$  is in dashed black. **Inset** trajectories of two particles at the extreme packing fractions:  $\phi = 0.8402$  (red) and  $\phi = 0.8457$  (blue). **Middle** Local slope  $\nu$  as a function of lag  $\tau$  for the same packing fractions. The black dashed curve correspond to the closest packing fraction to  $\phi_J$ . **Right** Evolution of the three times derived from the left curves, namely  $\tau_1$  (■),  $\tau_{sD}$  (▼) and  $\tau_D$  (●), as functions of the packing fraction around jamming. The time scale  $\tau^*$  (▲) at which the dynamical heterogeneities are maximal (as defined in B.2) is also represented. From Lechenault's thesis [47].

The evolution of  $\sigma_\phi^2(\tau)$  with the packing fraction is presented in fig.3.3-left. Note the very small values of  $\sigma_\phi(\tau)$  at all time scales, which indicates once again that the packing remains in a given structural arrangement. At low packing fractions and small  $\tau$  the mean square displacement displays a sub-diffusive behavior with a slope less than  $1/2$ . At longer time, diffusive motion is recovered ( $\sigma \sim \tau^{1/2}$ ). As the packing fraction is increased, the typical lag at which this cross-over occurs becomes larger and, at first sight,

displacements are below  $5 \cdot 10^{-3}$ .

does not seem to exhibit any special feature at  $\phi_J$  (corresponding to the black dashed line). At high packing fractions, an intermediate plateau appears before diffusion resumes.

However, a closer inspection of  $\sigma_\phi^2(\tau)$  reveals an intriguing behavior, that appears more clearly on the local logarithmic slope:

$$\nu_\phi(\tau) = \frac{\partial \log \sigma_\phi(\tau)}{\partial \log(\tau)} \quad (3.2)$$

shown in fig.3.3-middle. At small time scales,  $\nu < 1/2$  indicates a sub-diffusive behavior. At intermediate packing fractions, instead of reaching  $1/2$  from below,  $\nu$  overshoots and reaches values over  $1/2$  before reverting to  $1/2$  from above at long times. Physically, this means that after the sub-diffusive regime commonly observed in glassy systems, the particles become *super-diffusive* at intermediate times before eventually entering the long time diffusive regime. At higher packing fractions, this unusual intermediate superdiffusion disappears: one only observes the standard crossover between a plateau regime at early times and diffusion at long times.

In order to characterize these different regimes, we define three characteristic times:  $\tau_1(\phi)$  as the lag at which  $\nu(\tau)$  first reaches  $1/2$ , corresponding to the start of the super-diffusive regime,  $\tau_{sD}(\phi)$  when  $\nu(\tau)$  reaches a maximum value (peak of super-diffusive regime), and  $\tau_D(\phi)$  where  $\nu(\tau)$  has an inflection point, beyond which the system approaches the diffusive regime. These characteristic time scales are plotted as a function of the packing fraction in fig.3.3-right. Whereas  $\tau_1$  does not exhibit any special features across  $\phi_J$ , both  $\tau_{sD}$  and  $\tau_D$  peak at  $\phi_J$ . Since superdiffusion is tantamount to long-time correlations in the motion of particles, this result shows that dynamical correlations are maximal at  $\phi_J$ , supporting the interpretation of a critical behavior close to  $\phi_J$ , even if the system is far from the athermal frictionless particle case of [45].

**Dynamical heterogeneities** Lechenault *et al.* also analyzed the fluctuations of the density field relaxation using  $q_i^t(a, \tau) \equiv \exp\left(-\frac{\|\Delta\vec{r}_i^t(\tau)\|^2}{2a^2}\right)$ , the local relaxation induced by the displacements  $\Delta\vec{r}_i^t(\tau)$  of the particle  $i$  on the lag time  $\tau$ . The dynamical susceptibility  $\chi_4(a, \tau)$  directly captures the temporal fluctuations of  $\bar{Q}_t(a, \tau) = \langle q_i^t(a, \tau) \rangle_i$  since it can be rewritten:

$$\chi_4(a, \tau) = N.Var_t(\bar{Q}_t(a, \tau)) \quad (3.3)$$

A detailed explanation of the characterization of the dynamical heterogeneities through the  $\chi_4(a, \tau)$  is given in appendix (B.2). Let us simply mention here that there exists a time scale  $\tau^*$  and a length scale  $a^*$  at which the  $\chi_4$  is maximal, *i.e.* at which the dynamical heterogeneities are maximal. This timescale  $\tau^*$  can be subjoined to our timescale plot to complete the picture, as represented in fig. 3.3-right.

The increase of the timescales  $\tau_D$  and  $\tau^*$  at  $\phi_J$  suggest the existence of an associated growing length scale. Indeed, one can introduce the dynamical correlation function  $G_4(\vec{r}; a, \tau)$  (similar to the one defined in eq.(1.8)):

$$G_4(\vec{r}; a, \tau) = \int \langle \delta Q_t(\vec{r}; a, \tau) \cdot \delta Q_t(\vec{r} + \vec{r}'; a, \tau) \rangle_t d\vec{r}' \quad (3.4)$$

where  $\delta Q_t(\vec{r}; a, \tau) = Q_t(\vec{r}; a, \tau) - \langle Q_t(\vec{r}; a, \tau) \rangle_t$  and  $Q_t(\vec{r}; a, \tau) = \frac{1}{N} \sum_i q_i^t(\vec{r}; a, \tau)$ . Let us assume isotropy and consider only the radial decay of  $G_4(r)$ .

Lechenault *et al.* found that the dynamical correlation function obeys a critical scaling of the form:

$$G_4^*(\tau, \phi) = \frac{\lambda_\phi \mathcal{G}(\frac{r}{\xi_4})}{r^\eta} \quad \text{with} \quad \mathcal{G}(u) = e^{-u^{1/2}} \quad \text{and} \quad \eta \simeq 0 \quad (3.5)$$

where  $\lambda_\phi$  is a numerical prefactor, as is illustrated on the left panel of fig. 3.4.

Importantly, the length scale  $\xi_4(\phi)$  peaks at  $\phi_J$  (see fig. 3.4-right). This analysis confirms that the behavior of the typical length scale over which the dynamical correlation function decays and of the dynamical susceptibility as a function of the packing fraction are coherent. Lechenault proposed a fit  $\xi_4 \propto (\phi - \phi_J)^{-\nu}$  with  $\nu = 1/2$ , but the small range of packing fractions around  $\phi_J$  let open several other possibilities. We will propose in the following an exponent  $\nu = 1$ , which also fits reasonably well the data.

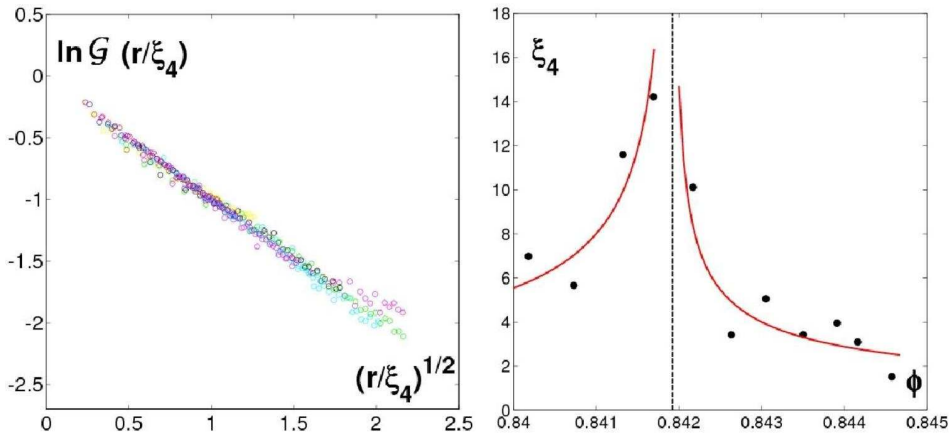


Figure 3.4: **Left** Rescaling of  $\ln(\mathcal{G}(r/\xi_4))$  as a function of  $(r/\xi_4)^{1/2}$  for 8 packing fractions around  $\phi_J$ . **Right** Dynamical length scale  $\xi_4(\phi)$  extracted from the scaling of  $G_4(r, \phi)$ . A fit  $\xi_4 \propto (\phi - \phi_J)^{-\nu}$  with  $\nu = 1/2$  (solid red) is displayed. From Lechenault *et al.* [47].

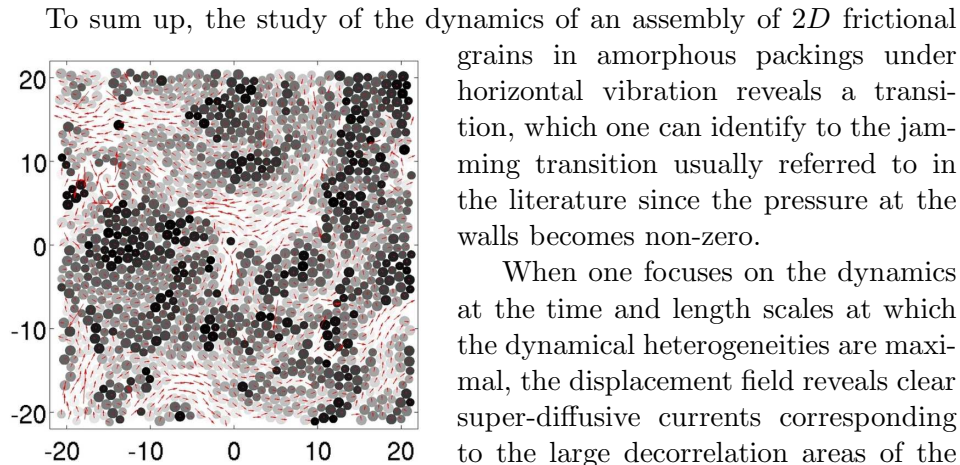


Figure 3.5: Dynamical heterogeneities at  $\phi_J$ :  $q(a^*, \tau^*)$  is in shades of gray (0 = white, 1 = black) and the displacement field is in red, magnified by a factor 20.

When one focuses on the dynamics at the time and length scales at which the dynamical heterogeneities are maximal, the displacement field reveals clear super-diffusive currents corresponding to the large decorrelation areas of the  $q$  maps (see fig. 3.5).

The dynamical correlations of the grains exhibit both a diverging time scale  $\tau^*$  and a diverging length scale  $\xi_4$  at  $\phi_J$ , revealing the presence of a nearby critical point. Of course, the divergences reported here are only *experimental* divergences. The truly critical nature of the transition we report at  $\phi_J$  hence remains an open question. In 3.2, we will support this view and provide additional evidences of a critical behavior at  $\phi_J$  with a different protocol and a different kind of analysis.

### 3.1.2 Further studies on the statistics of the displacements

Lechenault noticed that, in the Gaussian case, the dynamical structure factor only depends on the diffusion length  $\sigma(\tau)$ . He found that, though the displacements are not Gaussian, the dynamical structure factor could be rescaled by a characteristic lengthscale  $\zeta_\phi(\tau) \sim \sigma_\phi(\tau)$  onto a master curve, for which he proposed a modified Ornstein-Zernike form. Let us come back here in more details on these scaling properties.

**Probability distributions of the displacements.** In order to investigate further the displacements' statistics, we now turn to the probability distribution of the displacements in  $x$  and  $y$  directions probed over a lag time  $\tau$ . We have represented the distributions for all particles and instants for three significant packing fractions and three values of the lag time  $\tau$  in fig. 3.6. The horizontal axes have been normalized by the root mean square displacements  $\sigma_x(\tau)$  and  $\sigma_y(\tau)$ , and unit Gaussian are also plotted for comparison. It is clear that for all parameters, these statistics differ significantly from the Gaussian; in particular, their tails are overpopulated. This means that there is an abundance of extreme displacement events at all lag times and all densities.

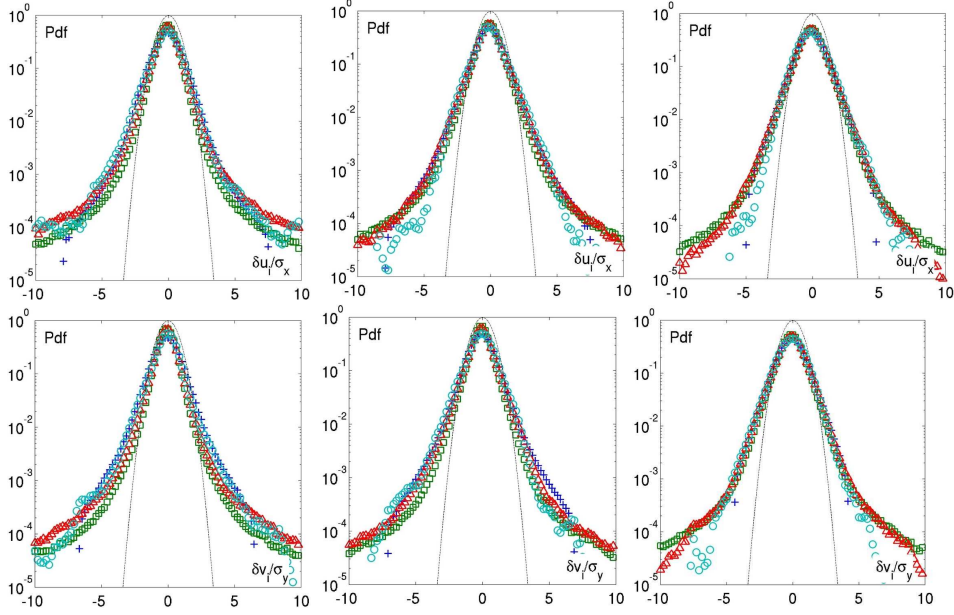


Figure 3.6: Distributions of displacements along  $x$  (top) and  $y$  (bottom) normalized by the corresponding diffusion length  $\sigma(\tau)$ , for  $\phi = 0.8402, 0.8417$  and  $0.8430$  from left to right. The probing lag times are  $\tau = 1(+)$ ,  $10(\square)$ ,  $100(\triangle)$  and  $1000(\circ)$ . Unitary Gaussian curves are displayed (dotted lines) for comparison.

**Generating function.** The main feature of these data is the fact that for each packing fraction, the curves approximately collapse onto a single curve. Thus the temporal behavior of the displacement statistics seems to be mostly encoded in the second moment dependence on  $\tau$ , and an alternative way to characterize the distributions is to look at the generating function  $\mathcal{F}_\tau(\lambda) = \langle e^{-\lambda \|\Delta \vec{r}_{p,t}(\tau)\|^2} \rangle$ , where  $\lambda$  is the equivalent of a wavenumber. If the displacement distributions were Gaussian, it can be shown<sup>4</sup> that  $\mathcal{F}_\tau(\lambda)$  would be Ornstein-Zernike (OZ) shaped, namely:

$$\mathcal{F}_{OZ}(\lambda, \tau) = \frac{1}{1 + 2\lambda\zeta_\phi(\tau)^2} \quad (3.6)$$

However, one finds a much better fit if one introduces an extra parameter  $\varepsilon_\phi(\tau)$  such that:

$$\mathcal{F}_\varepsilon(\lambda, \tau) = \frac{1}{1 + \left(2\lambda\zeta_\phi(\tau)^2\right)^{1-\varepsilon_\phi(\tau)}} \quad (3.7)$$

The generating function is represented on fig. 3.7-left, as well as the OZ and the OZ-modified fits. The correlation length  $\zeta_\phi(\tau)$  is found to correspond

<sup>4</sup>See [47](p.130) for instance for a detailed calculation.

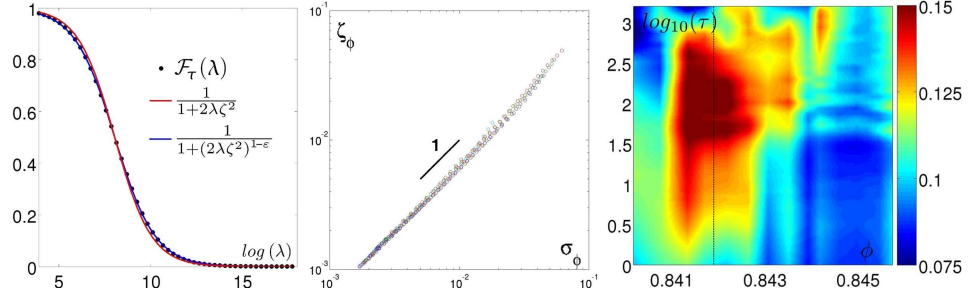


Figure 3.7: **Left**  $\mathcal{F}_\tau(\lambda)$  as a function of  $\log(\lambda)$  for a representative value of  $\tau$  (black),  $\phi \sim \phi_J$ . The red line corresponds to the Ornstein-Zernike fit and the blue line corresponds to the modified Ornstein-Zernike introduced in the text. **Center** Correlation length  $\zeta_\phi$  versus  $\sigma_\phi$  for several packing fractions. **Right**: Fitting parameter  $\varepsilon_\phi(\tau)$  as a function of  $\phi$  and  $\log_{10}(\tau)$ .

to  $\sigma_\phi(\tau)$  (see fig. 3.7-center), which allows convenient simplifications in the following.

The parameter  $\varepsilon_\phi(\tau)$  provides an alternative way to quantify the non-Gaussian behavior of the displacement statistics. We find that  $\varepsilon_\phi(\tau)$  deviates significantly from 0 in the vicinity of  $\phi_J$  (see fig. 3.7-right).  $\varepsilon_\phi(\tau)$  exhibits a well defined maximum for each packing fraction, and an overall maximum at  $\phi_J$ . Hence this fitting parameter seems to capture the transition's features quite accurately.

However, as we shall see now, if the above scaling function is correct, the moments of order greater or equal than 2 should diverge. Indeed, the derivative of the generating function can be linked to the second moment in the  $\lambda \rightarrow 0$  limit:

$$\frac{\partial \mathcal{F}_\tau(\lambda)}{\partial \lambda} = \left\langle -\|\Delta \vec{r}_{p,t}(\tau)\|^2 \cdot e^{-\lambda \cdot \|\Delta \vec{r}_{p,t}(\tau)\|^2} \right\rangle \quad (3.8)$$

and hence, since  $\sigma_x = \sigma_y$ :

$$\left. \frac{\partial \mathcal{F}_\tau}{\partial \lambda} \right|_{\lambda=0} = \langle -\|\Delta \vec{r}_{p,t}(\tau)\|^2 \rangle = -2\sigma_x(\tau)^2 \quad (3.9)$$

On the other hand, using the scaling forms in eq.(3.6-3.7) and the fact that  $\zeta_\phi(\tau) = \sigma_\phi(\tau)$ , we have the following generic form for  $\mathcal{F}_\tau(\lambda)$ :

$$\mathcal{F}_\tau(\lambda) = \frac{1}{1 + (2 \cdot \lambda \cdot \sigma_x(\tau)^2)^\gamma} \quad (3.10)$$

with  $\gamma = 1$  if the lag-displacement distributions are Gaussian and  $\gamma = 1 - \varepsilon_\phi(\tau)$  for the OZ-modified form. We can have explicitly its derivative as a function of  $\lambda$  and  $\gamma$ :

$$\frac{\partial \mathcal{F}_\tau(\lambda)}{\partial \lambda} = -\frac{2 \cdot \sigma_x^2 \cdot \gamma \cdot (2 \lambda \cdot \sigma_x)^{\gamma-1}}{(1 + (2 \lambda \cdot \sigma_x^2)^\gamma)^2} \quad (3.11)$$

In the Gaussian case one finds a finite value for  $\sigma_x(\tau)$ :

$$\sigma_x(\tau)^2 = -\frac{1}{2} \cdot \left. \frac{\partial \mathcal{F}_{OZ}(\lambda, \tau)}{\partial \lambda} \right|_{\lambda=0} \quad (3.12)$$

but this is not the case if  $\gamma < 1$  or equivalently  $\varepsilon_\phi(\tau) > 0$  for which the second moment irremediably diverges, as well as all the moments of greater order.

We can have a closer look at the scaling form in eq.(3.7) and check that it fits well the data even in the limit  $\lambda \rightarrow 0$  (see fig. 3.8): the generating function has a clear cusp in the  $\lambda \rightarrow 0$  limit, which is well described by the proposed scaling form.

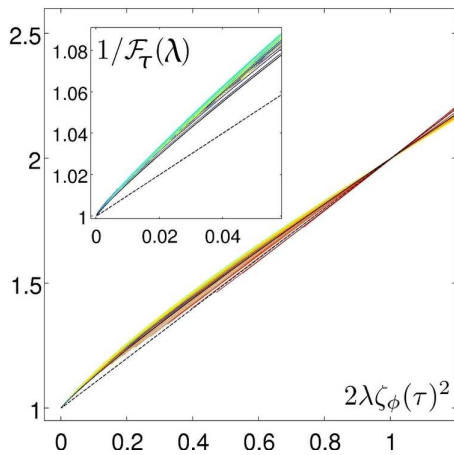


Figure 3.8:  $1/\mathcal{F}_\tau(\lambda)$  in function of  $2\lambda\zeta^2$  for different values of  $\tau$ . The black dotted line correspond to the Ornstein-Zernike fit, and the black curve to the modified Ornstein-Zernike fit, here indistinguishable from the other curves. **Inset:** Same, focused on the  $\lambda \rightarrow 0$  limit.

So it is consistent that the generating function has an OZ-modified form like the suggested one.

Actually, the preceding calculation triggered new analyzes, and very recent developments revealed that the displacements' statistics is increasingly well described by Lévy flights [98] as the transition is approached, which is coherent with the strong deviation from Gaussian behavior. This also explains why the second moment of the displacement distributions tends to diverge close to  $\phi_J$  and exhibits a superdiffusive behavior. As those abnormal distributions are governed by increasing dynamical correlations, the increase of dynamical heterogeneities one observes upon jamming is a natural consequence of the same underlying phenomenon.

This is still a “work in progress” matter though; a long version of the complete study, including the earlier results of Lechenault's thesis and these recent developments is due to appear by the end of 2009 in a detailed publication. So, for the moment, let us conclude by saying that the jamming transition has several signatures in the grains' dynamics; we will see in the next section that other – coherent – signatures of the same transition can be revealed through the analysis of the response function to a local perturbation.

## 3.2 The journey of an intruder

The results presented in the previous section are one piece of the effort that has been performed recently in order to better characterize the peak of dynamical heterogeneities upon jamming [81, 99]. In parallel, the evolution of the force network has also been widely investigated [67, 71], and several questions emerge: is jamming a question of percolation of the chain forces in a random and heterogeneous network? If so, is it a critical threshold like the classical percolation problem in a  $2D$  regular lattice? Can it be extended to the finite temperature/forcing case in a simple manner? To what extent are the dynamical heterogeneities related to the heterogeneity of the force network?

Following [70], we address these issues by perturbing our system with a stress. What is the response to this perturbation, and how does this response evolve on approach to jamming? To answer these burning questions, we have designed a protocol, starting from the same experimental apparatus but in which an intruder is dragged through the media. As previously, we can explore several packing fractions around  $\phi_J$ .

First of all, we will briefly summarize a few studies implying dragging protocols that are relevant for our purposes. Then we will present our protocol as an introduction to our results and interpretations, the latter being enclosed in an article, submitted to *Physical Review E* [96]. A short additional discussion will conclude this section.

### 3.2.1 State of the art

Several experimental works have studied the drag of a probe into assemblies of particles, mostly focusing on the comparison with the drag of a probe into a fluid. For instance the relation between the drag force and the velocity has been found to be linear at low packing fractions [100], while for denser packings either  $F \simeq cst$  or  $F \propto \ln(V)$  is found for drags at constant velocity [101, 102, 103, 104].

**Drag close to the glass transition** Only a few experimental works however have been directly addressing the question of the glass / jamming transitions. Among them, Habdas *et al.* [105] have studied the motion of a magnetic probe dragged at constant force in a colloidal suspension at several packing fractions close to the colloidal glass transition. The authors report the appearance and the increase of a yield stress when the glass transition is approached: below this force threshold the probe displays cage-like motion and stays trapped in the same region of space during the whole experimental time. Above the force threshold, the average velocity seems to obey a  $(F - F_0)^\alpha$  scaling, though the exponent  $\alpha$  could not be determined explicitly.

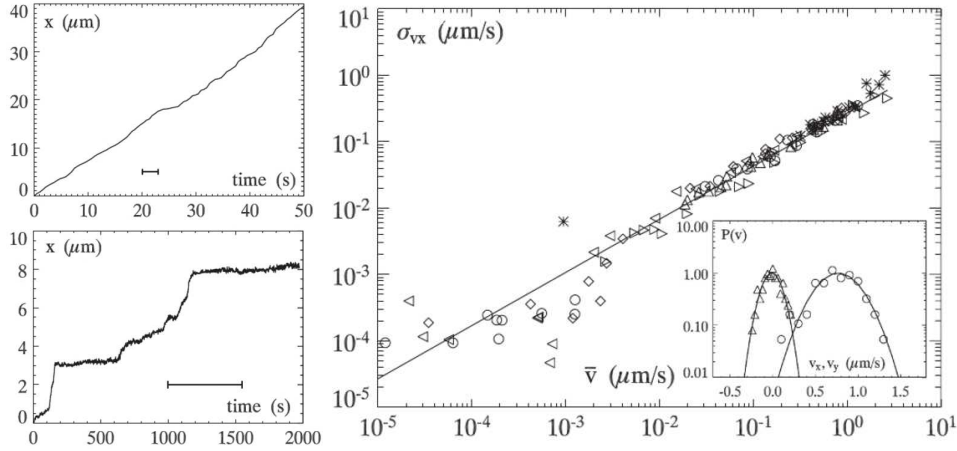


Figure 3.9: **Left** Position of the probe in the drag direction as a function of time. Scale bars correspond to  $r_{MB}/\bar{v}$ , the radius of the magnetic bead ( $r_{MB} = 2.25$   $\mu\text{m}$ ) divided by its average velocity. Top:  $F = 6.46$  pN,  $\phi = 0.55$ ,  $\bar{v} = 0.80$   $\mu\text{m/s}$ . Bottom:  $F = 0.58$  pN,  $\phi = 0.52$ ,  $\bar{v} = 0.0041$   $\mu\text{m/s}$ . **Right** Standard deviation of the instantaneous distribution of the displacements in the direction of the drag as a function of the average velocity. The fit (solid line) has a slope of 0.80. Different symbols stand for different volume fractions. **Inset** Pdf of the instantaneous velocities parallelly or perpendicularly to the drag. Solid lines are Gaussian fits. The dataset is the same than for the top-left plot. Adapted from Habdas *et al.* [105].

The authors report that the displacements evolve from a linear evolution to a step-like motion when the drag amplitude is lowered (see the left side of fig. 3.9). Importantly, the velocity fluctuations *do not grow* as the glass transition is approached. This can be seen in fig. 3.9-right where the standard deviation of the instantaneous velocity  $\sigma_x$  is plotted against the average velocity  $\bar{v}$  for different volume fractions, represented with different symbols. This highlights that  $\sigma_x$  is totally determined by  $\bar{v}$ , and not by the volume fraction. In other words, for the same force, denser suspensions exhibit lower fluctuations but also correspondingly slower velocities.

So the first conclusion one can draw is that a dragged intruder *does not* feel the increasingly heterogeneous dynamics of the particles close to the glass transition. As a consequence the intruder only probes the viscosity's dramatic increase and misses the heterogeneous nature of the structural relaxations. The low force limit – for which the intruder becomes similar to the other particles – is not workable because of the appearance of a yield stress.

However, the existence of a yield stress *below* the glass transition is rather intriguing. To explain this, one can evoke the steep dependence of the force-velocity relation suggested in [106] and presented in the next paragraph.

**Non-linear velocity/force dependence.** Gazuz *et al.* [106] have proposed a model from which they derive an exact expression for the friction in the case of a constant external force on a spherical probe particle embedded in a dense host. Within mode-coupling theory, they discuss the threshold on the external force needed to delocalize the probe and its relation to strong non-linear velocity/force curves.

In figure 3.10-left, the probe friction is represented as a function of the drag force for several packing fractions: note that there are two plateaus separated by a clear drop, one at low forces – *a priori* the analogous of Stoke's law – and one at high forces. This echoes on the velocity / force curves in fig. 3.10-right with two quasi-linear regimes separated by a steep increase of the velocity (note the logarithmic scale). Crucially, this abrupt increase is reminiscent even below the glass transition (in the model  $\phi_G \simeq 0.516$ , in the experiment  $\phi_G \simeq 0.58$ ).

This steep increase fits well the data of Hadbas *et al.* represented with open symbols in fig. 3.10-right. So it is likely that the experimental yield stress reported in [105] is due to the fact that the velocities at low forces become unreachable in the experimental time. In this case, the reported linear relation between  $\langle V \rangle$  and  $F_D$  recovered in the high force regime is not strictly speaking Stokes' law, which would correspond to the low force linear regime.

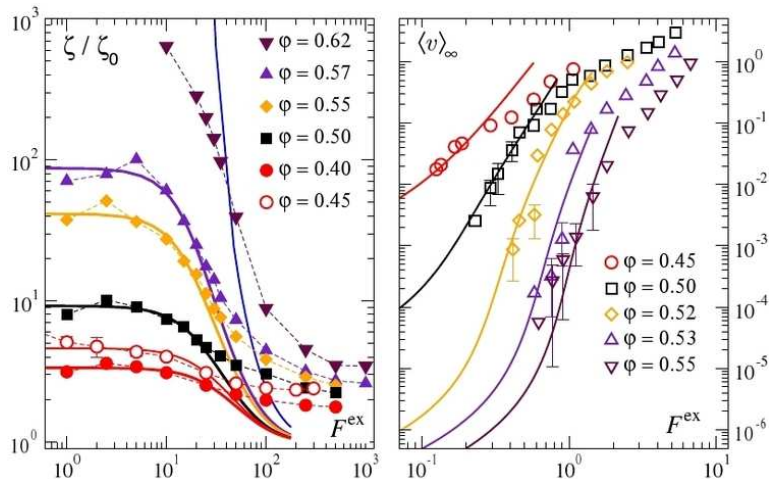


Figure 3.10: **Left** Probe friction  $\zeta$  as a function of the external force (in units of  $k_B T/a$ ) for several packing fractions  $\phi$ . Data stem from simulations of a quasi-hard-sphere system (symbols), from Brownian dynamics for monodisperse hard spheres (from [107], open symbols), and from the model described in [106] (solid lines), with  $\zeta_0$  a constant. **Right** Experimental force-velocity relations for a colloidal suspension (open symbols), from [105] and from the model (lines). Adapted from Gazuz *et al.* [106].

**Probing the critical nature of jamming.** In the work of Habdas *et al.* the intruder does not feel the heterogeneous nature of the relaxations. In contrast, one could reasonably expect that the drag of an intruder would strongly feel the heterogeneous nature of the relaxations *if these were driven by the contact / force network*. One can deduce that intruder protocols are better designed to probe the heterogeneous nature of the relaxations at the *jamming* transition. This statement is supported by several recent simulations of athermal, frictionless particles.

For instance, Reichhardt *et al.* [108] have simulated a two-dimensional system with periodic boundary conditions filled with 50:50 bidisperse harmonically repulsing disks. They prepare the packings by shrinking the grains, adding a few particles and expanding the grains back while thermally agitating the disks. With this preparation protocol, they find  $\phi_J \simeq 0.843$ . When the desired packing fraction is reached, the thermal agitation is stopped. Then one particle is selected and is dragged into the system at zero temperature with a constant force  $F_D$ . An overdamped equation determines the movements of all the particles in the system.

First of all, the authors report that the probability density functions of the probe velocity  $V$  evolves from an exponential tail below  $\phi \sim 0.83$  to a much broader tail close to jamming, that is well-fitted by a power-law with an exponent  $-3$  (see fig. 3.11).

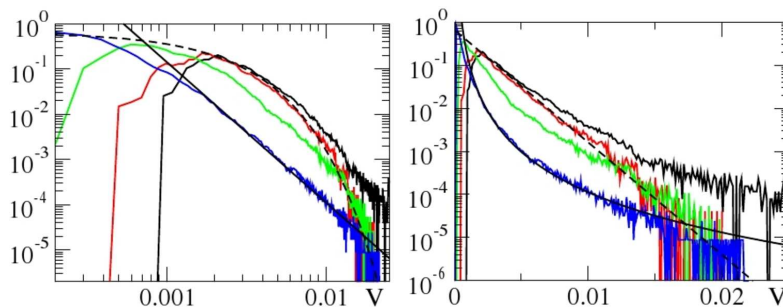


Figure 3.11:  $Pdf(V)$  for  $\phi = 0.823$  (black),  $0.833$  (red),  $0.8395$  (green), and  $0.8414$  (blue) for the same drag amplitude in log-log scale (left) and log-normal scale (right). The solid line is a power law fit with  $\alpha = -3.0$  and the dotted line is an exponential fit. From Reichhardt *et al.* [108].

Second, the authors report that a yield stress become apparent exactly at jamming: below  $\phi_J$  the probe always moves, while above  $\phi_J$  there exists a threshold force  $F_c$  below which the system is blocked. This can be seen on the average velocity dependence on the drag force for different packing fractions around  $\phi_J$ , as plotted in fig. 3.12-left. The yield stress curve  $F_c(\phi)$  is plotted in fig. 3.12-center, and one can see that the yield force grows as  $\phi$  increases. Since the drag is done at zero-temperature, no thermally-induced creep motion is observed, and the instantaneous response completely drives

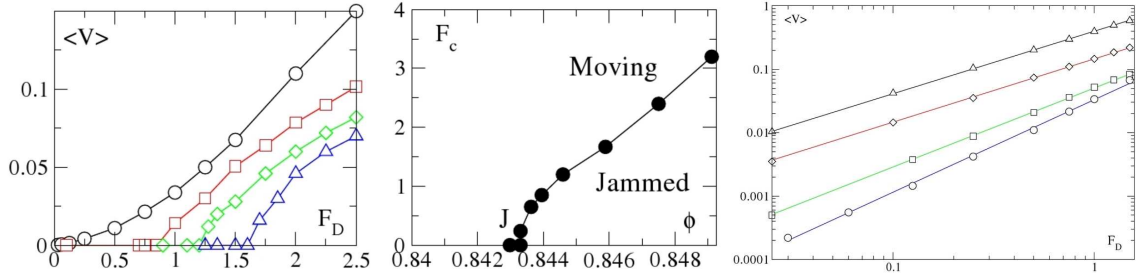


Figure 3.12: **Left**  $\langle V \rangle$  vs  $F_D$  below jamming at  $\phi = 0.8426$  (circles) and above jamming at  $\phi = 0.8439$  (squares),  $\phi = 0.8446$  (diamonds), and  $\phi = 0.846$  (triangles). Above jamming, a threshold force  $F_c$  is needed to depin the probe particle. **Center** The threshold force  $F_c$  vs  $\phi$  with point  $J$  denoting where the system becomes jammed. **Right**  $\langle V \rangle$  vs  $F_D$  and power law fits with exponent  $\beta$ , for  $\phi = 0.483$  (triangles,  $\beta = 1.0$ ),  $0.807$  (diamonds,  $\beta = 1.0$ ),  $0.8414$  (squares,  $\beta = 1.24$ ), and  $0.8426$  (circles,  $\beta = 1.47$ ). From Reichhardt *et al.* [108].

the further evolution of the system.

The authors also report some interesting scalings of the average velocity as a function of the drag force. Far below jamming, a linear relation  $\langle V \rangle \propto F_D$  similar to Stokes' law<sup>5</sup> is found. Close to jamming, the following scalings are evidenced:

$$\phi < \phi_J \quad \langle V \rangle \propto F_D \quad (3.13)$$

$$\phi > \phi_J \quad \langle V \rangle \propto (F_D - F_c)^\beta \quad \text{with } \beta > 1 \quad (3.14)$$

as illustrated in fig. 3.12-right.

In addition, previous work by Drocco *et al.* [109] on a similar system established that the lengthscale of the sets of moving particles diverges at  $\phi_c = \phi_J$ . For a given displacement of the probe, they look at the number of moving particles  $n_{moving}$  and observe that this number swells close to jamming (see fig. 3.13-left). They find the following scaling:

$$n_{moving} \propto (\phi_c - \phi)^{-\nu} \quad \text{with } \nu \in [1.2, 1.46] \quad (3.15)$$

as depicted in the right side of fig. 3.13.

Reichhardt *et al.* [108] argue that if the pushed particles are within a disklike jammed area of radius  $\xi$  surrounding the probe particle, then one can trivially deduce a scaling for  $\xi$  using the relation  $n_{moving} = \phi_J \xi^2$ . In addition, as the velocity of the probe particle decreases according to  $V \propto V_0/n_{moving}$  (where  $V_0$  is the velocity of the overdamped probe at  $\phi = 0$ ,

<sup>5</sup>Note that the second curve ( $\phi = 0.807$ , red diamonds) on the right plot of fig.3.12 has still an exponent  $\beta = 1$  but has a significantly lower effective friction. This may be also attributed to the effect reported in [106].

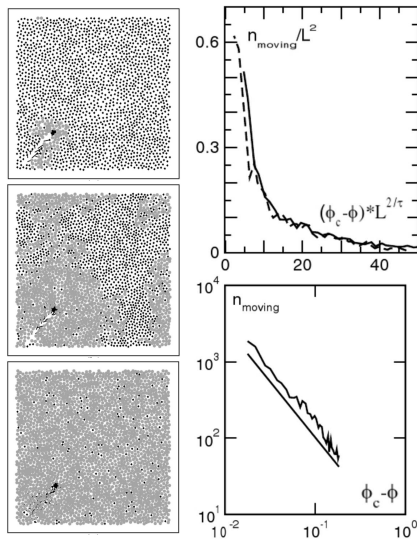


Figure 3.13: **Left** Moving disks (gray dots) and nonmoving disk (small black dots) for different packing fractions, from top to bottom:  $\phi = 0.656$ ,  $0.811$  and  $0.837$ . The probe is the large black disk (size exaggerated for clarity). **Right top** Finite-size scaling of  $n_{moving}$  for systems of size  $L = 48$  (dashed) and  $L = 60$  (solid). **Right bottom** Plot of  $n_{moving}$  against  $\phi_c - \phi$ . Adapted from Drocco *et al.* [109].

a quite unrealistic case), a scaling of the velocity against the packing fraction can be conjectured:  $V \propto V_0(\phi - \phi_J)^{2\nu}$ . The value  $\nu \sim 1$  is given, but care has to be taken since several other values have been reported elsewhere, like for instance  $0.7$  [45],  $0.6$  [110], or  $0.57$  [111]. Moreover the value  $\nu = 0.5$  is recurrently found in the literature [112, 113, 67].

### 3.2.2 Introducing our intruder

Now that it has been shown that a dragging protocol can unveil interesting behavior close to point  $J$ , one would like to see if such evidences of criticality also appear in our experimental system, and how strong are the similarities with other systems.

Let us first introduce our intruder. An overview of the experimental details has been made in 2.1.1. In brief, the “intruder” is a slightly bigger particle ( $d_{intruder} = 2$ ) inserted into the system and dragged along the  $x$ -direction – *i.e.* perpendicular to the vibrations – with a constant force. In practice, this is easily done by hanging a mass via a pulley, as depicted in fig. 2.5.

The very first question one can ask is the following: is this drag force really a constant force? If we write Newton’s second law, with  $M_I$  being the mass of the applied load,  $m$  the mass of the intruder and  $x$  its position, we have:

$$(m + M_I) \ddot{x}(t) = M_I \cdot g - R(t) \quad (3.16)$$

where  $R(t)$  is the resistance of the grains, a term involving various contributions. The constant force approximation is true as long as the inertia is negligible. The highest acceleration we have measured (for all forces

and all packing fractions) is  $\ddot{x}_{max} = 1.6 \text{ m}\cdot\text{s}^{-2}$ , the typical value of the intruder's acceleration during a burst being around  $0.2 \text{ m}\cdot\text{s}^{-2}$ . Hence the term  $(m + M_l) \ddot{x}(t)$  is negligible over  $M_l \cdot g$ . So, for all the data presented here, the system is overdamped and the constant force approximation is always true.

Let us call the drag  $F$  and express it in reduced units (like the *pressure*  $P$  introduced in 2.1.1), namely as the applied load divided by the total mass of the grains ( $M_{tot} = 2.365 \text{ kg}$ ). In these units, a force of  $F = \mu \simeq 0.5$  is sufficient to make the whole assembly of grains slip on the bottom glass plate.

We have explored the force /packing fraction diagram by using two protocols, both of them being close to the protocol used without intruder. After having increased stepwise the packing fraction, downward steps are performed during which the intruder is dragged. Schemes of these two protocols are drawn on fig. 3.14.

In the first protocol, we use a single mass (*i.e.* a single drag force) and we perform one drag per step. To be precise, the “teletransportations” of the intruder are performed before each increment of the piston: the intruder is delicately removed from the right side and replaced by three particles (two

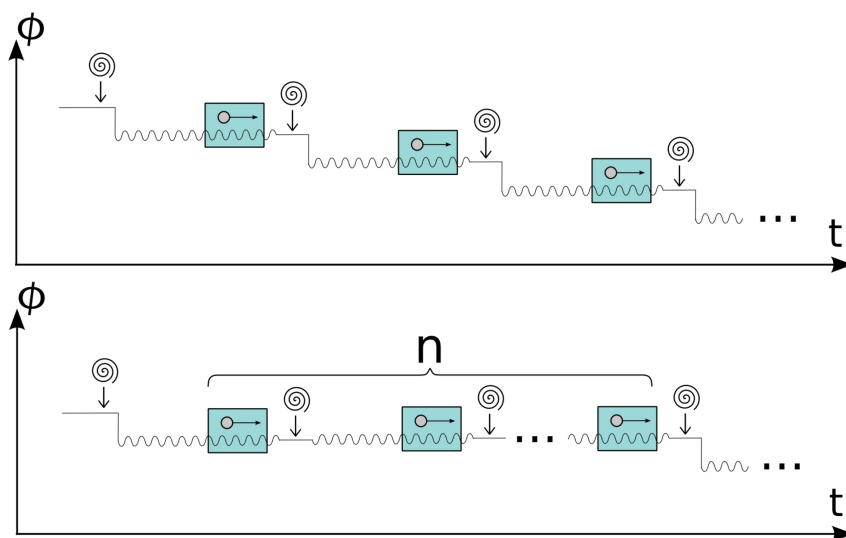


Figure 3.14: Schemes of the intruder protocols. **Top:** Temporal sequence of the first intruder protocol. In this protocol, one trajectory of the intruder is made at each step, with the same drag force every time. Vibration is represented by a curved line, spirals represent the moment where the intruder is “teletransported” from right to left and blue rectangles indicate the intervals on which the intruder is dragged through the media from left to right. **bottom:** Temporal sequence of the second intruder protocol. In this protocol, several drags with different pulling forces are performed at each packing fraction.

smalls and a big), then three particles are removed on the left side and the intruder is inserted again. After the increment of the piston, we let the system under vibration for up to 20 minutes in order to be sure that the “path” previously taken by the intruder has not left any trace; the pressure stabilizes and the force network has enough time to reorganize completely, randomizing the initial conditions. Only then the intruder is dragged. When the intruder quits the visualization area another iteration is made, until the intruder’s velocity becomes too high and browse the acquisition field in less than 10 frames.

With this protocol, we can explore various packing fractions on a line of iso-values of  $F$ . We have realized this protocol 3 times with the following masses  $m_1 = 68.4\text{g}$  ( $F_1 = 0.029$ ),  $m_2 = 150.4\text{g}$  ( $F_2 = 0.064$ ) and  $m_3 = 266.8\text{g}$  ( $F_3 = 0.113$ ) and with several packing fractions ranging from 0.8223 to 0.8418. These correspond to the three horizontal lines in the diagram on fig.3.15.

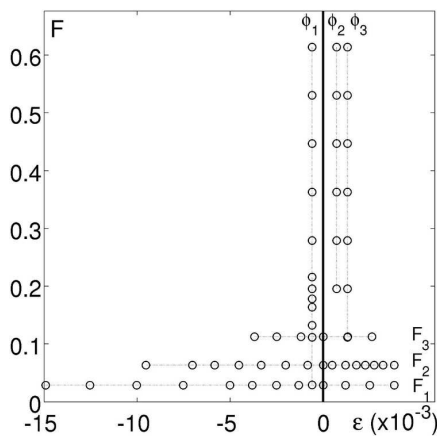


Figure 3.15: Force / reduced packing fraction diagram in the intruder’s experiment. Each point represents a trajectory of the intruder into the media.

In the second protocol, we perform several drags at each step of packing fraction, with different masses. With this protocol we are able to explore various drag forces on a line of iso-values of  $\phi$ . We have realized this protocol just once, with 3 different packing fractions ( $\phi_1 = 0.8383$ ,  $\phi_2 = 0.8304$  and  $\phi_3 = 0.8399$ ) with several drag forces going from 0.029 to 0.617. This corresponds to the three vertical lines in the diagram on fig.3.15.

### 3.2.3 Results and discussion

Most of the results are presented below, in article format. In addition, we have computed the RMSD of the displacements for the grains that are far from the intruder, namely in the four corner boxes of the system. The curves are reported for all the packing fractions at  $F_2$  in fig. 3.16-left, and a comparison with the RMSD of the particles without intruder is given in fig. 3.16-right. The dynamics of the grains in the whole system is considerably changed by the presence of the intruder. One can expect that all the

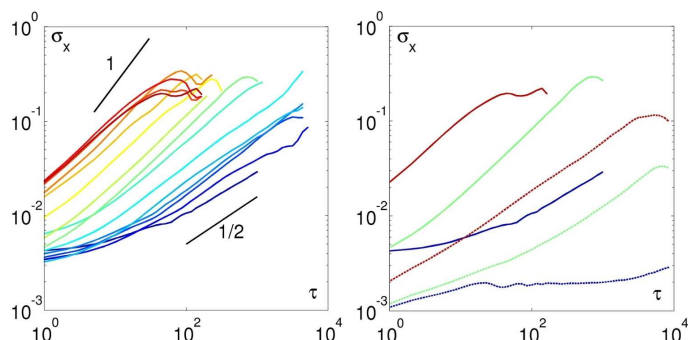


Figure 3.16: **Left** RMSD for the particles far from the intruder for 15 packing fractions from blue (dense) to red (loose) at  $F = F_2$ . **Right** Comparison between three RMSD curves of the left plot (solid) with the RMSD without intruder (dotted) at packing fractions at the same distances from jamming.

observations that can be made on the dynamics of this new system will not be directly comparable to Lechenault's. This is not totally true, and we will come back to this point in the conclusion of this chapter.

For the moment, let us introduce our results, enclosed in two articles. The first one is a Letter published in *Physical Review Letters* [95]: an integral version of this letter can be found in appendix A. The second article contains the same results but also several new measurements and a longer discussion that were not in the first one. The reader will find an integral version of this longer paper in the following pages. At the time of writing, this long version had been submitted to *Physical Review E*, and can be found online under reference [96].

In short, the motion of the intruder exhibits two transitions. The first one separates a continuous motion regime at comparatively low packing fractions and large dragging force from an intermittent motion at high packing fraction and low dragging force. This transition also marks the passage from a linear rheology to a stiffer response, so we call it *fluidisation*. The second transition is observed within the intermittent regime: here the motion of the intruder is made of intermittent bursts separated by long waiting times. We observe a peak in the relative fluctuations of the intruder's displacements and a critical scaling of the burst amplitudes distributions close to the jamming point  $\phi_J$  previously defined for this system. We also investigate the motion of the surrounding grains and show that the fluidisation transition is marked by the evolution of the reorganization patterns around the intruder, going from compact aggregates in the flowing regime to long-range branched shapes in the intermittent regime, suggesting an increasing role of the stress fluctuations. Remarkably, the distributions of the kinetic energy of these reorganization patterns also exhibits a critical scaling at the jamming transition, which coincides with the emergence of a wake of free volume below the jamming transition.

# Journey of an intruder through the fluidization and jamming transitions of a dense granular media

Raphaël Candelier\* and Olivier Dauchot†  
GIT-SPEC, CEA-Saclay, 91 191 Gif-sur-Yvette, France  
(Dated: November 15, 2009)

We study experimentally the motion of an intruder dragged into an amorphous monolayer of horizontally vibrated grains at high packing fractions. This motion exhibits two transitions. The first transition separates a continuous motion regime at comparatively low packing fractions and large dragging force from an intermittent motion one at high packing fraction and low dragging force. Associated to these different motions, we observe a transition from a linear rheology to a stiffer response. We thereby call “fluidization” this first transition. A second transition is observed *within* the intermittent regime, when the intruder’s motion is made of intermittent bursts separated by long waiting times. We observe a peak in the relative fluctuations of the intruder’s displacements and a critical scaling of the burst amplitudes distributions. This transition occurs at the jamming point  $\phi_J$  characterized in a previous study [1] and defined as the point where the static pressure (*i.e.* the pressure measured in the absence of vibration) vanishes. Investigating the motion of the surrounding grains, we show that below the fluidization transition, there is a permanent wake of free volume behind the intruder. This transition is marked by the evolution of the reorganization patterns around the intruder, which evolve from compact aggregates in the flowing regime to long-range branched shapes in the intermittent regime, suggesting an increasing role of the stress fluctuations. Remarkably, the distributions of the kinetic energy of these reorganization patterns also exhibits a critical scaling at the jamming transition.

PACS numbers: PACS number

Jamming occurs, when a system develops a yield stress in a disordered state [2–4] and has been reported in a wide class of systems such as colloids [5], foams [6], emulsions [7], granular materials [8, 9] as well as in various model situations [3, 10–12]. One possible mechanism for such a change between fluid and solid like behavior is that rearrangements of particles become progressively slower while the stress relaxation time grows dramatically. The dynamics becomes spatially heterogeneous and temporally intermittent, while the stress response appears more and more heterogeneous. A stringent manifestation of such inhomogeneities is the “stick-slip” response observed when the system is driven close to yielding and flows in rapid bursts. However the interplay between density fluctuations and stress relaxation is still poorly understood. Questions of interest are as follow: What is the nature of the re-arrangement events? How do these events depend on the external load and packing fraction? Also from a more fundamental viewpoint, whether the emergence of a yield stress coincides with dynamical arrest is still a matter of debate.

Microrheology is a promising technique providing local probes of the dynamics in complex fluid [13]. Studying the motion of an intruder embedded in the material of interest, one is able to investigate the microscopic origins of the complex-fluid behavior and in particular the link between microscopic mechanisms and macroscopic properties as given by conventional rheology. Applying

a force to the intruder, one explores the non-equilibrium and usually non-linear response, providing detailed insight into the structure-dynamics relationship. Previous drag experiments in colloids [5], foams [14], static [15] and shaken [16] granular media as well as simulations of structural glasses [10] were focusing on the velocity dependence of the drag force: proportionality is found for loose enough systems, reminding Stoke’s law, while an increasing yield stress appears for denser packing. Stress fluctuations have been studied in details in [17], and spatial reorganizations in [18], however a clear picture filling the gap between spatial fluctuations and rheological observations is still lacking.

In the present paper, we investigate the motion of an intruder dragged with a constant force, within an amorphous monolayer of horizontally vibrated grains, a system for which the jamming transition has been clearly identified and characterized in terms of the critical behavior of the dynamics in a previous study [1]. At moderate packing fractions, and comparatively high force, the intruder moves rapidly as soon as the force is applied. Above some threshold value of the packing fraction which increases with the applied force, the intruder exhibits an intermittent creep motion with strong fluctuations reminiscent of a “crackling noise” signal. Simultaneously, the force-velocity relation evolves from a linear rheology to a stiffer response, thereby suggesting to call “fluidization” this first transition. A second transition is observed *within* the intermittent regime, when the intruder’s motion is made of intermittent bursts separated by long waiting times. This transition is signed by a peak in the relative fluctuations of the intruder’s displacements and a critical scaling of the bursts amplitudes’ distri-

---

\*Electronic address: raphael.candelier@cea.fr

†Electronic address: olivier.dauchot@cea.fr

butions. This transition occurs at the jamming point  $\phi_J$  characterized in [1] and defined as the point where the static pressure (*i.e.* the pressure measured when the vibration is switched off) vanishes. In [1], the authors demonstrate that dynamical heterogeneities become critical at the transition. Here we investigate the motion of the grains surrounding the intruder. Below the fluidization transition a wake of free volume is observed behind the intruder and the fluidization transition is marked by the evolution of the reorganization patterns around the intruder, going from compact aggregates in the flowing regime to long-range branched shapes in the intermittent regime, suggesting an increasing role of the stress fluctuations. The distributions of the kinetic energy of these reorganization patterns also exhibits a critical scaling at the jamming transition.

This paper is an extended version of a recently published letter [19], in which both transitions have been reported. The purpose of the present paper is to provide a comprehensive study of the displacement fields surrounding the intruder and to take this opportunity to provide details on our analysis procedures as well as an extended discussion of our results. The paper organizes as follows : the experimental set-up and protocols are described in section I. In section II we first introduce the raw dynamical quantities and the phase diagram (II A), then we characterize the fluidization (II B) and jamming (II C) transitions. The dynamics around the intruder is analyzed in section III, both by the relation between the average flow and the spatial fluctuations (III A) and by the evolution of the averaged free volume around the intruder (III B). Finally, we study the bursts statistics in the intermittent regime close to jamming in section IV. A general discussion and a few concluding remarks are given in section V.

## I. EXPERIMENTAL SET-UP AND PROTOCOL

The experimental set-up has been described elsewhere [1] and we shall only recall here its most important characteristics and the modifications induced by the dragging procedure. The system is made of a monolayer of 8500 bi-disperse brass cylinders of diameters  $d_{small} = 4 \pm 0.01\text{mm}$  and  $d_{big} = 5 \pm 0.01\text{mm}$  laid out on a horizontal glass plate sinusoidally vibrated in its plane at a frequency of 10Hz and with a peak-to-peak amplitude of 10mm. The grains are confined in a cell, fixed in the laboratory frame, the volume of which can be adjusted by a lateral mobile wall controlled by a  $\mu\text{m}$  accuracy translation platen, which allows us to vary the packing fraction  $\phi$  of the grains by tiny amounts ( $\delta\phi/\phi \sim 5 \times 10^{-4}$ ). The pressure exerted on this wall is measured by a force sensor (see fig.1). The intruder consists in a larger particle ( $d_{intruder} = 2.d_{small}$ ) of same height introduced in the system and pulled by a mass via a pulley perpendicularly to the vibration. In all data presented here the resultant motion is strongly overdamped and the applied force can

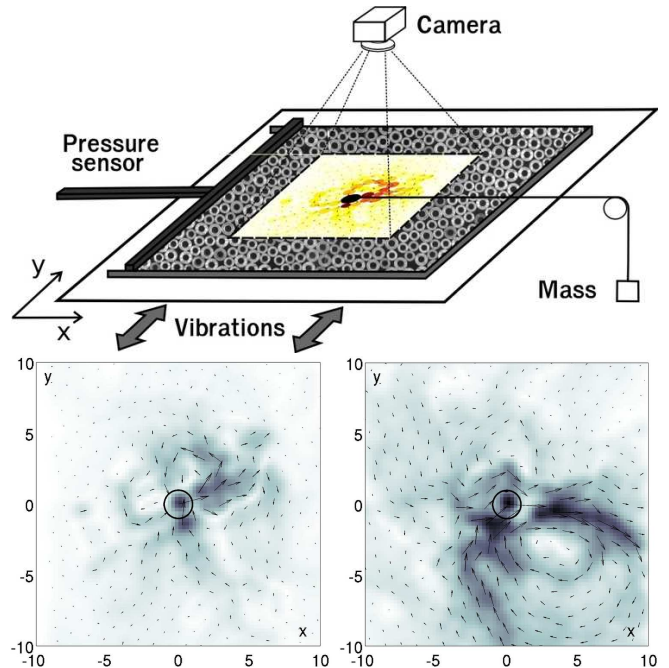


FIG. 1: (Color online) **Top** Experimental Setup (see text for details). **Bottom** Two samples of displacement fields around the intruder at  $\phi_J$  for similar  $x$ -displacements of the intruder ( $\Delta x = 2.14$  and  $2.08$ , in respectively 14 and 131 time steps). The arrows show the unmagnified grain displacements, while the interpolated amplitude field is in grey scale.

be considered as constant. We use a fishing wire that stands over the other grains and doesn't disturb their dynamics. The time unit is set to one plate oscillation while the length unit is chosen to be the diameter of the small particles. The drag forces  $F$  are expressed as the ratio of the applied mass onto the total mass of grains in the cell ( $M_{total} = 2.365\text{kg}$ ).

We have been using two protocols, setting either the drag force or the packing fraction constant. We explore the force / packing fraction diagram along constant force lines using three different drag forces ( $F_1 = 0.029$ ,  $F_2 = 0.064$  and  $F_3 = 0.113$ ) and varying the packing fractions from  $\phi = 0.8223$  to  $0.8418$ , and along constant packing fraction lines using three different packing fractions ( $\phi_1 = 0.8383$ ,  $\phi_2 = 0.8304$  and  $\phi_3 = 0.8399$ ) and varying the drag force from  $F = 0.029$  to  $0.617$ , as sketched in fig.2.

Starting from a low packing fraction  $\phi$ , we gradually compress the system until it reaches a highly jammed state following the same protocol as in [1]. Then we stepwise decrease the packing fraction. In the absence of the intruder, it was shown on the one hand that the average relaxation time increases monotonically with the packing fraction and on the other hand that the dynamics exhibits strong dynamical heterogeneities, the length-scale and time-scale of which exhibit a sharp peak at an intermediate packing fraction. The authors have shown that the spatial correlations of these dynamical heterogeneities exhibits a critical scaling at the transition. The

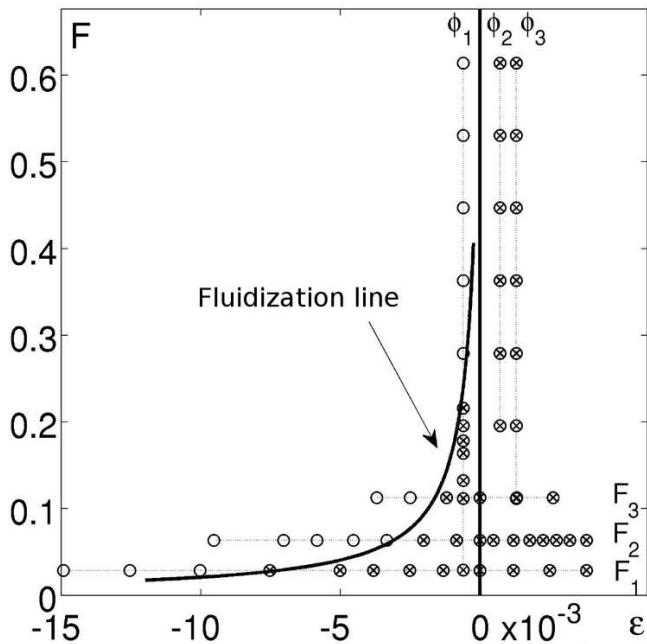


FIG. 2: Experimental conditions in a force - reduced packing fraction  $\varepsilon$  diagram. Each point corresponds to a trajectory of the intruder into the media. The horizontal and vertical dotted lines correspond to the experimental exploration paths, either at constant force or packing fraction.  $\circ$  (resp.  $\otimes$ ) denote the fluidized (resp. intermittent) behavior (see text for definition).

pressure measured at the wall in the absence of vibration falls to zero precisely below that packing fraction, hence called the jamming transition  $\phi_J$ . It is important to mention that for such high packing fractions, the structure as given by the neighborhood relation among the grains is frozen on experimental time-scales. Hence the observed transition is to be understood as the jamming of a given frozen configuration. Accordingly the value of  $\phi_J$  may slightly change from one run to another, since it may differ from one frozen configuration to another. In the present case, by monitoring the pressure at the wall while interrupting the vibration and without drag force, we could localize the jamming transition and obtain three close but different values  $\phi_J$  : 0.8369 ( $F_1$ ), 0.8383 ( $F_2$ ), 0.8379 ( $F_3$ ) and 0.8388 in the run where we explore iso- $\phi$  lines. These values also are slightly smaller than the value  $\phi_J = 0.8417$  reported in [1], maybe an effect of the geometrical distortion induced locally by the size of the intruder, twice larger than the other grains. In the following we will use either the packing fraction  $\phi$  or the reduced packing fraction  $\varepsilon = (\phi - \phi_J)/\phi_J$ .

In the present study, before each step, the intruder is removed from the position it has reached, replaced by one big and two small grains, and inserted at its initial position in place of one big and two small grains. Then a downward step in packing fraction is eventually done, and the system is kept under vibration up to one hour in order to "equilibrate" the configuration. At that point,

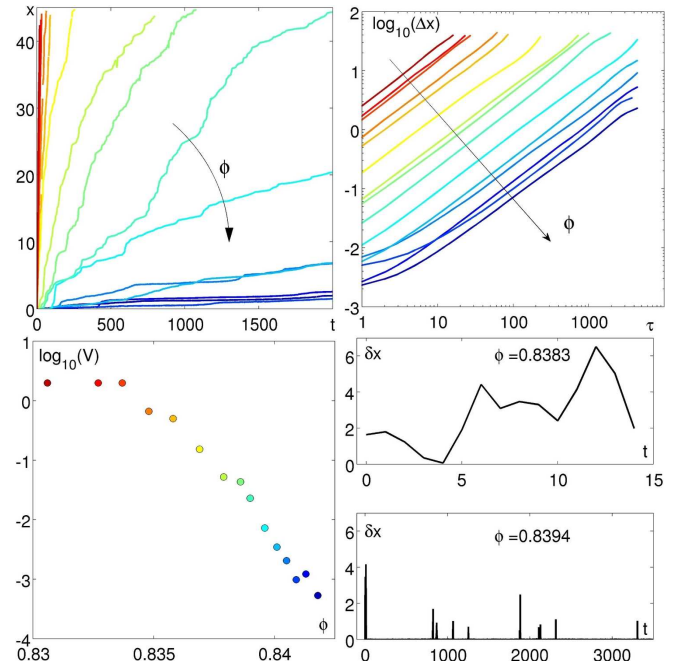


FIG. 3: (Color online) **Top left:** Trajectories of the intruder for several packing fractions, from  $\phi = 0.8306$  (red) to  $\phi = 0.8418$  (blue), at constant force ( $F = F_2$ ). The trajectories at the highest packing fractions are truncated. **Top right:**  $\log_{10}$  of the average displacement of the intruder  $\Delta x$  in function of the lag time  $\tau$  for the same packing fractions and the same drag force. **Bottom left:**  $\log_{10}$  of the average velocity of the intruder in function of the packing fraction  $\phi$ , same packing fractions and drag force. **Bottom right:** Instantaneous displacements of the intruder at a high drag force ( $F = 0.363$ ) for two very close packing fractions on both sides of the fluidization and jamming transition, here indistinguishable. At  $\phi = 0.8383$  the intruder is always moving while at  $\phi = 0.8394$  one can observe intermittent bursts of activity separated by long waiting intervals.

the pressure has the same value as without the intruder for the corresponding packing fraction, indicating that the system has recovered from the small perturbation induced by the intruder's "teletransportation". Only then the force is applied and the intruder is dragged through the cell, while its stroboscopic motion together with that of a set of 1800 surrounding grains in the center of the sample is tracked by a digital video camera triggered in phase with the oscillations of the plate.

## II. FLUIDIZATION AND JAMMING

### A. Phase diagram

When looking at the trajectories of the intruder along the drag direction  $x$  (see fig.3-top left), one immediately notices that the typical velocity dramatically changes within a tiny variation of the packing fraction : the intruder browses the entire system in a few time steps

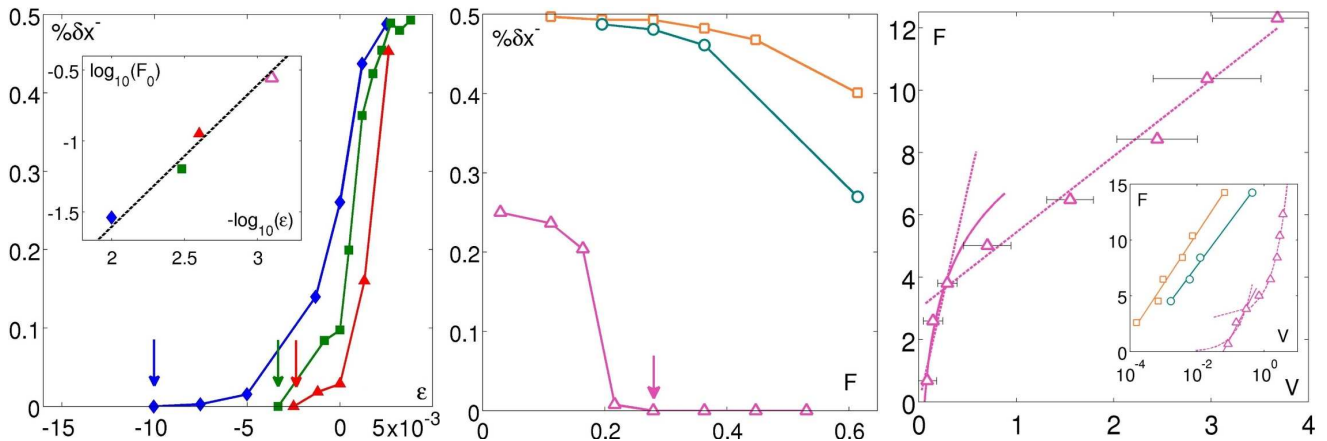


FIG. 4: (Color online) **Left** Ratio of negative displacements  $\% \delta x^-$  in function of the reduced packing fraction  $\varepsilon$ , for three different forces :  $F_1$  ( $\blacklozenge$ ),  $F_2$  ( $\blacksquare$ ) and  $F_3$  ( $\blacktriangle$ ). For clarity, only one point with a ratio of 0 is shown. **Inset** Fluidizations force in function of the reduced packing fraction  $\varepsilon = (\phi - \phi_J)/\phi_J$ . Each point correspond to the moment where the ratio of negative displacements reaches 0. These points are also marked with arrows in the left and middle figures. **Middle** Ratio of negative displacements in function of the drag force  $F$ , for three different packing fractions :  $\phi_1$  ( $\triangle$ ),  $\phi_2$  ( $\circ$ ) and  $\phi_3$  ( $\square$ ). **Right** Applied drag force in function of the average velocity of the intruder in a *lin – lin* plot at  $\phi_1$ . **Inset** Idem in a *lin – log* plot for different packing fractions :  $\phi_1$  ( $\triangle$ ),  $\phi_2$  ( $\circ$ ) and  $\phi_3$  ( $\square$ ). Fits are eye-guiding affine (dotted) or logarithmic (plain) behaviors.

for low packing fractions, and conversely seems to be arrested for the highest values of  $\phi$ . For a given drag force, the average displacement probed over a lag time  $\tau$ ,  $\Delta x(\tau) = \langle x(t+\tau) - x(t) \rangle_t$  is roughly  $V \cdot \tau$ , where  $V$  is the intruder’s average velocity.  $V$  spans four decades from  $5 \times 10^{-4}$  to 5 while varying the packing fraction of only a few percent ( $\delta\phi/\phi = 2 \times 10^{-2}$ ), illustrating the dramatic freeze of the dynamics (fig.3-top right). For the highest packing fractions, one may notice a systematic bending of the curves at short times indicating that the intruder does not feel instantaneously the bias induced by the drag force.

A closer inspection of the dynamics reveals two salient, distinct regimes of the intruder’s motion. For loose packings and large drags, the intruder moves continuously, while for dense packings and small drags the intruder’s motion is highly intermittent. Anticipating on the following, let us call this transition “fluidization” and emphasize that it is distinct from the jamming one as illustrated on the phase diagram (fig.2). Only for the largest forces, both transitions become asymptotically close, as illustrated on figure 3-bottom left, where the instantaneous displacement of the intruder is shown for two packing fractions just below and above the transition. Just below the transition the intruder is moving continuously fast like in a fluid – note the time-scale on the horizontal axis– while just above it one observes violent bursts separated by extremely long waiting times, indicating that the medium is not fluidized. We now characterize in more details the nature of these two transitions.

## B. Fluidization

The intruder’s motion results from the drag force competing against the resistance of the surrounding grains. When the drag force is low enough – or if the packing is dense enough – the configuration can sustain the drag stress until some rearrangement of the force network, induced by the vibration, allows the intruder to move forward. In the meantime, the intruder’s motion is cage-like and almost isotropic, going forward and backward roughly half of the time. Figure 4-left (resp. middle) displays the percentage of time the intruder is going backwards  $\% \delta x^-$  as a function of the relative packing fraction  $\varepsilon$  for the three constant forces  $F_1, F_2, F_3$  (resp. as a function of the dragging force for the three packing fractions  $\phi_1, \phi_2, \phi_3$ ). In the extreme cases for which the system is most of the time stuck in jammed states  $\% \delta x^-$  is very close to 0.5. As the drag force becomes stronger as compared to the resistance of the surrounding grains, the intruder will be less and less often blocked. As a result the percentage of backward steps will be smaller, and eventually will drop to 0 when the intruder motion becomes continuous. This is precisely how we have chosen to identify the fluidization transition pointed out by an arrow on the figure. The most striking feature is that we could not observe fluidization for the two packing fractions larger than  $\phi_J$ .  $\% \delta x^-$  decreases with the force, but remains far from zero even for forces as large as 0.6, that is of the order of the force needed to drag *all* the grains on the glass plate in the absence of vibration. Our data suggests a divergence of the fluidization line at the jamming transition :  $F_{flow} \sim \varepsilon^{-1}$  (see inset of figure 4-left). Looking at the force-velocity relation as shown on figure 4-right, we observe that an affine behavior  $F - F_{flow} \propto V$  in the

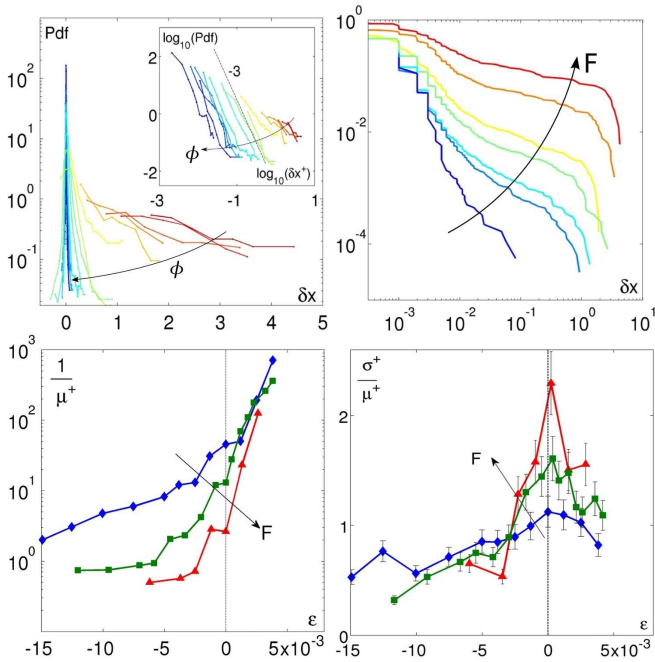


FIG. 5: (Color online) **Top left** Pdf of the instantaneous displacements in the drag direction  $\delta x$  at a constant force  $F = F_2$  for several values of  $\phi$ . **Inset** same for the positive displacements only, in  $\log - \log$  scale. **Top right** Cumulated Pdf of the instantaneous displacements in the drag direction  $\delta x$  at a constant packing fraction  $\phi = \phi_1$  for several values of  $F$  (right). **Bottom** Inverse average  $1/\mu^+$  (left) and standard deviation over average  $\sigma^+/\mu^+$  (right) of the instantaneous positive displacements in the drag direction as functions of the reduced packing fraction  $\epsilon$ . Different curves correspond to different drag forces :  $F_1$  ( $\blacklozenge$ ),  $F_2$  ( $\blacksquare$ ) and  $F_3$  ( $\blacktriangle$ )

fluidized motion regime, *i.e.* above the fluidization line, whereas in the intermittent regime either  $F \propto \ln(V)$  or  $F \propto V$  are possible. Note however that in the latter case the response is clearly stiffer than in the fluidized regime. This demonstrates that the fluidization line also separates two rheological behaviors. Such a fluidization transition has been previously reported in other experimental studies. However a straightforward comparison can not be made without further enquiries, which we shall report to the discussion part.

### C. Jamming

We now characterize the intruder dynamics when approaching the jamming transition. When looking at the intruder's instantaneous displacements  $\delta x$  along the drag direction in the intermittent regime (fig.3-bottom right and fig.9-left), one immediately notices very strong fluctuations, with bursts of widely fluctuating magnitude in the direction of the drag. As a result the distributions of  $\delta x$  (fig.5-top left) exhibit an important skewness toward the positive displacements for the packing fractions above fluidization. In order to characterize these positive dis-

placements  $\delta x^+$ , we compute the average value over time  $\mu^+ = \langle \delta x^+ \rangle_t$  and the relative fluctuations :

$$\frac{\sigma^+}{\mu^+} = \frac{\sqrt{\langle (\delta x^+ - \mu^+)^2 \rangle_t}}{\mu^+}. \quad (1)$$

Figure 5-bottom left shows that  $1/\mu^+$ , the typical time the intruder takes to move one particle diameter, increases monotonically with  $\epsilon$  and faster than exponentially. The stronger the dragging force the sharper the increase. No significant behavior is observed when crossing the jamming transition. On the contrary, figure 5-bottom right reveals a peak of  $\sigma^+/\mu^+$  precisely at  $\phi_J$  for the three dragging forces. Note that the peak sharpens when the drag force is stronger. Indeed, as discussed in the previous section, when  $F$  increases the fluidization line approaches the jamming transition. This has two consequences. The displacement bursts become larger when they occur – as can be seen on figure 5-top left from the cumulated distribution of the intruder displacements for increasing forces – and the range of packing fraction separating the non fluctuating continuous motion in the fluidized regime from the strongly intermittent one at jamming shrinks. Finally let us mention that in the intermittent regime the distributions of  $\delta x^+$  decay as power-laws with an exponent close to  $-3$  (see inset of figure 5-top left), a result similar to the one reported in a recent simulation, where a probe is dragged into an assembly of harmonically repulsing disks [20].

The above results reveal that the strong spatio-temporal heterogeneities of the dynamics reported in the absence of intruder [1] can also be seen in the response of the intruder to the dragging force. This is related to the fact that microrheology gives access to non-linear responses and thereby probes the strength required to pull free the probe from the transient local structure. Before addressing in further details the critical nature of the fluctuations reported here above, we will concentrate on the response of the grains surrounding the intruder. This will ultimately allow us to perform the statistical analysis of the rearrangement events as a whole, involving both the intruder and the surrounding grains.

## III. AROUND THE INTRUDER

### A. Average flow and spatial fluctuations

As already suggested in figure 1, the instantaneous displacement field around the intruder during a burst is rather complex. They are typically asymmetric, with a main vortex on one or the other side of the intruder. Averaged over many bursts (see figure 6-top right), the displacement field recovers the intruder's left-right symmetry and exhibit a two vortices pattern. Further insight into the dependence of this flow on the packing fraction is obtained when looking at the profiles of the  $x$ -component of the velocity along the direction of the drag

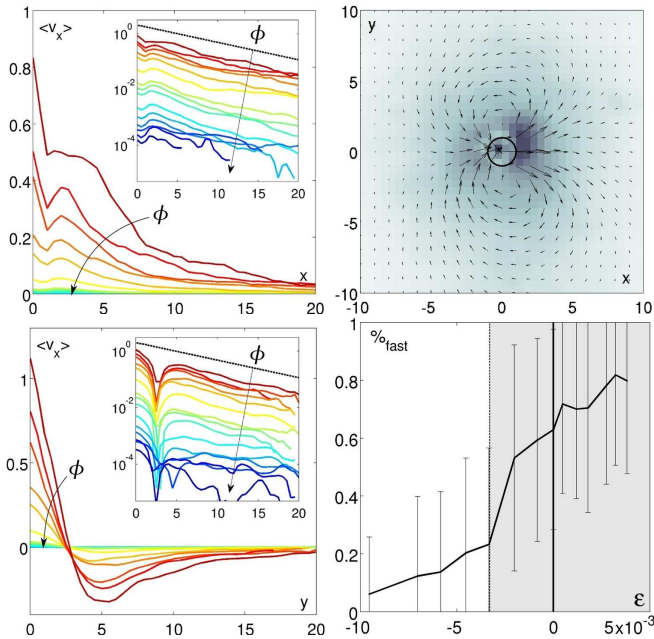


FIG. 6: (Color online) **Left** Velocity profiles : average velocity in the  $x$ -direction along the horizontal (top) and vertical (bottom) axis, for 15 packing fractions. **Inset** Same in absolute values and  $\log - \text{lin}$ . The dark dotted line is an exponential decaying guide with a characteristic length  $\lambda_x = 7$ . **Top-right** Displacement field around the intruder at  $\phi = 0.8386$ , averaged over time. The arrows are magnified by a factor 3. **Bottom-right** Average percentage of particles in the connex clusters of particles faster than  $v_{max}/2$  in function of the reduced packing fraction. Error bars show the standard deviation. The grey area correspond to the intermittent regime. In all plots,  $F = F_2$ .

( $x$ -direction) and perpendicular to the drag ( $y$ -direction) (see figure 6-right top and bottom). As evidenced in the insets, one observes that the velocity field decreases exponentially with the distance to the intruder, and amazingly that the typical length-scales  $\lambda_x \simeq 7$  and  $\lambda_y \simeq 10$  associated with such a dependence are totally independent from the packing fraction. This is also confirmed by the localization of the center of the vortices, easily located on the  $y$ -profile, which remains at the same distance from the intruder at all packing fractions. Hence, as far as the averaged flow is concerned, only its overall magnitude depends on the packing fraction and scales like  $V$ , the averaged velocity of the intruder.

In order to study the fluctuations of the displacement field, one could imagine to subtract the averaged field; however without a prescription for the analytical form of this field or outstanding statistics, this is a rather uncontrolled operation, especially in the vicinity of Jamming where fluctuations grow. An alternative procedure is to define first a maximal displacement for the grains,  $v_{max}$ , as the average displacement of the intruder's closest neighbors, and then to define the "fast particles" cluster as the connex cluster of particles around the intruder which move more than  $v_{max}/2$ . The average number of

particles in this fast cluster is plotted on figure 6-bottom right as a function of the packing fraction: it grows from 10% to 80% in the tiny interval between  $\phi = 0.8306$  and  $\phi = 0.8409$ , underlining how sharply the spatial extent of the reorganizations grows as the system goes toward dynamical arrest. It is however surprising that the number of fast particles increases, considering that the averaged flow scales entirely with the velocity of the intruder which we have scaled out by defining the "fast" particles relatively to the average velocity around the intruder. Such a difference between the averaged flow behavior and the instantaneous one can only be explained by the existence of strong heterogeneities in the instantaneous fields. The amplitude of the fluctuations of the number of fast particles, as indicated by the error bars on figure 6-bottom right is already an indication that it is indeed the case.

A further characterization of these heterogeneities is provided by the shape of the clusters made of the  $p\%$  fastest particles at each time step; typical examples with  $p = 15\%$  are shown on fig.7-top for three packing fractions below, at, and above  $\phi_0$  the fluidization packing fraction. One clearly observes that these instantaneous rearrangements evolve with the packing fraction from dense to branched patterns with long chains spanning the whole system. The number of neighbors  $n_{neigh}$  inside these clusters is a good indicator of the level of branching since its typical value is 6 for perfectly dense clusters and 2 for perfect strings. The well defined plateau in the dependence of  $\langle n_{neigh} \rangle$  with  $p$  (figure 7-middle left) corresponds to the clusters which contain enough particles to have a non-trivial shape but do not reach the boundaries of the acquisition field. The average number of neighbors at the plateau (fig.7-middle right) decreases significantly with the packing fraction providing a quantitative evaluation of the clusters' evolution from dense aggregates to branched structures. The contour fractal dimension  $d_f^c$  calculated with the classical compass method [21] also gives insight on branching. The mean value  $\langle d_f^c \rangle(p)$  has a nice maximum for the range of  $p$  corresponding to the plateau in  $\langle n_{neigh} \rangle(p)$ . For a value of  $p = 40\%$ , that is for clusters large enough to assess the fractal dimension without spanning the acquisition field, we observe a significant increase of  $d_f^c(\phi)$  at  $\phi_0$ , the packing fraction where the intruder's motion becomes intermittent.

Altogether, the patterns observed in the instantaneous displacement field during the relaxation events suggest that the force chains network, whose importance has been visually exemplified in photo-elastic disks experiments of an intruder dragged in a Couette cell [9], starts playing a significant role as soon as the system crosses the fluidization transition. However, one can not elude the role of the density field, which we now investigate computing the free volume field around the intruder.

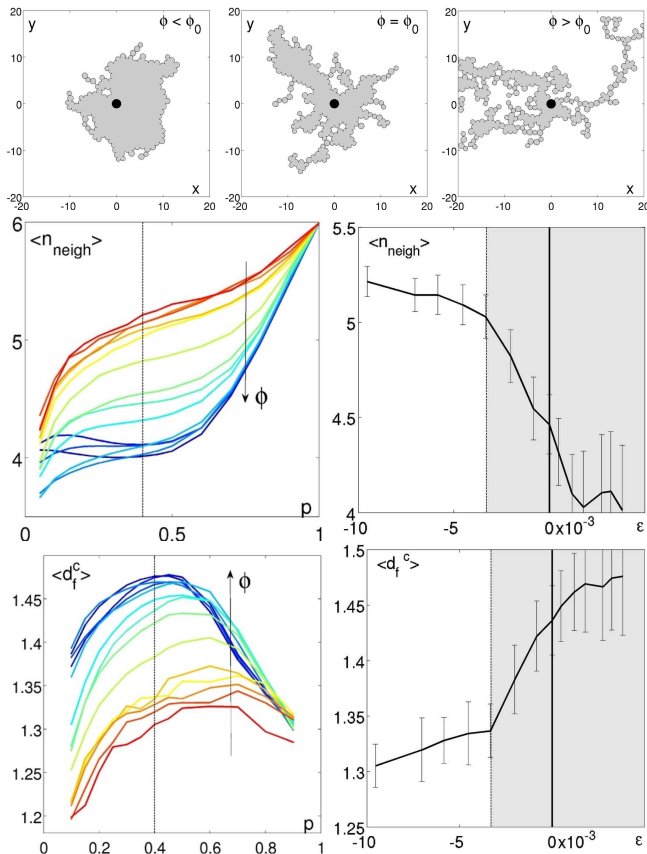


FIG. 7: (Color online) **Top** Typical contours of clusters of the  $p = 15\%$  fastest particles, for three packing fractions, from left to right :  $\phi = 0.8337$  ( $\phi < \phi_0$ ),  $\phi = 0.8358$  ( $\phi = \phi_0$ ) and  $\phi = 0.8396$  ( $\phi > \phi_0$ ). The intruder is marked by a black disk and moves from left to right. **Middle left** Average number of neighbors  $\langle n_{neigh} \rangle$  in function of  $p$ , for different packing fractions. The black dotted line is at  $p = 40\%$ , in the middle of the plateau. **Middle right**  $\langle n_{neigh} \rangle$  in the clusters of  $p = 40\%$  fastest particles, as a function of  $\varepsilon$ . The grey area correspond to the intermittent regime, and error bars show the standard deviation. **Bottom left** Average fractal dimension of the clusters contours ( $d_f^c$ ) as a function of  $p$  for different packing fractions. The black dotted line is at  $p = 40\%$ . **Bottom right**  $\langle d_f^c \rangle$  as a function of  $\varepsilon$  for  $p = 40\%$ . The grey area correspond to the intermittent regime, and error bars show the standard deviation.  $F = F_2$  for all plots.

## B. Free volume

We then examine the density field around the intruder. For that purpose, we compute the free volume field extracted from Laguerre's tessellation [42] of the configurations at each time step: the free volume  $\mathcal{V}_f$  of a Voronoi cell is the area difference with the minimal possible regular hexagon around the grain normalized by the surface of the grain. Figure 8 displays the averaged free volume field around the intruder for three packing fractions, below, above, and at the jamming transition. Above  $\phi_J$ , there is a very small amount of decompaction around the intruder without significant signature of the intruder

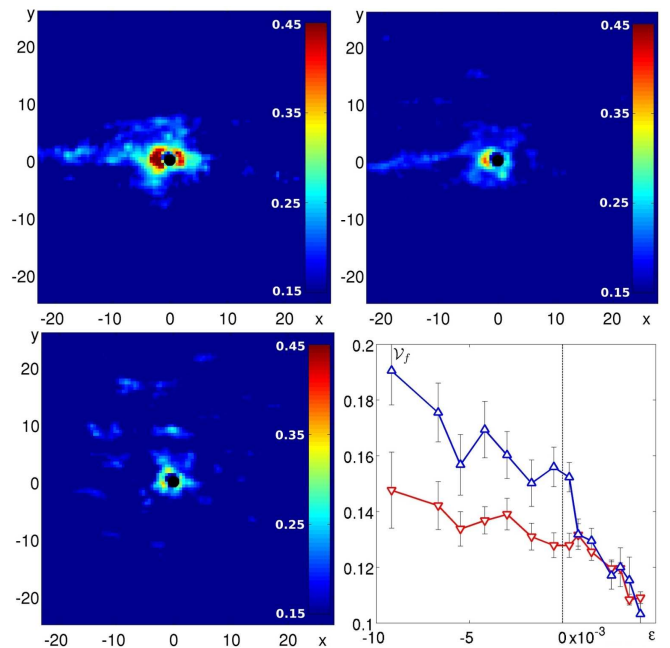


FIG. 8: (Color online) **Top and bottom-left** Average free volume fields around the intruder for three packing fractions:  $\phi = 0.8327$  ( $\phi < \phi_J$ , top-left),  $\phi = 0.8386$  ( $\phi \simeq \phi_J$ , top-right),  $\phi = 0.8405$  ( $\phi > \phi_J$ , bottom-left). **Bottom-right** Average free volume ( $\langle \mathcal{V}_f \rangle$ ) before ( $\nabla$ ) and after ( $\Delta$ ) the intruder in function of the reduced packing fraction. Error bars represent the standard deviation over time of the free volume in each point of space, averaged on the computation window.

motion, seemingly an effect of the size difference between the intruder and the surrounding grains disturbing the local organization of the packing. On the contrary, as the packing fraction decreases below jamming, two holes grow, first on the back of the intruder and then on its front.

As a consequence, one observes a clear signature of the intruder's motion, namely the apparition of a forward-backward asymmetry which can be quantified by computing for instance the average free volume in front of and behind the intruder (figure 8-bottom right)[43]. One observes that above  $\phi_J$ , there is no more sign of the asymmetry associated with the intruder motion.

Altogether, we have seen that the averaged flow around the intruder is surprisingly insensitive to the transition, apart from a simple scaling factor indexed on the average velocity of the probe. On the contrary, the fluctuations reveal a rather complex interplay of the density and stress fluctuations. Below the fluidization transition, the intruder motion is dominated by important free volume rearrangements, which concentrate in dense clusters of fast moving grains around the intruder. As soon as the system enters the intermittent regime, these clusters start to branch, indicating the existence of inhomogeneities in the rigidity of the system. The instantaneous displacements spread on larger and larger scales; and progressively the free volume fluctuations become distributed throughout

the system. Above  $\phi_J$  these last type of rearrangement completely dominate the intruder motion.

#### IV. BURST STATISTICS CLOSE TO JAMMING

In the above section, we have seen that the temporally intermittent motion of the intruder also corresponds to spatially heterogeneous rearranging regions. We will now investigate the intruder displacements and the kinetic energy of these regions, focusing on the temporal correlations at the root of this dynamics of bursts. Figure 9-bottom displays the instantaneous displacement  $\delta x(t)$ , and the kinetic energy involved in a rearrangement  $\delta E(t) = \Sigma \delta x_i^2(t)$ , where the sum is performed on the clusters of particles faster than  $v_{max}/2$ , as defined in section III A. For three different packing fractions chosen above the fluidization transition, one clearly observes a sequence of distinguishable and well separated bursts, suggesting “crackling noise”-like signals [22, 23].

Note that the signals of  $\delta x(t)$  and  $\delta E(t)$  are very similar. However the correlation is not as strong as one would first imagine by visual inspection. Each burst in the displacements signal corresponds indeed to a burst in the kinetic energy one but the bursts might be shifted in time and the intruder’s displacements sometimes precede, sometimes follow the energy ones. In addition, the amplitude of the bursts only weakly correlate and there are some occasions where there is a burst of activity in the system without a displacement of the intruder itself (see an example on fig. 9), but these are marginal events.

The first step in analyzing such kind of signals is to coarsegrain the statistical distribution of the jumps to capture the size and duration of the relevant bursts. One common way to do so is to define a threshold, or resolution coefficient, in order to delimit the temporal limits of each burst : given a signal  $u(t)$  and a threshold  $\hat{u}$ , one can define bursts or avalanches as the connex portions of the signal that stand above  $\hat{u}$  ; every burst have a duration  $T_u^i$  and an integrated amplitude  $S_u^i$  (see fig.9-top left). Choosing the threshold is a delicate problem given the large variations of the displacements’ amplitudes, the complete loss of small events for the loosest packings and the fact that the background noise limits the detection of small bursts at high packing fractions. In the following we have set all the thresholds at the value where the difference between the cumulated distributions of the local minimums and maximums of  $u(t)$  exhibits a peak. On one hand this corresponds to the point where the minimums and maximums in  $u(t)$  are best separated, and on the other hand it points out to the threshold value for which the number of bursts is maximal, naturally enforcing the statistics. We have checked that multiplying the so-obtained thresholds by a factor from 1/2 to 2 doesn’t change the following results.

First we observe on figure 10-top right that the waiting times separating two successive bursts are exponentially distributed the characteristic time of which  $\tau_w \simeq 2$  is in-

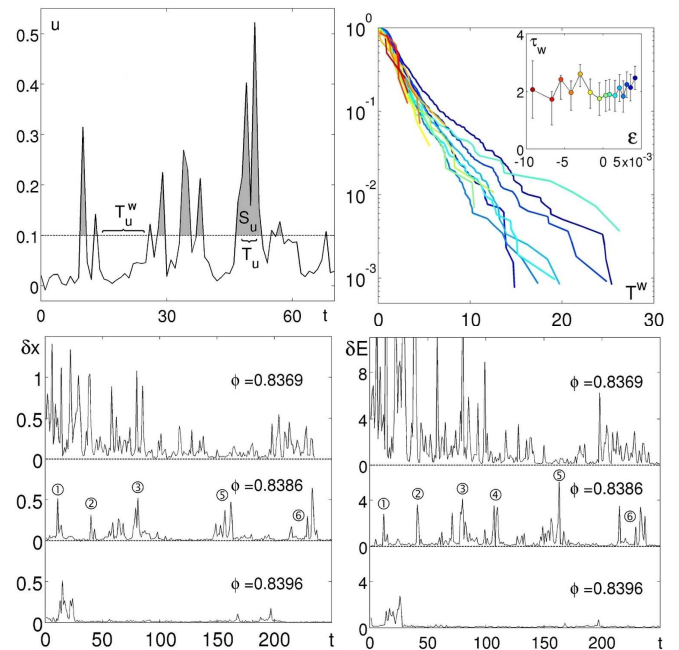


FIG. 9: (Color online) **Top left** Definition of the bursts of activity : given a threshold  $\hat{u}$  on a signal  $u(t)$ , each connex portion of signal above the threshold defines a burst.  $T_u$  is the duration of the burst while  $S_u$  is its area (in grey). The waiting times between bursts are noted  $T_u^w$ . **Top Right** Cumulated probability density functions of the time intervals  $T_u^w$  between bursts of displacements for 15 packing fractions from  $\phi = 0.8306$  (red) to  $0.8418$  (blue), at the constant drag force  $F_2$ . *Inset* Average waiting time  $\tau_w$  for the same packing fractions estimated by an exponential fit. Error bars represent the 95% confidence bounds of the fit. **Bottom left** Instantaneous displacements  $\delta x(t)$  of the probe for three packing fractions. **Bottom right** Energy of the grains  $\delta E(t)$  around the intruder for the same packing fractions. Note that all peaks can be found in both signals, except some rare events like the peak number 4.  $F = F_2$  for all bottom plots.

dependent of the packing fraction (see inset). Two conclusions can be drawn: (i) the bursts follow a Poissonian process and can be considered as independent events, and (ii)  $\tau_w$  remains very small compared to the total time of the experiments. We catch a large number of bursts, even at the highest packing fractions. Note that the use of a constant threshold to define the bursts would have lead to a dramatic increase of these waiting times in the intermittent regime and for the highest packing fractions the number of bursts would have been vanishingly small.

We focus now on the statistics of the bursts themselves. Let us note  $T$  and  $L$ , respectively  $T_E$  and  $E$ , the duration and the integrated amplitude of the bursts recorded on the signal of the displacements of the probe, respectively of the kinetic energy of the surrounding fastest grains. Obviously these quantities are not independent one from another. The first step in the analysis (see figure 10-left), shows that :

$$L(T, \phi) = L_0(\phi)T^{1/z} \quad \text{and} \quad E(T_E, \phi) = E_0(\phi)T_E^{1/z}, \quad (2)$$

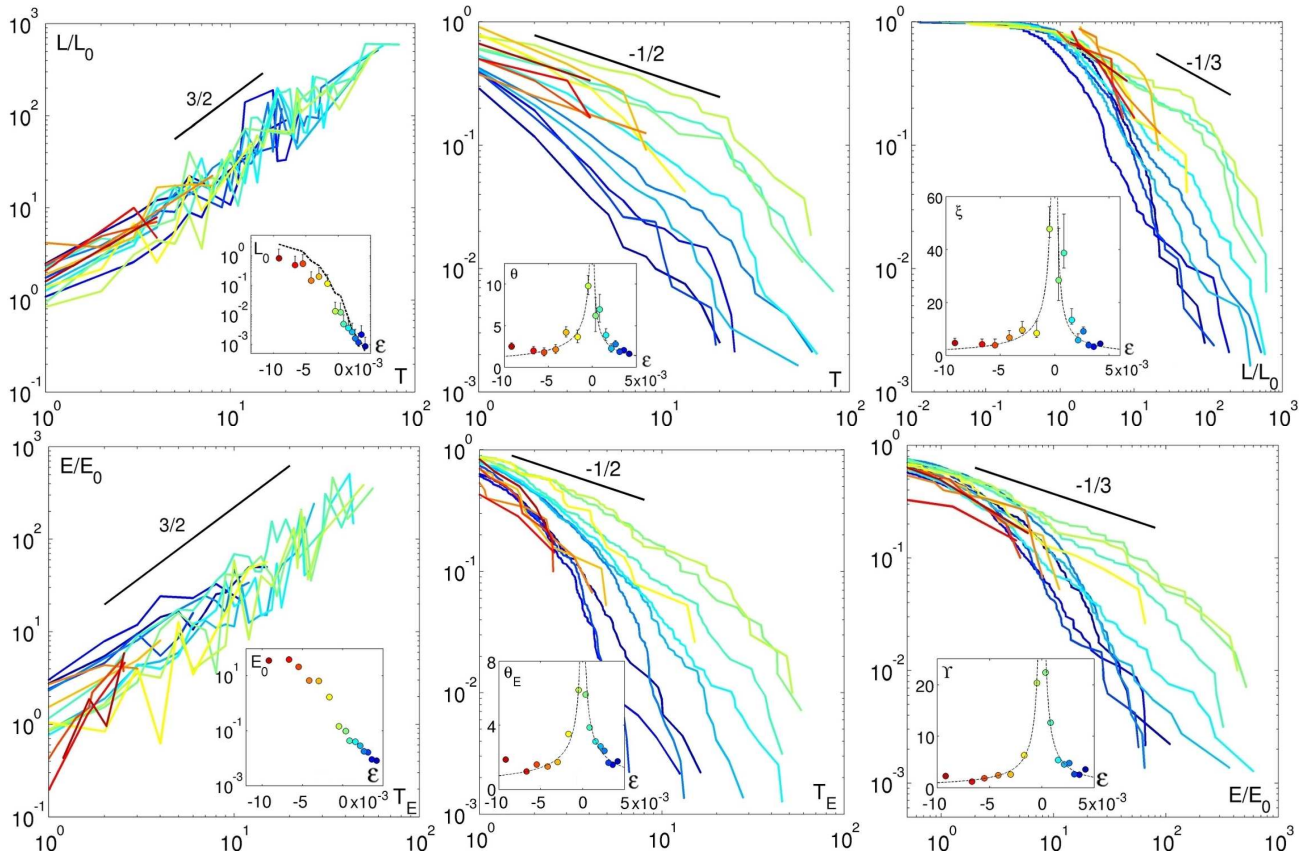


FIG. 10: (Color online) **Top left:** Rescaled length  $L/L_0$  as a function of  $T$ . *Inset* Scaling factor  $L_0$  as a function of  $\varepsilon$ . The black dotted line corresponds to the average speed of the intruder. **Top middle:** Cumulated Pdf of the burst durations  $T$  in the intruder's displacement signal. *Inset* Cut-off  $\theta(\varepsilon)$  of the distribution of  $T$ . The eye-guiding lines are power laws with an exponent  $-2/3$ . **Top right:** Cumulated Pdf of the rescaled length  $L/L_0$ . *Inset* Cut-off  $\xi(\varepsilon)$  of the distribution of  $L/L_0$ . The eye-guiding lines are power laws, with an exponent  $-1$ . **Bottom left:** Rescaled energy  $E/E_0$  as a function of  $T_E$ . *Inset* Scaling factor  $E_0$  as a function of  $\varepsilon$ . **Bottom middle:** Cumulated Pdf of the burst durations  $T_E$  in the energy signal. *Inset* Cut-off  $\theta_E(\varepsilon)$  of the distribution of  $T_E$ . The eye-guiding lines are power laws with an exponent  $-2/3$ . **Bottom right:** Cumulated Pdf of the rescaled energy  $E/E_0$ . *Inset* Cut-off  $\Upsilon(\varepsilon)$  of the distribution of  $E/E_0$ . The eye-guiding lines are power laws, with an exponent  $-1$ .

where  $L_0$  and  $E_0$  can be interpreted as the typical displacement and energy associated with a burst and  $z = 2/3$  is usually called the *dynamical exponent*.  $L_0$  depends on  $\phi$  in a similar way as the average velocity of the intruder does, consistently with the previous observation that the average waiting time  $\tau_w$  is independent from  $\phi$ .

The second observation concerns the distributions of  $T, T_E$  and  $L/L_0, E/E_0$ . Again we find identical behaviors for the intruder displacement and the kinetic energy of the fastest surrounding grains (fig. 10-middle and right). All the above quantities are largely distributed, with a large value cutoff, which depends on the packing fraction. Visual inspection of the tails of the distribution already indicates that the cutoff dependence on the packing fraction is not monotonic. In all plots the jamming packing fraction corresponds to the light green curves. The distributions are the largest for that precise packing fraction. Such behaviors can be encoded in the following scaling

relations:

$$\rho(T) \propto T^{-(1+\alpha)} \cdot f\left(\frac{T}{\theta(\varepsilon)}\right), \quad (3)$$

$$\rho(T_E) \propto T_E^{-(1+\alpha)} \cdot f_E\left(\frac{T_E}{\theta_E(\varepsilon)}\right), \quad (4)$$

$$\rho(L/L_0) \propto (L/L_0)^{-(1+\beta)} \cdot g\left(\frac{L}{\xi(\varepsilon)}\right), \quad (5)$$

$$\rho(E/E_0) \propto (E/E_0)^{-(1+\beta)} \cdot g_E\left(\frac{E}{\Upsilon(\varepsilon)}\right), \quad (6)$$

where the exponents  $\alpha \simeq 1/2$  and  $\beta \simeq 1/3$  satisfy the expected relation  $\alpha \cdot z = \beta$ . Note that given the lack of statistics these exponents are not the results of a fit but only indicative values. One then easily extracts the scaling variables, which are the cutoffs of the distributions and are simply proportional to their mean values [44]. Their dependence on the packing fraction are plotted in the insets of figure 10 and exhibit a sharp peak at the

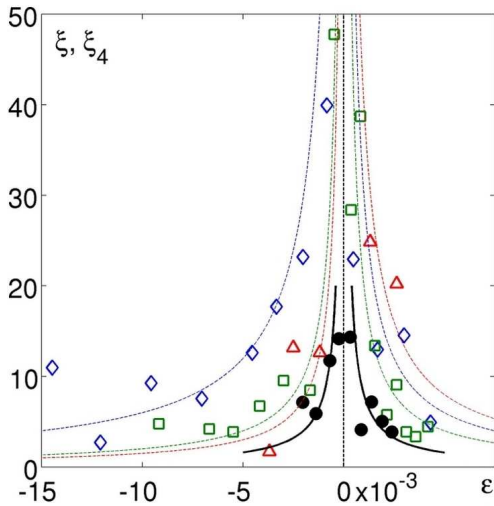


FIG. 11: (Color online) Comparison of the evolution of dynamical lengthscales : the cut-off of the distribution of the bursts of displacement's amplitudes  $\xi$  is plotted for 3 different forces ( $\diamond F_1$ ,  $\square F_2$  and  $\triangle F_3$ ) and compared to ( $\bullet$ ) the long-range correlation length  $\xi_4$ , revealed from the dynamics of the grains without the intruder. The dotted and solid curves are guiding the eye like  $\varepsilon^{-1}$ .

jamming transition, suggesting a critical behavior and thereby ensuring the self-consistency of the above scaling analysis. This critical behavior is well described by:

$$\theta(\varepsilon) \propto \theta_E(\varepsilon) \propto \varepsilon^{-\eta}, \quad (7)$$

$$\xi(\varepsilon) \propto \Upsilon(\varepsilon) \propto \varepsilon^{-\nu}, \quad (8)$$

where  $\eta \simeq -2/3$  and  $\nu \simeq -1$  also satisfy the relation  $\eta = \nu.z$ .

Altogether the above analysis provides strong evidences of a critical behavior of the intruder motion at the jamming transition, enforcing the first evidences of dynamical criticality reported in [1]. Figure 11 reports the lengthscale  $\xi$  measured here for the three different dragging forces, together with the dynamical correlation length  $\xi_4$ , which is the correlation length of the local density relaxations, and which was computed in [1]. The authors reported a dependence of  $\xi_4$  with the distance to jamming compatible with  $\xi_4 \sim \varepsilon^{-1/2}$ , however it can not really be discriminated from  $\xi_4 \sim \varepsilon^{-1}$ , as reported in the present work for the lengthscale  $\xi$ . Indeed, the fits of  $\xi$  and  $\xi_4$  both give a typical 95% confidence interval with a width of  $\pm 0.6$  on the exponent  $\nu$ . The fact that both lengthscales behave in a similar way at the transition suggests a fluctuation-dissipation-like relation between the non-linear response studied here and dynamical heterogeneities, as recently discussed in the context of Mode Coupling Theory [24]. In the following we discuss our results as compared to other microrheological studies in dense systems of particles, and try to precise the kind of criticality we are facing at jamming.

## V. DISCUSSION AND CONCLUDING REMARKS

We have experimentally studied the motion of an intruder dragged into an amorphous monolayer of horizontally vibrated grains at high packing fractions. A first “fluidization” transition separates a continuous motion regime, where the force-velocity relation is affine, from an intermittent motion one, where the force-velocity relation is clearly stiffer. The force threshold increases with the packing fraction and seemingly diverges at the jamming transition defined as the packing fraction where the pressure goes to zero in the absence of vibration. Below this threshold the intruder motion is intermittent. We have reported the existence of a second transition, where the fluctuations associated with this intermittent motion exhibit a critical behavior. This evidence is supported by the analysis of the motion of the probe but also by that of the surrounding grains. The bursting events are characterized by increasingly heterogeneous patterns in the instantaneous displacement field around the intruder and an increasingly spreading redistribution of the free volume.

Several other experimental, numerical and theoretical investigations of the response of a locally driven particle in a dense system report similar observations. Our aim here is to discuss similarities and differences among these studies, in an attempt to shed some light on sometime apparently controversial results. To our knowledge the first measurements were conducted in colloidal suspensions [5]. At low packing fractions, the authors report a linear force-velocity relation. At higher packing fraction, but *below* the glass transition a yield stress  $F_0$  develops below which the probe remains trapped. For larger forces, the probe is delocalized by the applied force, the bead is pulled with a fluctuating velocity and a non-linear force-velocity relation holds. As emphasized by the authors themselves, the existence of a force threshold below the glass transition, where the spontaneous fluctuations alone still allow the particles to escapes their cages and relax, is rather intriguing. Indeed, in a recent work [25], the force-velocity relation in dense suspensions has been investigated theoretically in the context of Mode Coupling Theory and compared to some of the above experimental data [5] and to numerical simulations of a slightly polydisperse quasi-hard-sphere system undergoing strongly damped Newtonian dynamics. This time a force threshold is predicted to delocalize the probe particle *above* the glass transition. Below the glass transition a strongly non-linear force-velocity relation is predicted and reported in the simulations. This steep dependence of the velocity on the applied force could explain the above observation of a threshold in an experiment where the lower resolution on the velocity is always finite.

Recent simulations consider the motion of a single probe particle driven with a constant force in a binary mixture of two-dimensional disks with stiff spring repulsive interactions at zero temperature. [20, 26]. As the

packing fraction is increased towards jamming, the average velocity of the probe particle decreases and the velocity fluctuations show an increasingly intermittent or avalanche-like behavior. The velocity distributions are exponential away from jamming and have a power law character when approaching it within less than one percent. These observations are very similar to those reported in the present study. The averaged velocity dependence on the packing fraction exhibits the same faster than exponential decrease when approaching jamming and the power-law character of the velocity distributions close to jamming are identical. However the authors report the existence of a critical threshold force that must be applied for the probe particle to move through the sample, which increases when increasing the packing fraction *above* jamming, whereas we never observed a complete arrest of our probe. In the simulations, once the probe stops, it cannot move any more because there is no temperature. In the present experiments the vibration allows the system to explore new force chains configurations and thereby to provide the intruder new opportunities of moving. As a final remark on the force-velocity relation, we would like to emphasize that the affine relation, which we observe above threshold when the motion is continuous, is not to be confused with the linear response of Stoke’s law. On the contrary, we believe that our observations correspond to the highest force regime reported in [25], where the non-linear response ultimately recovers a linear behavior.

An important difference between our system and the systems described above is that we are dealing with frictional particles. The role of friction close to jamming is an important issue. Recent important progress have been made in this matter [27–29], but many open questions remain unsolved. The isostatic criteria for mechanical stability  $z = 2d$  valid for frictionless systems *a priori* turns into a double inequality  $d + 1 < z < 2d$  in the presence of friction, suggesting that friction could blur the critical character of jamming reported in frictionless systems. It was suggested in [20] that the absence of power-law behavior in the velocity distribution observed in [17] might indeed be an effect of friction. Our observations clearly demonstrate on the contrary that the jamming transition remains critical in the presence of friction. Such a result suggests the existence of a generalized isostaticity criteria for frictional systems as proposed recently [29].

Not only the intruder motion exhibits the strongest intermittency at jamming, but also the statistics of the bursts obey critical scalings. The later are reminiscent of many other phenomena such as earthquakes [30], Barkhausen noise [23], crack tips dynamics in heterogeneous materials [31], generically assimilated to the so-called *crackling noise* [22]. It is also a distinct behavior of various random failure and load redistribution models [32], which can be used to describe stress redistribution in stick-slip granular experiments [33]. These similarities, even at some quantitative level – see in table I a comparison of some of the exponents obtained in dif-

System [Ref.]	$1 + \alpha$	$1 + \beta$	$z$
Here	$\sim 3/2$	$\sim 1/3$	$\sim 2/3$
Barkhausen noise [23]	1.5 - 2.3	1.24 - 1.77	$1/2 - 2/3$
Crack tips [34–38]	1.2 - 1.9	1.47 - 1.51	/
Stick skip (grains) [39–41]	1.8 - 2.1	1.67 - 1.94	/

TABLE I: Comparison of the critical exponents for several systems displaying “crackling noise”-like signals.

ferent systems – should not hide important differences among these phenomena even at the conceptual level. First the kind of criticality reported here has little to do with self organized criticality, often associated with crackling noise observations [22]. Second in many situations, an external parameter is increased (i.e. the loading force, the magnetic field) and the system fails once it has overcome some randomly distributed threshold. *A contrario* in the present situation, the dragging force is kept constant, the system is vibrated and it explores successive configurations. To what extent the study of these different dynamics are complementary is an interesting issue. Further investigations with an intruder dragged at constant velocity should provide interesting clues in this direction.

Altogether, investigating the motion of a probe dragged at constant force in a dense granular media, we have identified a force threshold diverging at the jamming transition, below which the motion of the probe is intermittent and exhibits criticality at jamming. More generally, we believe that micro and macro-rheological studies combined to statistical observations such as dynamical correlations are key elements to further investigate the underlying mechanisms of the jamming transition in frictional systems.

### Acknowledgments

We would like to thank L. Ponsou, E. Bouchaud, D. Bonamy, S. Aumaitre for helpful discussions, B. Dubrulle and M. Bonetti for clever advises on fractal dimensions computation, and F. Paradis, B. Saint-Yves and C. Coulais for their helpful hands when running the experiment and analysing the data. We also thank V. Padilla and C. Gasquet for technical assistance on the experiment. This work was supported by ANR DYNHET 07-BLAN-0157-01.

- [1] F. Lechenault, O. Dauchot, G. Biroli, and J. Bouchaud, *Europhysics Letters* **83**, 46003 (2008).
- [2] A. Liu and S. Nagel, *Nature* **396**, 21 (1998).
- [3] C. O'Hern, S. Langer, A. Liu, and S. Nagel, *Phys. Rev. Lett.* **88**, 75507 (2002).
- [4] C. O'Hern, L. Silbert, A. Liu, and S. Nagel, *Phys. Rev. E* **68**, 11306 (2003).
- [5] P. Habdas, D. Schaar, A. Levitt, and E. Weeks, *Europhysics Letters* **67**, 477 (2004).
- [6] S. Khan, C. Schnepper, and R. Armstrong, *Journal of Rheology* **32**, 69 (1988).
- [7] J. Brujic, P. Wang, G. Marty, C. Song, C. Briscoe, and H. Makse, *Phys. Rev. Lett.* **98**, 248001 (2007).
- [8] G. MiDi, *The European Physical Journal E-Soft Matter* **14**, 341 (2004).
- [9] T. Majmudar, M. Sperl, S. Luding, and R. Behringer, *Phys. Rev. Lett.* **98**, 058001 (2007), URL [doi:10.1103/PhysRevLett.98.058001](https://doi.org/10.1103/PhysRevLett.98.058001).
- [10] M. Hastings, C. Olson Reichhardt, and C. Reichhardt, *Physical Review Letters* **90**, 98302 (2003).
- [11] W. Ellenbroek, E. Somfai, M. van Hecke, and W. van Saarloos, *Phys. Rev. Lett.* **97**, 258001 (2006).
- [12] N. Xu and C. O'Hern, *Phys. Rev. E* **73**, 61303 (2006).
- [13] T. Waigh, *Reports on Progress in Physics* **68**, 685 (2005).
- [14] B. Dollet, F. Elias, C. Quilliet, C. Raufaste, M. Aubouy, and F. Graner, *Physical Review E* **71**, 31403 (2005).
- [15] R. Albert, M. A. Pfeifer, A.-L. Barabási, and P. Schiffer, *Phys. Rev. Lett.* **82**, 205 (1999).
- [16] O. Zik, J. Stavans, and Y. Rabin, *EPL (Europhysics Letters)* **17**, 315 (1992).
- [17] J. Geng and R. P. Behringer, *Phys. Rev. E* **71**, 011302 (2005).
- [18] É. Kolb, J. Cviklinski, J. Lanuza, P. Claudin, and É. Clément, *Physical Review E (Statistical, Nonlinear, and Soft Matter Physics)* **69**, 031306 (pages 5) (2004), URL <http://link.aps.org/abstract/PRE/v69/e031306>.
- [19] R. Candelier and O. Dauchot, *PRL (Physical Review Letters)* (2009).
- [20] C. J. O. Reichhardt and C. Reichhardt, *Fluctuations, jamming, and yielding for a driven probe particle in disordered disk assemblies* (2009).
- [21] B. Kaye, *A Random Walk Through Fractal Dimensions* (VCH, 1989).
- [22] J. Sethna, K. Dahmen, and C. Myers, *Nature* **410**, 242 (2001).
- [23] *The Science of Hysteresis* pp. 181–267 (2006).
- [24] M. Tarzia, G. Biroli, J.-P. Bouchaud, and A. Lefevre, *Anomalous non-linear response of glassy liquids: general arguments and a mode-coupling approach* (2008), URL <http://www.citebase.org/abstract?id=oai:arXiv.org:0812.3514>.
- [25] I. Gazuz, A. M. Puertas, and M. Fuchs, *Physical Review Letters* **102**, 248302+ (2009).
- [26] J. Drocco, M. Hastings, C. Reichhardt, and C. Reichhardt, *Phys. Rev. Lett.* **95**, 88001 (2005).
- [27] E. Somfai, M. van Hecke, W. Ellenbroek, K. Shundyak, and W. van Saarloos, *Phys. Rev. E* **75**, 20301 (2007).
- [28] C. Song, P. Wang, and H. Makse, *Nature* **453**, 629 (2008).
- [29] S. Henkes, M. van Hecke, and W. van Saarloos, *Critical jamming of frictional grains in the generalized isotaticity picture* (2009), URL <http://www.citebase.org/abstract?id=oai:arXiv.org:0907.3451>.
- [30] B. Gutenberg and C. Richter, *Seismicity of the Earth and Associated Phenomena* (Princeton, 1954), 2nd ed.
- [31] K. J. rgen Må løy, S. Santucci, J. Schmittbuhl, and R. Toussaint, *Physical Review Letters* **96**, 045501 (pages 4) (2006), URL <http://link.aps.org/abstract/PRL/v96/e045501>.
- [32] P. Hemmer, A. Hansen, and S. Pradhan, *Modelling Critical and Catastrophic Phenomena in Geoscience* (Springer, 2006).
- [33] F. Dalton, F. Farrelly, A. Petri, L. Pietronero, L. Pitolli, and G. Pontuale, *Phys. Rev. Lett.* **95**, 138001 (2005).
- [34] D. Lockner, J. Byerlee, V. Kuksenko, A. Ponomarev, and A. Sidorin (1991).
- [35] P. Diodati, F. Marchesoni, and S. Piazza, *Phys. Rev. Lett.* **67**, 2239 (1991).
- [36] G. Cannelli, R. Cantelli, and F. Cordero, *Phys. Rev. Lett.* **70**, 3923 (1993).
- [37] C. Maes, A. Van Moffaert, H. Frederix, and H. Strauven, *Phys. Rev. B* **57**, 4987 (1998).
- [38] A. Guarino, S. Ciliberto, A. Garcimartin, M. Zei, and R. Scorretti, *The European Physical Journal B* **26**, 141 (2002).
- [39] F. Dalton and D. Corcoran, *Phys. Rev. E* **63**, 061312 (2001).
- [40] M. Bretz, R. Zaretski, S. Field, N. Mitarai, and F. Nori, *Europhysics Letters* **74**, 1116 (2006).
- [41] J. Feder, H. Nordhagen, and W. A. Watters, [arXiv:nlin/0504034v1](https://arxiv.org/abs/nlin/0504034v1).
- [42] Laguerre's tessellation is similar to Delaunay's, but power distances are used instead of distances in order to take polydispersity into account.
- [43] The averaging windows are rectangles that start at the position of the intruder, with a height of 10 diameters of small grains and the maximal possible length
- [44] Given a random variable  $x$ , if the distribution of  $x$  is a power law with a cut-off  $b$ , *i.e.* of the form  $\rho(x) = x^{-1+a} f(x/b)$ , the average value of  $x$  is :  $\langle x \rangle = b \times \frac{\int_0^{+\infty} u^{-a} f(u) du}{\int_0^{+\infty} u^{-(1+a)} f(u) du} = b \times cst$ . One can therefore reproduce the evolution of the cut-offs as a function of the packing fraction by taking the experimental averages.

### 3.3 Toward jamming

Up to now, we have been more interested in *unjamming* protocols than in *jamming* protocols, and essentially little is known on the ways followed by the system when it reaches states beyond jamming. What happens in the long aging phases observed during the preparation protocol? How does the energy landscape evolve as the packing fraction increases and how does it influence the dynamics? Another question with both a practical and a conceptual importance would be to know if we can reach the same jammed configurations with a much faster protocol.

In this section, our aim is to trigger further analysis of assemblies of grains increasingly confined toward jamming. One first attempt was to study the relaxation during aging, but it didn't led to conclusive results. In yet another protocol, in which the assembly of grains is brought up to a certain packing fraction and then reorganized, we will see that the relaxation shows an interesting scaling.

#### 3.3.1 Aging

In this protocol, we study the dynamics of the grains while the packing fraction is stepwise increased. Since the force measured at the wall relaxes slower and slower, the acquisition times have to be increased accordingly. We have performed 8 steps from  $\phi = 0.8404$  to  $\phi = 0.8456$  with 10,000 to 71,000 oscillations.

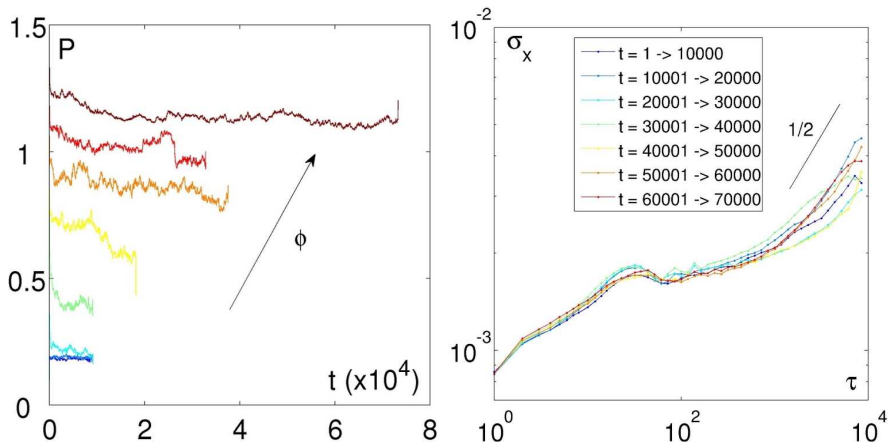


Figure 3.17: **Left** Pressure signals for 8 steps of increasing packing fraction. Time is expressed in number of oscillations of the bottom plate. The signals are smoothed with a 50 oscillations averaging window. **Right** Root mean square displacement in the  $x$ -direction,  $\sigma_x(\tau)$ , in function of the probing lag time  $\tau$  for several starting times. The packing fraction is  $\phi = 0.8456$ , corresponding to the highest curve in the left figure.

The force signals are shown in fig. 3.17-left. When the packing fraction increases, the force signal decays in a characteristic time that evolves sharply. Rapidly, the system is not able to relax in the experimental times scales.

Given those weakly decaying force signals, it is unclear whether we can measure aging in the dynamics or not. In fact, the root mean square displacements of the grains in one direction in a lag time  $\tau$ , defined from a starting time  $t_w$ :

$$\sigma_x(t_w, \tau) = \sqrt{\langle \Delta x(t_w, t_w + \tau)^2 \rangle_p} \quad (3.17)$$

are equivalent for several starting times  $t_w$  at the same packing fraction in all our data (*e.g.* see fig. 3.17 right for the highest packing fraction). One can see the characteristic plateau at the intermediate time lags, followed by the diffusive regime with a slope 1/2. The time scale at which diffusion is recovered is indistinguishable in all our curves.

This led us to the conclusion that even though the assembly of grains in the ascending steps seem to be in a non stationary state it is experimentally quite difficult to characterize these aging effects in the dynamics of the particles. The relaxation should have a long enough characteristic time scale so that we can perform some statistical analysis but still reasonable to be explored in an experiment.

If we had to design a new protocol, we would acquire much less images in a much longer experimental time. This should let us explore the dynamics of the looser packings, from the moment where the piston moves and the force increases to the moment where the force comes back to its lower value. However, it seems that in the densest states the time needed to entirely relax increases sharply – and may become infinite – such that no aging experiment will ever probe this decay, at least with this apparatus.

### 3.3.2 The “parachutist” protocol

So far, we have been using only protocols in which we increase stepwise the packing fraction and let the pressure relax. Imagine now that we can “parachute” the system *directly* in a dense state. The way the system relaxes could give us some precious information, different from those obtained by the stepwise protocols.

**Protocol.** A few protocols can be tried in order to do this. One is to realize a quench, *i.e.* perform directly a large increment with the piston. This is unfortunately not possible with our apparatus, since we are certain to reach a state where the force sensor will break, if not the entire apparatus. Another way to parachute the system is to stir the grains once the desired packing fraction has been reached. The *parachutist protocol* is therefore the following: we bring the system up to a certain packing fraction following

the usual stepwise protocol, then we stop the vibration, stir the grains, and start the vibration again while measuring the pressure at the wall.

**Results.** Our first observation is that it is not possible to stir the system above a certain packing fraction, namely  $\phi_{max} \simeq 0.8404$ . When we bring the system above  $\phi_{max}$  with the stepwise protocol and try to stir the grains, the forces amongst them increase extremely fast and everything blocks.

On the inset of figure 3.18-left, one can see the relaxation of the force at the walls after four stirs at different packing fractions. It turns out that they follow an exponential decay:

$$P = P_0.e^{-\frac{t}{\tau_{stir}}} \quad (3.18)$$

All the curves for the 16 acquisitions we have done collapse, as shown in fig. 3.18-left. The signal eventually reaches some ground value for the loosest packing fractions, where it leaves the exponential relaxation.

Fig. 3.18-right shows the evolution of  $\tau_{stir}$  as a function of  $\phi$ : it grows sharply close to  $\phi_J$ . Two fits have been performed. First a power-law fit

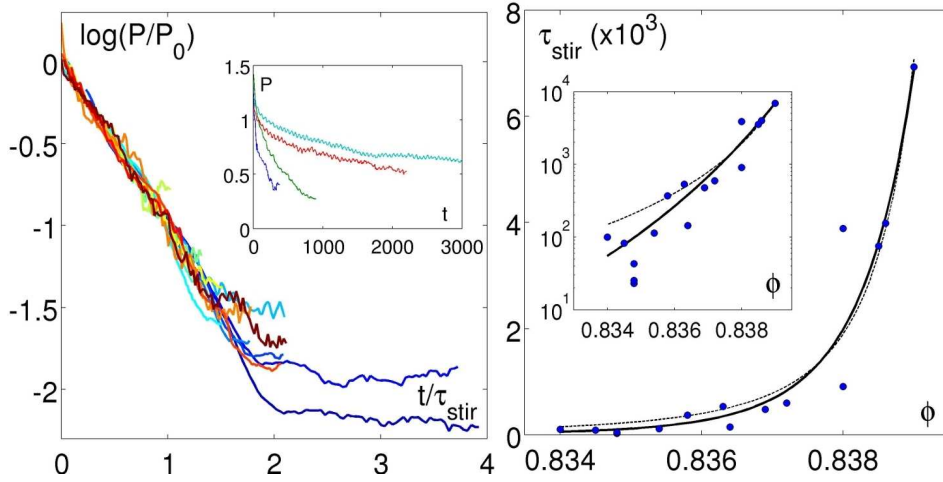


Figure 3.18: **Left** Relaxation of the pressure signal after stirring, when the vibration is restored, for 16 realizations at different packing fractions from 0.8340 to 0.8390. The time is divided by the typical decay time  $\tau_{stir}$  and the pressure is divided by its initial value  $P_0$ . **Inset** Raw signals  $P(t)$  for four different packing fractions:  $\phi = 0.8358$  (blue), 0.8372 (green), 0.8386 (red) and 0.8390 (lightblue). Time is in number of oscillations of the bottom plate. **Right** Typical decay time  $\tau_{stir}(\phi)$  against the packing fractions  $\phi$  at which the stirs have been realized. Time is in number of oscillations. VFT (solid) and power-law (dotted) fits are added. The system is still far from jamming since  $\phi_J$  is expected at  $\sim 0.845$ . **Inset** Same in log-lin.

(dotted curve) of the form:

$$\tau_{stir}(\phi) \sim (\phi_0 - \phi)^{-\alpha} \quad (3.19)$$

gives  $\alpha = 2.77$  and  $\phi_0 = 0.8406 \sim \phi_{max}$ . This fit does not describe well the data at the lowest packing fractions, and the fact that we find  $\phi_0 \sim \phi_{max}$  suggests that the parameters of the fit are driven by the highest values of the data set. This is easily confirmed by fitting the data without the five highest points: the exponent changes to  $\alpha = 4.43$  and  $\phi_0$  moves to 0.849, indicating that the fit is not robust.

So we have performed a second fit, this time with a Vogel-Fulcher-Tamman (VFT - solid curve) law:

$$\tau_{stir}(\phi) \sim \exp\left(\frac{D\phi_0}{\phi - \phi_0}\right) \quad (3.20)$$

with  $D = 0.25$  and  $\phi_0 = 0.8516 \sim \phi_J$ . If one performs the same fit on the data set without the five highest values, one finds  $D = 0.26$  and  $\phi_0 = 0.8545$ , which is a more stable behavior. However, note that the data are quite distant from  $\phi_J$ , such that no unambiguous conclusion can be drawn from this fit.

**Discussion.** A physical picture due to Goldstein [114] is that close to the glass transition the system explores only a part of its configuration space. The exponential relaxation of the pressure reported in fig. 3.18-left is interesting since the energy landscapes at different packing fractions have no reason *a priori* to be similar, neither the different regions of the landscape at a given packing fraction. The fact that the curves collapse suggests that the way the landscape is explored is similar (*i*) in all regions of phase space and (*ii*) for different packing fractions, the only relevant parameter being the typical relation time  $\tau_{stir}(\phi)$ .

Can we say more on the ability the system has to navigate into the configuration space? We can consider 2 arguments:

1. First, the rearrangements involving many particles become harder and harder as the packing fraction increases, due of the lack of available room, so the barriers between local minimums become higher and higher<sup>6</sup>.
2. Second, we know that for hard particles some configurations are impossible due to steric repulsion. When the number of particles is low, the number of these forbidden configurations is negligible compared to the total number of configurations. But as the system becomes denser

---

<sup>6</sup>Eventually, there may be a point where some infinite barriers collapse and separate the phase space in several distinct regions.

and denser, the relative number of forbidden states increases, up to some point where no configuration remains possible anymore.

Putting these considerations altogether, we can sketch the evolution of the energy landscape and imagine the path of our system in this moving landscape (see fig. 3.19)<sup>7</sup>.

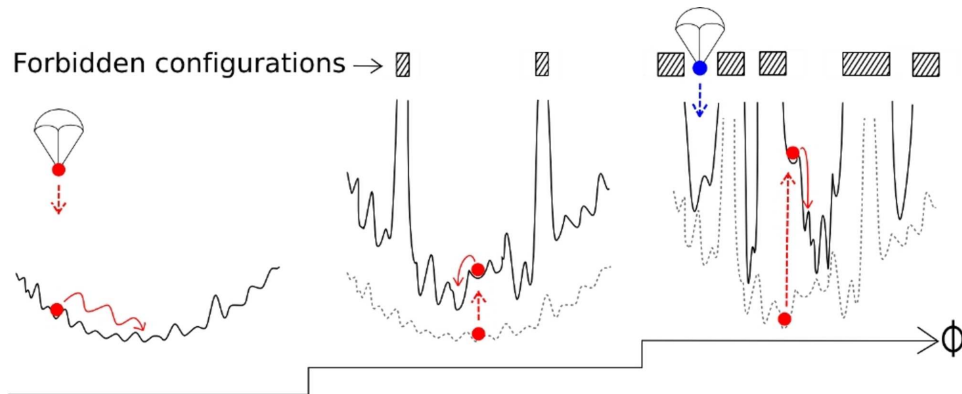


Figure 3.19: Cartoon view of the stepwise protocols in the energy landscape. **Left** The system (red dot) is dropped somewhere in the energy landscape, and is free to evolve. **Middle** An increment of packing fraction is done. The landscape changes, and the system relaxes. Some configurations become impossible. **Right** Another increment of packing fraction is done. More and more configurations become impossible. The blue dot represents another run where the system is parachuted somewhere randomly.

This sketch is without a doubt purely speculative. Nevertheless, it explains how the system can benefit from the stepwise protocol to reach the densest states: as it explores the landscape and finds – or approaches – a local minimum during each step, and as the landscape is not completely changed during the increments, the system is already well-positioned to explore this new landscape *i.e.* close to the new nearest local minima. This is how the system can reach highly packed states.

On the contrary, if one tries to parachute the system somewhere at random with the stirring procedure, one has to find a path between the forbidden steps. The fact that this operation is not possible around  $\phi_{max}$  indicates that the relative number of forbidden configurations sharply increases in our tiny range of packing fraction.

Is it because the phase space separates into several regions? Or because the paths between regions become very narrow and one cannot find them

<sup>7</sup>Note that many dimensions are not shown, so even if the number of forbidden states increases, no prediction is made here *a priori* on the ability of the system to go from one state to another.

with a brutal stir? Is it because these regions are on the contrary well-separated and become smaller and smaller? Clearly, we are not able to answer these questions on the basis of the present observations.

### 3.4 Discussion and perspectives

#### A view on jamming in frictional systems

Here we attempt to summarize what is jamming in the vibrating experiment; we propose a view equivalent to the one presented in Lechenault's thesis [47], illustrated by the cartoon in fig. 3.20 representing a view of the configuration space of the system. In this scheme the different degrees of freedom are separated, the steric constraints being along the vertical axis and the frictional constraints being along the horizontal axis. The dark grey areas correspond to the regions accessible at constant pseudo-energy.

In this view the system would first undergo a *dynamical* transition at  $\phi_D$ , where barriers appear due to the reduction of the steric degrees of freedom. Those barriers are high enough to be uncrossable: in mean field approaches, where the real system is in the infinite dimension limit, the barriers are infinite. One then easily understands that on approach to  $\phi_D$  it becomes harder and harder for the system to navigate from one region to another as the paths get narrower.

At  $\phi_D$ , the different regions get disconnected and the system loses ergodicity. In real space, this would correspond to the fact that the structure cannot evolve anymore: grains have to interpenetrate to trigger a reorganization, even at large scale. This is coherent with the fact that the lengthscales of the displacements probed beyond  $\phi_D$  are very small.

According to this scenario, in our system the jamming transition would be different from this dynamical transition, and would happen for even

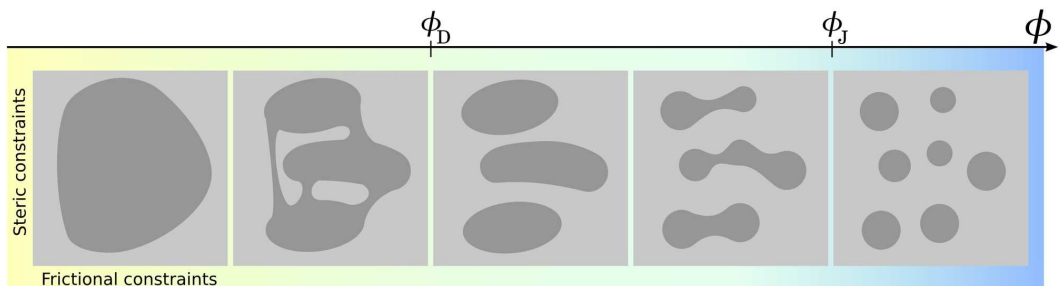


Figure 3.20: Cartoon view of the phase space of our frictional system as a function of the packing fraction. In this scheme the steric degrees of freedom are represented vertically and the frictional degrees of freedom are represented horizontally. See text for details.

denser packings where new barriers appear, this time due to the reduction of frictional degrees of freedom. In real space, this would correspond to the fact that the spatial fluctuations of coordination become noticeable as the density increases and that isostatic aggregates grow. These aggregates behave in a rigid manner: internal recasts are lost and the accessible configuration space shrinks. At very high packing fractions, accessible regions separate once again and the system remains trapped in one of these areas. In real space the force network percolates through the media, and a static pressure develops.

This description of our system of frictional grains is coherent with the observations of the non-monotonic behavior of the dynamical susceptibility close to  $\phi_J$ . One can also try to explain the phenomenology of the intruder's experiments within this framework: one can conjecture that the fluidisation transition we report when an intruder is dragged through the media corresponds to a reminiscence of the dynamical transition. Indeed, the system is able to cross higher barriers as the drag increases, shifting the phenomenology to higher pseudo-energy values or conversely to higher packing fractions. On the contrary, the fact that the jamming transition occurs at the same moment indicates that the barriers associated with the frictional degrees of freedom are much steeper, such that in the range of drags we used no difference is observed. An emerging feature is that, roughly whatever the way we study the system, the same underlying changes in the configurational landscape are probed. One can speculate that this is the reason why similar critical signatures have been observed even if we have been using very different protocols.

Note that in this above view, frictionless particles do not feel jamming. This would be coherent with the fact that no critical signature has yet been observed in simulations of frictionless spheres in the non-zero temperature case. An experiment with reduced friction, using lubricated grains for instance, could be an interesting investigation in this matter.

### Are we all intruders?

One of the guiding line in the study of the jamming phenomenology is to observe the response of the various systems to a perturbation. In linear response theory, one can relate the response of the order parameter to a small external excitation to the intrinsic fluctuations of this order parameter. In the present case, we have seen that the appropriate order parameter is already a dynamical quantity. Biroli and Bouchaud [115] have shown that following the same ideas, one can derive a lower bound for the dynamical susceptibility, and Lechenault *et al.* [81] have checked that this bound is tight in the experimental granular system.

In the present study, the intruder probes the instantaneous dynamics of the system, not the temporal correlations – at least not directly. Why do

we then obtain a signature of the transition? The answer lies in the fact that we are not probing a linear but rather a strongly non-linear regime. Bouchaud and Biroli [116] have indeed showed that the instantaneous non-linear response is an alternative way to extract dynamical lengthscales. This has been recently confirmed in a highly technical experiment in glycerol [32]. Our observations can be interpreted as a very crude realization of the same non-linear fluctuation-dissipation-like principle. So, finally, aren't all the particles in this granular system like a modest occasional intruder, unaware of being one, as soon as nonlinear effects are expected? These questions are of general interest, and further studies in this matter are in preparation, involving in particular a microrheological description.

### Local rheology

The acquisition of rigidity is intimately related to jamming, because of the isostaticity criterion and of several phenomenological evidences like the appearance of a yield stress or a delayed creep response. When a stress is applied, the material flows when it is far below jamming and breaks when it is jammed. What happens in the meanwhile? When does a viscous fluid becomes a fragile solid? Conventional rheology is a way to answer these questions by measuring the squishiness of materials: how viscous is a liquid, how elastic is a solid. But rheological measurements have several drawbacks, one of them being that it provides an *average* measurement of the bulk response, and therefore fails at describing local measurements in heterogeneous materials.

Microrheology can overcome this limitation. As a matter of fact there are two classes of microrheology techniques: *passive* microrheology measures the motion of the particles due to thermal or Brownian fluctuations; the work of Lechenault *et al.* on the statistics of the displacements under vibration was performed in this spirit. Here, we have followed a different approach with the application of a local stress, usually referred to as *active* microrheology. Actually, three modes of operation are available in active rheology measurements [117]: a viscometry measurement is obtained by applying constant force, a creep response is measured after the application of a pulse-like excitation, or a measure of the frequency dependent viscoelastic moduli can be performed in response to an oscillatory stress. To our knowledge, the last two techniques have not been employed so far on amorphous assemblies of frictional particles close to jamming. Some experiments by C. Coulais and O. Dauchot are in preparation, and will surely enforce our comprehension of jamming by providing connections between the macroscopic behavior of the materials and the local relaxations.

## Chapter 4

# Through the cooling glass

### Contents

---

4.1	State of the art . . . . .	115
4.2	The building blocks of dyn. heterogeneities . .	121
4.3	The fate of facilitation . . . . .	131
4.4	And what about real liquids? . . . . .	141
4.5	A few other ideas . . . . .	149
4.6	Discussion and perspectives . . . . .	166

---

*“In our country,” said Alice, still panting a little, “you’d generally get to somewhere else – if you ran very fast for a long time, as we’ve been doing.”*

*“A slow sort of country!” said the Queen.*

*“Now, here, you see, it takes all the running you can do, to keep in the same place.*

*If you want to get somewhere else, you must run at least twice as fast as that!”*

*– Lewis Carroll, Through the looking glass, and what Alice found there (1871)*

If, instead of a looking glass, Alice had made a journey through a cooling glass, she would have faced some different, but as intriguing time stretching phenomena. In order to illustrate this, let us imagine we bring Alice to visit a glass factory. Without using any mushroom she would surely feel very small compared to this impressive machinery: in a 9m-wide and 45m-long glass furnace, approximately 1200 tons of glass-former raw material are heated up to 1550°C. Once molten, the temperature of the glass is stabilized to ~ 1200°C and is fed into a 50m-long bath of molten tin. As the glass floats over the tin bath, the temperature is gradually reduced from 1200°C until the sheet can be lifted from the tin at approximately 600°C. – “What are these rollers for?” asked Alice. Well, they control the thickness and the width of the glass ribbon, and ... no, do not touch them! Well, you see, finally the glass is further cooled gradually, so that it anneals without strain, and is cut by machines. All the way down this huge cooling protocol, the rheologic properties of the glass change continuously. In particular, its viscosity strongly increases below ~ 600°C, making it sluggish and malleable. This property has been used from time immemorial to shape glass ...

– “But nobody really understands why.” the Queen interrupted, springing from nowhere.

– “What do you mean?” asked Alice. “When the glass cools down, it becomes a solid. It’s crystal clear.”

– “It’s glass clear!” the Queen bellowed. “Glass is not like other materials, because it is A-MOR-PHOUS. Consider, my dear, that the inner structure of the glass you call *solid* is in fact very much like that of a *liquid*. A liquid that does not flow.”

– “And why does not it flow, if the structure is the same?” Alice cautiously asked .

– “If I only knew! I would command liquids to self-contain themselves, and we would not have crockery problems anymore.” the Queen answered.

– “It reminds me of a mad tea party at Mr. Hatta’s ...” murmured Alice.

– “Excellent idea! Let’s go now and ask him. He is an expert in unsolvable problems.” said the Queen, while bringing Alice out.

– “But how can he solve problems if they are unsolvable?” said Alice before vanishing with the Queen.

Indeed, Alice, this is a very good question. Let’s now follow our own road to investigate more carefully and – we hope – more rationally, how glasses form.

Actually, the “glass transition” is a generic term referring to the dramatic slowdown one can observe in the dynamics of several amorphous systems when the temperature is lowered (*e.g.* silica or glycerol) or when they are compacted (*e.g.* gels, colloids, emulsions, granular materials). The strong phenomenological similarities between thermal and athermal systems is incidentally of huge practical importance, since some systems are easier to study depending on what one wants to probe.

This chapter starts with an extensive study of the cyclic shear experiment: we will first give a summary of the well-established features for this experimental device and of the dynamics of granular materials close to the glass transition in general. Then, instead of directly addressing the question of *Why* does the dynamics of such systems dramatically slow down, we can start with the question of *How*. This will be addressed in two sections, whose results are contained into articles. Next, the study of a liquid of softly interacting particles will give some insights into the possible structural origin of the relaxations. A short section will then summarize a few other attempts to link the structure and the dynamics, and finally we will give a general discussion and open some perspectives.

## 4.1 State of the art

### 4.1.1 The granulo-utopia

Granular materials and colloids are convenient experimental systems to probe directly spatio-temporal correlations since one can quite easily track a large amount of particles. In  $3D$ , up to the impressive number of 380,000 spheres can be localized with X-ray tomography techniques [118], but the dynamics is hardly accessible on a broad range of time scales. In colloids, thousands of particles can be tracked for a long time with confocal microscopy techniques; although the scanning times of the samples are not a limitation as long as one wants to characterize the long-term relaxations (like it is usually done), they may become problematic when one tries to understand the microscopic origin of the relaxations.

In the case of  $2D$  grains, one can track all of them with the spatial and temporal accuracy of modern cameras. This gives access to the precise inner structure of the packings and their evolution on a broad range of time scales. Even if experimental accuracy is always limited, this brings the available knowledge on these experimental systems closer to what can be probed numerically, and in particular the microscopic origin of the dynamical heterogeneities in the late relaxation or the link between dynamics and structure.

In the introduction chapter, we have just touched upon the microscopic interpretation of the dynamical slowdown. We have not mentioned yet that – probably dreaming of this “granular utopia”<sup>1</sup> – Guillaume Marty has made several attempts to characterize the dynamics at a microscopic level during his thesis [20], and that this work led to the first direct experimental evidence of the dynamical heterogeneities in dense granular medias [40]. Let us recall in this section the main results obtained by Guillaume Marty on the cyclic shear experiment, and take this opportunity to cite other works in various systems that exhibit the very same phenomenology.

### 4.1.2 A glassy dynamics

**Cages.** When one looks at the trajectories of the particles in the cyclic shear experiment, like the one plotted in fig. 4.1-left, one immediately notices that the particles can spend long times in the same regions of space, and sometimes hop from one region to another.

This effect has been evidenced in numerous other systems. For instance, Pouliquen *et al.* [34] have observed in a  $3D$  shearing cell filled with grains “fluctuating motion characterized by ball-like regions”, as shown in the close-up on the middle panel of fig. 4.1.

---

<sup>1</sup>The cyclic shear experiment has indeed been enshrined “Granulotopia”.

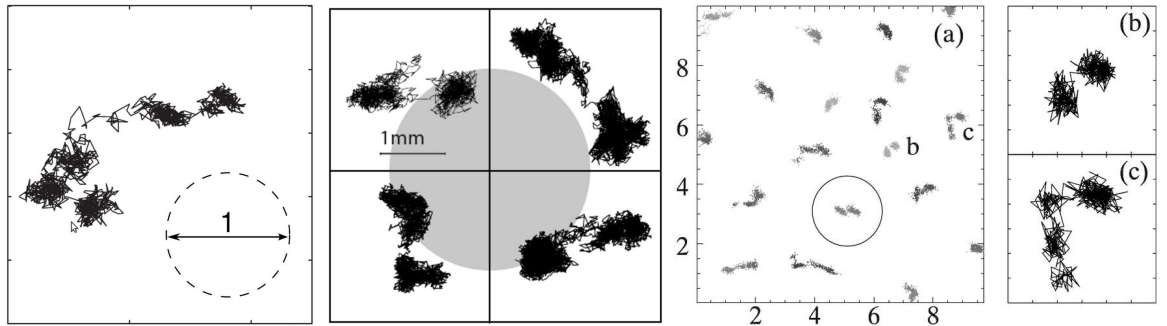


Figure 4.1: Illustrations of the cage effect. **Left** Trajectory of a small particle over 1500 cycles in the cyclic shear experiment. The dashed disk has the diameter of the particle. From Marty [20]. **Middle** Trajectories plotted for time slots between 2500 and 5000 cycles in the experiment of Pouliquen *et al.* The grey disk has the diameter of a bead. From Pouliquen *et al.* [34]. **Right** Trajectories of colloidal particles within a  $2.5 \mu\text{m}$  thick region from a sample with  $\phi = 0.52$ , over a 2 h period. The axes are in  $\mu\text{m}$ , and the circle illustrates the particle size. From Weeks *et al.* [33]. Magnification of the trajectories of two particles denoted (b) and (c) are represented at the extreme right.

Why is it so? Simply because when the packing is dense enough the grains are blocked by their neighbors, and cannot move as freely as in a granular gas for instance. Each particle remains trapped at the same position, until it can make a cage jump. This effect is hence called *the cage effect*.

In colloids, the same behavior had been previously reported by Weeks *et al.* [33]. We reproduce in fig. 4.1-right the trajectories that are so-commented by the authors: “[the] particles alternate between being trapped in a local cage, and a slight jump to a new location when the cage rearranges. Note that the jump distances are typically shorter than the particle radius; this is not a projection effect.”

Its is indeed commonly observed that the cage jump amplitudes are significantly shorter than a particle diameter. This implies that the neighboring relationships among the particles remain most of the time unchanged.

**Displacement statistics.** Coming back to the cyclic shear experiment, one can look at the statistics of the displacements. Let us call:

$$\Delta x_t(\tau) = x(t + \tau) - x(t) \quad (4.1)$$

the displacement along the  $x$ -direction between  $t$  and  $t + \tau$ , and the root mean square displacement over the lag time  $\tau$ :

$$\sigma_x(\tau) = \langle \Delta x_t^2(\tau) \rangle_t^{1/2} \quad (4.2)$$

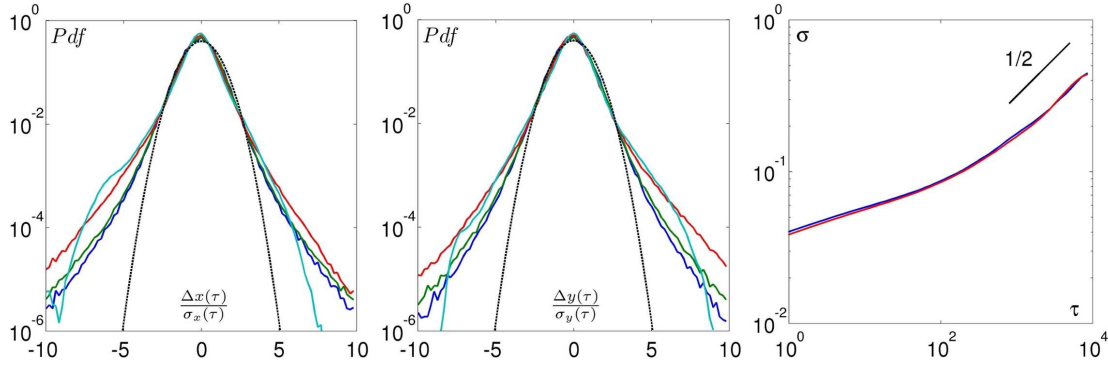


Figure 4.2: **Left** and **middle**: Probability distribution functions of the displacements along the direction of the shear ( $x$ -axis, left) and perpendicularly to the shear ( $y$ -axis, middle) divided by the corresponding root mean square displacement, for log-spaced probing time scales namely  $\tau = 1$  ( $\blacktriangledown$ ), 10 ( $\blacktriangledown$ ), 100 ( $\blacktriangledown$ ) and 1000 ( $\blacktriangledown$ ). **Right** Root mean square displacements  $\sigma_x$  (blue) and  $\sigma_y$  (red) as functions of the probing lag time  $\tau$ . The 1/2 slope, corresponding to the diffusive behavior, is asymptotically reached.

The Pdf of the displacements along both directions over a few lag times, averaged over all the particles and times and divided by the corresponding root mean square displacements are represented on the two left panels of fig. 4.2.

One immediately notices that the Pdf are strikingly similar along the direction parallel to the shear and perpendicular to the shear. The root mean square displacements along both directions, shown on the right-side of fig. 4.2, are also identical for all values of  $\tau$ . This indicates that despite the strongly anisotropic forcing, the motion of the particles is isotropic, at every time scales. In all the following, we will therefore assume the isotropy of the displacements<sup>2</sup>.

On top of the displacement distributions, the unit Gaussian are shown for comparison. Clearly, at all time scales the distributions deviate significantly from the Gaussian with overpopulated tails, which are responsible for an intermittent dynamics. Guillaume Marty has shown that these distributions display a stronger non-Gaussianity parameter at intermediate times scales, an effect that will be reworded below in terms of dynamical heterogeneities.

<sup>2</sup>Note that though the isotropy of the displacements in the center of the shearing cell at all time scales is well established, the isotropy of the force network is not demonstrated so far.

**Root mean square displacements and cages** One can compare the root mean square displacement (RMSD) curves obtained by Guillaume Marty represented in fig. 4.2-right to the ones obtained in other systems. In fig. 4.3, three other examples of RMSD or MSD are shown, taken from a simulation, a colloidal assembly and a granular system. The heterogeneous nature of the forcing does not allow one to directly compare the time scales, but the same general behavior is observed, namely:

- A ballistic regime at very short timescales, below the typical collision time. This regime is lacking in the cyclic shear experiment, since the collision time is meaningless in this apparatus: one cannot probe the stroboscoped dynamics below the cycle scale (by definition).
- A plateau at intermediate timescales, widening as the glass transition is approached (see for instance the bottom plot of fig. 4.3).
- The recovering of a diffusive regime on long timescales.

The apparition of the plateau can be easily related to the cage effect: as long as a particle is trapped by its neighbors it cannot diffuse freely in the media, and the slope of the RMSD remains below 1/2.

The recovering of a diffusive regime at long time scales indicates that the particles can still escape their cages, if one waits long enough. The crossover at the end of the plateau hence both points out a time and a length

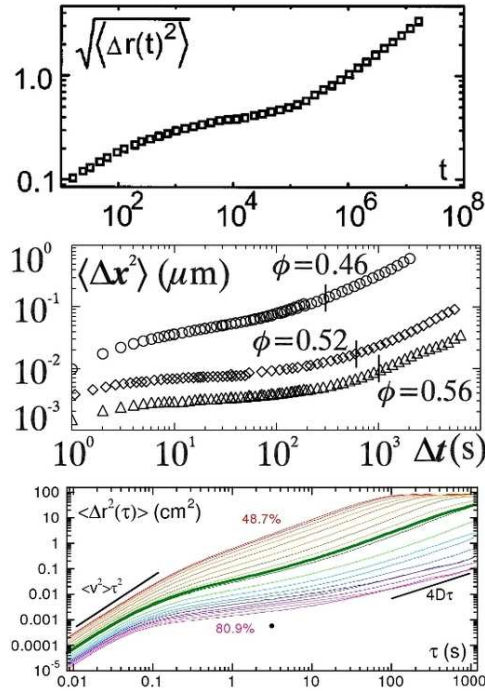


Figure 4.3: **Top** Evolution of the RMSD for polydisperse hard spheres simulated by a Monte-Carlo algorithm. Time is in Monte-Carlo steps. From Doliwa and Heuer [119]. **Center** MSD in colloids for 3 packing fractions close to the glass transition. From Weeks *et al.* [120]. **Bottom** MSD of the large grains in the fluidized bed experiment for several packing fractions from 0.487 (red) to 0.809 (pink). Black lines indicate the slopes expected in the ballistic and the diffusive regimes. From Abate and Durian [83].

scale: the typical timescale of the cage duration and the typical lengthscale of the jumps. Marty measured this cross-over and gave an estimation of the typical cage time<sup>3</sup> at  $\tau_{cage} \sim 300$ .

As can be seen on the bottom plots of fig. 4.3, the cross-over between the plateau and the diffusive regime drifts to the long times as the glass transition is approached. One can make a connection with the delaying late relaxation of the structure factor in supercooled liquids, since the plateau of the intermediate scattering function ends at the same time scale than the plateau of the RMSD (see for instance [119] for a direct comparison). However, although informative, the RMSD can not distinguish uniform from heterogeneous dynamics, and one needs further characterizations to unveil the heterogeneous dynamics.

### 4.1.3 Dynamical heterogeneities

In the same spirit, Dauchot *et al.* [40] have measured the structure factor  $F_s(k, \tau)$  as defined in eq.(1.6). It is shown in fig. 4.4-left as a function of the probing lag time  $\tau$  for different values of the wave-vector  $k$ . Consistently with the lack of ballistic regime on the MSD curves, the early  $\beta$ -relaxation is not present. One immediately notices the growth of a plateau for the small values of the wave-vector, the signature of the slow relaxation. Note also that the curves are well described by stretched exponentials (black curves) at all  $k$ , as in usual glass formers.

The authors suggest that this slow relaxation is due to dynamical heterogeneities, and compute the corresponding dynamical susceptibility:

$$\chi_4^{F_s} = N \langle [F_s(k, \tau) - \langle F_s(k, \tau) \rangle]^2 \rangle \quad (4.3)$$

The results are shown in the right side of fig. 4.4 and exhibit two effects: first a peak appears at each value of the wave-vector, simply telling that for each length scale there exists a time scale for which the spatial heterogeneity is maximal, corresponding to the moment where half the system has decorrelated. Second, an overall maximum indicates specific time and length scales at which the dynamical heterogeneities are maximal<sup>4</sup>.

In addition, the authors have measured the spatial correlator  $G_4(r, \tau)$  as defined in eq.(1.8) and found that – for probing time and length parameters close to the ones leading to the strongest dynamical heterogeneities – this

---

<sup>3</sup>This is not an accurate definition of the cage time though, because the cross-over is quite large in general. In addition, the standard deviation is much more sensitive to the bigger displacements than to the small ones, which makes the RMSD take off at the time scale when the first cage jumps occur. This leads to an underestimated value of the typical cage durations, as we shall see in the following.

<sup>4</sup>This plot is indeed the analogous of the “banana” plot defined in appendix B.2. Note that the length scale  $a^*$  for which the dynamical heterogeneities are maximal is of the order of  $10^{-1}$  here and cannot be compared to the values measured in the vibrating experiment close to jamming, as reported in 3.1.1.

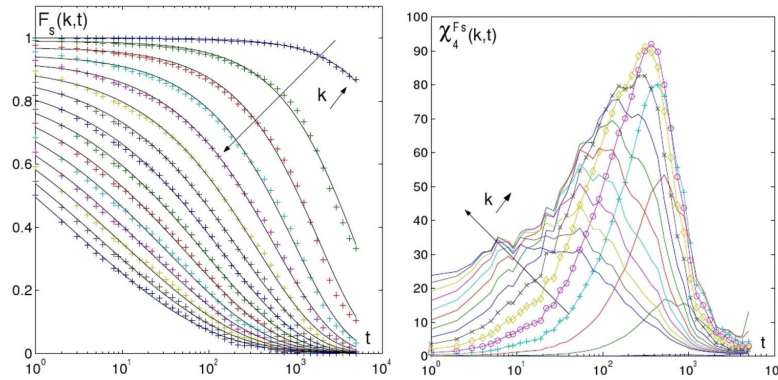


Figure 4.4: **Left**  $F_s(k,t)$  as a function of time for different odd values of the wave-vector  $k = 1, 3, \dots, 29$  from top to bottom (as indicated by the arrow and the increasing  $k \nearrow$ ). The black lines are fits of the form  $\exp[-(t/\tau(k))^{\beta(k)}]$ . **Right**  $\chi_4^{F_s}$  for the same values of  $k$ . Adapted from Dauchot *et al.* [40].

function decays with a characteristic length scale of  $\xi_4 \sim 7$  grain diameters. This characteristic length is in good agreement with the amplitude of the  $\chi_4$ , which indicates the typical size of the decorrelation patterns in number of grains. Spatially, these decorrelation patterns have tortuous shapes like the currents depicted in fig. 4.5.

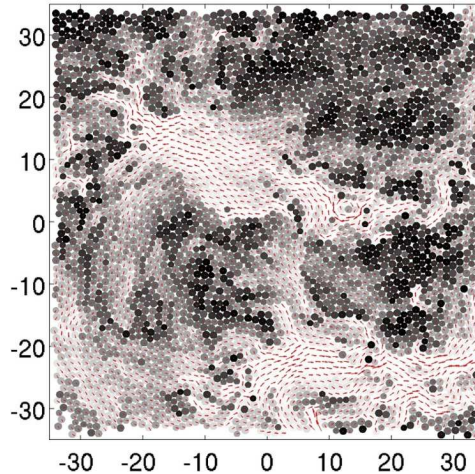


Figure 4.5: Dynamical heterogeneities in the cyclic shear experiment. The  $3\times$  magnified displacement field is shown with red arrows. Fast particles are drawn in lighter grey, revealing large decorrelation areas containing roughly  $\chi_4^{max} \sim 100$  particles.

## 4.2 The building blocks of dynamical heterogeneities

An open question in the glass community is to unveil the underlying mechanisms leading to dynamical heterogeneities, and several models have been developed to address this issue [121, 39, 26, 115, 122]. It has been suggested [33] that the dynamical heterogeneities are intimately linked with the cage effect, but no precise mechanism has been proposed so far, and some questions call for clarification. For instance, cage jumps are defined at the single particle scale and one needs to explicit a *cooperation* mechanism to explain the spatial extension of dynamical heterogeneities. In addition, several time scales are at play, such as the cage time, the jump time<sup>5</sup>, the diffusion recovering time and the time at which dynamical heterogeneities are maximal. How do they organize? We have seen that dynamical heterogeneities are maximal when probed on certain length and time scales, the latter being rather long. How are large decorrelation patterns built up during this timescale?

At this point, the microscopic mechanisms at play during cage escapes deserve a short discussion. Let us start with some general arguments and then present our cage separation algorithm. Knowing the cage jumps “times and places” will enable us in the following to build a scenario for the bloom of dynamical heterogeneities based upon experimental evidence.

### 4.2.1 More on cage Jumps

**General arguments** We not discuss in more details the nature of cage jumps. To give a definition, one can simply say that they are a succession of moves in the same direction<sup>6</sup>, in contrast with the cage which can be seen as a sequence of vibrations around “an equilibrium position”. Cage jumps are therefore *by definition* an irreversible set of correlated displacements changing the average position of a particle.

We would like to emphasize that a cage escape is not an event involving just one particle. In a granular gas of hard spheres a single particle can move without disturbing its neighbors; it is yet harder to imagine in a liquid of hard spheres, and at the packing fractions at which the cage jumps are usually observed, this type of motion is not possible anymore. One could imagine that cage jumps are the prerogative of some isolated rattling particles benefiting of some void in the packing. But this would not be coherent with the fact that the cages, defined as the trajectories between the jumps, last for a long time. In addition, jumps are occurring in any direction, while rattlers move back and forth along a given direction. Hence we can already

---

<sup>5</sup>Note that, as little is known about the distributions of these two times, their typical values may be as well ill-defined.

<sup>6</sup>Indeed, cage jumps are usually not strictly speaking instantaneous, and involve at least a few displacements.

deduce that cage escapes should be the individual manifestations of some *cooperative* events.

One can then accept the idea of cooperative motion but for an inappropriate reason, like the fact that it seems a plausible and efficient manner to create a void large enough to let some particles move freely. A simplistic model would be to assume that some of the neighbors move apart to “free” a trapped particle, the later being able to renew its neighborhood. This view is schemed on fig. 4.6.

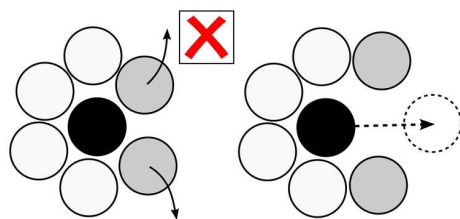


Figure 4.6: Schematic view of an unrealistic cage jumping mechanism: some neighboring particles move apart to free the central particle.

This is indeed an incorrect view for several reasons: *(i)* renewing the neighborhood requires large displacements, typically of the order of the particle diameter, while cage escapes occur on a length scale significantly below the typical size of the particles. *(ii)* When the packing is dense enough, no particle is able to move apart by itself. The scheme of fig. 4.6-left misses to take into account the surrounding particles, which would block the grey grains. *(iii)* The freed particle would have so much space that it would certainly become a rattler, which – as we have already argued – is not the case.

Another interesting remark is that if one single particle cannot move due to steric constraints, it seems at first sight even harder for a set of particles. But several cooperative movements are possible even when there is little space and high steric constraints. We have seen in chapter 3 that an intruder can move of several grain diameters even in a highly jammed structure! This costs huge reorganizations of the surrounding grains, however.

Actually, we can argue that on one hand the rotation of a disk-shaped set of particles should have a low energetic cost, as well as the string-like displacement of particles, which only requires a little space at the front of the string to make a potentially infinite number of grains move. Every reorganization pattern being more or less a composition of vortices and currents, one can figure out that several reorganizations with relatively low energy costs can operate. In other words, when one considers bigger and bigger sets of particles, the number of internal degrees of freedom increases, as well as the probability to find a low energy internal reorganization.

Experimental characterizations on how cage jumps occur will be given in the sequel: all our following analysis rests on the decomposition of trajectories into cages and the localization of the cage jumps. So let us now introduce our cage jump decomposition algorithm.

**Catching cages** Consider the trajectory shown in the left panel fig. 4.7-a); it is a portion of a trajectory taken from the cyclic shear experiment, with a total length of  $T = 6500$  cycles for this example, and for which three cages can be readily observed. Our jumping criterion is defined through the following time-dependent quantity:

$$\forall t \in [t_i, t_f], \quad \tilde{p}(t) = \left[ \langle d_1(t_2)^2 \rangle_{t_2 \in S_2} \cdot \langle d_2(t_1)^2 \rangle_{t_1 \in S_1} \right]^{1/2} \quad (4.4)$$

where  $S_1 = \{t_i; t\}$  and  $S_2 = \{t; t_f\}$  are the two subsets of points before and after time  $t$ ,  $d_i(t_j)$  stands for the Euclidian distance of the position at  $t_j$  to the center of mass of the subset  $S_i$ , and  $\langle \cdot \rangle_{t_j \in S_j}$  denotes an average over the subset  $S_j$ .  $\tilde{p}(t)$  is therefore the product of the root mean square distances between all the points of the subsets to the barycenter of the *other* subset.

How does this quantity pinpoint cage jumps? If there were no cage jump in the trajectory, the barycenters of the two subsets would always be close to each other and to the global center of mass, leading to a roughly constant  $\tilde{p}(t) \simeq \sigma_c^2$  where  $\sigma_c$  is the size of the cage. If there is a cage jump,  $\tilde{p}(t)$  grows above  $\sigma_c^2$  and peaks when the centers of mass are best separated, defining the cage jump.

The main weakness of this quantity is that it relies on the fact that the equilibrium position is well-defined by the barycenter, *i.e.* that there are enough points in each subset. This is not always the case, especially when close to the bounds  $t_i$  and  $t_f$ . To illustrate this, we have shown  $\tilde{p}(t)$  as the green curve in the right panel of fig. 4.7-a): one can see the peaks corresponding to the cage jumps in the center of the interval, but spurious bursts show up at the bounds. To eliminate them, we consider:

$$\forall t \in [t_i; t_f], \quad p(t) = \xi(t) \cdot \tilde{p}(t) \quad \text{with} \quad \xi(t) = \frac{2[(t_f - t)(t - t_i)]^{1/2}}{t_f - t_i} \quad (4.5)$$

where  $\xi(t)$  is a shape function that counterweights the lack of statistics in the subsets. The resulting quantity  $p(t)$  clearly exhibits two peaks corresponding to the cage jumps.

Then, the algorithm consists of an iterative procedure, illustrated on fig. 4.7. A branch stops as soon as no value stands above the threshold  $p_{th} = \sigma_{C0}^2$ ;  $\sigma_{C0}$  is the length scale of the cross-over in the RMSD curves, naturally pointing out the lower bound of the jump amplitudes. Here are the following steps:

- a) The whole trajectory is taken into account. As the global maximum of  $p(t)$  is above  $p_{th}$ , a cage jump is set at  $t_1^j$  (marked with a small red dot). The trajectory is cut in two pieces, analyzed separately in b) and c).
- b) The trajectory of interest is limited at  $[t_i; t_1^j]$ . The secondary peak of a) is now the global maximum: another cage jump is found at  $t_2^j$  (marked with a small red dot), generating the two new branches d) and e). 

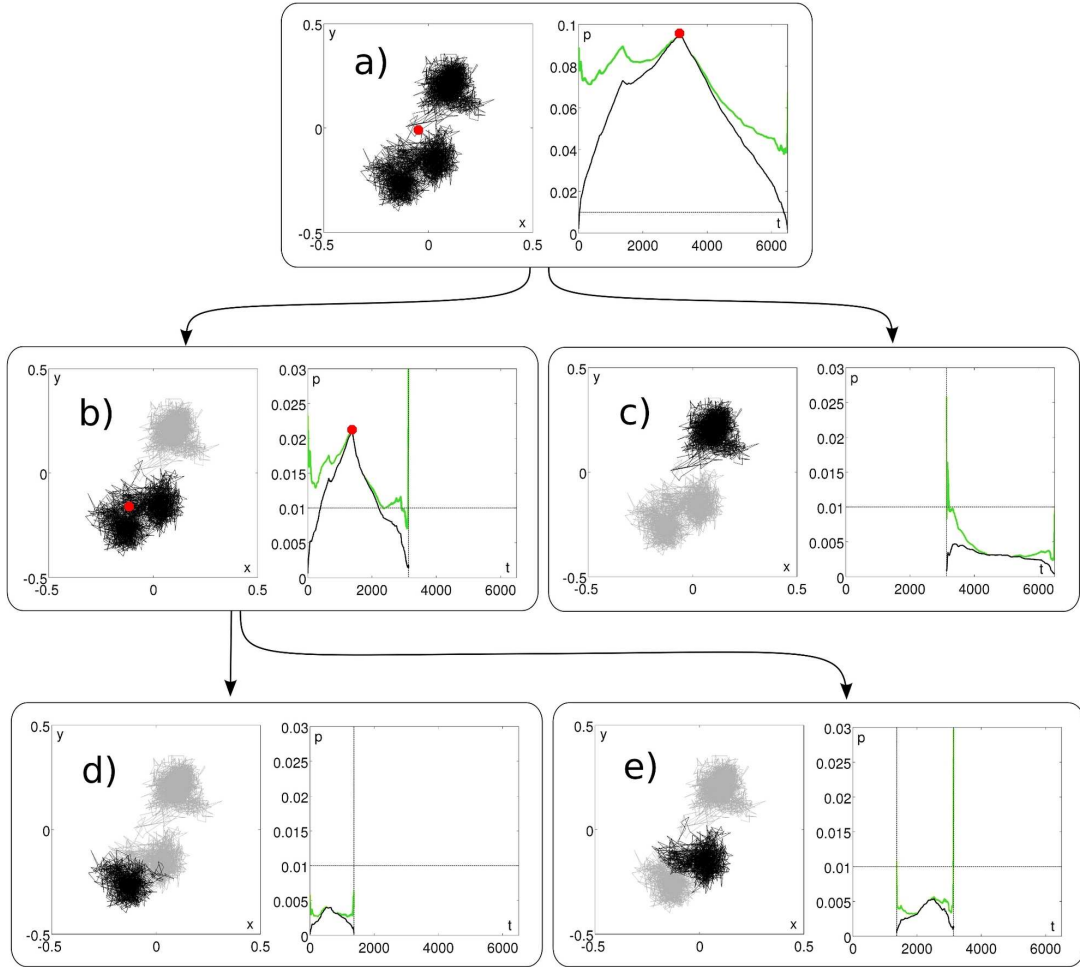


Figure 4.7: The cage detection algorithm, applied on a trajectory of the cyclic shear experiment. *a-e*) represent the same quantities at different steps. In each: **Left** Whole trajectory (grey) and sub-trajectory of interest at this step (black). If a jump is found, a red dot marks its location. **Right**  $p(t)$  in the sub-trajectory of interest (black curve) as a function of  $t$ . The quantity  $\tilde{p}(t) = p(t)/\zeta(t)$  is shown in green for comparison. The threshold level  $p_{th}$  of the algorithm is the horizontal dotted line, here at  $10^{-2}$ . If a cage jump is found, a red dot indicates its location.

- c) The trajectory of interest is  $[t_1^j; t_f]$ . As  $\forall(t), p(t) < p_{th}$  no cage jump is found and the branch stops.
- d) The trajectory of interest is  $[t_i; t_2^j]$ . No cage jump is found and the branch stops.
- e) The trajectory of interest is  $[t_2^j; t_1^j]$ . No cage jump is found and the branch

stops.

This algorithm is robust: we have checked that it leads to equivalent results when one inputs only a piece of trajectory, at least for the cage jumps that are not very close to the boundaries.

More generally, we can ask the question of the relevance of the results. The ratio between the typical *jump size*  $\delta$  and the typical *cage size*  $\sigma$  (see definition in fig. 4.8-left) has a determinant role, since one can hardly detect the cage jumps if their amplitudes are very small compared to the fluctuations around the equilibrium position.

To precise this, let us consider the case where these fluctuations are Gaussian. In this case, the value of the maximum  $\tilde{p}_m$  can be easily calculated, and one finds:

$$\tilde{p}_m = 2\sigma^2 + \delta^2 \quad \text{such that} \quad \tilde{p}_m/\sigma^2 = 2 + \left(\frac{\delta}{\sigma}\right)^2 \quad (4.6)$$

We can then *a posteriori* compute the average jump size  $\delta$  and cage size  $\sigma$  for all the studied data sets. The distributions of these quantities are roughly

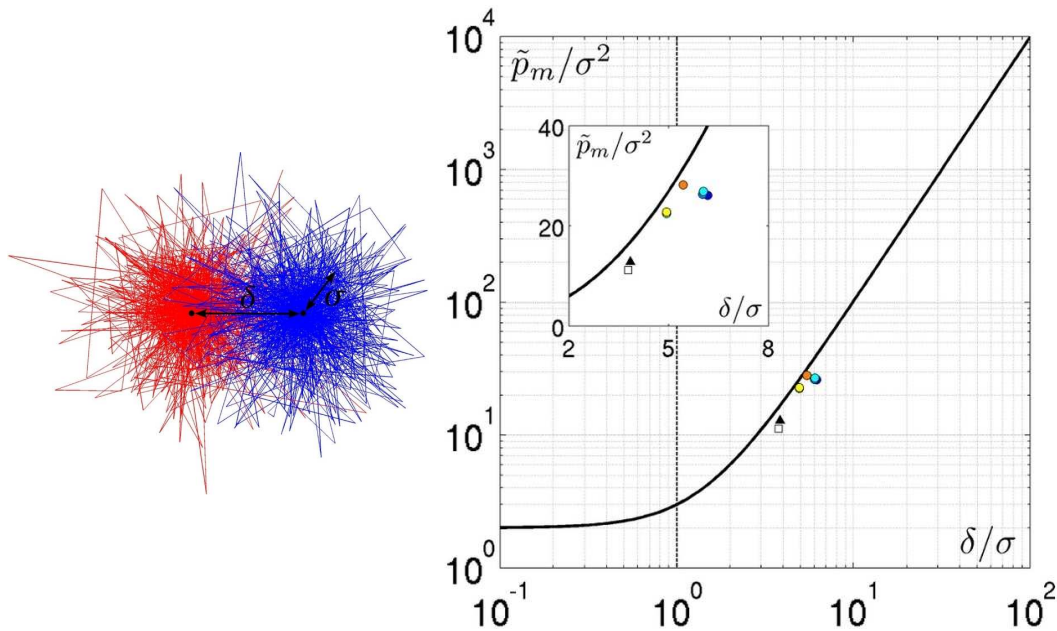


Figure 4.8: **Left** Definition of the jump size  $\delta$  and the cage size  $\sigma$  on a piece of trajectory. **Right** Comparison of  $\tilde{p}_m/\sigma^2$  as a function of  $\delta/\sigma$  for all the studied data sets: the cyclic shear experiment ( $\square$ ), the glass former simulation ( $\blacktriangle$ ) and the 6 densest states of the fluidized bed experiment, from  $\phi = 0.758$  (blue) to 0.802 (red). The analytical curve proposed in 4.6 is displayed for comparison. **Inset** Same in *lin – lin*, zoomed.

$\chi_2$ -distributed, validating the Gaussian approximation for  $\sigma$ . One can see in fig. 4.8-right that the ratio  $\delta/\sigma$  is clearly greater than one and that the data stand close to the black curve, which validates the decomposition. Since this is an *a posteriori* verification, it cannot be the only indicator of the success of the decomposition algorithm, and other checks have to be performed: (i) eye-checking of  $\sim 1\%$  of the trajectories, and coherence with the following observation, namely (ii) the correlation between the density field relaxation and the binarized fact that particles jump and (iii) the formation of clusters of neighboring cage jumps *at the same time*.

### 4.2.2 Results

Our first results with this technique are presented in the next few pages in an article format. This Letter has been published in *Physical Review Letters* (see [35] for precise references).

As a summary, we introduce our caging algorithm and apply it on the data of the cyclic shear experiment. We show that dynamical heterogeneities result from a two time scale process: on one hand there are cooperative events consisting of cage jumps clustered within a very short time scale, and on another hand, on larger time scales, such clusters appear aggregated both temporally and spatially in avalanches. These avalanches build up the large scales dynamical heterogeneities. In addition, we compute the local distance to affinity introduced by Falk and Langer [123] and show that the clusters of cooperative cage jumps are responsible for most of the nonaffine displacements<sup>7</sup>.

---

<sup>7</sup>See B.1.3 for a detailed calculus.

## Building Blocks of Dynamical Heterogeneities in Dense Granular Media

R. Candelier,<sup>1</sup> O. Dauchot,<sup>1</sup> and G. Biroli<sup>2</sup>

<sup>1</sup>CEA SPEC, CNRS URA 2464, F-91191 Gif-sur-Yvette, France

<sup>2</sup>Institut de Physique Théorique, CEA, IPhT, F-91191 Gif-sur-Yvette, France, and CNRS, URA 2306, F-91191 Gif-sur-Yvette, France

(Received 2 November 2008; published 27 February 2009)

We investigate experimentally the connection between short time dynamics and long time dynamical heterogeneities within a dense granular media under cyclic shear. We show that dynamical heterogeneities result from a two time scales process. Short time but already collective events consisting in clustered cage jumps concentrate most of the nonaffine displacements. On larger time scales, such clusters appear aggregated both temporally and spatially in avalanches which eventually build the large scales dynamical heterogeneities. Our results indicate that facilitation plays an important role in the relaxation process although it does not appear to be conserved as proposed in many models studied in the literature.

DOI: 10.1103/PhysRevLett.102.088001

PACS numbers: 45.70.Mg, 45.70.Ht, 61.43.-j

Mechanically driven grains exhibit a dramatic slowing down of their dynamics when their volume fraction is increased above a certain value. This phenomenon, generically called jamming transition, shares a lot of experimental features with the glass transition and, indeed, it has been suggested that they are both governed by similar underlying physical mechanisms [1]. Whether such mechanisms originate from an ideal transition of any kind remains, however, a matter of debate [2–4]. One of the major recent advances in these fields has been the discovery of dynamic heterogeneity (DH). Experimental and numerical works have shown that the dynamics become increasingly correlated in space approaching the glass and the jamming transitions (see [5] for a recent review, and [6–10] more specifically for granular media). This clearly shows that the slowing down of the dynamics is related to a collective phenomenon, possibly to a true phase transition. Different theories have been developed in order to explain quantitatively this phenomenon. The crucial last missing piece consists in understanding what is the underlying mechanism leading to dynamic heterogeneity and, hence, responsible for the slow relaxation. Many different possible origins have been highlighted in the literature: dynamic facilitation [11], soft modes [12,13], proximity to a mode coupling transition [14,15], growing amorphous order [16,17], etc. At this stage, it is therefore crucial to perform detailed studies aimed at unveiling what are the building blocks of DH.

The aim of this Letter is to perform such a type of analysis for a granular system close to its jamming transition. Our starting point consists in identifying the elementary irreversible relaxation processes that we shall call cage jumps in reference to the well-known interpretation of the slowing down of the dynamics in terms of caging [5]. Our analysis shows that DH is the result of two processes taking place on different time scales. On short time scales, clustered cage jumps concentrate most of the nonaffine displacements. On larger time scales such clusters, that are already collective events, aggregate both temporally

and spatially in avalanches and ultimately build the large scales dynamical heterogeneities. We find that dynamic facilitation [11,18] clearly plays a major role in the development of the avalanche process, although it seems to be irrelevant in triggering it. A detailed discussion of our findings on the basis of the current theoretical literature is presented in the conclusion.

The experimental setup, the same as in [6,7], consists in a horizontal monolayer of about 8300 bi-disperse steel cylinders of diameter 5 and 6 mm in equal proportions quasistatically sheared at constant volume fraction  $\phi = 0.84$ . The shear is periodic, with an amplitude  $\theta_{\max} = \pm 5^\circ$ . A high resolution camera takes images each time the system is back to its initial position  $\theta = 0^\circ$ . Both the camera resolution and a better control of the lightening uniformity now allow the tracking of  $N = 4055$  grains in the center of the device without any loss. A typical experiment lasts 10 000 cycles. We choose the time unit to be one back and forth cycle, and the length unit to be the diameter of small particles. Redoing the same analysis, as in previous studies [6,7], we observe that: (i) the dynamics is isotropic, subdiffusive at short times, and diffusive at long times; subdiffusion stems from the trapping of the particles within cages of size  $\sigma_c = 0.1$ , a value slightly smaller than in [6,7], presumably because of small changes in packing fraction and/or shear amplitude; (ii) introducing

$$Q_{p,t}(a, \tau) = \exp\left(-\frac{\|\Delta\vec{r}_p(t, t + \tau)\|^2}{2a^2}\right), \quad (1)$$

where  $\Delta\vec{r}_p(t, t + \tau)$  is the displacement of the particle  $p$  between  $t$  and  $t + \tau$  and  $a$  is a probing length scale. The computation of the four points correlation function  $\chi_4(a, \tau) = N(\langle Q_t(a, \tau)^2 \rangle - \langle Q_t(a, \tau) \rangle^2)$ , where  $Q_t(a, \tau) = \frac{1}{N} \sum_p Q_{p,t}(a, \tau)$ , reveals that the dynamical correlation length is maximal for  $\tau^* = 720$  and  $a^* = 0.15$ .

In the present study, we first segment the trajectories in separated cages introducing a novel algorithm. Consider a trajectory  $S(t)_{t \in [0, T]}$  on a total time  $T$  and split it at an

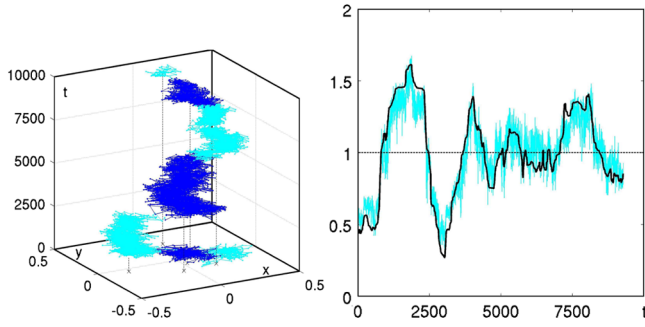


FIG. 1 (color online). Left: 3D visualization of the trajectory of a single particle. The color changes every time the algorithm detects a cage jump. Right: Comparison between the relative averaged relaxation  $Q_t(a^*, \tau^*) / \langle Q_t \rangle$  (in gray/cyan areas) and the relative percentage  $P_t(\tau^*) / \langle P_t \rangle$  of particles that have not jumped between  $t$  and  $t + \tau^*$  (in dark areas),  $\tau^* = 720$ .

arbitrary cut time  $t_c$  into two sets of successive points:  $S_1$  for  $t_1 \in [0, t_c]$  and  $S_2$  for  $t_2 \in [t_c, T]$ . Then we measure how well separated are the two sets of points:

$$p(t_c) = \xi(t_c) [\langle d_1(t_2)^2 \rangle_{t_2 \in S_2} \langle d_2(t_1)^2 \rangle_{t_1 \in S_1}]^{1/2}, \quad (2)$$

where  $d_k(t_i)$  is the distance between the point at time  $t_i$  and the center of mass of the subset  $S_k$ . The average  $\langle \rangle_{S_k}$  is computed over the subset  $S_k$ .  $\xi(t_c) = \sqrt{t_c/T * (1 - t_c/T)}$ , the standard deviation of the number of steps in a given set for a uniformly distributed process is the natural normalization that eliminates the large fluctuations arising when  $t_c$  is too close to the bounds of  $[0, T]$ . We define a cage jump at  $t_c$  when  $p(t_c)$  is maximal. The procedure is then repeated iteratively for every subtrajectory until  $p_{\max}(t_c) < \sigma_c^2$ . The left-hand side of Fig. 1 illustrates how, using the above algorithm, we successfully segment the trajectories into cages separated by jumps. Cage jumps are defined within a resolution of 10 cycles. A direct and important observation is that the distribution of the time spent in each cage is exponential and characterized by an average ‘‘cage time’’  $\tau_c = 1160$ . For comparison,  $Q_t(a^*, \tau = 1000) \simeq 0.5$  [7]. This means that in average a particle jumps only once on the time scale over which  $Q_t(a^*, \tau)$  relaxes. The right-hand side of Fig. 1 displays the relative values of  $Q_t(a^*, \tau^*)$  together with  $P_t(\tau^*)$  the relative percentage of particles that have not jumped during  $\tau^*$ . The correlation is straightforward: the bursts of cage jumps caught by the algorithm are responsible for the major relaxation events of the system. Anticipating on the following, one can also check that the cage jumps detected by the algorithm are also exactly located in the areas where the decorrelation is maximal (compare Fig. 4 middle and right panels).

The left-hand side of Fig. 2 reveals that cage jumps occur intermittently both in space and time. There are very long intervals without a jump in a whole region of space separated by sudden and *collective* relaxation events. When clustering the cage jumps which are adjacent in space (neighboring particles) and time (separated by less than the jump resolution, i.e., 10 cycles) one can extract

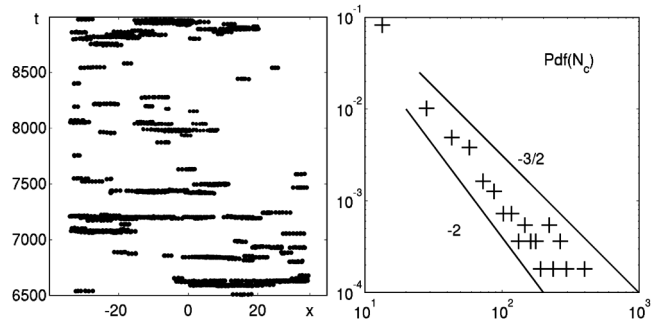


FIG. 2. Left: Spatiotemporal position of the cage jumps: only one direction in space is shown ( $x$  axis). Each point represents a cage jump. The very flat clouds of points are clusters of *collective* and *instantaneous* cage jumps. Right: Probability distribution of clusters sizes.

two important features. The duration of these clusters follows an exponential distribution with an average value which remains small, typically of the order of 10 cycles. On the contrary, cage jumps are not isolated in space: the cluster size distribution has very fat tails. In the regime of sizes experimentally available, it is well described by a power law  $\rho(N_c) \simeq N_c^{-\alpha}$ , where  $N_c$  is the number of grains within a cluster and  $\alpha \in [3/2, 2]$  (see the right-hand side of Fig. 2). Experimentally the average cluster size equals 18 and has a standard deviation of 34. We now compute the square difference between the actual local deformation around a grain  $i$ , and the one it would have if it were in a region of uniform strain  $\underline{\epsilon}$ :

$$D_i^2(t, \tau) = \sum_j [\tilde{r}_{ij}(t + \tau) - \underline{\epsilon} \cdot \tilde{r}_{ij}(t)]^2, \quad (3)$$

where the index  $j$  runs over the neighboring grains of reference grain  $i$  and  $\tilde{r}_{ij}(t) = \tilde{r}_j(t) - \tilde{r}_i(t)$ .  $\Delta_i^2(t, \tau) = \text{Min}_{\underline{\epsilon}}(D_i^2(t, \tau))$  is the local deviation from affine deformation during the time interval  $\tau$  (see [19] for details). We

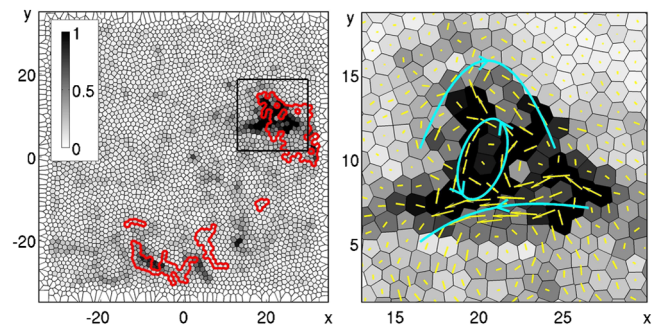


FIG. 3 (color online). Left: Clusters of cage jumps concentrate the highly nonaffine domains: the distance to affinity parameter  $\Delta(t, \tau)$  (in levels of gray) is compared to the location of clusters of collective cage jumps (with red boundaries) ( $\tau = 30$ ). Right: Zoom on a highly nonaffine region (box on the left figure). The displacements of the particles, magnified by a factor 2, are in light grey (yellow). For convenience, the main streams creating intense local shears are eye guided.

observe (Fig. 3) that the clusters of cage jumps concentrate the highly-nonaffine deformations and can be identified as the elementary irreversible events of the dynamics.

We shall now unveil how the above short term events build up large collective relaxation on long time scales. The heavy tails in the distribution of the cluster sizes (right-hand side of Fig. 2) suggests that the collective cage jumps aggregate into some kind of avalanche process: a first cluster triggers the apparition of successive bursts nearby shortly after, which in turn trigger other nearby bursts. Such avalanches would provide a natural mechanism for the formation of the long term dynamical heterogeneities, as we shall see now. The left-hand side of Fig. 4 compares the cumulative distribution ( $cPdf$ ) of the lag times between adjacent clusters (red circles) to that of independent events following a Poissonian process with the same average lag time (dark line). Both cumulative distributions intersect at a lag time corresponding precisely to the time scale of the dynamical heterogeneities  $\tau^*$ : compared to the Poissonian process, there is an excess of short lag times when  $\tau < \tau^*$ , i.e.,  $\text{Prob}(\text{lag} < \tau) = cPdf(\tau)$  is larger than for the Poissonian process, and an excess of large lag times when  $\tau > \tau^*$ , i.e.,  $\text{Prob}(\text{lag} > \tau) = 1 - cPdf(\tau)$  is again larger than for the Poissonian process, leading to an under representation of intermediate lag times. [Note that the Poissonian distribution computed from a randomly generated data set with the same cardinality and the same average (green squares) is identical to the analytical curve, excluding any finite size effect in the above observation.] In the inset, one can see the two lag time distributions corresponding to events separated by, respectively, less and more than  $\tau^*$ ; these exponential distributions reveal two very different typical decay times ( $\tau_s = 120$  and  $\tau_l = 1190$ ). This separation of times underlines the aggregation of the clusters of cage jumps into separated avalanches. The short time scale  $\tau_s$  corresponds

to the delay between two successive events within a given avalanche, whereas the long one  $\tau_l$  is the time separating two avalanches at a similar location.  $\tau_l$  nicely corresponds to the typical cage time of individual particles  $\tau_c = 1160$ , indicating that almost no particle jumps twice within the same avalanche. Spatially, we compute the distance between avalanches as the minimal distance between all the couples of clusters separated by a lag time less than  $2\tau_s$  and belonging to different avalanches. The minimal distance between avalanches points toward an average distance of 27 and a standard deviation of 14, indicating a clear spatial separation between avalanches. Also, the fractal dimension of clusters  $d_F$  gives a geometrical characterization of the structure of the dynamically correlated regions. Within the statistical accuracy,  $d_F$  increases from 1.3 towards 2 during the aggregation process. Thus, as in numerical studies on glass-forming liquids [20,21], we find that dynamically correlated regions become thicker on larger time scales. Finally, selecting a time interval of length  $\tau^*$ , initiated at the beginning of a given avalanche, Fig. 4 compares the spatial organization of the clusters in the avalanche and the local relaxation of the system as measured by the field  $Q_{p,i}(a^*, \tau^*)$ . The correspondence is very good: the aggregation of all the clusters within an avalanche is ultimately building a large decorrelation area, also seen on the correlation function  $Q_{p,i}(a^*, \tau^*)$ . More interestingly, each cluster in the middle panel of Fig. 4 is colored according to a color gradient corresponding to the time at which it occurs, thereby underlining the way a first cluster of cage jumps has given rise to successive neighboring clusters.

To summarize, we have identified a two time scales process that give rise to DH and is responsible for macroscopic relaxation. At short times, the particles collectively jump within clusters whose sizes are very largely distributed. These clustered jumps trigger other ones nearby within an avalanche process. The lifetime of such ava-

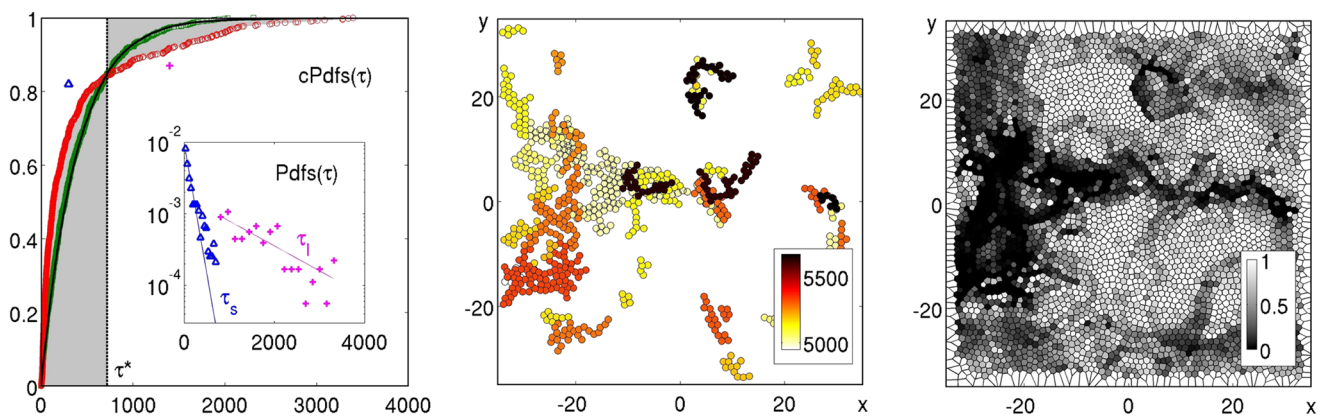


FIG. 4 (color online). Left: Cumulated probability distribution of the duration between spatially adjacent clusters. Experimental data are in red circles, while green squares stand for a set of equal cardinality generated from an exponential distribution with the same mean value. The black curve is the analytical version of this same distribution. The actual distribution and the exponential ones cross at the lag time  $\tau^* = 720$ . Inset: Distribution of the lags below  $\tau^*$  (blue triangles) and above (magenta crosses). Middle: Spatial location of successive clusters of cage jumps. Colors correspond to the time at which clusters occur. Right: Spatial field of the two point correlation function  $Q_{p,i}(a^*, \tau^*)$ .

lanches is much smaller than the time scale between two avalanches in a similar location or, analogously, between successive cage jumps of a given grain. DH are strongest on a time scale which corresponds to the crossover between these last two. It is interesting to discuss our results within the perspectives provided by current theoretical approaches. Dynamic facilitation (DF) is one mechanism put forward to explain slow and glassy dynamics. Theoretical approaches based on DF usually focus on kinetically constrained models [11,22,23]. They are characterized by a common mechanism leading to slow dynamics: relaxation is due to mobile facilitating regions that are rare and move slowly across the system. Here, we find a dynamics characterized by avalanches inside which clusters are facilitating each other. It is important to remark that the fraction of particles relaxing because of facilitation, i.e., belonging to a cluster but the first one (in time) of an avalanche, is close to 0.85. However, in our system facilitation is not conserved as in kinetically constrained models since the first cluster of an avalanche is far from any other possible facilitating region. Why then do particles jump in the first cluster of an avalanche? This is hardly a pure random event since it is already a collective phenomenon clustered in space and time. Promising candidates to explain it are the so-called soft modes or soft regions. It has been shown that for hard spheres close to jamming [12] and for moderately supercooled liquids [13] a significant fraction of the dynamical evolution takes place along the soft modes and dynamic heterogeneity is strongly correlated with the softest regions. One can then conjecture that the first clusters of avalanches correlate with the softest regions of the system. The resulting scenario is a mixture of the one based on soft modes and the one based on DF: dynamical evolution starts from the softest regions but then propagate on larger length scales by dynamic facilitation. Note that the relationship between these two pictures has also been discussed recently in an analysis of a kinetically constrained model [24]. Still, without having computed the soft modes in a frictional packing one cannot eliminate other possible (maybe complementary) mechanisms such as hopping between local minima in energy landscape [25]. It is also interesting to remark that the mode coupling theory of the glass transition is based on the emergence of soft modes and predicts [26], as we find, that dynamical correlated structures thicken in time. Obviously, all such conjectures call for further investigation. From the experimental point of view, one would like to identify the soft modes and check their correlation with the clusters we identified. Repeating the present study in simulations of glass-forming liquids would be certainly very instructive. One could check whether the building blocks of DH are the

same ones we identified for granular media. Finally, it would be interesting to know how the processes we identified evolved with density and, in particular, which of the DF and soft modes become more important when increasing the density.

We would like to thank J.P. Bouchaud, P. Harrowell, S. Aumaitre, F. Lechenault for helpful discussions as well as V. Padilla and C. Gasquet for technical assistance on the experiment.

- 
- [1] A. Liu and S. Nagel, *Nature (London)* **396**, 21 (1998).
  - [2] G. Biroli, *Nature Phys.* **3**, 222 (2007).
  - [3] R. Mari, F. Krzakala, and J. Kurchan, arXiv:0806.3665.
  - [4] L. Berthier and T. Witten, arXiv:0810.4405.
  - [5] L. Berthier and G. Biroli, *Encyclopedia of Complexity and Systems Science* (Springer, New York, 2008).
  - [6] G. Marty and O. Dauchot, *Phys. Rev. Lett.* **94**, 015701 (2005).
  - [7] O. Dauchot, G. Marty, and G. Biroli, *Phys. Rev. Lett.* **95**, 265701 (2005).
  - [8] A. Abate and D. Durian, *Phys. Rev. E* **74**, 031308 (2006).
  - [9] F. Lechenault, O. Dauchot, G. Biroli, and J.P. Bouchaud, *Europhys. Lett.* **83**, 46003 (2008).
  - [10] F. Lechenault, O. Dauchot, G. Biroli, and J.P. Bouchaud, *Europhys. Lett.* **83**, 46002 (2008).
  - [11] J.P. Garrahan and D. Chandler, *Phys. Rev. Lett.* **89**, 035704 (2002).
  - [12] C. Brito and M. Wyart, *J. Stat. Mech.* (2007) L08003.
  - [13] A. Widmer-Cooper, H. Perry, P. Harrowell, and D.R. Reichman, *Nature Phys.* **4**, 711 (2008).
  - [14] C. Donati, S. Franz, S. Glotzer, and G. Parisi, *J. Non-Cryst. Solids* **307**, 215 (2002).
  - [15] G. Biroli and J. Bouchaud, *Europhys. Lett.* **67**, 21 (2004).
  - [16] V. Lubchenko and P.G. Wolynes, *Annu. Rev. Phys. Chem.* **58**, 235(2007).
  - [17] G. Biroli, J.-P. Bouchaud, A. Cavagna, T. Grigera, and P. Verrocchio, *Nature Phys.* **4**, 771 (2008).
  - [18] G.H. Fredrickson and H.C. Andersen, *Phys. Rev. Lett.* **53**, 1244 (1984).
  - [19] M. Falk and J. Langer, *Phys. Rev. E* **57**, 7192 (1998).
  - [20] C. Donati, S. Glotzer, P. Poole, W. Kob, and S. Plimpton, *Phys. Rev. E* **60**, 3107 (1999).
  - [21] G. Appignanesi, J. Rodriguez Fris, R. Montani, and W. Kob, *Phys. Rev. Lett.* **96**, 057801 (2006).
  - [22] F. Ritort and P. Sollich, *Adv. Phys.* **52**, 219 (2003).
  - [23] C. Toninelli, G. Biroli, and D. Fisher, *Phys. Rev. Lett.* **96**, 035702 (2006).
  - [24] D.J. Ashton and J.P. Garrahan, arXiv:0808.2412.
  - [25] B. Doliwa and A. Heuer, *Phys. Rev. E* **67**, 031506 (2003).
  - [26] G. Biroli, J.-P. Bouchaud, K. Miyasaka, and D.R. Reichman, *Phys. Rev. Lett.* **97**, 195701 (2006).

### 4.3 Toward the glass transition: the fate of facilitation

Given this analysis, we would like now to investigate how strongly the presence of avalanching clusters of cage jumps depends (*i*) on the studied system and (*ii*) on the intensive parameters. To what extent do the preceding results depend on the fact that the system is made of frictional hard spheres? Is the described phenomenology a consequence of the cyclic shear forcing, or is it a broader feature going beyond the scope of our experiment? How does it evolve with the packing fraction?

We have already mentioned that the packing fraction cannot be tuned in our cyclic shear experiment. So, in order to answer the above questions we have treated the data of the fluidized bed experiment in the same way: this is indeed a different experimental setup in which the energy is directly injected in the bulk and not from the boundaries and, crucially, the dynamics of the particles is accessible at several packing fractions. Let us first recall briefly the previous results obtained by Keys *et al.* [84] for this system, and give a short discussion on the quality of the data sets before presenting our analysis.

**Previous results for the fluidized bed experiment.** Keys *et al.* [84] have measured the dynamical susceptibility in the fluidized bed experiment,

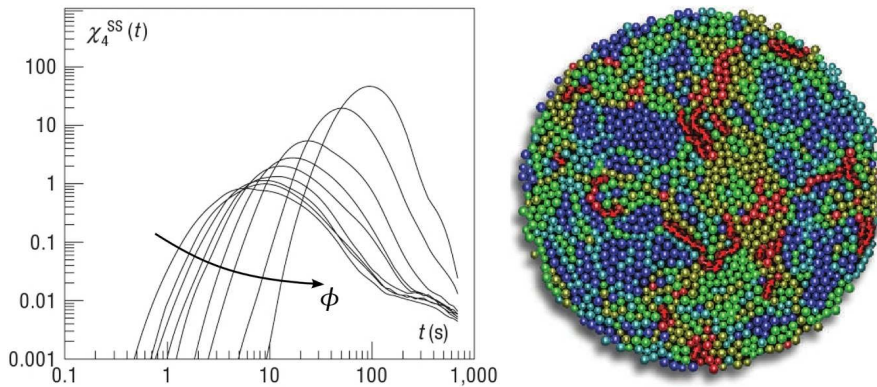


Figure 4.9: **Left** Self contribution to the four point susceptibility as a function of the time interval  $t$  for a sequence of area fractions in the fluidized bed experiment, from  $\phi = 0.587$  to  $0.807$ . **Right** An instantaneous bead configuration where the color of the beads indicates the mobility over a time interval corresponding to the timescale for both maximum cluster size and string length. The 10% most mobile beads are red, forming string-like clusters, and cooler colors correspond to slower particles.  $\phi = 0.773$ . From Keys *et al.* [84].

fixing the probing length scale to half the typical bead diameter and varying the packing fraction. The  $\chi_4$  for the self contribution to the structure factor displays the same peak as a function of the probing lag time, and the amplitude of the peak grows as  $\phi$  is increased, suggesting that the dynamical heterogeneities grow as the fluidized bed turns into a glass (see fig. 4.9-left).

The fact that the dynamics become increasingly correlated in space has also been reported in several other studies (see [6] for a review). Fig. 4.9-right shows the equivalent of a decorrelation map, on which one clearly sees that the dynamics is heterogeneous. The authors emphasize the fact that the faster clusters have string-like shapes.

**Discussion of the data of the fluidized bed experiment.** Since we will use some of the data stemming from the fluidized bed experiment (those reported in [84], and three denser runs of the same dataset), we would like to mention here two observations that we made when analyzing the data and were not mentioned in [84] though they need to be taken into account when treating the data. Let us recall that the system consists of a bidisperse mixture of steel beads rolling onto a sieve, the motion of which being excited with an upflow of air.

First, the sieve has an influence on the particles' dynamics. Typical trajectories of a single particle are shown in fig. 4.10.

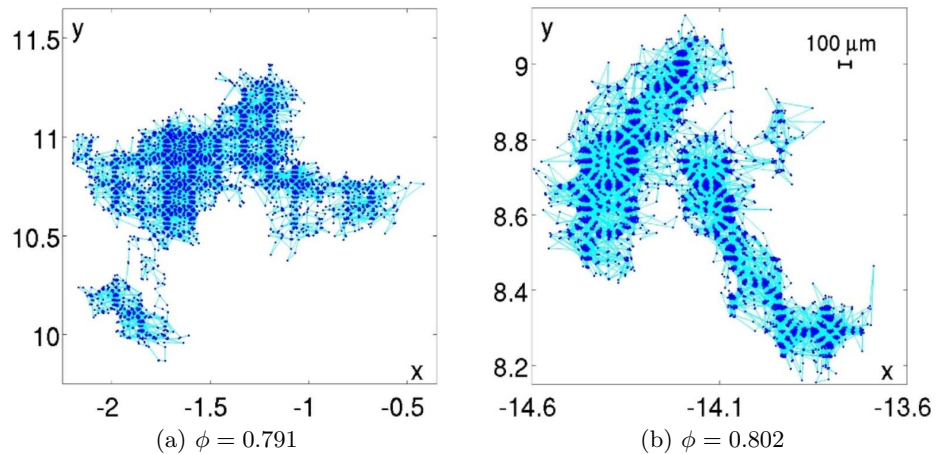


Figure 4.10: Trajectories of a single particle for 2 packing fractions. The positions of the particle are the dark blue dots.

The regular pattern one can observe on these images strikingly reminds the patterns of a regular sieve: the particles, instead of levitating above the sieve, are resting on it and are preferentially localized in the holes of the mesh. As a consequence the dynamics of the particles is rather like a succession of hops on a regular lattice than the motion of particles in a continuous space.

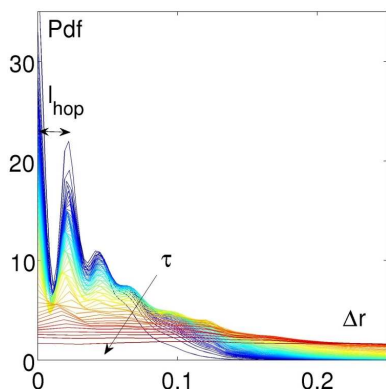


Figure 4.11: Pdf of the displacement's amplitudes  $\Delta r(\tau)$  for several lags  $\tau$  logarithmically spaced from 1 (blue) to 10,000 (red), at  $\phi = 0.802$ . The Pdf at short time scales is sensitive to the pair function of the mesh holes, and the typical size of a hop can be easily extracted.

From the trajectories of the particles, one can extract the Pdf of the displacements amplitudes probed over a lag time  $\tau$ :  $\Delta r(\tau) = \|\vec{r}(t+\tau) - \vec{r}(t)\|$  (see fig. 4.11), and measure the typical size of a hop,  $l_{hop}$ , induced by the mesh as the distance between the first two peaks. We find  $l_{hop} = 0.020$ , *i.e.*  $62 \mu\text{m}$ , which is coherent with the announced mesh size of  $100 \mu\text{m}$  given the fact that the sieve forms a complex polygonal lattice.

For the sake of the cage jump decomposition algorithm (which we will introduce next), this length is below all the cross-overs between the subdiffusive and diffusive regimes in the root mean square displacements curves, *i.e.* below the typical cage jump size, at every packing fraction (see fig. 4.14). Hence the influence of the mesh is limited to the displacements probed below a certain timescale (maximally  $\tau = 100$  for  $\phi = 0.802$ ), and will not interfere with the cage jump analysis.

The second point is that the trajectories of the particles exhibit large convection rolls over the course of the experiment (see fig.4.12). This kind of convection pattern is challenging to avoid experimentally in large and loose assemblies of grains. The main problem is that strong correlations in the dynamics due to this global movement could eventually hide the dynamical correlations due to the proximity to the glass transition.

From an empirical point of view, there are two ways to avoid these convection rolls. The first one is to have a small size system. For instance, when one compares the root mean square displacements curves given in [83] and in [84] (same experimental setup but different total number of particles), two very different behavior can be observed (see fig. 4.13). At first sight, both plots look very similar: for the short times a ballistic regime is observed, then the characteristic plateau at intermediate time scales and finally a diffusive regime on the longest time scales. But there is a major difference: in the small system, the diffusive regime on long time scale is nicely recovering a slope of 1, whereas in the large system the regime after the plateau is clearly more than diffusive, the slope being around 1.5 as illustrated in fig. 4.13-bottom and fig. 4.14. This is due to the presence of convection. Unfortunately, the computation of the four point correlation function *must*

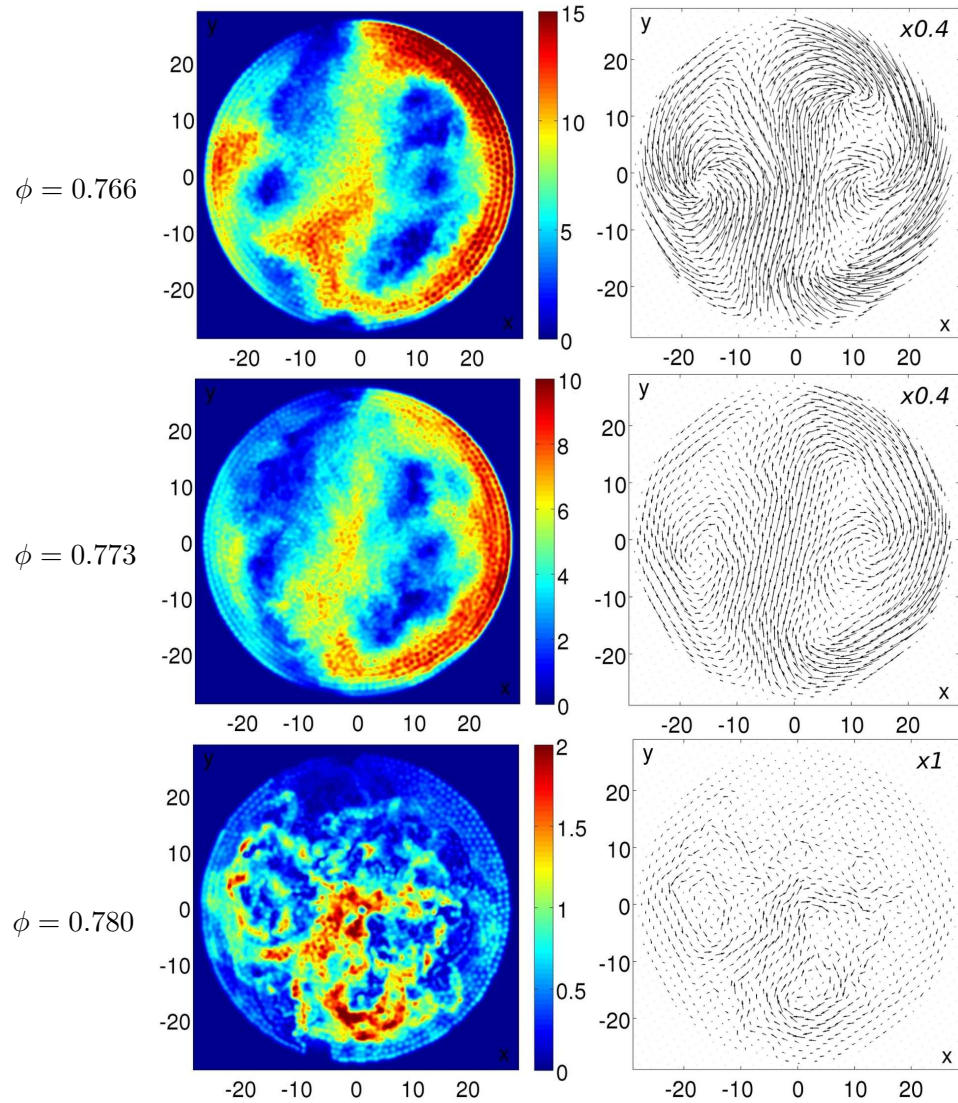


Figure 4.12: Flow of particles in the fluidized bed experiment. **Left** Average amplitude  $\langle \Delta r(\tau) \rangle_t$  of the displacement on  $\tau = 5,000$  time steps. **Right** Corresponding velocity field computed on  $\tau = 5,000$ . The scaling factors are shown in the top-right corners. The packing fractions are, from top to bottom: 0.766, 0.773 (densest of [84]) and 0.780 (loosest of the unpublished set).

be performed in a large system because it is highly sensitive to size effects. Extracting a reliable growing dynamical lengthscale seems difficult in the small system.

The second way to avoid convection is to have a system close enough to the glass transition. Indeed, the angular velocity of these vortices decreases

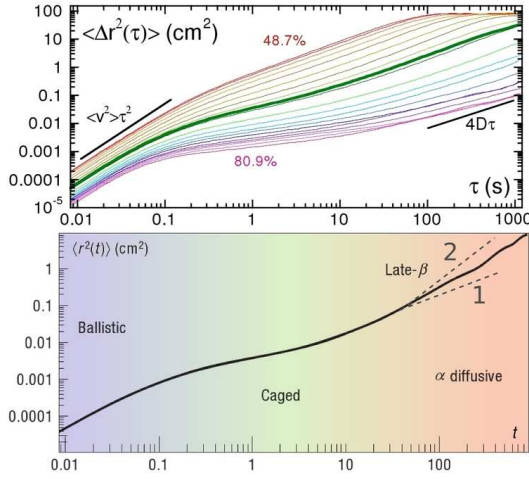


Figure 4.13: **Top** MSD of the big particles in the fluidized bed experiment with a number of particles  $262 < N < 444$  for several packing fractions. From Abate and Durian [83]. The long time scales dynamics nicely recover a diffusive regime. **Bottom** MSD of the big particles for the experiment with a higher number of particles  $N = 1904$  for  $\phi = 0.773$ . The long time scales dynamics is clearly more than diffusive. Adapted from Keys *et al.* [84].

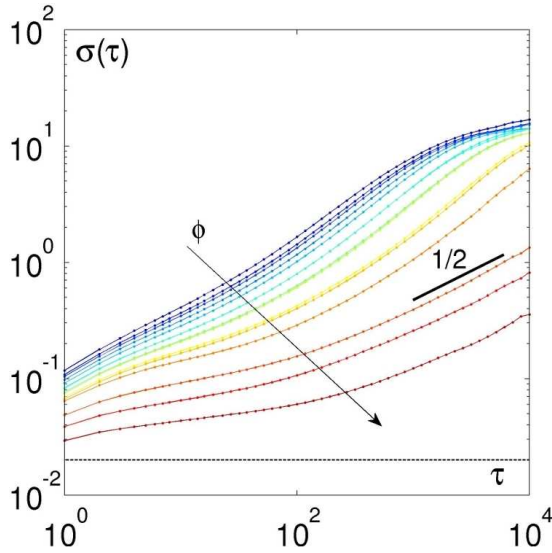


Figure 4.14: RMSD for 15 values of  $\phi$  (from blue to red). The data for the 3 densest packing fractions are unpublished. The horizontal dotted line's ordinate is at  $l_{hop}$ .

rapidly when  $\phi$  increases, and the correlations induced by this large scale convection also decrease. In parallel, the dynamical correlations due to the glass transition increase, such that eventually they become the dominant contribution in the dynamical correlations.

Fortunately, in addition to the 12 values of the packing fraction presented in [84], there are 3 unpublished data sets with higher packing fractions ( $\phi = 0.780, 0.791$  and  $0.802$ ). When one looks at the dynamics on long time scales for those denser runs, convection does no longer appear (see the bottom plots of fig. 4.12), and the root mean square displacements for those 3 packing fractions readily recover a slope of  $1/2$ , *i.e.* a diffusive regime, as illustrated in fig.4.14.

As a conclusion of the second point of this discussion, we can say that in the fluidized bed experiment the 12 lower packing fractions display non-negligible convection patterns, while the 3 denser do not. The effect of these convections patterns of the computation of the dynamical correlations is a delicate point; Keys *et al.* have carefully checked that the typical time of the shear rate of the convection rolls is comfortably above the typical time of the dynamical heterogeneities at each packing fraction. For our concerns, this time is therefore *a fortiori* far above the typical facilitation time  $\tau_S$  introduced in 4.3 and [85], which is far below  $\tau_\alpha$  at high packing fractions.

In the following, we will focus on the 6 densest states since several quantities with little sensibility to long-time convection rolls can still be computed.

**Our analysis.** The reader will find our results in the next few pages, enclosed in an article format. This Letter has been submitted for publication in *Physical Review Letters* (see [85] for precise references).

In brief, this new analysis revealed that roughly the same phenomenology is observed, and highlighted the role and fate of facilitation as the packing fraction increases. First, having located the cage jumps, we show that these elementary relaxation events form cooperative clusters as well. Second, when increasing the packing fraction, both the size of the clusters grow and their spatio-temporal organization evolves from a rather scattered, random-like distribution towards much more concentrated and collective events. Finally, this highlights the role of facilitation among clusters, both at low packing fraction where a *single* highly connected structure of *conserved* facilitation is found, and at high packing fraction where the patterns are rather *distinct* avalanches, suggesting that facilitation becomes *non-conservative*. Crucially, we find that the correlation time amongst clusters remains roughly constant. This suggests that the facilitation process is ruled by the structural properties of the packing rather than by the dynamical constraints.

# Evolution of dynamical facilitation approaching the granular glass transition

R. Candelier,<sup>1</sup> O. Dauchot,<sup>1</sup> and G. Biroli<sup>2</sup>

<sup>1</sup>*SPEC, CEA-Saclay, URA 2464 CNRS, 91 191 Gif-sur-Yvette, France*

<sup>2</sup>*Institut de Physique Théorique, CEA, IPhT, F-91191 Gif-sur-Yvette, France and CNRS, URA 2306*

We investigate the relaxation dynamics of a dense monolayer of bidisperse beads by analyzing the experimental data previously obtained in a fluidized bed. We show that the dynamics is formed by elementary relaxation events called cage jumps. These aggregate on a very short time into clusters. Increasing the packing fraction makes the spatio-temporal organization of the clusters evolve from a rather scattered and random distribution towards a collection of sparse and large events, called avalanches. The avalanche process is a manifestation of dynamical facilitation. The study of its evolution with density reveals that dynamical facilitation becomes less conserved and play a lesser role for the structural relaxation approaching the granular glass transition.

PACS numbers:

The dynamics of supercooled liquids [1, 2], colloids [3] and agitated granular media [4] dramatically slows down as these systems approach the glass transition. Surprisingly, particles configurations close to the transition still look like the ones of a high temperature liquid. Instead, dynamical trajectories do show significant modifications. The motion becomes intermittent at the microscopic scale: typically a particle rattles for a long time inside a “cage” formed by its neighbours, before jumping into another “cage”. Henceforth we shall call this event cage jump. Consecutive cage jumps lead to structural relaxation and long time diffusion. This phenomenon has been visually observed in colloids [5], granular media [6–8] and numerical simulations of supercooled liquids [9]. Another very important feature of glassy dynamics is the emergence of dynamical heterogeneity: there is by now experimental [3, 10–15] and numerical evidence [16, 17] that dynamics becomes spatially correlated approaching the glass transition; there appear spatially localized regions relaxing much faster than the average. Providing a microscopic explanation for these phenomena has become a central issue in the field. Despite a number of theoretical proposals [18–23], there is still no consensus. One particularly debated question is the role of dynamical facilitation ( $DF$ ) in glassy dynamics.  $DF$  means that a local relaxation has a very high probability of happening nearby another relaxation after a certain time, which is short compared to the macroscopic relaxation time but large compared to the microscopic one. Effective models based on kinetic constrains [22, 24] posit that  $DF$  is the underlying cause of particle mobility by assuming that a region of jammed atoms can become unjammed and exhibit mobility only when it is adjacent to a region already unjammed. Within the models this is due to the existence of mobility inducing defects, which cannot disappear (or appear) except if there is another defect nearby. This constraint implies that local relaxations cannot start or end without correspondingly being preceded or followed in space and time by other local relaxations. We will refer to this property as *conservation* of  $DF$ . In other

approaches [25], instead,  $DF$  is an important piece of the theoretical description but not the driving mechanism of glassy dynamics.

Clearly, understanding how consecutive cage jumps conspire together and lead to macroscopic relaxation would be very instrumental in clarifying the role of dynamical facilitation and in explaining the emergence of dynamical heterogeneity. A first attempt in this direction has been made in the study of granular media [8], where we unveiled that dynamical heterogeneities arise from the aggregation of quasi-instantaneous clusters of cage jumps into long lasting avalanches. The dynamical process leading to avalanches provides a clear evidence of the important role played by  $DF$ : a local relaxation due to a cluster of cage jumps is typically followed nearby in space and in time by another cluster relaxation, and so on and so forth until the entire avalanche process is formed. In order to understand precisely the role played by  $DF$ , and to discriminate amongst the various theoretical scenarii, it is now crucial to characterize the evolution of the avalanche process when approaching the glass transition.

To this aim we focus on the 2D fluidized bed of beads studied in [14], whose experimental data were generously provided by the authors. The system is made of a 1:1 bidisperse mixture of  $N$  steel beads of diameters  $d_S = 0.318\text{cm}$  and  $d_L = 0.397\text{cm}$  ( $d_L/d_S = 1.25$ ), with respective masses of 0.130g and 0.266g, confined to a circular cell of diameter  $17.7\text{cm} = 55.7d_S$ . Bead motion is excited by an upward flow of air at a fixed superficial flow speed of  $545 \pm 10\text{cm}\cdot\text{s}^{-1}$  (resp.  $500 \pm 10\text{cm}\cdot\text{s}^{-1}$ ) for the 3 loosest (resp. densest) packing fractions. The original acquisition frame rate is 120 Hz; we retain one frame out of ten and follow the trajectories over 10,800 frames. To avoid boundary effects, we consider a circular region of interest of diameter  $D = 45d_S$ . All lengths are expressed in number of small grain diameters, and times in number of frames ( $\frac{1}{12}\text{s}$ ). We study packing fraction ranging from  $\phi = 0.758$  to  $\phi = 0.802$  ( $N = 1,790$  to  $1,975$ ). The data for the three most dense packings were not discussed in [14].

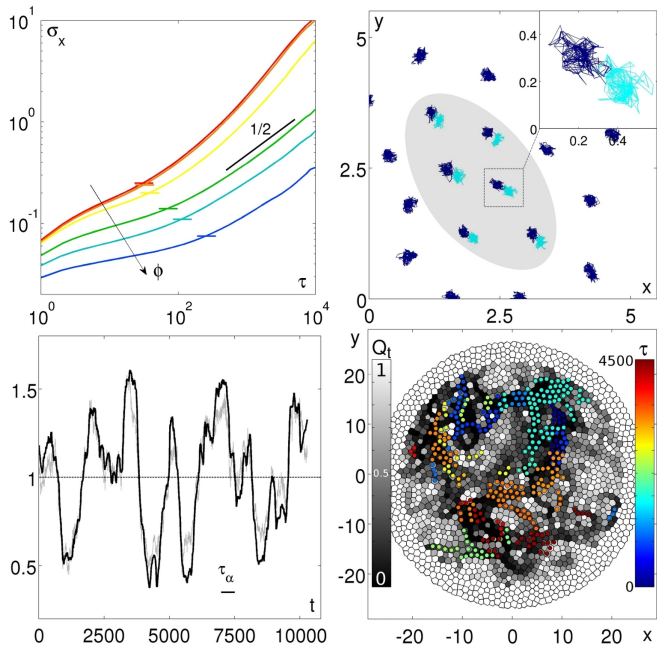


FIG. 1: (color online) Dynamics and cooperative jumps. Top-left: Root mean square displacement along the  $x$ -direction  $\sigma_x(\tau)$  for the 6 packing fractions  $\phi = 0.758$  (red) to  $0.802$  (blue). The horizontal dashes are located at the thresholds of the cage jump detection algorithm. Top-right: Trajectories of a few particles at  $\phi = 0.802$  for 1,000 time frames. The color changes from blue (black) to cyan (light grey) when a cage jump is detected. All cage jumps in the grey area appear within 15 time steps, defining a cooperative cluster. Bottom-left: Comparison between the relative spatially averaged relaxation  $Q_t(\tau_\alpha)/\langle Q_t \rangle_t$  (grey) and the relative percentage  $P_t(\tau_\alpha)/\langle P_t \rangle_t$  of particles that haven't jumped between  $t$  and  $t + \tau_\alpha$  (black) at  $\phi = 0.773$ ,  $\tau_\alpha = 512$ . Bottom-right: Clusters of cage jumps appeared between  $t$  and  $t + \tau_\alpha$  superimposed on the map of  $Q_{p,t}(\tau_\alpha)$  (grey-scale, left colorbar). The times  $\tau$  at which clusters occur are color coded (right colorbar),  $\phi = 0.802$ ,  $\tau_\alpha = 4536$ .

In fig. 1 top-left we plot the root mean square displacement along the  $x$ -axis on a lag time  $\tau$ ,  $\sigma_x(\tau)$ , which shows all the well-known characteristics observed when approaching the glass transition: a sub-diffusive plateau at intermediate time scales, which enlarges when increasing the packing fraction, and the final recovery of a diffusive regime on long times. For the three loosest packings the slope is greater than  $1/2$ , indicating the presence of slow convection rolls. This effect becomes stronger at even lower densities. Here we retain only the highest packing fraction, for which this does not interfere with the timescales of the analysis.

In order to analyze the microscopic relaxation processes, we apply the same procedure as developed in [8] which allows one to obtain a coarse grained description of the dynamical evolution in terms of cage jumps: within a trajectory  $S(t)_{t \in [0, T]}$ , the time of the largest cage jump is given by the position  $t_c$  of the maximum of  $p(t) = \xi(t) \cdot [\langle d_1(t)^2 \rangle_{S_2} \cdot \langle d_2(t)^2 \rangle_{S_1}]^{1/2}$ , where  $S_1$  and  $S_2$  are the

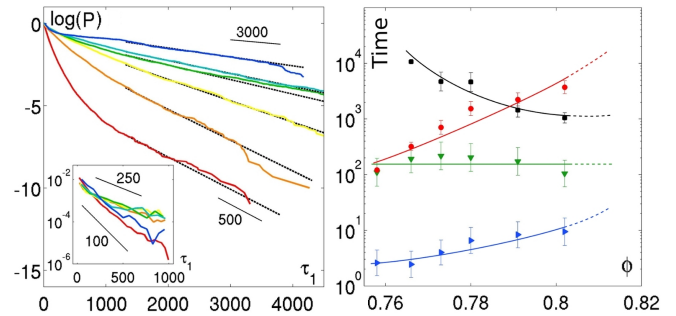


FIG. 2: (color online) Times scales as a function of packing fraction. Left: Distributions of  $\tau$ , the lag time between adjacent clusters; *Main plot*  $P(\tau > \tau_1)$  – black dotted lines are exponential fits at large  $\tau_1$ . *Inset* Pdf( $\tau$ ) for the population of short lag times (see text for more details) – black lines are indicative exponential decays. Right:  $\tau_{1/2}$  (●),  $\tau_{cl}$  (▲),  $\tau_S$  (▼), and  $\tau_f$  (■).

trajectory subsets  $S\{t \in [0, t_c]\}$  and  $S\{t \in [t_c, T]\}$ ,  $d_k(t)$  is the distance between the position at time  $t$  and the center of mass of the subset  $S_k$ , the average  $\langle \cdot \rangle_{S_k}$  is computed over the subset  $S_k$  and  $\xi(t) = \sqrt{t_c/T(1 - t_c/T)}$  is a natural statistical normalization. The procedure is repeated iteratively for every sub-trajectory until  $\max(p) < \sigma_c^2$ , where the thresholds  $\sigma_c(\phi)$  are defined at the cross-over between subdiffusive and diffusive regimes in  $\sigma_x(\tau)$  (see fig.1-top left) and correspond to the sizes of a cage. This algorithm allows us to locate the cage jumps within a resolution of 15 time steps (see fig. 1-top right, which shows that cage jumps are well defined dynamical events). The evolution of the temporal correlation function is given by  $Q_t(\tau) = \langle Q_{p,t}(\tau) \rangle_p$  with

$$Q_{p,t}(\tau) = \exp\left(-\frac{\|\Delta\vec{r}_p(t, t+\tau)\|^2}{2a^2}\right),$$

where  $\Delta\vec{r}_p(t, t+\tau)$  is the displacement of particle  $p$  between  $t$  and  $t+\tau$  and the length scale  $a$  is set to  $0.2$ . Fig. 1-bottom left shows that for  $\tau = \tau_\alpha$ , the relaxation time defined by  $\langle Q_t(\tau) \rangle_t = 1/2$ ,  $Q_t(\tau)$  is very well described by  $P_t(\tau)$ , the percentage of particles that have not jumped between  $t$  and  $t+\tau$ .

Subsequent cage jumps aggregate into clumps that we call cooperative clusters and whose very short duration is denoted  $\tau_{cl}$ . This is clear from fig. 1-bottom right, which shows that the large decorrelation patterns observed on time-scales  $\tau_\alpha$  issue from the aggregation of several clusters of particles hopping at successive times. In order to substantiate more quantitatively the existence of clusters we focus on the distribution of the lags  $\tau$  separating the clusters that are adjacent in space and time. Figure 2-top left displays  $P(\tau > \tau_1)$ , the probability of observing  $\tau$  larger than  $\tau_1$ . As in [8], these cumulated distributions are well described by the addition of two processes :

$$P(\tau > \tau_1) = \left(p_S e^{-\frac{\tau_1}{\tau_S}} + (1 - p_S) e^{-\frac{\tau_1}{\tau_L}}\right);$$

$p_S$  is the fraction of short lag times. The short time scale,  $\tau_S$ , physically corresponds to dynamic facilitation events:

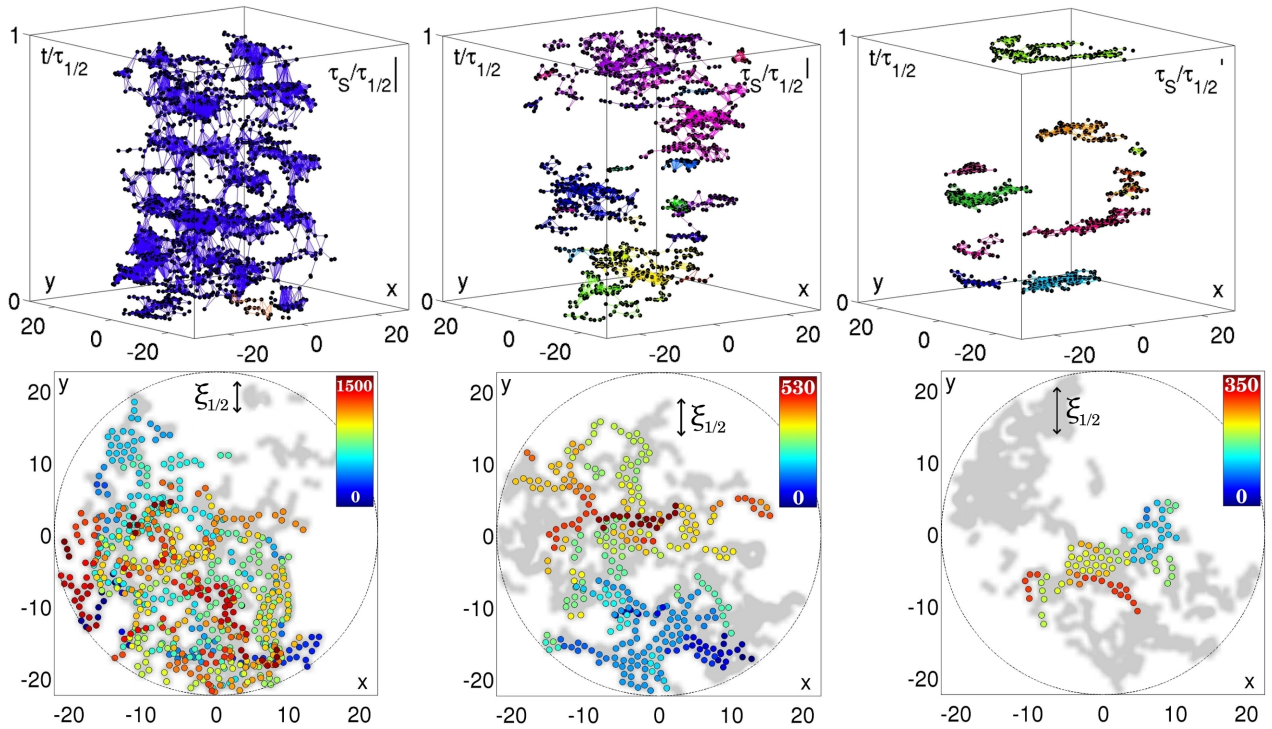


FIG. 3: (color online) Top: Facilitation patterns in space and time during the typical relaxation time  $\tau_{1/2}(\phi)$  for 3 packing fractions : from left to right  $\phi = 0.780, 0.791, 0.802$  and  $\tau_{1/2} = 1540, 2250, 3730$ . The two directions of space are in the horizontal plane and time is the vertical axis. The ratio  $\tau_S/\tau_{1/2}$  is given in the upper-right corners. Jumps are represented with black dots, and all possible tetrahedrons which edges are the facilitating links between jumps are shown, forming volumes. Each separate connected structure has a different color. Bottom: Jumps occurring in  $\tau_{1/2}$  (in grey), same packing fractions. The jumps belonging to one arbitrarily chosen connected structure are colored according to the time at which they occur.

cluster relaxations followed closely in time and in space by other cluster relaxations. The long time scale  $\tau_L$  corresponds to the average time spent in a cage. Technically, we extract first  $\tau_L$  and  $p_S$  by fitting the large  $\tau_1$  regime, then we subtract the large  $\tau_1$  contribution and obtain the exponential distribution for the short lag times displayed in the inset of fig. 2-top left and from which one easily estimates  $\tau_S$ .

We now come to the central discussion of this work: the evolution of the above dynamical patterns, identical to the ones observed in [8], when the packing fraction is increased towards the glass transition. One observes on fig. 2-top left that the relaxation time  $\tau_\alpha$  or its alternative estimation  $\tau_{1/2}$ , the time needed for observing half of the particles to jump once, increases strongly with the packing fraction, while the cooperative clusters typically last a short time  $\tau_{cl}$  varying from 2 to 10, not a significant variation given our temporal resolution on the detection of the cage jumps.  $\tau_S$  remains bounded between 100 and 250 without clear tendency, while  $\tau_L$  increases from 511 to 3,041, following the slowing down of the dynamics. Note that  $\tau_S$  is larger than  $\tau_{cl}$  thus confirming that clusters are well defined dynamical events.

Clearly, the picture of clusters dynamically facilitating each others only makes sense when  $\tau_L$  becomes larger than  $\tau_S$ , that is above  $\phi^* \sim 0.77$ , which would be anal-

ogous to the onset temperature in supercooled liquids. The way in which clusters aggregate and the resulting facilitation patterns are represented in fig. 3-top for three packing fractions in 3D space/time, the time axis being rescaled with respect to the relaxation time  $\tau_{1/2}$ . We draw all cage jumps (black dots) and link the ones separated by a lag time less than  $\tau_S$ . This defines a network whose vertices are the cage jumps and whose edges are the orientated links towards facilitated jumps. For the loosest packing fraction, all jumps are connected by a facilitation link and form a highly interconnected monolith where facilitation appears to be conserved. When raising  $\phi$ , an increasing number of adjacent clusters become separated by more than a few  $\tau_S$  within a time interval equal to the relaxation time (the ratios  $\tau_{1/2}/\tau_S$  and  $\tau_L/\tau_S$  increase up to 20 and 30). Eventually, the facilitation network does not percolate in time anymore and separated avalanches form. The average duration of the avalanches, that we call facilitation time,  $\tau_f$ , decreases and becomes smaller than  $\tau_{1/2}$  for the largest  $\phi$ . At that point facilitation is clearly not conserved anymore. In agreement with the above discussion, we find that  $p_S$  decreases from 90% to 40%, suggesting that facilitation occurs for a decreasing number of clusters. It would be interesting to check whether at even higher density  $\tau_f$  becomes of the order of  $\tau_S$ : each avalanche would reduce to a single cluster

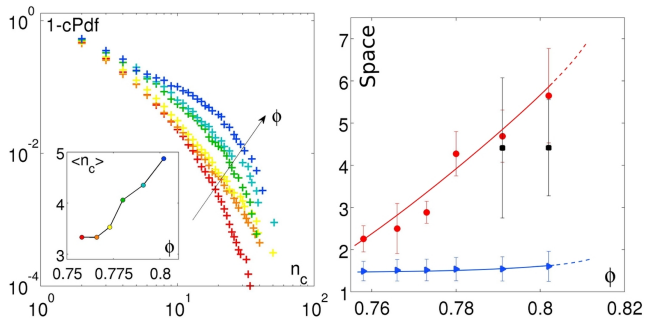


FIG. 4: (color online) Length scales as functions of the packing fraction. Left: Cumulated Pdf of the clusters' number of particles  $n_c$  for the 6 packing fractions  $\phi = 0.758$  (red) to  $0.802$  (blue); *Inset* Mean value of  $n_c$  over all clusters, as a function of  $\phi$ . Right:  $\xi_{cl}$  ( $\blacktriangle$ ),  $\xi_{1/2}$  ( $\bullet$ ), and  $\xi_{ava}$  ( $\blacksquare$ ). Plain lines are guides for the eyes, dashed lines are extrapolations.

and facilitation would disappear completely.

Finally, we address the evolution of the dynamical correlation length-scale  $\xi_{1/2}$  estimated as the correlation length of the facilitation pattern (assuming by ergodicity that spatial and time averages coincide).  $\xi_{1/2}$  is approximately equal to the average width of the backbone forming the pattern. Figure 3-bottom displays the spatial projection of cage jump during  $\tau_{1/2}$ . In grey, one sees the half of the particles which have jumped and we have colored those belonging to one arbitrarily chosen connected structure. For the lowest  $\phi$  (left panel)  $\tau_f > \tau_{1/2}$  and almost all cage jumps belong to the same large, eventually infinite connected structure.  $\xi_{1/2}$  is roughly the cluster size, thus showing that the pattern is formed by dynamically independent clusters. In this regime, the pattern is so much intertwined that a cluster is facilitated by several others. Thus, dynamical correlations do not propagate farther than the size of one single cluster. At higher  $\phi$ s, the distributions of the cluster sizes  $n_c$  (see fig. 4-top left) have larger tails and their experimental average  $\langle n_c \rangle$  grows from 3.4 to 5. For the packing fraction corresponding to the middle panel of Fig. 3-bottom,  $\tau_f \simeq \tau_{1/2}$ , the clusters are slightly larger and more concentrated and  $\xi_{1/2}$  is increased, as shown in fig. 4-top right. Finally, at the highest density (right panel of Fig. 3-bottom), when avalanches are well formed and separated, we find that  $\xi_{1/2}$  is again increased and has become of the order of the avalanche size  $\xi_{ava}$ . At this packing fraction,  $\tau_f < \tau_{1/2}$  and the clusters are even more grouped.

To summarize, analyzing data coming from a fluidized monolayer experiment, we have confirmed the role of the spatio-temporal organization of cage jumps in the relaxation dynamics previously pointed out in our cyclic shear experiment. In both cases such cage jumps occur in cooperative clusters which give rise to facilitation. Above a characteristic packing fraction, akin to the onset temperature in liquids, facilitation starts to play a role in the dynamics. Increasing the packing fraction facilita-

tion patterns evolve from a single connected structure percolating in time to isolated denser avalanches of finite duration. Dynamical correlations are, at first, of the size of clusters and then, in the latter regime, are of the size of the avalanches. Finally, approaching the granular glass transition, the cluster size increases whereas the number of facilitated clusters inside an avalanche decreases. Thus the cooperative relaxation of the first cluster of an avalanche plays a larger role and facilitation a lesser one. Investigating whether our findings also hold for supercooled liquids would certainly be of great interest.

We thank A.R. Abate and D.J. Durian for sharing their data and J.-P. Bouchaud, D.R. Reichman and L. Berthier for feedback on this manuscript. This work was supported by ANR DYNHET 07-BLAN-0157-01.

- [1] M. Ediger, C. Angell, and S. Nagel, *J. Phys. Chem.* **100**, 13200 (1996).
- [2] P. Debenedetti and F. Stillinger, *Nature* **410**, 259 (2001).
- [3] E. Weeks, J. Crocker, A. Levitt, A. Schofield, and D. Weitz, *Science* **287**, 627 (2000).
- [4] O. Dauchot, in *Ageing and the Glass Transition*, edited by MPRS (Springer, 2007), chap. 4, p. 161.
- [5] E. Weeks and D. Weitz, *Ph. Rev. Let.* **89**, 95704 (2002).
- [6] O. Pouliquen, M. Belzons, and M. Nicolas, *Ph. Rev. Let.* **91**, 014301 (2003).
- [7] G. Marty and O. Dauchot, *Ph. Rev. Let.* **94**, 15701 (2005).
- [8] R. Candelier, O. Dauchot, and G. Biroli, *Ph. Rev. Let.* **102**, 088001 (2009).
- [9] S. Kudchadkar and J. Wiest, *The Journal of Chemical Physics* **103**, 8566 (1995).
- [10] M. Ediger, *An. rev. of phys. chem.* **51**, 99 (2000).
- [11] L. Berthier, G. Biroli, J. Bouchaud, L. Cipelletti, D. El Masri, D. L'Hote, F. Ladieu, and M. Pierno, *Science(Washington, D. C.)* **310**, 1797 (2005).
- [12] O. Dauchot, G. Marty, and G. Biroli, *Ph. Rev. Let.* **95**, 265701 (2005).
- [13] F. Lechenault, O. Dauchot, G. Biroli, and J. Bouchaud, *Europhysics Letters* **83**, 46003 (2008).
- [14] A. Keys, A. Abate, S. Glotzer, and D. Durian, *Nature Physics* **3**, 260 (2007).
- [15] L. Cipelletti and L. Ramos, *Cond. Mat.* **17**, R253 (2005).
- [16] M. Hurley and P. Harrowell, *Ph. Rev. E* **52**, 1694 (1995).
- [17] W. Kob, C. Donati, S. Plimpton, P. Poole, and S. Glotzer, *Ph. Rev. Let.* **79**, 2827 (1997).
- [18] G. Tarjus, S. Kivelson, Z. Nussinov, and P. Viot, *Journal of Physics Cond. Matter* **17**, 1143 (2005).
- [19] H. Shintani and H. Tanaka, *Nature Physics* **2**, 200 (2006).
- [20] V. Lubchenko and P. G. Wolynes, *J. Chem. Phys.* **121**, 2852 (2004).
- [21] G. Biroli, J.-P. Bouchaud, A. Cavagna, T. Grigera, and P. Verrocchio, *Nature Physics* **4**, 771 (2008).
- [22] J. P. Garrahan and D. Chandler, *PRL* **89**, 035704 (2002).
- [23] C. Brito and M. Wyart, *J. Stat. Mech.* **8**, L08003 (2007).
- [24] G. Fredrickson and H. Andersen, *PRL* **53**, 1244 (1984).
- [25] S. Bhattacharyya, B. Bachi, and P. Wolynes, *PNAS* **105**, 16077 (2008).

## 4.4 And what about real liquids?

*She didn't want to know how a thing was done, but why. That can be embarrassing. You ask Why to a lot of things and you wind up very unhappy indeed, if you keep at it.*

– Ray Bradbury, *Fahrenheit 451* (1953)

Given the preceding success in applying our analysis in a second granular system with a different forcing, we wanted to try it on yet another system much closer to real liquids, namely a simulation of purely repulsive softly interacting disks.

### 4.4.1 Relaxation originates from soft modes

Broaching the subject of the construction of dynamical heterogeneities in such a system has a special flavor since a large amount of studies did a formidable spadework in the last decade. Recently Widmer-Cooper *et al.* [26] gave some evidences that the dynamical relaxation originates from lo-

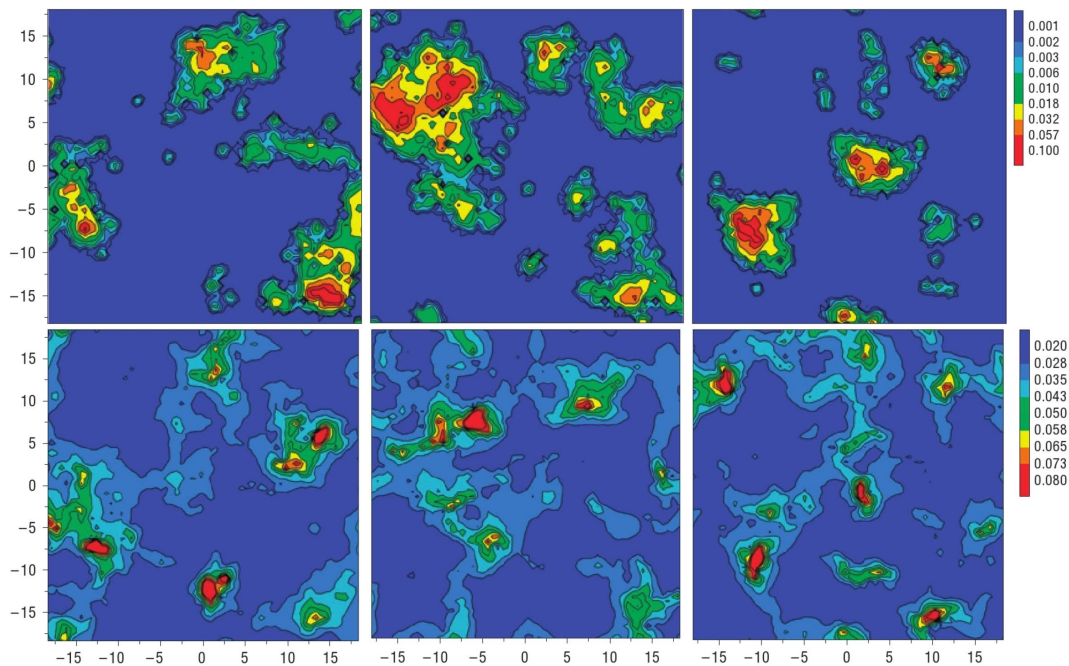


Figure 4.15: Spatial distribution of irreversible reorganization vs. the low-frequency normal modes. **Top** Contour plots of the probability ( $\log_{10}$ ) of a particle losing 4 original neighbors, within  $200\tau_0$  over 100 iso-configurational runs for 3 different initial configurations. **Bottom** Contour plots of the participation fraction summed over the 30 lowest-frequency modes for the quenched initial configurations of the same 3 configurations. From Widmer-Cooper *et al.* [26].

calized soft modes in a system close to the one presented in 2.1.4 (additive -  $N = 1024$ ), a very important result since this may be the first time that a structural quantity can predict the dynamics on timescales of the order of the  $\alpha$ -relaxation,  $\tau_\alpha$ .

In brief, the authors reduce the dynamics to its irreversible part by defining an “irreversible reorganization” as the fact of losing 4 neighbors or more<sup>8</sup>. Then they record the number of times each particle meets this criterion in 100 isoconfigurations lasting  $200 \tau_0$  (corresponding to  $\sim 2000$  collisions,  $\tau_\alpha = 673 \tau_0$  for comparison<sup>9</sup>) and obtain maps as the ones depicted in the top of fig. 4.15. For comparison, the participation ratios for the 1.5% lowest soft modes at  $t = 0$  for the corresponding initial configurations are represented in the bottom figures of 4.15. Note that the authors have used quenched modes, so they have used only the information about the bottom of the local potential minima.

The authors emphasize “a strong correlation between the mode maps and the irreversible reorganization maps”. Although the correlation is not perfectly 1:1, one can reasonably admit that it exists. In addition, recent developments have shown that the lowest soft modes maps fluctuates from one configuration to another, but that averaging those maps on a few successive configurations greatly enhance the correlation with the dynamics. Probably the main result of this work is that, knowing the initial structure, one can predict with a reasonable success the evolution of the dynamics up to the impressive time scale of  $\sim \tau_\alpha/3$ .

However, as the authors remark, this is not always the case: sometimes significant variations of the quenched modes occur on very short time scales, like on the configuration represented in fig. 4.16-left, which strongly evolves in only  $10\tau_0$  as illustrated by fig. 4.16-middle. In this example, the particles with a high irreversible reorganization probability in the next  $200 \tau_0$ , represented with white dots in fig. 4.16-right, are naturally matching the later map. In this precise case, the former map clearly fails to predict the evolution of the dynamics over  $\tau_\alpha/3$ .

#### 4.4.2 Structure-induced dynamical correlations in supercooled liquids

These results are of considerable interest for our purposes. Indeed, one of the most important remaining question is the origin of the clusters of cooperative cage jumps. This issue is hardly accessible in the cyclic shear experiment and the fluidized bed experiment, since we do not have access to the potentials / force network. Also, the limited resolution on the positions

---

<sup>8</sup>Note that this is at odd with our definition of irreversible displacements. The length-scale of the cage jumps is of the order of  $10^{-1}$ , so a particle hardly changes even one single neighbor in a jump; however, jumps already traduce an irreversible motion.

<sup>9</sup> $\tau_0$  is the unit of time. It roughly corresponds to 10 collision events.

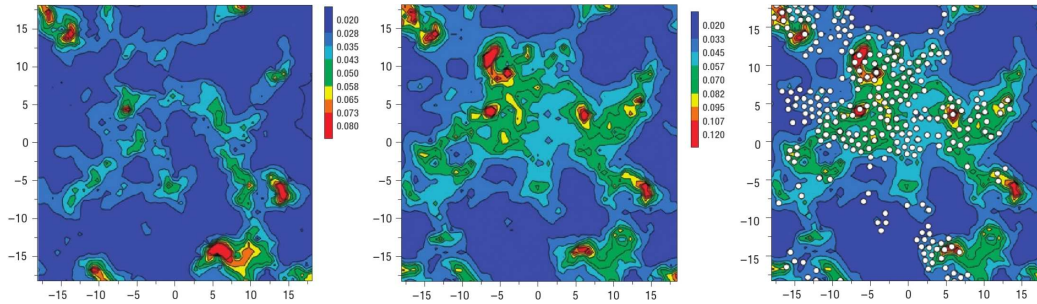


Figure 4.16: Rapid variations in normal mode structure. **Left** Contour plot of the participation fraction summed over the 30 lowest-frequency modes for a quenched configuration. **Middle** Contour plot of the maximum value of the participation fraction observed over five  $10\tau_0$  runs starting from the same configuration than on the left panel. Note the important changes. **Right** Particles whose iso-configurational probability of losing 4 initial nearest neighbors within  $200\tau$  is  $\geq 0.01$  (white circles) overlaid on the middle plot. From Widmer-Cooper *et al.* [26].

does not allow for an easy computation of the normal modes. In addition, as discussed in the introduction (see 1.2.4) friction is a big issue when one wants to compute the normal modes, making this computation hardly accessible to experiments. The final argument is that the isoconfigurational trick is the exclusive prerogative of numerical works, and it is a very powerful tool to extract what in the structure is responsible for the dynamics. We therefore had a lot of scientific exchanges with these authors which led to the mapping between their observations and ours. The main results of this collaboration are presented in the next few pages in an article format. This Letter is still a work in progress but will soon be submitted for publication in *Physical Review Letters* ([38]).

In short, we first show that a scenario similar to the one reported previously can be drawn in this system: cage jumps describe well the non-trivial dynamics and the spatial patterns formed by the dynamical heterogeneities which correspond to the avalanches of clusters of cage jumps in the same time lag. The correspondence can even be pushed to a quantitative level since the rescaled timescales match, indicating that both systems share the same “level of glassiness”. We then show that the clusters of cage jumps appear in regions of high isoconfigurational Debye-Waller factor (IDWF), a quantity that probes the purely structural propensity of a region to decorrelate. Importantly, the IDWF is computed with the evolution of several configurations on a *very short* time scale and is able to predict the preferential locations of the cage jumps on *long* time scales, typically of the order of  $\tau_\alpha/4$ , which is the typical decorrelation time of the IDWF and is less than one order of magnitude smaller than the timescale of structural

relaxation. We highlight the fact that cage jumps do not appear in *all* the high IDWF regions in each evolution of the isoconfigurations, a signature of their stochastic nature. Finally, in a general discussion we establish some connections with recent studies, and draw the guidelines for future work.

# Avalanches and Dynamical Correlations in supercooled liquids

R. Candelier,<sup>1</sup> A. Widmer-Cooper,<sup>2</sup> J. K. Kummerfeld,<sup>3</sup> O. Dauchot,<sup>1</sup> G. Biroli,<sup>4</sup> P. Harrowell,<sup>3</sup> and D.R. Reichman<sup>5</sup>

<sup>1</sup>*SPEC, CEA-Saclay, URA 2464 CNRS, 91 191 Gif-sur-Yvette, France*

<sup>2</sup>*Materials Sciences Division, Lawrence Berkeley National Laboratory, Berkeley, California, 94720, USA*

<sup>3</sup>*Department of Chemistry, University of Sydney, Sydney, New South Wales 2006, Australia*

<sup>4</sup>*Institut de Physique Théorique, CEA, IPhT, F-91191 Gif-sur-Yvette, France and CNRS, URA 2306*

<sup>5</sup>*Columbia University, 3000 Broadway, New York, New York, 10027, USA*

We identify the pattern of microscopic dynamical relaxation for a two dimensional glass forming liquid. On short timescales, bursts of irreversible particle motion, called cage jumps, aggregate into clusters. On larger time scales, clusters aggregate both spatially and temporally into avalanches. This propagation of mobility, or dynamic facilitation, takes place along the soft regions of the systems, which have been identified by computing isoconfigurational Debye-Waller maps. Our results characterize the way in which dynamical heterogeneity evolves in moderately supercooled liquids and reveal that it is astonishingly similar to the one found for dense glassy granular media.

PACS numbers:

Identifying the physical mechanisms responsible for the slowing down of the dynamics of supercooled liquids is still an open problem despite several decades of intense research. While traditional descriptions of glassy systems have mainly focused on energy landscape concepts[1] and spatially averaged quantities, recent work has centered on the real space properties reflected in the dramatically heterogeneous dynamics shared by nearly all glass-forming materials. Concomitantly, investigations of the behavior of dense driven granular media have uncovered tantalizing similarities with the dynamics of supercooled liquids[2–5] and provided new inspirations for research on the glass transition. Among the most notable findings related to the real space dynamical properties in supercooled liquids as well as granular media is the evidence that dynamic facilitation [6?] and sizable dynamic correlations [7] play an important role. This is supported by the detailed analysis of microscopic dynamics which has identified correlated particle motion in clusters, strings and other motifs. [8? , 9]. A natural question [10] related to these findings is what, if any, structural features are correlated with the heterogeneity noted in the real space dynamics. Important progress in this direction has been obtained [11], through the introduction of the quantitative notion of “propensity”, and then later in [12? , 13], where it has been shown that irreversible motion is correlated with the spatial characteristics of soft modes.

In this paper we address the following three questions: First, do supercooled liquids exhibit the same hierarchical organization of dynamics (i.e. cage escapes within clusters within avalanches) as recently reported in granular materials [9? ]? Second, to what degree are these different scales of collective motion determined by the underlying structure? And reciprocally, to what extent is the evolution of the structure related to the relaxation events within a given realization of the dynamics?

We shall address these questions by performing computer simulations on a new two-dimensional model of

glass-forming liquid and applying the cluster analysis developed in [9]. This new model is distinguished from previous 2D mixtures [14] in that supercooled liquid dynamics may be simulated without the formation of palpable crystalline micro-domains. Our main results are that the glassy dynamics of dense driven granular systems [9] and supercooled liquids turn out to be astonishingly similar even at the microscopic level. *This is remarkable given the fact that granular systems are driven non-equilibrium systems with dissipative contact interactions while supercooled liquids are equilibrium conservative systems.* Quasi-instantaneous clusters of nearby relaxing particles are typically followed by adjacent clusters showing how long term dynamical correlations emerge. This dynamic facilitation leads to the formation of finite size and finite duration avalanches located on the “soft” regions of the configuration as probed by the isoconfigurational average of the Debye-Waller factor. Finally the clusters of relaxing particles induce non-local reorganisation of the structure as probed by the dynamics itself of the Debye-Waller factor.

As a model for a supercooled liquid we focus on a 2D non-additive binary mixture of  $N = 5,760$  particles enclosed in a square box with periodic boundary conditions, interacting via purely repulsive potentials of the form  $u_{ab}(r) = \varepsilon(\sigma_{ab}/r)^{12}$ . The mole fraction of the smaller particles is taken to be  $x_1 = 0.3167$ . All units are reduced so that  $\sigma_{11} = \varepsilon = m = 1.0$ ,  $m$  being the mass of both types of particle. We use non-additive potentials, namely  $\sigma_{12} = 1.1 \times \sigma_{11}$  and  $\sigma_{22} = 1.4 \times \sigma_{11}$  to avoid the formation of crystalline domains. The temperature dependence of the structural and dynamical properties of this model were characterized in [? ]. Molecular dynamics simulations were carried out at constant NVT ( $T=0.4$ ) using the Nose-Poincare Hamiltonian [? ] after equilibration at constant NPT as described in [12]. All time units are scaled in such a way that the structural relaxation time  $\tau_\alpha$ , defined as the time required for the self

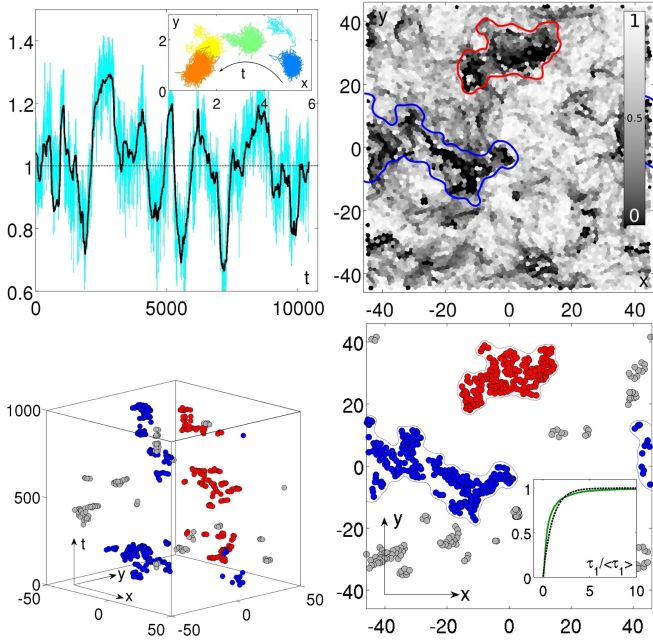


FIG. 1: (color online) Cooperative cage jumps form large decorrelation patterns. Top left: Comparison between the relative averaged relaxation  $Q_t(a^*, \tau^*)/\langle Q_t \rangle_t$  (cyan) and the relative percentage  $P_t(\tau^*)/\langle P_t \rangle_t$  of particles that have not jumped between  $t_0$  and  $t_0 + \tau^*$  (black). *Inset* Trajectory of a single particle over  $14\tau_\alpha$ . Color changes when the particle jumps. Top right: Map of  $Q_t(\tau^*)$ . Bottom left: Spatio-temporal view of the cage jumps between  $t$  and  $t + \tau^*$ . The jumps corresponding to two arbitrarily chosen avalanches are painted in blue and red. Bottom right: Map of the cage jumps occurring between  $t$  and  $t + \tau^*$ . Note that the blue and red avalanches lie in distinct regions of space. *Inset* Cumulative Pdf of the reduced time lag between adjacent clusters  $\tau_1$  (green), compared to the corresponding curve for a random distribution of clusters (black).

intermediate scattering function to decay of  $1/2$ , equals  $10^3$ . The typical collision time is  $0.12$  in these units.

We choose as a measure of the local mobility (or relaxation) of a particle  $p$ :

$$Q_{p,t}(a, \tau) = \exp\left(-\frac{\|\Delta\vec{r}_p(t, t + \tau)\|^2}{2a^2}\right), \quad (1)$$

where  $\Delta\vec{r}_p(t, t + \tau)$  is the displacement of the particle  $p$  between  $t$  and  $t + \tau$  and  $a$  is the length scale over which the motion is probed. A global measure of the dynamics is provided by the correlation function,  $Q_t(a, \tau) = \frac{1}{N} \sum_p Q_{p,t}(a, \tau)$ , and its fluctuations  $\chi_4(a, \tau) = N \text{Var}(Q_t(a, \tau))$ . As in [15], we focus on the values of  $a$  and  $\tau$  corresponding to maximal dynamic heterogeneity, i.e. highest value of  $\chi_4(a, \tau)$  (see [15] for details). This leads to  $a^* = 0.29$  and  $\tau^* = 1078$ . Note that the latter is very close to the relaxation time  $\tau_\alpha = 1000$ .

In order to analyze the microscopic dynamics and study possible connections with the dynamics of dense driven granular media, we follow the same procedure as in [9]. This allows one to separate the dynamics along a given trajectory into periods of inefficient vibrational

motion separated by relaxation events also called cage jumps. (see inset of the top left panel of fig. 1). One has to bear in mind that a particle undergoing a cage jump does not necessarily change neighbors. In the top left panel of fig. 1 we compare the relative values of  $Q_t(a^*, \tau^*)$  to those of  $P_t(\tau^*)$ , which is the percentage of particles that have not jumped during the time  $\tau^*$ . The two curves track each other, showing that cage jumps provides a powerful coarse grained description of the dynamics. In addition, we also show that the cage jumps are exactly located in the areas where the decorrelation is maximal (compare fig. 1 right top and bottom). We repeat the same spatio-temporal analysis performed for the two dimensional granular media studied in [9]. The outcome is remarkably similar. First, cage jumps aggregate into clusters, which are formed by cage jumps adjacent in space (as measured by the neighboring particles) and time (separated by less than  $\tau_{th} = 28$ , which is twice the precision of the cage detection algorithm). The size of these clusters are largely distributed with an average value of  $7.6$  cage jumps per cluster. Second, clusters aggregate into avalanches in which the first cluster triggers the appearance of successive clusters nearby shortly after, see fig. 1 bottom left. This is clearly demonstrated as in [9] by focusing on the cumulative Pdf of the lag times  $\tau_1$  separating each cluster from the nearest adjacent one, normalized by its average value  $\langle \tau_1 \rangle$ . See the inset of fig. 1, bottom right, where this Pdf is compared to the equivalent distribution for randomly distributed clusters in space and time. One can see a clear excess of both small and large lags: the Pdf can be extremely well fit by the union of two data sets corresponding to Poissonian processes with two different timescales  $\tau_S = 240$  and,  $\tau_L = 1746$ . The short time scale corresponds to the existence of a correlation among adjacent clusters. The large one is related to the average time spent in a cage. This leads to a very peculiar type of dynamical correlation, which in the literature is often called dynamical facilitation [6?]: local relaxations are followed closely in space and in time by other local relaxations. The concatenation of these events leads to the dynamical heterogeneity observed on the timescale  $\tau_\alpha$ . However, at least for the degree of supercooling considered here, we find that facilitation is not conserved in the following sense: avalanches are well separated, indicating that there are relaxation events, which cannot be explained by the facilitation mechanism.

It is interesting to compare the actual values of these parameters to those of the granular system investigated

	$a^*$	$\xi_4$	$\tau_\alpha$	$\tau^*$	$\tau_S$	$\tau_L$
Supercooled Liquid	0.29	2.9	1000	1078	240	1746
Dense Granular Media	0.12	3.1	1000	915	155	1384

TABLE I: Comparison of length and time scales normalized so that  $\tau_\alpha = 1000$ . See definitions in the text.

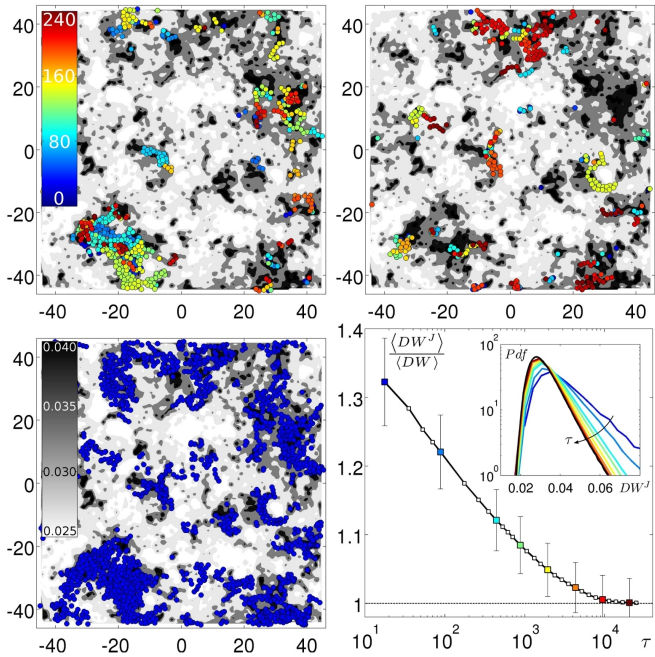


FIG. 2: (color online) Top: Cage jumps occurring between  $t$  (blue) and  $t + \tau_S$  (red) for two different isoconfigurational trajectories, on top of a  $DW$  factor map computed at time  $t$  (in grey). Bottom left: Cage jumps occurring in 6 isoconfigurational trajectories between  $t$  and  $t + \tau_S$  (in blue) tile the high  $DW$  regions. Colorbar indicates the  $DW$  values in levels of grey. Bottom right: Average  $\langle DW^J \rangle$  over the particles having jumped between  $t$  and  $t + \tau$ , divided by the average  $\langle DW \rangle$  over all particles, as a function of the lag time  $\tau$ . *Inset* Pdf of  $DW^J$  for the particles jumping in  $[t; t + \tau]$  for several values of  $\tau$ . The black curve is the Pdf for all particles.

previously. This comparison is performed in Table I, where we also report the value of the dynamical correlation length  $\xi_4$ , obtained from the spatial range of the dynamical correlator  $G_4$  (whose integral is equal to  $\chi_4$ ), see e.g. [16]. The dynamics are strikingly similar, a non-trivial result given the difference between an equilibrated thermal liquid and a non-equilibrium steady state of vibrated grains. One difference we find is that the average distance between avalanches is somewhat smaller in the liquid case than in the granular one:  $\sim 10$  as compared to  $\sim 27$ . Recent results [?] obtained by changing the density of the granular sample show that our model of a supercooled liquid would compare with a granular system characterized by a slightly smaller density.

We shall now investigate whether one can find a property closely connected to the structure at time  $t$ , which would allow one to predict where clusters will appear in the future and even some aspects of avalanche evolution. On the basis of previous work [12, 13] a natural candidate for such a feature are the so-called soft modes. Here we will use another means of identifying the location of "soft" regions or modes by using the isoconfigurational Debye-Waller (DW) factor [12, 17]. Starting from the system configuration at time  $t$ , one computes the local Debye-Waller factor for particle  $i$ :

$DW_i = \langle [\vec{r}_i(t) - \langle \vec{r}_i \rangle_{\delta t}]^2 \rangle_{\delta t, c}$ , where the average is over the isoconfiguration ensemble as well as over a short time interval  $\delta t$  which in this work is taken to be 25.

Starting from the same equilibrated configuration, we have run 6 isotrajectories and have obtained the cage jumps for all of them. Remarkably, all of the cage jumps occurring in the interval of time  $[t, t + \tau_S]$  fall on top of high  $DW$  areas, see fig. 2-top. Note that  $\tau_S \gg 25$ , thus the correlation between the  $DW$  map at time  $t$  (a nearly instantaneous structural quantity), and the dynamics taking place at longer times, is non-trivial.

Comparing the two top panels of Fig 2, we find that different isoconfigurational trajectories lead to cage jumps that take place at different times and in different regions although they are always located on top of high  $DW$  areas. This means that although clusters are very likely to be in soft regions, when and where they exactly appear is a stochastic event. The two top panels of Fig 2 strongly imply that a significant part of the avalanche structure of facilitated motion, and not just the initial cluster in an avalanche, occurs on top of the real-space geometric structure encoded in the soft mode map. Remarkably, we find that merging all cage jumps that occur in the interval of time  $\tau_S$  in the 6 isoconfigurational trajectories cover nearly all the high  $DW$  areas, as shown in fig. 2 (bottom left). A similar comparison with localized low frequency normal modes, along the lines of [12], shows less, but still significant, correlation. We interpret this as a signature of anharmonic effects appearing in the vibrational structure of our model of a supercooled liquid. Indeed, it is likely that there are several potential energy minima in the basin in which the liquid is confined at short times. The local  $DW$ s allow one to overcome this difficulty and still provide a measure of local softness. The above results are in agreement with the previous conclusion of Berthier and Jack [18], who found that structural properties are better predictors of dynamics on large as opposed to short length scales.

In order to present a more quantitative proof of the correlation between  $DW$ s and cage jumps, we have computed the  $DW$  at time  $t$  averaged only over particles that jump between  $t$  and  $t + \tau$  as a function of the lag time  $\tau$ . This quantity, normalized with respect to  $\langle DW(t) \rangle_t$  for all particles, is shown in fig. 2 (bottom right). We find that at short times the average  $DW$  for the jumping particles is substantially higher than the  $DW$  averaged over all particles. This correlation disappears for larger times comparable to times over which the  $DW$  maps decorrelate, which we find to be roughly of the order of  $\tau_\alpha/3$ .

A final issue worth investigating concerns the relation between cage jumps and  $DW$  map renewal. We find that decorrelation is a distinctly non-local process. More precisely, we have discovered that a cage jump at time  $t$  correlates with changes of the  $DW$ s that happen shortly after and extend quite far away. This is demonstrated visually in fig. 3(left). In order to provide a quantitative

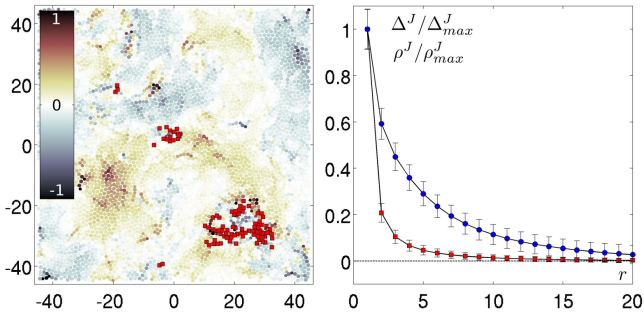


FIG. 3: (color online) Left: Cage jumps occurring in  $\tau = 17$  on top of a map of the relative difference  $(DW(t + \tau) - DW(t))/\langle DW \rangle$ . Right: Normalized  $\Delta^J(r) = \langle |\delta DW_i| \rangle_r^J - \langle |\delta DW_i| \rangle_\infty^J$  (blue circles) where  $\langle |\delta DW_i| \rangle_r^J$  is the absolute difference of  $DW$  over  $\tau = 17$  averaged over the particles in the disk of radius  $r$  around a given cage jump. The analogous quantity for the density of jumps  $\rho^J(r) = \langle \delta_i \rangle_r^J - \langle \delta_i \rangle_\infty^J$  (red squares) where  $\delta_i$  is 1 if particle  $i$  jumps between  $t$  and  $t + \tau$  and 0 otherwise. Error bars are given by the standard deviation.

proof we consider  $|DW(t) - DW(t + \tau)|$  averaged over all particles, that are at distance  $r$  from a cage jump taking place at time  $t$  and subtract from that quantity its  $r = \infty$  value. In fig. 3(right) we show this quantity, called  $\Delta^J(r)$ , for  $\tau = 17$ . One finds that  $\Delta^J(r)$  is quite long ranged, in particular much more than the cage jump correlation function  $\rho^J(r)$ , see fig. 3(right) and its caption for a precise definition of  $\rho^J(r)$ . What is mediating the non-local interaction between cage jumps and DWs is an intriguing question. One possibility is that a slowly varying spatial field, like the thermal strain discussed in [19], plays an important role by providing long ranged dynamical interactions.

The picture that emerges from our study is that the dynamics occurs, as in the dense granular system studied in [9? ], via a two time scale process that gives rise to dynamical heterogeneities and induces macroscopic relaxation. At short times, the particles collectively jump within clusters whose sizes are very widely distributed. These clustered jumps trigger other ones nearby, leading to well separated large scale avalanches.

We find that this dynamical facilitation process is coupled to the structure : mobility preferentially follows the soft regions and has a non-local influence on the evolution of the topography of hard and soft areas. The resulting picture of facilitation is quite different from the one based on the propagation of a conserved mobility field.

Studying the evolution of dynamical properties with decreasing temperature following the same analysis would allow for direct tests of prominent theories of the glass transition. For example, in the picture based on kinetically constrained models of glasses [6] facilitation should become more relevant and conserved upon lower-

ing the temperature. In the random first order transition theory [20], the dynamics should be correlated with soft regions for moderately supercooled liquids but, closer to the glass transition, the relaxation should be dominated by other processes. Three of us [? ] have performed such analysis for granular media and found that facilitation becomes *less* conserved as the density is increased. Performing a similar analysis for our model of supercooled liquids would be extremely important. Work in this direction is in progress.

We would like to thank J.-P. Bouchaud and L. Berthier for fruitful discussions. GB, RC and OD were partially supported by ANR DYNHET 07-BLAN-0157-01. DRR would like to thank the National Science Foundation for financial support. PH is supported through the Discovery program of the Australian Research Council. AW thanks the School of Chemistry at the University of Sydney for computer time on the Silica cluster.

- 
- [1] M. Goldstein, J. Chem. Phys. **51**, 3728 (1969).
  - [2] G. Marty and O. Dauchot, Phys. Rev. Lett. **94**, 15701 (2005).
  - [3] A. Abate and D. Durian, Phys. Rev. E **74**, 031308 (2006).
  - [4] C. O'Hern, S. Langer, A. Liu, and S. Nagel, Phys. Rev. Lett. **88**, 75507 (2002).
  - [5] A. Liu and S. Nagel, Nature **396**, 21 (1998).
  - [6] J. P. Garrahan and D. Chandler, PRL **89**, 035704 (2002).
  - [7] L. Berthier, G. Biroli, J. Bouchaud, L. Cipelletti, D. El Masri, D. L'Hote, F. Ladieu, and M. Pierno, Science(Washington, D. C.) **310**, 1797 (2005).
  - [8] C. Donati, S. Glotzer, P. Poole, W. Kob, and S. Plimpton, Phys. Rev. E **60**, 3107 (1999).
  - [9] R. Candelier, O. Dauchot, and G. Biroli, Physical Review Letters **102**, 088001 (2009).
  - [10] M. Ediger, C. Angell, and S. Nagel, J. Phys. Chem. **100**, 13200 (1996).
  - [11] A. Widmer-Cooper, P. Harrowell, and H. Fynewever, Phys. Rev. Lett. **93**, 135701 (2004).
  - [12] A. Widmer-Cooper, H. Perry, P. Harrowell, and D. R. Reichman, Nature Physics **4**, 711 (2008).
  - [13] C. Brito and M. Wyart, J. Stat. Mech. **8**, L08003 (2007).
  - [14] D. N. Perera and P. Harrowell, J. Non-Cryst. Solids **235**, 314 (1998).
  - [15] F. Lechenault, O. Dauchot, G. Biroli, and J. Bouchaud, Europhysics Letters **83**, 46003 (2008).
  - [16] S. Glotzer, V. Novikov, and T. Schröder, The Journal of Chemical Physics **112**, 509 (2000).
  - [17] A. Widmer-Cooper and P. Harrowell, Phys. Rev. Lett. **96**, 185701 (2006).
  - [18] L. Berthier and R. Jack, Phys. Rev. E **76**, 041509 (2007).
  - [19] A. Widmer-Cooper and P. Harrowell (2009), arXiv:0906.1766.
  - [20] T. R. Kirkpatrick, D. Thirumalai, and P. G. Wolynes, Phys. Rev. A **40**, 1045 (1989).

## 4.5 A few other ideas on the relation between dynamics and structure

Aside from the active main stream presented so far in this chapter, during this thesis we have done the groundwork in some other directions. These studies are neither concluded nor conclusive, but they are not information-less. In this section we first present our attempt to understand the detailed dynamics during a cycle of the cyclic shear experiment by means of a simulation. In a second part we will present the computation of several quantities stemming from the literature. Finally, a short study of a monodisperse system will set the basis for a few remarks of the general conclusion of this chapter.

### 4.5.1 Anatomy of a cycle

*Cycle tracks will abound in Utopia.  
Sometimes following beside the great high roads.  
– H.G. Wells, A Modern Utopia (1905)*

A question one can raise is the origin of cooperative motion in the cyclic shear experiment, evidenced via the clusters of cage jumps analysis. We have seen that this is a general feature of glass formers, but – to now – why this experimental system mimics the dynamics of glass-formers remains a profound mystery. Bridging the gap between the displacements during the shear and the statistical observations of the stroboscoped displacements could be an important achievement in this experimental device, and could give useful information on the essence of cooperative motion different from a soft mode analysis for instance.

At the cycle scale, a strong hypothesis we can do is to assume that the motion is driven both by the force network and by the friction with the bottom glass plate<sup>10</sup>. The packing fraction in the cell remains constant during shear, but the force network strongly evolves during a cycle. Can we characterize the typical evolution of the force network, and locate the cooperative events? To answer this question, we have two measures stemmed from the torque signal (global measure) and from a simulation (local measure).

### The shearing experiment's simulation

We have performed a simulation in collaboration with Matthieu Renouf from *INSA Lyon* that aimed at reproducing numerically the precise experimental apparatus. The goal was to measure the force network, which is the missing part of our experimental data. Unfortunately, reaching the packing fraction of 0.84 took almost one year of trials and CPU time, and still the dynamics

---

<sup>10</sup>Indeed, as we shear quasi-statically no inertial effect come into play.

of the particles over 1,000 cycles is different from the real system. A short discussion of the differences between the simulation and the experiment is given as an introduction.

**Discussion on the shearing experiment's simulation's data.** First of all, the displacements during a cycle have a different phenomenology. Here are two images showing the trajectories of the particles during one cycle:

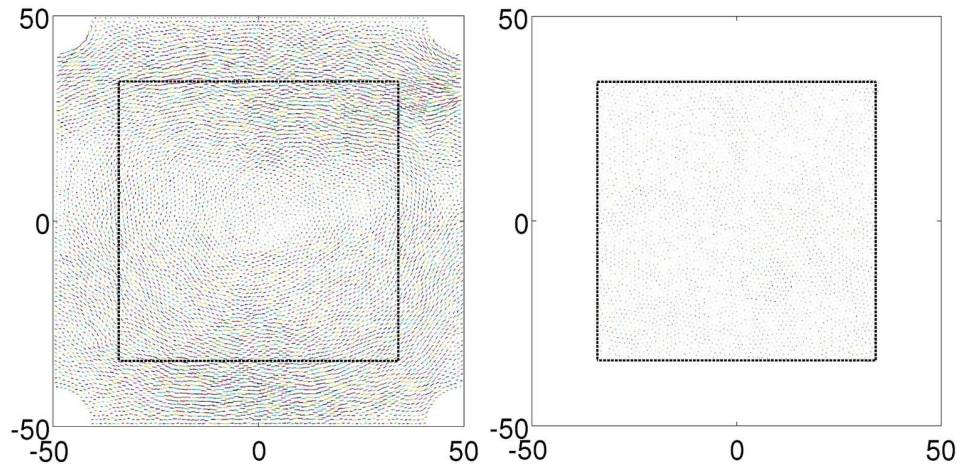


Figure 4.17: **Left** Unmagnified trajectories in the simulation, for all the particles during one single cycle decomposed in 400 discrete steps, at  $\phi = 0.819$ . The average shear has been subtracted at every time, and the dotted rectangle represents the visualization area of the camera in the experiment. **Right** Unmagnified (and therefore hard to see) displacements in a cycle of the cyclic shear experiment at  $\phi = 0.84$ .

Clearly, there is a difference of one order of magnitude in the displacements' amplitude. Note also that the dynamics is more heterogeneous along the vertical direction in the simulation.

Second, not only the displacements are larger in the simulation, they are also strongly correlated in time. When one integrates the trajectories on 1,000 cycles at  $\phi = 0.819$ , two large convection rolls appear (see left panel of fig. 4.18). Note that in this time lag a particle can move up to 30 diameters of grains! In the real experiment, grains typically move of 0.1 in the same number of cycles. At  $\phi = 0.830$ , these two convection rolls are smaller but one particle still moves of 5 diameters of grains on average (see fig. 4.18-right).

Finally, another major difference between the experiment and the simulation is that the displacements are strongly anisotropic in the simulation. Considering the displacement of  $N = 3,783$  particles in the center of the

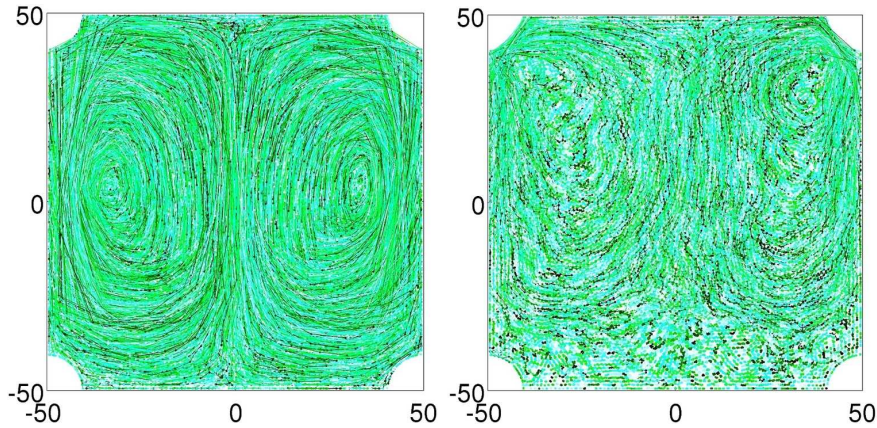


Figure 4.18: Convection in the shearing experiment's simulation: unmagnified trajectories of the particles on 1,000 cycles, at  $\phi = 0.819$  (**Left**) and  $\phi = 0.830$  (**Right**).

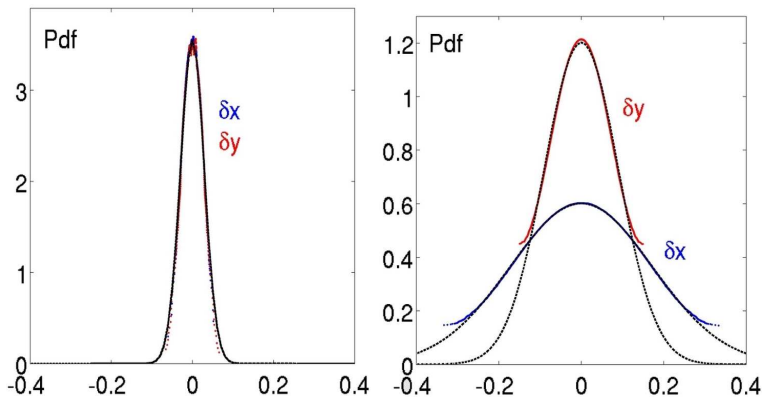


Figure 4.19: Pdf of the displacements parallel ( $x$ ) and perpendicular ( $y$ ) to the shear during one cycle of the experiment (**Left**,  $\phi = 0.84$ ) or the simulation (**Right**,  $\phi = 0.819$ ).

shearing cell, one can draw the Pdf<sup>11</sup> of the displacements over a single cycle along the  $x$  and  $y$  directions, as plotted in fig. 4.19 for the experiment and the simulation.

The distributions shown in the left plot are taken from the experiment: one clearly sees that the distributions of  $\delta x$  and  $\delta y$  are indistinguishable. They are well approximated by Gaussians (at the scale of one cycle, the large tails are not visible) with standard deviations of  $\sigma_x = \sigma_y = 4.1 \times 10^{-2}$ . On the contrary, the distributions shown on the right plot, stemming from

<sup>11</sup>Here the distributions are computed using the Kolmogorov algorithm described in [124]. This is a powerful method to represent Gaussian distributions when one has only access to a small statistics. Black dotted lines correspond to the Gaussian fit.

the simulation, display a strong anisotropy with  $\sigma_x = 0.69$  and  $\sigma_y = 0.29$ .

As a conclusion we can say that for the moment it is not possible to compare the dynamics in this simulation and in the experiment. However, despite the important differences presented above, one can argue that the dynamics in the simulation will become closer to the experiment's as the packing fraction is increased; in particular it is reasonable to expect that the global amplitude of the displacements will decrease and that the convection

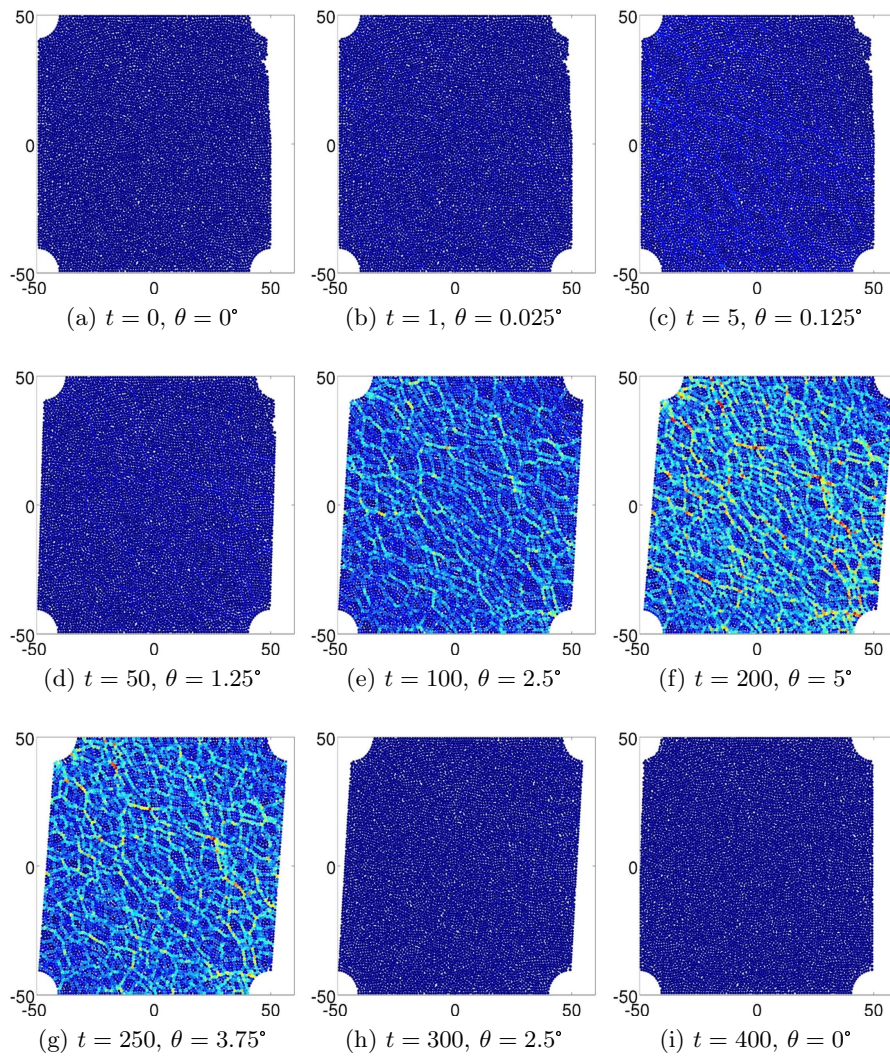


Figure 4.20: Normal stress  $\sigma_N$  during one cycle. The upper bar is going to the right from  $t = 0$  to  $t = 200$ , and then to the left from  $t = 201$  to  $t = 400$ . The shear angle  $\theta$  increases and decreases. Units are the same on all plots,  $\phi = 0.819$ .

will vanish. As the global evolution of the force network during a cycle in the simulation does not change in the range of packing fractions we have explored in the simulation so far (from 0.819 to 0.830), one can speculate that the following results may be *qualitatively* similar at higher packing fractions. A second speculation is that it may also be *qualitatively* similar to the experiment. Given these daring assumptions, we can briefly describe the evolution of the force network in the simulation.

**Evolution of the force network in the simulation.** A few representations of the normal stress network during the shear are shown in fig. 4.20. Clearly, the average amplitude of the normal stress  $\sigma_N$  increases as the assembly of grains is sheared. If we compare fig. 4.20 (e) and (h) which correspond to the same position of the cell, but for opposite shear rates  $\dot{\gamma}$  and  $-\dot{\gamma}$ , we see that the average amplitude is remarkably different. It seems that a major increase of the force network appears between  $\theta = 1.25^\circ$  and  $2.5^\circ$  when the shear strain increases, and it decreases between  $\theta = 3.75^\circ$  and  $2.5^\circ$ .

The probability density functions of the average value of the normal stress  $\sigma_N$ , computed on the whole set of grains for different times during the cycle and normalized by the average value  $\langle \sigma_N \rangle$  at this time, are shown in fig.4.21-left.

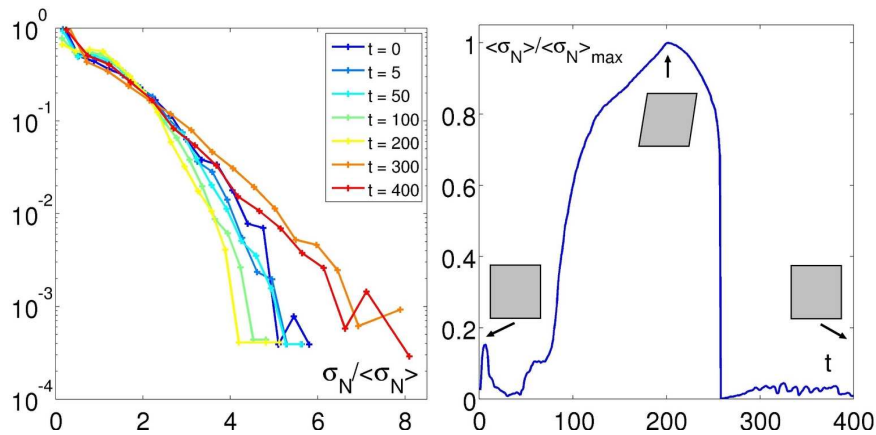


Figure 4.21: Stress during the shear cycle. **Left** Pdf of the normal stress  $\sigma_N$  normalized by the average normal stress  $\langle \sigma_N \rangle$ . The shear angle is increasing from  $t = 0$  to  $t = 200$  and decreasing from  $t = 201$  to  $t = 400$ . **Right** Average normal stress  $\langle \sigma_N \rangle$  through time, normalized by its maximal value.

They are roughly exponential<sup>12</sup>. However, the tails of the Pdf have a deviation from the exponential that is maximal at  $t = 200$ , *i.e.* at the maximal

<sup>12</sup>This echoes many experimental works on the statistics of constraints in *static* piles of grains. See for instance [125, 126]

shear angle.

The average value of the normal stress (see fig. 4.21-right) is maximal when the shear angle is maximal, but the curve is not symmetric around this peak. First of all, when the shear increases continuously the normal stress grows non-monotonically by bursts, especially at the low angles. An important burst occurs around  $t = 100$  ( $\theta = 2.5^\circ$ ). On the contrary, when the cell is returning to its original position – still at a constant shear rate – the normal stress decreases monotonically, faster and faster such that it drops to zero in a very sharp manner. After this steep decrease, there are only a few fluctuations but no major rearrangement.

One would like to have more statistics in order to establish the distribution of the maximal stress during a cycle, or to see if the steep falling down occurs always at the same angle or not for instance. This short study clearly shows that the force network amplitude increases significantly during the shear. We interpret this increase as the appearance of several local, non optimal deformations due to the global shear, similarly to the famous dilatancy effect for hard spheres described by O. Reynolds in 1885 [127].

**Evolution of the torque during one cycle.** We can have another evidence of this effect, experimentally. Figure 4.22 shows that the evolution of the torque needed to drive the system<sup>13</sup> is non-monotonous during a cycle. When starting from the rectangular position *i.e.*  $\theta = 0^\circ$  and applying a constant shear rate, the torque increases convexly. When the maximal shear is reached, the cell starts to come back to its initial position. At this point the sign of the torque changes, but its absolute value is lower than before the turnaround and decreases in a less pronounced manner until the cell returns to the rectangular position again.

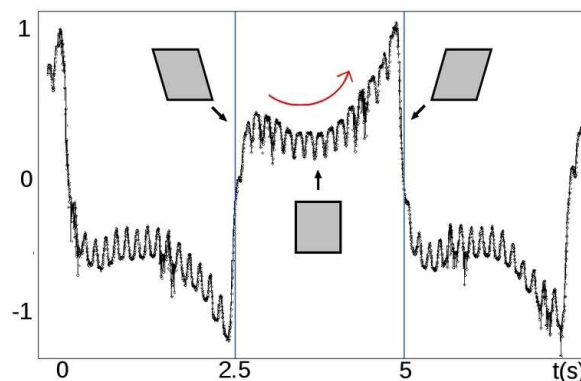


Figure 4.22: Torque signal during cyclic shear. The blue vertical lines delimit half a cycle: the angle goes from  $\theta = -5^\circ$  to  $5^\circ$ . The torque first decreases until  $\theta = 0^\circ$ , and then increase more sharply. The signal is expressed in Volts ( $1 \text{ V} \equiv 0.25 \text{ N.m}$ ).

As a conclusion, one can see that though we can globally describe the evolution of the force network, we are far from being able to locate the

<sup>13</sup>Indeed the motor is set up to apply a constant shear rate. The torque acquisition is presented in 2.1.2.

cooperative reorganization events. In the experiment, the precision of the torque sensor is strongly limited by the internal stresses of the device (see the small oscillations on fig. 4.22), such that we cannot measure fine details of the torque evolution. In the simulation, both the precautions introduced in the preliminary discussion paragraph and the lack of statistics grandly weaken the analogy.

Guide lines for future work on this matter are (i) to refine the simulation, first by increasing the packing fraction and then maybe by taking into account the friction with the bottom plate, and (ii) to conduct the experiments with photoelastic disks to access the statistics of the contacts, like in [128, 71].

#### 4.5.2 A few other ideas that did not really worked, and why

*One day Alice came to a fork in the road and saw a Cheshire cat in a tree. Which road do I take? she asked. Where do you want to go? was his response. I do not know, Alice answered. Then, said the cat, it does not matter.*  
– Lewis Carroll, Alice’s Adventures in Wonderland (1865)

Here, let us present several structural quantities that we were not able to link with neither the cage jumps nor the dynamical heterogeneities. A few explanations on why no correlation is observed or cannot be observed are given.

**Free volume.** The first quantity one can try to compute is the free volume per particle. The idea is to associate the ability to move to the voids present in the packing. We define the free volume as:

$$\mathcal{F}_i = \frac{S_c^i - S_h^i}{S_h^i} \quad (4.7)$$

where  $S_c^i$  is the surface of the voronoi cell associated to the particle  $i$ , and  $S_h^i$  the area of the hexagon fitting particle  $i$ . This approach does not give rise to any correlation between the dynamics and the free volume, as one can see in fig. 4.23.

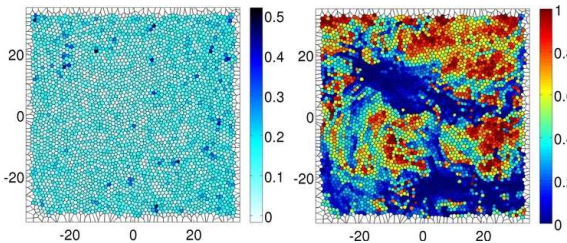


Figure 4.23: **Left** Free volume  $\mathcal{F}$  at an arbitrary time  $t$ . **Right** Local relaxation  $q_i^t(\tau^*)$  induced by the displacements between  $t$  and  $t + \tau^*$ . From the cyclic shear experiment.

The voids in the system are scattered everywhere in the media, such that on a coarsegrained scale they are homogeneously distributed and fail to

describe the spatial heterogeneity of the dynamics. In addition, the average amount of free volume does not evolve and has small temporal fluctuations, while the dynamics is highly intermittent.

**Defects.** A persistent idea is that the defects of the packing (defined as the particles with a number of neighbors different from 6, in  $2D$ ) may be responsible for the sluggish dynamics. However, though it is true that a low concentration of crystallographic defects like vacancies or dislocations can control the mechanical properties of a crystal, the situation is completely different in dense amorphous media.

In this matter we can cite the work of Aharonov *et al.* [129]: in a  $2D$  mixture of softly repulsive discs, the authors emphasize the role of “fluid-like” defects, namely small particles enclosed in heptagons (or even octagons), and large particles enclosed in pentagons (or even squares). While in the glass phase the authors observe only defects of the opposite type, *i.e.* small particles in heptagons and large particles in pentagons, all types of defects are observed in the liquid phase (see fig. 4.24-left and middle). They therefore propose that “*the concentration of liquid-like defects is a superior indicator of the glass transition in comparison with relaxation times*”.

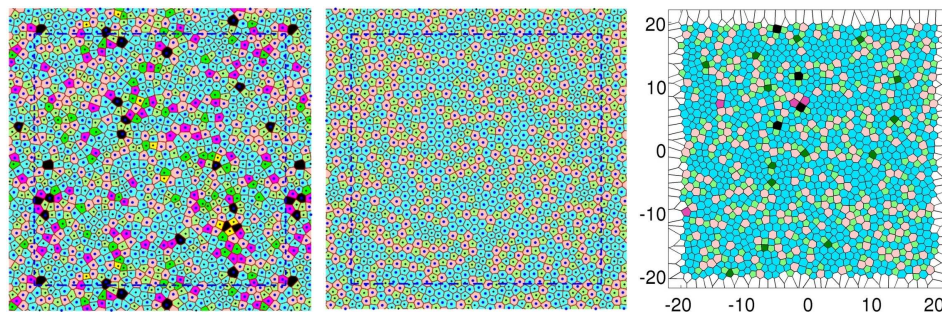


Figure 4.24: Defect on both sides of the transition. **Left** Typical Voronoi construction in the liquid state at  $T = 3$ . Small particles in pentagons (resp. heptagons) are light green (dark green) and large particles in pentagons (heptagons) are violet (pink). **Middle** Typical Voronoi construction in the glass phase at  $T = 0.1$ . Left and middle plots are from Aharonov *et al.* [129]. **Right** Typical Voronoi construction in the vibrating experiment at  $\phi = 0.8457 > \phi_J > \phi_G$ , same color code. Clearly, liquid-like defects are still present.

However, when one plots the same color-coded Voronoi tessellation in the data of the vibrating experiment for the very dense states that are above jamming and therefore far above the glass transition, several liquid-like defects are still present. And as the structure is not evolving on the experimental timescales, they will not vanish even with infinite patience.

So, the statement of Aharonov *et al.* fails in this system.

Importantly, the number of unlikely defects in the glass phase strongly depends on the protocol and especially on the cooling rate, so we believe that it *cannot* be an indicator of the “glassiness” of a state, but simply an approximate measure of its history.

**Medium range crystalline ordering** A variation on the role of the structural defects has been proposed recently by Tanaka & coworkers [130, 131], who looked into “medium range crystalline ordering” (MRCO). In numerical and experimental studies, these authors emphasize the role of the bond-oriental order parameter  $\psi_6$  defined for each particle  $j$  as:

$$\psi_6^j = \frac{1}{n_j} \sum_{k=1}^{n_j} e^{i6\theta_{jk}} \quad (4.8)$$

where  $n_j$  is the number of neighbors of  $j$ , the sum is made over the  $n_j$  neighbors and  $\theta_{jk}$  is the angle between the vector  $\vec{j}\vec{k}$  and a reference direction.  $\psi_6$  is a complex number, whose modulus  $\bar{\psi}_6$  is 1 if the neighbors are located at the vertices of a perfect hexagon and decreases to zero as the local disorder increases. Its phase  $\phi_6$  indicates the local orientation of the hexagonal order.

The authors find a correlation between  $\bar{\psi}_6$  and the classical Debye-Waller (DW) factor, as illustrated on fig. 4.25-left: in the highly ordered regions (red) the particles have a smaller DW-factor than in less ordered regions. In a granular experiment [131], the authors observe the well-known patterns of dynamical heterogeneities (see fig. 4.25-middle) and highlight the fact that the  $\bar{\psi}_6$  exhibit MRCO, whose spatial distribution correspond to clusters of slow particles.

The statement that such a correlation exists is a very strong one, and, actually, we could not observe any correlation of this kind in our systems. For instance, in the cyclic shear experiment, we have plotted several maps of the modulus and phase of the bond-orientational parameter averaged over the time at which dynamical heterogeneities are maximal  $\tau^* \simeq \tau_\alpha$ , like the ones depicted in the top panel of fig. 4.26. Interestingly, large domains appear, indeed denoting the presence of medium-range order<sup>14</sup>. The 2-point correlation function  $q_i^t(\tau^*) = \exp(-\Delta r(\tau)^2/2\sigma(\tau)^2)$  map starting at the same initial time is given for a comparison in the bottom-left panel. One clearly observes that the decorrelation domains do not match the above patterns.

Maybe the strongest evidence of the absence of such a correlation in our data is the representation of  $q_i^t(\tau^*)$  versus  $\bar{\psi}_6$  for every particle, as in

---

<sup>14</sup>Marty had already shown [20] that the translational order decays very rapidly on lengthscales of the order of 1-2 but that the orientational order typically decays over a larger lengthscale, of the order of 5-6.

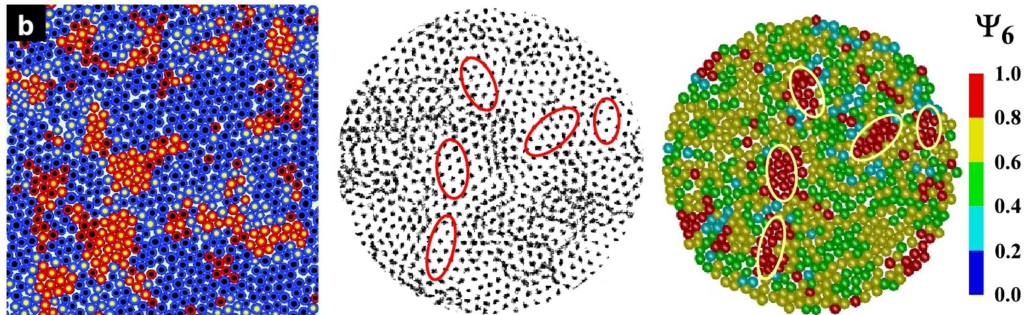


Figure 4.25: Dynamic heterogeneity and MRCO. **Left** Correlation between  $\bar{\psi}_6$  and the DW factor at  $\phi = 0.631$  for polydisperse simulated soft disks ( $\Delta = 9\%$ ). The outer region of each particle is colored red for  $\bar{\psi}_6 > 0.75$ , otherwise blue. The inner region is colored in yellow if  $\langle \Delta r^2(\tau_\alpha) \rangle < 0.063$ . From Kawasaki *et al.* [130]. **Middle** Particle trajectories on  $\tau_\alpha$  in a driven quasi-2D granular matter at  $\phi = 0.774$ . **Right** The corresponding bond-orientation modulus  $\bar{\psi}_6$ , averaged over  $\tau_\alpha$ . From Watanabe and Tanaka [131]

fig. 4.26-bottom-right. This cloud of point strikingly establishes that even a small correlation cannot be found.

Several reasons can be invoked for the absence of correlation. The interested reader is invited to follow the controversy in [132] and [133]. We would just like to underline that it is a strong statement to assume that the less mobile regions are mainly arranged in crystalline order: a closer look at fig. 4.25-left reveals that amongst the particles that move less than a certain arbitrary criterion (yellow particles) there are 163 particles with a  $\bar{\psi}_6 > 0.75$ , *i.e.* in hexagonal order, and 167 with  $\bar{\psi}_6 < 0.75$ . Actually, fig. 4.25-left simply demonstrates that the particles with an hexagonal neighborhood count among them less mobile particles ( $\sim 35\%$ ) than the particles with a disordered neighborhood ( $\sim 78\%$ ). So, it is true that when there are crystallite domains, they concentrate a higher proportion of slow particles, but this cannot explain the whole story since in the disordered regions there is still an important heterogeneity in the dynamics. Especially in the systems where no micro-crystallization is observed, like in the non-additive simulation presented in 2.1.4, or in systems where the typical size of the micro-crystallites is far below the size of the dynamical heterogeneities, like the cyclic shear experiment.

**String-like motions.** It has been suggested in some models (*e.g.* [134]) and in experiments (*e.g.* the fluidized bed experiment [84]) that the reorganizations of the particles in glass-formers have “string-like” shapes, and that this features become increasingly salient as the glass transition is approached [135].

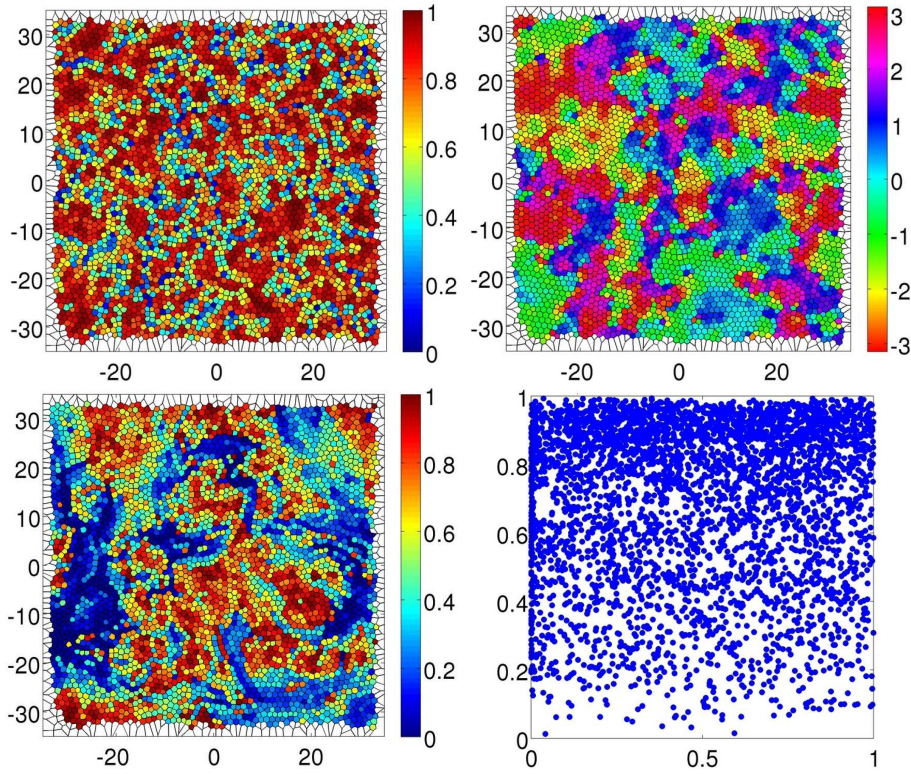


Figure 4.26: Comparison between the bond-orientational parameter and the relaxation in the cyclic shear experiment. **Top left** Modulus  $\langle \bar{\psi}_6 \rangle$  averaged over  $\tau^*$ . **Top right** Local orientation of the hexagonal order,  $\langle \phi_6 \rangle$ , averaged over  $\tau^*$ . Colors represent the angle with the horizontal line oriented to the right. **Bottom left** Local relaxation  $q_i^t(\tau^*)$  induced by the displacements between  $t$  and  $t + \tau^*$ . **Bottom right**  $\langle \bar{\psi}_6 \rangle$  (vertical axis) vs  $q_i^t(\tau^*)$  (horizontal axis).

Clearly, this statement cannot stand for the large decorrelation patterns of the dynamical heterogeneities, formed of vortices and large currents, but could well describe the “cracks” one can see on short time scales, and that we call the clusters of cage jumps. Rephrasing this idea, one can ask the following question: do the cage jumps have a preferential direction, and is this direction pointing to a neighboring particle?

To check this, we have computed the angular Pdf of the angle between the displacement during a jump and the direction of the neighbors (in the sense of Voronoi) just before the jump. The result is presented in fig. 4.27-left:

This Pdf does not exhibit any special behavior around 0, corresponding to the direction of the displacement, and is identical to the randomly distributed angles case within the experimental accuracy. So in the cyclic

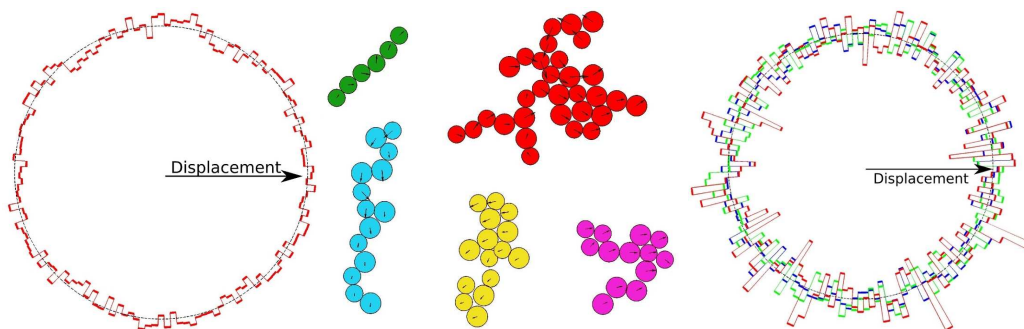


Figure 4.27: **Left** Probability to find a neighbor at any angle from the direction of motion, depicted by the arrow. The black dashed circle indicates the uniform distribution. **Middle** Examples of clusters from the cyclic shear experiment., with the displacements  $3\times$  magnified. Some are clearly string-like, other are not. **Right** Same as the left plot, for the 3 densest states of the fluidized bed experiment,  $\phi = 0.780$  (blue),  $0.791$  (green) and  $0.802$  (red).

shear experiment, the prediction fails. This is confirmed by a visual inspection of the clusters' shapes; though some of them are like strings, several other form denser aggregates, and even for the clusters with a string shape the displacements are not oriented in the direction of the moving neighbors.

One could argue that this experiment is at a fixed packing fraction, and that the clusters could change shapes on approach to the glass transition. Our point is that we *already* observe dynamical heterogeneities, and that string-like motion is not at the root of it.

To conclude this point, we can add that even if in the fluidized bed experiment the motion of the fastest beads has been observed to be preferentially string-like [84], the jumps are not either preferentially oriented along the direction of a neighbor (see fig.4.27-right).

**The puzzling  $\vartheta$ .** Last but not least, let us finish this panorama by the computation of the following quantity: we call  $\vartheta_i^t(\tau)$  the angle between two vectors, the first one being the displacement  $\Delta\vec{r}_i^t(t, \tau)$  of the particle  $i$  between  $t$  and  $t + \tau$ , and the second being the vector  $\vec{V}_i$  linking the position of the particle to the farthest vertex of its Voronoï cell. Intriguingly, this quantity does not have a uniform Pdf, like depicted in fig. 4.28.d

The fact that the distribution of  $\vartheta$  has an excess of values close to 0 indicates that a correlation exists between the purely structural vector  $\vec{V}$  and the future displacements, and that this correlation is maximal around  $\tau^* \sim \tau_\alpha$ , the typical time scale of the relaxation.

However, this is where the correlations end. All our further attempts to link this quantity to the dynamical heterogeneities failed, especially when

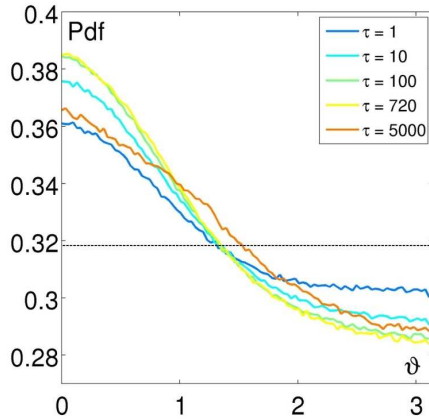


Figure 4.28: Pdf of  $\vartheta_i^t(\tau)$  for five values of  $\tau$ . The uniform distribution is represented by the horizontal dashed line. Note that the correlation is maximal for  $\tau \sim \tau^* = 720$ . From the cyclic shear experiment.

we tried to correlate  $\vec{V}_i$  with the direction of the next cage jumps instead of the next displacements.

Our interpretation is the following:  $\vec{V}$  roughly indicates in which direction each Voronoï cell is discarded (when it is), and this basically rules the “shape” of the cage. If the cage is elongated, the vibrations around the equilibrium position are preferentially going along this direction, hence creating the correlation. However, the shape of the cell/cage does not predict the direction of the next cage jump, which is a *cooperative* event. The correlation presented above is maximal around  $\tau_\alpha$  because this is the typical relaxation time of the shape of the cage. This example highlights the danger of abrupt correlations attempts.

**What is required for a *structural* quantity to describe well the heterogeneous *dynamics* of glass formers?** To sum up, we can state the two following criteria that are required for a structural quantity to well describe the dynamical heterogeneities:

- The criterium of *temporal intermittency*. A structural quantity that aims at describing the intermittent dynamics has to be intermittent itself, on the same characteristic time scale. This time scale is much longer than the collision time and much shorter than the diffusion time.

This criterium is tremendously difficult to satisfy for a *purely structural* quantity. To give a concrete idea, remember that the dynamics may be either totally arrested or over-active in a whole region of space, eventually spanning the whole system when it is finite. This criterium directly eliminates all the conservative quantities (*e.g.* free volume) or “statistically conserved” (*e.g.* defects).

- The criterium of *delocalization*. Recently, Berthier and Jack [136] argued against a connection between structure and dynamics at the par-

ticle level, but showed that it should exist for larger length scales. What is the length scale stemming from this second criterium? Our analysis tend to say that it is the cluster scale, which may be quite small for systems far from the transition but is expected to grow as the system goes glassy.

So far, the only quantity we have tried that meets the prescribed two criteria is the isoconfigurational Debye-Waller factor defined by Widmer-Cooper *et al.* . However, though it is quite clear that it is a quantity that is freed from the details of the dynamics, the precise structural features it probes are still quite ambiguous, and call for further investigations.

### 4.5.3 What would a crystal think of all this?

*Thoughts are formless, coded... impulses without shape or substance or direction – until you convey them to someone else. Then they precipitate, and become ideas that you can put out on the table and examine.*  
– Theodore Sturgeon, *The Dreaming Jewels* (1950)

If a glass former was dreaming like a jewel, it probably would have the same kind of thoughts: one can indeed recognize in the above quote an interesting description of the clusters of cage jumps as “impulses without precise shape or direction”.

Actually, recent studies by Reis, Ingale and Shattuck [92, 93] on a monodisperse vibrated assembly of beads report that several features classically attributed to the glass transition can also appear when an ordered crystal forms. First of all, cage-like motion is observed, both by direct observation of the trajectories or the MSD curves, exhibiting a plateau before recovering a diffusive regime (see fig. 4.29-left). In addition, at “high” packing fractions the intermediate scattering function also develops a plateau before a late relaxation regime, as illustrated in fig 4.29-right. Stretched exponentials describe well the late relaxation, and the associated time scale follows a Vogel-Fulcher-Tamman behavior.

So, where does the analogy between a fluid going toward an ordered solid state and a disordered solid state stops? Surprisingly, this is a rather poorly investigated question in the glass-makers community. In particular, one issue that has not been addressed yet is the comparison of the growth of the time and length scales *within* the liquid phase; it is indeed expected in “crystal-formers” that above the liquidus point  $\phi_l$  some crystallites bloom inside the liquid phase, leading to strongly heterogeneous relaxations. But if one removes the crystallites from the analysis and keep only the liquid phase, which is in a supercooled state, can one observe growing dynamical heterogeneities as the packing fraction increases<sup>15</sup>? If so, are they similar to

---

<sup>15</sup>This is hardly feasible in real liquids, but can be achieved in simulations or experiments where the positions of the particles are accessible.

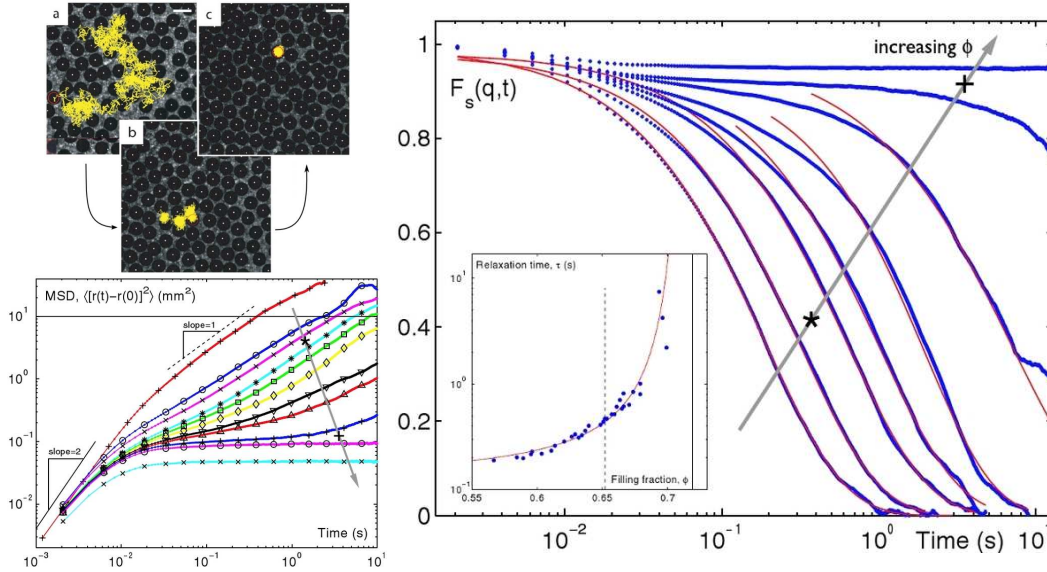


Figure 4.29: **Left top** Experimental frames with superposed typical trajectories of a single particle at  $\phi = 0,567$  (a),  $\phi = 0.701$  (b) and  $\phi = 0.749$  (c). The scale bar is 2 mm. **Left bottom** Time dependence of the MSD for several packing fractions between  $\phi = 0.570$  and  $\phi = 0.771$ . The red curve is for a single particle. **Right** Intermediate scattering function, with  $qD = 2, 14$ , for various packing fractions ranging from  $\phi = 0.570$  to  $0.754$ . The blue curves are fits to stretched exponentials. **Inset** Relaxation time  $\tau_\alpha$  extracted from the intermediate scattering function as a function of packing fraction. The red curve is a fit to the Vogel-Fulcher law. Dashed and solid lines represent the location of the liquidus and solidus points, respectively. In the bottom-left and right plot, arrows indicate increasing  $\phi$ , the symbols ( $\star$ ) and ( $+$ ) being located at respectively  $\phi_l$  and  $\phi_s$ . Adapted from Reis *et al.* [93].

the dynamical heterogeneities of the glass formers? For instance, we would like to know if the cage jumps reported in the work of Reis *et al.* are the fate of particles passing from crystallites to the liquid phase or if they appear in the supercooled liquid phase exclusively. We would also like to know if they organize in cooperative events or not.

Unfortunately, we were not able to address these questions in the data of [93], which are focusing on a too small region of space. To illustrate the importance of these finite size effects for our concerns, we can compute the henceforth famous “banana plot”<sup>16</sup>, showing  $\chi_4$  as a function of the probing lengthscale ( $a$ ) and timescale ( $\tau$ ) (see fig. 4.30-top for two representative packing fractions) *without removing the crystallites*. The dynamical suscep-

<sup>16</sup>See appendix B.2.1 for a definition.

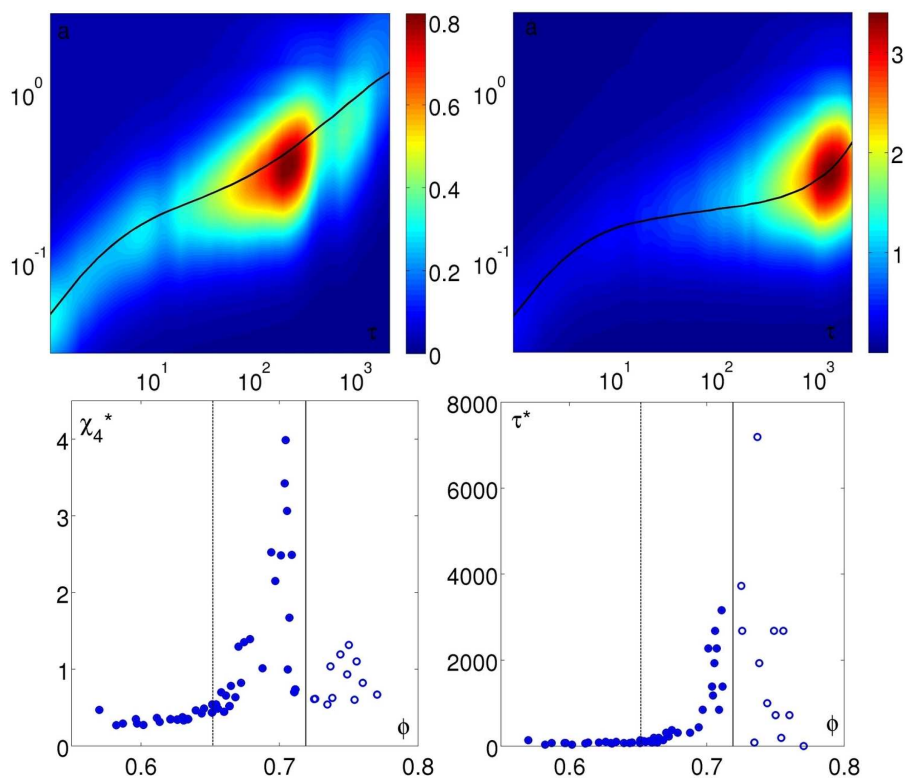


Figure 4.30: **Top** Banana plots ( $\chi_4(a, \tau)$ ) for two representative packing fractions in the monodisperse experiment, namely at  $\phi = 0.672$  (left) and  $\phi = 0.704$  (right). The corresponding RMSD curves are shown in black. **Bottom left**  $\chi_4^*$  as a function of the packing fraction. **Bottom right**  $\tau^*$  as a function of the packing fraction. In both bottom plots the packing fractions of the liquidus (dotted,  $\phi_l = 0.652$ ) and solidus (solid,  $\phi_s = 0.719$ ) points determined in [92] are indicated with vertical lines. Open symbols indicate the points where  $\tau^*$  is experimentally out of reach; the values may therefore be strongly biased.

tibility, probed on the time and scales at which it is maximal, display a peak between the liquidus and the solidus points (see fig. 4.30-bottom left). If one assumes the picture of the liquid-crystal coexistence, this corresponds to the moment where the dynamical heterogeneity “artificially” induced by the intimate mixing of crystallites in the fluid phase is maximal.

The time scale associated to this heterogeneity sharply grows as the solidus point is reached because the crystallites are long-lasting structures. One can see however that the measure of  $\tau^*$  is only relevant below  $\phi \lesssim 0.70$  since the banana strongly shifts to the long time scales; above this packing fraction the experimental data fail to pinpoint  $\tau^*$ , which diverges. This explains the fuzzy values represented with open symbols in fig. 4.30-bottom

right.

Note that the values of the  $\chi_4^*$  are extremely small: the maximum is 4. This number is undervalued since we expect the crystallites to be bigger than that at the maximally heterogeneous point. Actually, this is an effect of the very small size of the system: we have  $\sim 100$  particles in the visualization area in the best cases. It strongly biases the spatial correlations and leads to unrealistic values. For instance, one can see that we robustly find values less than 1 at low packing fractions; a spatio-temporal correlation of half a particle is hardly meaningful!

So, for the moment, these questions are on the sidelines. We believe that further experiments / simulations in this matter could clarify the necessary conditions for the formation /avoidance of the crystalline phase, and if one can attribute some features of the glassy dynamics to an avoided crystallization.

We can not avoid to mention here the work of Sausset and Tarjus [137, 138] on simulated 2D Lennard-Jones liquids embedded in a negatively curved space. This is a way to introduce some *frustration* in the packing, whose strength is directly determined by the curvature of the hyperbolic plane. As a result, the liquid does not crystallize but forms a glass upon cooling; for instance the authors report a slow relaxation and dynamical heterogeneities. Interestingly, the buildup of spatial correlations associated with the relevant structural local order parameter controls the slowdown of the relaxations as the temperature is lowered and is directly connected to the growth of a dynamical lengthscale. Such work illustrates the desire for unveiling the conditions in which frustration controls the dynamics. The crucial missing part is now to explain the origin of frustration in real liquids; and maybe the most frustrating point is to ignore where does the frustration come from.

## 4.6 Discussion and perspectives

To sum up, our approach to study the dynamics in glass-formers is based on the knowledge of the cage jumps (CJ). We have built an algorithm to accurately detect them, and the resulting set of CJ is just a very small fraction of the displacements (0.4‰ of the total particle/times) but describes well in space and time the structural relaxation. We can therefore reduce the dynamics to the only jumps to characterize its main features.

It appears that above a certain density the unitary relaxation events are already cooperative, forming clusters. Our study of the clusters in space and time revealed the interplay and evolution of several time and length scales.

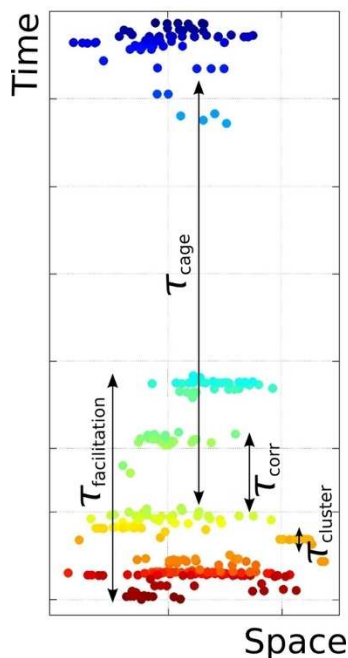


Figure 4.31: Illustration of the time scales at play in a specific region of space. Each dot is a CJ, and space is projected on one axis.

Considering only one specific region of space, three timescales describe the dynamics (see fig. 4.31). The shortest one is the time of the cluster itself,  $\tau_{cluster}$ . It is quasi-instantaneous, and its value is of the order of the precision of the detection algorithm, such that no propagation is seen inside the clusters.

Then, two time scales describing the relative position of the clusters can be extracted. The longest time corresponds to the long lags during which no CJ happen, and is equivalent to the cage time  $\tau_{cage}$ . The shortest one corresponds to the typical time between two adjacent clusters in space and time, which we define as the correlation time  $\tau_{corr}$ . This reflects *facilitation*, in the sense that the distribution of clusters in space and time is not at random, *i.e.* that concentrated aggregates of clusters form; the counterpart is the formation of voids. So one can define the facilitation time  $\tau_{facilitation}$  as the typical duration of the avalanches of clusters, as depicted in fig. 4.31.

The notion of *causality* has been little explored. For instance, the bottom panels of fig. 3 in [85] show that there is some *propagation* among the clusters of an avalanche in the densest states of the fluidized bed experiment. We have made the same observation in the cyclic shear experiment, but only on some avalanches. However no quantification of this effect has been done. In addition, we let open the possibility of an underlying mechanism which would express itself in terms of clustered CJ.

One can then link the cage time to the timescale of structural relaxation,

$\tau_\alpha$ . Under the assumption that all particles obey the same jumping distribution – an exponential with a typical decay on  $\tau_{cage}$  – the typical time needed so that half the particles jump at least once  $\tau_{1/2}$  can be easily deduced:

$$\tau_{1/2} \simeq \tau_{cage} \cdot \ln(2) \sim 0.7 \tau_{cage} \quad (4.9)$$

Note then that the typical structural relaxation time is defined when half the particles have decorrelated, and that the timescale  $\tau^*$  at which dynamical heterogeneities are maximal requires – by definition – that also half the particles have decorrelated. Hence:

$$\tau_\alpha \simeq \tau_{1/2} \simeq \tau^* \quad (4.10)$$

The two above relations are very general. In addition, one can also deduce from the timescales relations a rough estimate of the number of jumps per avalanche. Indeed, if there is one jump per avalanche, one has  $\tau_S \ll \tau_{cage}$  and  $\tau_L \sim \tau_{cage}$ , while if there are two jumps or more per avalanche one has  $\tau_S \sim \tau_{cage}$  and  $\tau_L \gg \tau_{cage}$ . All studied systems correspond to the first case. Given the fact that jump events facilitate each other, it is a remarkable feature that each particle jumps only once in each avalanche<sup>17</sup>. We have no suggestion so far to explain this *locking* mechanism, but it surely deserves further attention.

Then, some lengthscales can be associated to these times (see fig. 4.32). We can easily separate the lengthscales that are *below* the particle scale, like the typical cage size and jump size, and the lengthscales *above* like the typical size of the dynamical heterogeneities  $\xi_4^*$ . Note that as the clusters have large-tails distributions, they do not have a typical size and one has to content with experimental averages.

When the packing fraction increases, we observe two salient effects. First, the typical cage time and the structural relaxation time sharply increases, as expected. Second, on the contrary the correlation time is constant. This has several consequences: avalanches become more and more concentrated in space and time; this means, that their typical duration, normalized by to the typical relaxation time  $\tau_\alpha$ , decreases. The facilitation patterns evolve from a monolithic structure towards several distinct avalanches; this means that facilitation is less and less conserved. The space-time patterns projected on the spatial plane evolve from an homogeneously scattered set of dynamical events to well separated dense aggregates; this means that the lengthscale of the dynamical heterogeneities increases.

The observations that we have made in the data of the fluidized bed experiment certainly call for confirmation in other systems. For instance, an appropriate sanity check would be to perform such an analysis onto a simulation of a liquid at several temperatures. This would confirm the above

---

<sup>17</sup>The average number of jumps per particle in an avalanche is 1.27 in the cyclic shear experiment and 1.12 in the densest state of the fluidized bed experiment.

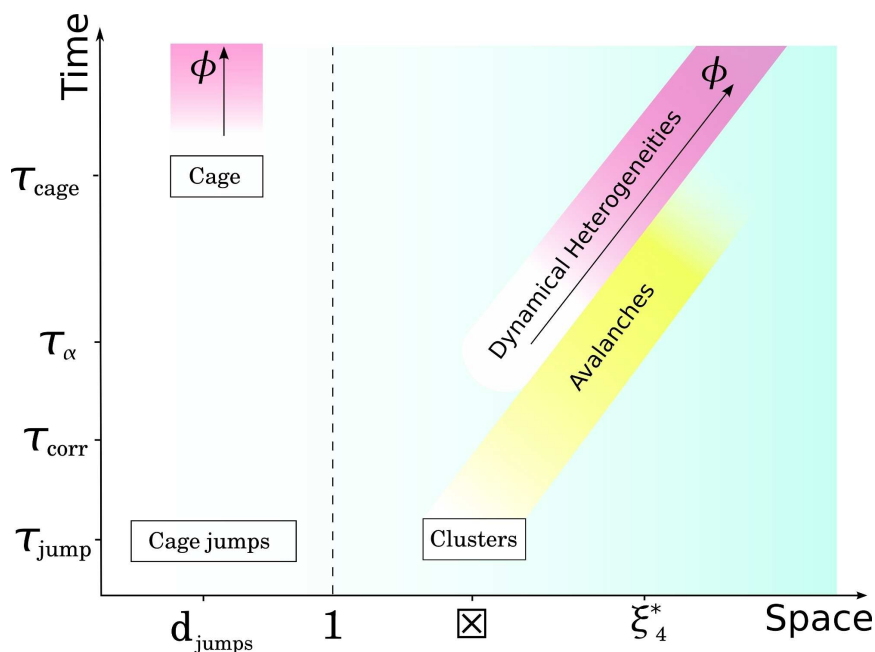


Figure 4.32: A sketch for the time and length scales in the studied regime.

scenario and may give insights on the regimes that are even closer to the glass transition. Are the avalanches reduced to single clusters, the size of which would diverge? Up to what point does the facilitation time remain constant? These exciting questions may then find an answer.

Another interesting track is to search for the origin of cooperative motion. This is what we have done in [38], and our main result is that the iso-configurational Debye-Waller factor (IDWF) computed on very short time scales nicely predicts where the cage jumps have a high probability to occur on much longer time scales of the order of  $\tau_{\alpha}/4$ . Altogether with the previous results of Widmer-Cooper *et al.* [26], namely the fact that irreversible reorganizations originate from localized soft modes, a coherent framework emerges in which the shape of the metabasin in which the system lies, probed by both the quenched normal modes and the IDWF, determines a finite part of the future evolution of the system. Care has to be taken anyway, and several checks have to be done to understand deeper what the IDWF exactly probes in the structure.

The question of the structural origin of the slow relaxation in amorphous matter is still a challenging issue. In light of our results we cannot say *what* in the structure is driving the dynamics, but we can say that *something* in the structure determines a finite part of the dynamics. Arriving to this statement may be only a small step for the understanding of glass formers in general, but it seemed like a giant leap for us.

# General conclusion

## Summary and discussion

In this thesis, several systems made of dense assemblies of particles have been studied. Beyond their peculiarities, some general properties can be drawn, and especially the noteworthy similarities with the phenomenology of glass formers. We have studied both the dynamics of supercooled liquid-like situations, *i.e.* below the glass transition, as well as the jamming of out-of-equilibrium configurations, *i.e.* above the glass transition.

On the one hand, the tremendous dynamical slowdown of the particles is related to the delayed structural relaxation, which has been shown to be intrinsically heterogeneous. On the other hand, the dynamics close to jamming also exhibits a heterogeneous behavior, but for other reasons, namely because it signs the critical nature of this second transition. A large part of our work has been devoted to characterizing these both types of dynamical heterogeneities, and the associated tools (*e.g.* the four point dynamical susceptibility) have been extensively used to unveil growing dynamical lengthscales in these different contexts.

On one hand, the growth of dynamical correlations patterns in the supercooled branch when the temperature is lowered or, equivalently, when the packing fraction is increased has been demonstrated in a wide class of glassy systems. Here, we have explored the general microscopic mechanisms at the root of the large dynamical correlations: in our “micromechanical” description the elementary relaxation events are the clusters of cooperative jumps, which sign the trajectories with the well-known cage effect. We have investigated in detail first how these clusters construct large decorrelation patterns on intermediate timescales for a fixed packing fraction, and then the evolution of the resulting scenario as the packing fraction increases. The problem is henceforth reduced to the question of the nature of the cooperative events. Though soft modes are very good candidates to explain cooperative events in liquid simulations, the question remains wide open in experimental systems where such quantities are much harder to probe, especially in granular experiments where the driving plays a crucial role.

On the other hand, the peak of dynamical heterogeneities across jamming unveils a different phenomenology, namely the appearance of mechan-

ical rigidity. In frictionless systems at zero-temperature and zero-applied stress, the critical nature of point  $J$  has been well-established in the past few years for either hard and soft particles; our experimental studies also show signatures of a critical behavior in vibrated frictional grains with or without applied stress. The corresponding micromechanisms at the origin of the super-diffusive events are still to disclose. In this task, the crucial role of the force network altogether with the fact that the transition occurs at the level of the frictional degrees of freedom force the experimentalist to observe indirect signatures, either through the dynamics of the particles or through the response to a perturbation.

The scope of the work presented in this thesis is limited, though, to the two-dimensional case. “Real materials” are in  $3D$ , and whether or not our results can be extended to higher dimensions than  $2D$  is an important but hard to answer issue. In  $3D$ , several practical drawbacks appear: in granular experiments one has to deal both with the hardly avoidable presence of gravity and with the challenge to track the particles, and in simulations the size of the accessible systems is severely reduced. Conceptual differences also come into play in  $3D$ . The cooperative events, which are at the basis of our analysis of the dynamics in supercooled liquids, may be of different sizes and shapes. The mechanism leading to dynamical heterogeneities itself may significantly differ as the number of degrees of freedom increases.

### A few ideas for future work

Coming back to  $2D$  systems, let us now give some guidelines for future experimental work. We have already emphasized in the discussion of chapter 3 the benefits of a microrheological approach to understand jamming, and in the discussion of chapter 4 the need for a micromechanical analysis of simulations with a variable temperature. Here, we would like to go one step further and propose two other *a priori* fruitful axes for experimental work.

First, we have highlighted all along this work the differences between the glass and jamming transitions. On the experimental side, however, there is no setup probing *both* transitions. We have been using two different setups with different drivings and protocols; this only allows a very few comparison points: the lengthscales permit a scaling of the dynamics through the measure of dynamical quantities, and the packing fraction is a – rough – measurement of the state of the system. So, we believe that one unifying experiment would be of great use to compare quantitatively the phenomenologies of both transitions. With grains, several practical problems hamper such a realization: boundary drivings (*e.g.* quasi-static cyclic shear) does not allow to reach very dense states while bulk drivings (*e.g.* vibration or air upflow) create convection rolls in the looser states, rendering delicate the analyzes on the supercooled branch. So, maybe the answer to these experimental problems will come from the NIPA colloidal particles, which can

either undergo a colloidal glass transition as the packing fraction is increased and jam because of their temperature-dependent expanding ability.

Second, a set of experiments could be explored in parallel to focus on the differences between ordered and disordered matter. Unveiling the presence and evolution of dynamical heterogeneities with monodisperse beads could bring new insights on the dynamical heterogeneities of amorphous systems. For instance, following the work of Pronk and Frenkel [139] one would like to know how they evolve during the transition from disordered to ordered solid as a function of polydispersity. In the scope of jamming, the acquisition of rigidity for monodisperse hard spheres raises several questions of interest: for frictionless disks the isostaticity criterion is at  $z_{iso} = 4$  and the crystal has  $z_c = 6$ . Is rigidity appearing before crystallization, or is the crystal a singular point in the  $z(\phi)$  curves, where the average number of neighbors sharply increases from  $z < z_{iso}$  to  $z_c$ ? The same question can be addressed for frictional spheres, for which a different behavior may occur.

The realization of this roadmap will take at least a few more years. We believe that several interesting studies are still to undertake, and that condensed matter is far from having revealed all its secrets. The amount of *known* is yet mingy compared to the *unknown*. So, pioneers, take your pick and take your picks!





## Appendix A

# Letter on the intruder

In the next pages the reader will find a Letter about the intruder's experiment. This is the short version of the long intruder paper (see page 93). Due to the short format letter, only the principal results have been selected to highlight one main message, namely the fact that a critical behavior can be probed in our system close to jamming with a perturbation-response protocol like the intruder.

This Letter has been published in *Physical Review Letters* in 2009 [95].

## Creep Motion of an Intruder within a Granular Glass Close to Jamming

R. Candelier and O. Dauchot

*SPEC, CEA-Saclay, URA 2464 CNRS, 91 191 Gif-sur-Yvette, France*

(Received 15 June 2009; published 17 September 2009)

We experimentally study the dynamics of an intruder dragged at a constant force in a horizontally vibrated monolayer of grains. At moderate packing fractions, the intruder moves rapidly as soon as the force is applied. Above some threshold value it has an intermittent creep motion with strong fluctuations reminiscent of “crackling noise”. These fluctuations are critical at the jamming transition  $\phi_J$  unveiled in a previous study. The transition separates a regime with local free volume rearrangements from a regime where the displacement field is strongly heterogeneous and resembles force chain patterns.

DOI: 10.1103/PhysRevLett.103.128001

PACS numbers: 45.70.-n, 83.80.Fg

The understanding of the mechanical properties of amorphous media such as granular media, foams, emulsions, suspensions or structural glasses has raised formidable interest in the past decades [1]. At high packing fractions, such materials eventually jam and sustain a finite shear stress before yielding [2–4]. Several experiments on granular systems have emphasized the role of dynamical heterogeneities in the glassy like increase of the structural relaxation time [5]. More recently it was shown that dynamical heterogeneities, albeit of another type, also control the time scales of the jamming transition of a horizontally vibrated granular monolayer [6]. However these experiments do not provide any direct measurement of a mechanical response function. Conversely many experiments report on the stress-strain relation in dense granular packings [7], but do not have an easy access to the dynamics of individual grains. Investigating the drag of an intruder, the subject of this Letter, is a possible way of bridging the gap between dynamical and mechanical properties. Experiments in colloids [3], foams [2] and granular media [8–11] as well as simulations of structural glasses [12] were performed along this line. For loose packings and large drag, that is in the so-called fluidized regime, the velocity dependence of the drag force  $F$  follows Stokes’ law,  $F \propto V$  [8]. For denser packings, experiments report either  $F \simeq \text{cst}$  or  $F \propto \ln(V)$  [2,9–11] when the velocity is fixed, and  $F = F_Y + V^\gamma$ , with  $\gamma \leq 1$  and  $F_Y$  a finite yield force, when the force is imposed [3,12]. In both cases, the dynamics has been described as very intermittent. Stress fluctuations have been investigated in detail in [10], but very little is known about the displacement field and the velocity fluctuations.

In this Letter we study the dynamics of an intruder dragged by a constant force, in a bidisperse monolayer of horizontally vibrated grains. The experiment is run in the same setup (Fig. 1) and following the same protocol as in [6], where the jamming transition has been identified without ambiguity: at  $\phi_J$  the pressure measured in the absence of vibration vanishes and dynamical heterogeneities exhibit a critical behavior. Here, we observe that close to  $\phi_J$ ,

the intruder motion is reminiscent of a “crackling noise” signal [13], with critical fluctuations at the transition. Investigating the displacements and the free volume fields around the intruder, we conclude that the transition separates a regime dominated by local free volume rearrangements from a regime dominated by the rearrangements of the force network. This transition is distinct from fluidization [11], observed at a looser packing fraction which depends on the applied force, when the intruder recovers a continuous motion.

The experimental setup (Fig. 1) has been described elsewhere and we shall only recall here its most important elements together with the modifications imposed by the drag of the intruder. A monolayer of 8500 bidisperse brass cylinders of diameters  $d_{\text{small}} = 4/5 d_{\text{big}} = 4 \pm 0.01$  mm lays out on a horizontal glass plate vibrated horizontally ( $f = 10$  Hz,  $A = 10$  mm). The grains are confined in a cell fixed in the laboratory frame. The packing fraction,  $\phi$ , can be varied by tiny amounts ( $\delta\phi/\phi \sim 5 \times 10^{-4}$ ) and the pressure exerted on the moving lateral wall is measured by a force sensor. The intruder consists in a larger particle of same height ( $d_{\text{intruder}} = 2 \cdot d_{\text{small}}$ ) introduced in the system and pulled by a mass  $M$  via a pulley perpendicularly to the vibration. The fishing wire, which stands over the other

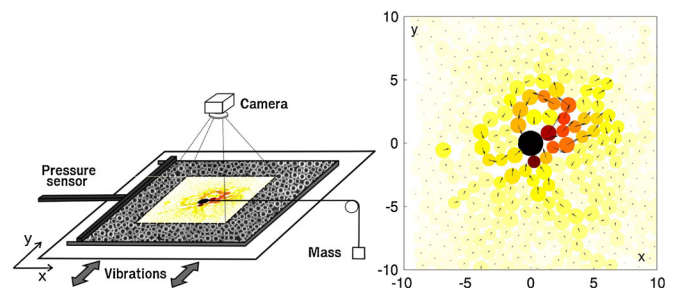


FIG. 1 (color online). *Left*: a monolayer of disks is vibrated horizontally, while dragging an intruder at constant force. Both the intruders and the surrounding grains are tracked by a CCD camera; *Right*: a strongly intermittent and heterogeneous response is observed, see text for details.

grains, does not disturb the dynamics. Most of the results presented here are related to experiments performed at a constant force ( $F_1 = 0.67N$ ,  $F_2 = 1.48N$ ,  $F_3 = 2.62N$ ) and varying the packing fraction  $\phi$  in the range [0.82–0.85] but we also conducted experiments at constant packing fractions, ( $\phi_1 = 0.8383$ ,  $\phi_2 = 0.8394$ ,  $\phi_3 = 0.8399$ ) increasing the force from  $0.67N$  to  $14.25N$ . For comparison, the total weight of the grains is  $23.11N$  and the force registered at the wall when the grains are highly compressed is of the order of  $50N$ . Note that in the present study the inertial time scale  $t_{in} = \sqrt{md/F} = 10^{-3}$  is always much shorter than the vibration one. Also the typical acceleration of the intruder never exceeds  $0.2 \text{ ms}^{-2}$  so that  $m \frac{d^2x}{dt^2}$  is always much smaller than  $F = Mg$ . The motion is completely overdamped and the elementary time scale is really that of the vibration. The time unit is set to one plate oscillation while the length unit is chosen to be the diameter of the small particles.

Starting from a low packing fraction  $\phi$ , we gradually compress the system until it reaches a highly jammed state following the same protocol as in [6]. Then we stepwise decrease the volume fraction. In the absence of an intruder, it was shown that the average relaxation time increases monotonically with the packing fraction, while the dynamics exhibits strong dynamical heterogeneities, the length scale and time scale of which exhibit a sharp peak at an intermediate packing fraction. The pressure measured at the wall in the absence of vibration falls to zero precisely below that packing fraction, hence called the jamming transition  $\phi_J$ . In the present study, the intruder is inserted at its initial position in place of one big and two small grains before each downward step in the packing fraction and the system is kept under vibration until the pressure has recovered its value in the absence of the intruder. Only then the force is applied on the wire and the intruder is dragged through the cell, while its motion together with that of a set of 1800 surrounding grains is tracked by a digital video camera triggered in phase with the oscillations of the plate.

At low packing fraction, and large enough force, the intruder motion is continuous. When increasing the packing fraction, it becomes intermittent above some threshold, which increases with the applied force (Fig. 2, left). Performing experiments at a given packing fraction and increasing the force, one observes that the applied force is proportional to the average velocity of the intruder  $F \propto V$  in the continuous motion regime, whereas  $F \propto \ln V$  in the intermittent one (Fig. 2, right). We thereby identify this transition with the fluidization one [11]. Note that for the largest packing fraction  $\phi_2$  and  $\phi_3$ , we could not observe the fluidization. As a result, there is a very strong contrast between the continuous motion of the intruder observed at  $\phi = \phi_1$  for large enough forces, say  $F = 10N$ , and the strongly intermittent one observed at  $\phi = \phi_2$  for the same large force. Typically the intruder averaged velocity loses 3 orders of magnitude and its velocity fluctuations gain more

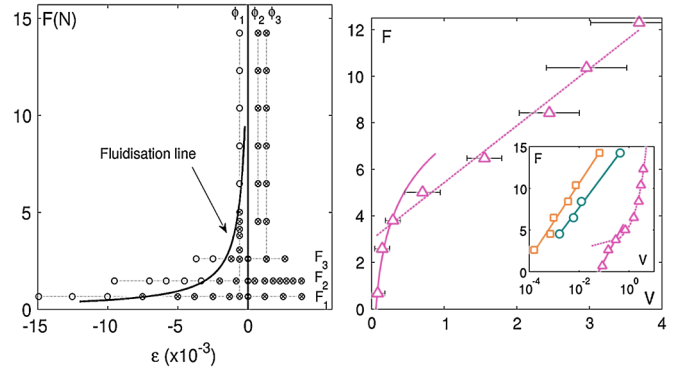


FIG. 2 (color online). From flow to jammed states: *Left*: Parameter space, (force  $F$ —relative packing fraction  $\epsilon = (\phi - \phi_J)/\phi_J$ ): at low  $\phi$  and large  $F$ , ( $\circ$ ) the packing is fluidized, the intruder motion is continuous and  $F \propto V$ ; at large  $\phi$  and low  $F$  ( $\otimes$ ), the intruder exhibits an intermittent motion and  $F \propto \ln V$ . The horizontal and vertical dotted lines indicate the path followed in the parameter space in the present study. *Right*:  $F$  versus  $V$  along the paths  $\phi_1$  ( $\Delta$ ),  $\phi_2$  ( $\circ$ ) and  $\phi_3$  ( $\square$ ); *Inset*: same in log-lin.

than 5 orders of magnitude, while  $\phi$  is increased by less than 1%, already suggesting the existence of a sharp transition.

We now focus on the experiments performed at constant and rather small force. When looking at the intruder displacements  $\delta x$  along the dragging direction during one vibration cycle (Fig. 3, top left), one immediately notices very strong fluctuations, with bursts of widely fluctuating magnitude. More quantitatively, the probability density functions of  $\delta x$  (Fig. 3, middle left) exhibit an important skewness towards the positive displacements. We characterize the positive part of the distribution, i.e., the displacements in the direction of the drag force,  $\delta x^+$ , by computing the average value  $\mu^+ = \langle \delta x^+ \rangle$  and the relative fluctuations  $\sigma^+/\mu^+ = \langle (\delta x^+ - \mu^+)^2 \rangle^{1/2}/\mu^+$ . One observes (Fig. 3, bottom left) that  $1/\mu^+$  increases continuously by 3 orders of magnitude, while varying the packing fraction of only a few percent,  $\delta\phi/\phi = 2 \times 10^{-2}$ , and that  $\sigma^+/\mu^+$  exhibits a peak at an intermediate packing fraction. Both behaviors are directly reminiscent of what has been recalled above for the dynamics in the absence of an intruder. We could check indeed that the peak observed in the fluctuations of the intruder motion coincides with a vanishing pressure in the absence of vibration and thereby locate it at  $\phi_J$  without ambiguity. Note however that the precise value of  $\phi_J$  depends on the precise packing that has been selected when the system has been compressed and that the small and nonmonotonic variations of  $\phi_J = 0.8369$ ,  $0.8383$ ,  $0.8379$  for the three forces  $F_1$ ,  $F_2$ ,  $F_3$  together with the small difference with the value  $\phi_J = 0.842$  reported in [6] must be attributed to differences in the initial conditions and more generally in the compression protocol (see [14,15] for a detailed discussion in the case of hard spheres). Figure 3, bottom left, displays both  $1/\mu^+$  and  $\sigma^+/\mu^+$  as a function of  $\epsilon = (\phi - \phi_J)/\phi$  the relative

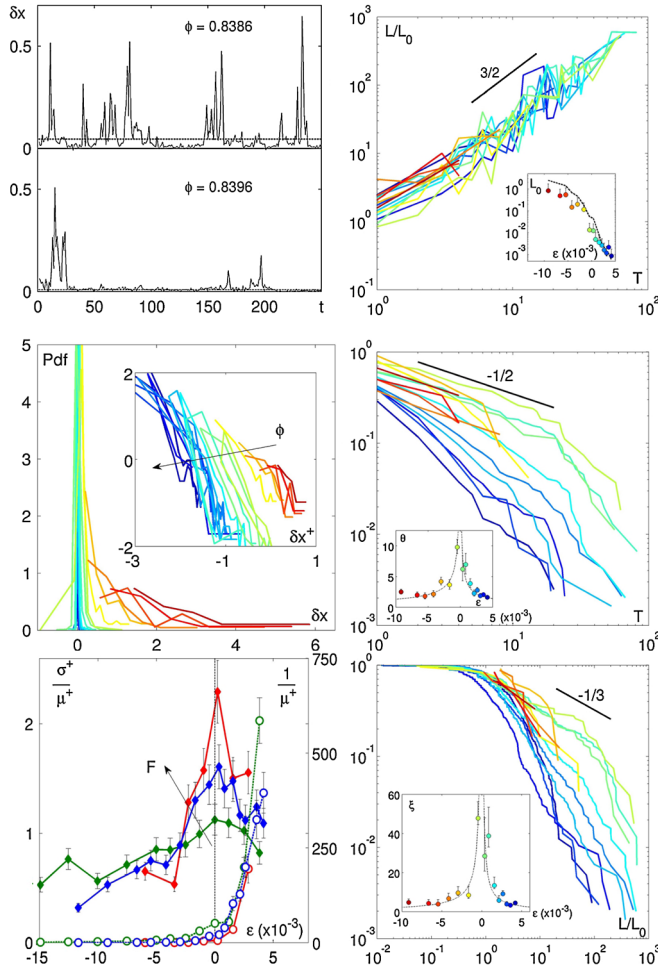


FIG. 3 (color online). Intruder displacements statistics:  $F = F_2$  and packing fractions ranges from  $\phi = 0.8306$  [red (light gray)] to  $0.8418$  [blue (dark gray)] when not otherwise specified. *Top Left*: Instantaneous displacements  $\delta x(t)$  for  $\phi = 0.8386$  and  $\phi = 0.8396$ . *Middle Left*: Distributions of  $\delta x$ . *Inset*: same in log-log. *Bottom Left* Inverse average  $1/\mu^+$  [(○) right axis] and standard deviation over average  $\sigma^+/\mu^+$  [(◆) left axis] of  $\delta x^+$  as a function of the reduced packing fraction  $\epsilon$  for the three applied force  $F_1$  [red (light gray)],  $F_2$  [blue (dark gray)] and  $F_3$  [green (medium gray)]. *Top Right*: Scaling of the rescaled size  $L/L_0$  of the bursts with their duration  $T$ . *Inset*:  $L_0$  and  $V$  (black dotted line) as a function of  $\phi$ . *Middle Right*: Cumulated distributions of the durations  $T$  of the displacement bursts; *Inset*: Cutoff of the distributions  $\theta(\epsilon)$  versus  $\phi$ . *Bottom Right*: Cumulated distributions of the rescaled size  $L/L_0$ . *Inset*: Cutoff of the distributions  $\xi(\epsilon)$  versus  $\phi$ .

distance to  $\phi_J$  for the three dragging forces. The peak in the fluctuations is clearly separated from the divergence of  $1/\mu^+$  and is a new signature of the jamming transition.

To complete the characterization of the intruder motion, we analyze the duration  $T$  and the size  $L$  associated with the displacement bursts, as is commonly done in crackling noise or Barkhausen noise experiments [13]. We impose a given reference level  $\delta x_0$  and define bursts as the period of times where  $\delta x$  is above this level. The duration  $T$  of a given burst is defined as the interval within two successive

intersections of  $\delta x$  with  $\delta x_0$ , while the size  $L$  is defined as the integral of  $\delta x$  between the same points. Figure 3, top right, shows that  $L(\phi, T) \sim L_0(\phi)T^{1/z}$ , with a dynamical exponents  $z = 2/3$ , and  $L_0$  a scaling length, which can be interpreted as a typical value of  $L$ . Note that it is different from its average value because of the power-law shape of the distributions of  $L$ . Indeed, despite some weakness of our statistics, the cumulated distributions of  $T$  (Fig. 3, middle right), respectively of  $L/L_0$  (Fig. 3, bottom right) can be described as power laws truncated by a scaling function:  $T^{-\alpha}f(T/\theta(\phi))$ , respectively  $(L/L_0)^{-\beta}g(L/\xi(\phi))$ . The cutoff dependence on the packing fraction  $\theta(\phi)$ , resp.  $\xi(\phi)$  are estimated by computing the averages of  $T$ , resp.  $L/L_0$  and display a diverging behavior at  $\phi_J$ :  $\theta(\phi) \propto |\phi - \phi_J|^{-\eta}$ , resp.  $\xi(\phi) \propto |\phi - \phi_J|^{-\nu}$ . Our statistics are not large enough to extract precisely the exponents  $\alpha$ ,  $\beta$ ,  $\eta$  and  $\nu$ ; however estimates of  $\alpha = 1/2$ ,  $\beta = 1/3$ ,  $\eta = 2/3$  and  $\nu = 1$  are consistent with the data and satisfy the relations  $\alpha z = \beta$  and  $\eta = \nu z$ . Also, the same analysis performed on the kinetic energy of the surrounding grains—not shown here—is consistent with the above determination. The dynamical exponent  $z = 2/3$ , different from the  $1/2$  value expected for inertial mechanisms, underlines the role played by the collective dissipative mechanisms.

Finally, we characterize the dynamics around the intruder. The averaged displacement field (Fig. 4, top left) is composed of two symmetric recirculation vortices. This pattern is very robust as evidenced by the shape invariance of the displacement profiles along the direction perpendicular to the drag (Fig. 4, top right). In particular, the exponential decay of the displacement amplitude keeps the same characteristic length across the transition (see inset). Such a smooth and continuous behavior is in contrast with the existence of the sharp transition described above and must be related to the similar absence of signature of the transition when considering the average relaxation time or  $\mu^+(\phi)$ . Again the transition is to be found in the strongly heterogeneous instantaneous displacement field (Fig. 1, right), which exhibits characteristic chainlike motions. This tendency of forming chainlike motions is strongly enforced for a packing fraction larger than  $\phi_J$ . We also compute the averaged free volume, extracted from Laguerre's tessellation of the packing, around the intruder (Fig. 4, bottom left) and observe a small asymmetry between the front and the back of the intruder. Computing for instance the average free volume in a small window in front of and behind the intruder (see Fig. 4, bottom right), one sees that below  $\phi_J$  there is a significant excess of free volume leaving like a “wake” far behind the intruder, whereas above  $\phi_J$  this asymmetry rapidly vanishes together with a strong decrease of the available free volume.

Altogether, the following pictures emerge. The jamming transition, which is marked by a critical behavior of the fluctuations of the intruder displacements separate a regime where the intermittent motion is dominated by rapid

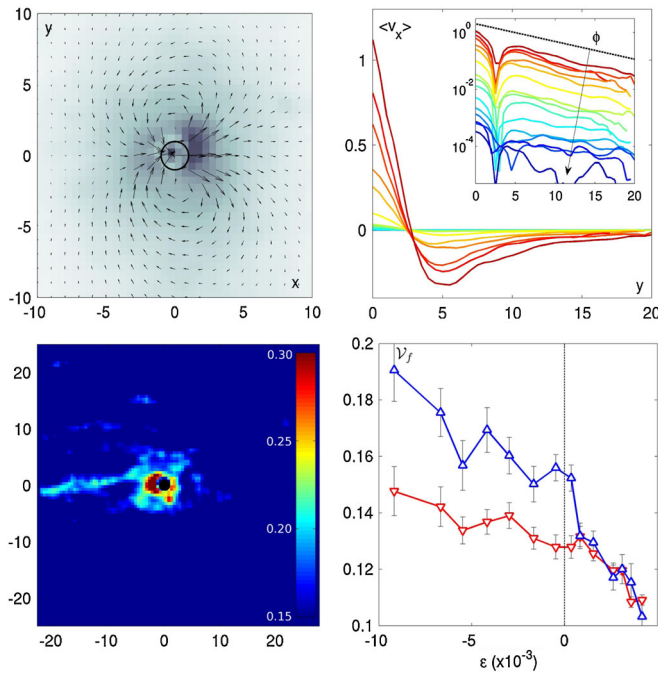


FIG. 4 (color online). Displacements and free volume around the intruder (the intruder goes from left to right;  $F = F_2$ ,  $\phi = \phi_j = 0.8386$ ). *Top Left*: Interpolated average displacement field: the darker, the faster. *Top Right*:  $y$  profiles of the average velocity along the drag direction (same packing fractions as in Fig. 3). *Bottom Left*: Average free volume field. *Bottom Right*: Average free volume vs  $\epsilon$  in front (red  $\nabla$ ) and behind (blue  $\triangle$ ) the intruder.

reorganization of the free volume from one where the motion takes the form of chainlike structures, which are very much reminiscent of the strong force network suggesting the dominant role of the stress fluctuations [16]. Note that the frictional force with the bottom plane is completely negligible as compared to the drag force and the displacements' distribution of the intruder is completely determined by the *collective resistance* of the other grains organized in chain forces. As compared to previous studies of the motion of an intruder in a granular packing [8–11], we have confirmed the transition from a linear viscosuslike dependence of the dragging force with the velocity in the fluidized regime to a logarithmic dependence in the intermittent one. The originality of the present study is to unveil critical features *inside* the intermittent regime and associate them with the jamming transition. The observation of “crackling noise” statistics suggests a possible deeper correspondence in the underlying physical properties with other intermittent phenomena such as the creep motion observed under yield stress in amorphous media [17], the subcritical material failure [18] and more generally, the pinning-depinning transition [19]. We be-

lieve that performing the kind of microrheology experiment sketched out in the present study is a promising path for a better understanding of the jamming of frictional systems.

We would like to thank L. Ponson for having suggested the “crackling noise” analysis, E. Bouchaud, and S. Aumaitre for helpful discussions, as well as F. Paradis, B. Saint-Yves and C. Coulais. We also thank V. Padilla and C. Gasquet for technical assistance on the experiment. This work was supported by ANR DYNHET 07-BLAN-0157-01.

- 
- [1] Jaeger *et al.*, *Rev. Mod. Phys.* **68**, 1259 (1996); A. Liu and S. Nagel, *Nature (London)* **396**, 21 (1998); Cates *et al.*, *Phys. Rev. Lett.* **81**, 1841 (1998); M. Falk and J. Langer, *Phys. Rev. E* **57**, 7192 (1998); Varnik *et al.*, *J. Chem. Phys.* **120**, 2788 (2004); C. Maloney and A. Lemaitre, *Phys. Rev. Lett.* **93**, 195501 (2004); M. Wyart, *Ann. Phys. (Paris)* **30**, 1 (2005).
  - [2] Dollet *et al.*, *Phys. Rev. E* **71**, 031403 (2005).
  - [3] Habdas *et al.*, *Europhys. Lett.* **67**, 477 (2004).
  - [4] N. Xu and C. O’Hern, *Phys. Rev. E* **73**, 061303 (2006); P. Coussot, *Rheometry of Pastes, Suspensions, and Granular Materials* (John Wiley & Sons, New York, 2005); Da Cruz *et al.*, *Phys. Rev. E* **66**, 051305 (2002).
  - [5] G. Marty and O. Dauchot, *Phys. Rev. Lett.* **94**, 015701 (2005); Dauchot *et al.*, *Phys. Rev. Lett.* **95**, 265701 (2005); A. Abate and D. Durian, *Phys. Rev. E* **74**, 031308 (2006); A. Keys *et al.*, *Nature Phys.* **3**, 260 (2007).
  - [6] Lechenault *et al.*, *Europhys. Lett.* **83**, 46 003 (2008).
  - [7] Howell *et al.*, *Phys. Rev. Lett.* **82**, 5241 (1999); G. MiDi, *Eur. Phys. J. E* **14**, 341 (2004); D. Fenistein and M. van Hecke, *Nature (London)* **425**, 256 (2003).
  - [8] Zik *et al.*, *Europhys. Lett.* **17**, 315 (1992); Kolb *et al.*, *Phys. Rev. E* **69**, 031306 (2004).
  - [9] Albert *et al.*, *Phys. Rev. Lett.* **82**, 205 (1999); Chehata *et al.*, *Phys. Fluids* **15**, 1622 (2003).
  - [10] J. Geng and R. Behringer, *Phys. Rev. E* **71**, 011302 (2005).
  - [11] Dalton *et al.*, *Phys. Rev. Lett.* **95**, 138001 (2005); Baldassari *et al.*, *Phys. Rev. Lett.* **96**, 118002 (2006).
  - [12] Hastings *et al.*, *Phys. Rev. Lett.* **90**, 098302 (2003); Leonforte *et al.*, *Phys. Rev. B* **70**, 014203 (2004).
  - [13] C. R. M. James, P. Sethna, and Karin A. Dahmen, *Nature (London)* **410**, 242 (2001); G. Durin and S. Zapperi, in *The Science of Hysteresis*, edited by Bertotti and Mayergoyz (Academic Press, Amsterdam, 2006).
  - [14] G. Parisi and F. Zamponi, arXiv:0802.2180 [*Rev. Mod. Phys.* (to be published)].
  - [15] L. Berthier and T. Witten, *Europhys. Lett.* **86**, 10001 (2009).
  - [16] Howell *et al.*, *Phys. Rev. Lett.* **82**, 5241 (1999).
  - [17] Falk *et al.*, *Phys. Rev. E* **70**, 011507 (2004).
  - [18] Bonamy *et al.*, *Phys. Rev. Lett.* **101**, 045501 (2008).
  - [19] Chauve *et al.*, *Phys. Rev. B* **62**, 6241 (2000).



# Appendix B

## Recipes

In this appendix, we would like to develop a few technical points that deserve attention. We will start with geometrical considerations, namely the computation of Laguerre’s tessellation, how one can set the ROI to get the largest possible reliable dataset and the computation of the “distance to affinity” used in [35] (p.127). We will then move on the computation of dynamical quantities, and especially the dynamical heterogeneities.

### B.1 Geometrical recipes

#### B.1.1 Laguerre tessellation

*La guerre! C’est une chose trop grave pour la confier à des militaires.*<sup>1</sup>  
– Georges Clémenceau (1886)

With monodisperse packings, Delaunay tessellation is the classical tool to determine neighborhood: three particles are neighbors if there is no other particle standing in the circumcircle of the triangle made of the centers of the three particles. Taking the dual of the tessellation, one can construct the Voronoï cells, *i.e.* the polygons made of the median of every segment of the neighboring network, as depicted in fig. B.1.

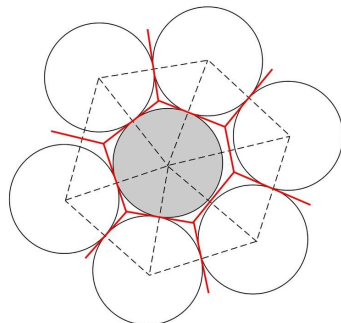


Figure B.1: Delaunay tessellation for a monodisperse packing. The black dotted segments are the neighboring links of the Delaunay tessellation, while the red segments delimit the Voronoï polygons.

---

<sup>1</sup>War! It’s too serious to be entrusted to the army.

However, if there is polydispersity amongst the grains, some problems appear. First, with a high polydispersity it can happen that two grains in contact are not considered as neighbors (see fig. B.2-(a)). Second, even for low polydispersities, the medians between particles of different sizes always intersect the biggest particle, thus producing non-natural Voronoï cells (see fig. B.2-(b))

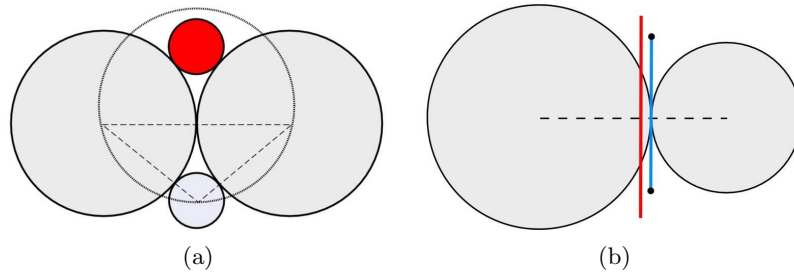


Figure B.2: Two problems with the Delaunay tessellation in polydisperse packings. **(a)** The red particle is inside the circumcircle of the triangle formed by the centers of the grey particles, so the grey particles are not neighbors in the sense of Delaunay, even if they are touching. **(b)** The median of the segment linking two particles with different sizes crosses the biggest particle (red line). On the contrary, Laguerre's tessellation give Voronoï cells in which every segment is tangent to the particles (blue line).

A convenient way to avoid those problems is to consider the *radical* or *Laguerre's* tessellation [140, 141] instead of Delaunay's. In Laguerre's method, power distances are used instead of classical Euclidian distances, such that the distance  $D_i(M)$  between a point  $M$  with coordinates  $(x, y)$  and a particle  $i$  of radius  $R_i$  whose center is in  $(x_i, y_i)$  is defined by:

$$D_i^2(M) = (x - x_i)^2 + (y - y_i)^2 - R_i^2 \quad (\text{B.1})$$

In Euclidian space, this distance corresponds to the length of the segments passing by  $M$  and tangent to the particle (see fig. B.3-left).

The tessellation criterion is therefore the following: for every triplet of particles one searches the point where the power distances to these particles are equal, and if no other power distance to another particle is shorter the particles are declared as neighbors. It has been shown that the resulting tiling is exact<sup>2</sup>.

An illustration of the difference between Delaunay's and Laguerre's tessellations is given in fig. B.3-right. One sees that the difference is quite weak; this is due to the small polydispersity used in this example. We have been

<sup>2</sup>See [142] for details.

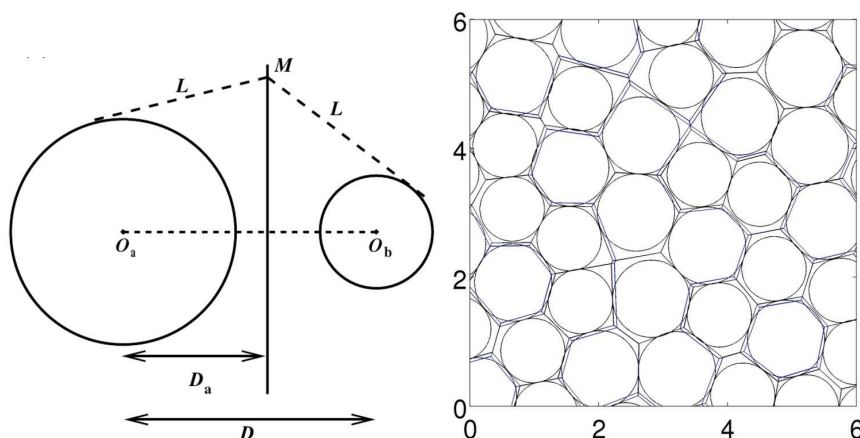


Figure B.3: **Left** Illustration of the radical tessellation: point  $M$  is a equal “power distance” from the two disks. From [143]. **Right** Comparison between the Delaunay (blue) and Laguerre tessellation (black) in one configuration of the cyclic shear experiment. The difference is weak due to the small polydispersity (the diameter ratio is  $\sigma_B/\sigma_S = 1.2$ ).

using Laguerre tessellation in all the studies presented in this manuscript<sup>34</sup>.

### B.1.2 Region Of Interest

Defining a Region Of Interest (ROI) over which the data analysis is performed is often an obscure issue. But smartly chosen ROIs can enforce the statistics in small data sets. Here, we explain how one can set the ROI to get the maximal possible statistics; simply, two principles have to be taken into account:

- The ROI should be neither spatial (*e.g.* all the particles inside a defined perimeter) nor particular (*e.g.* a set of particles are always in the ROI and the rest never), but instead the ROI should be defined both in space and time, namely by setting the fact that each particle / time is inside the ROI or not.
- Then, one determines the ROI in the following way: at every moment the particles in the ROI are the particles whose neighboring *cannot* be changed by the addition of a particle anywhere, with respect to the steric constraints.

An example of such a computation is represented in fig. B.4.

<sup>3</sup>Note that yet another tiling is sometimes used in the literature, the *navigation map*. See for instance [143] for a definition.

<sup>4</sup>The Laguerre computation is done via *CGAL* (Computational Geometry Algorithms Library - <http://www.cgal.org/>).

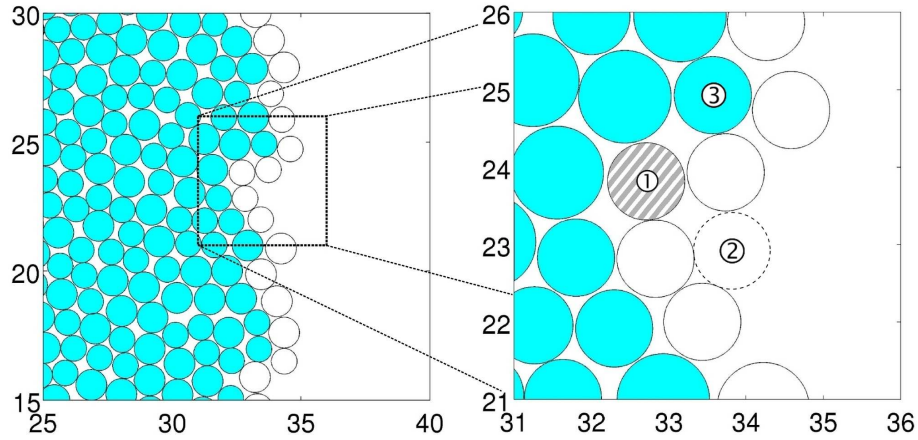
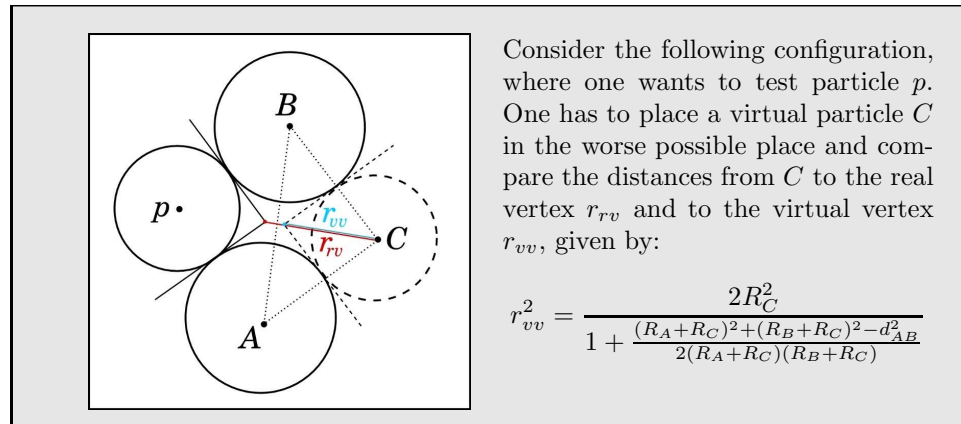


Figure B.4: **Left** Example of packing, close to the boundaries. The particles painted in cyan are flagged as inside the ROI at this moment. **Right** Zoom on a region of the left packing. The dashed grey particle ① is *not* inside the ROI since a virtual particle can be added (dotted-line particle ②) to become one of its neighbors. On the other hand, note that particle ③ is *inside* the ROI though it is clearly more on the left than ①.



### B.1.3 Distance to affinity

A measure that we used in [35] (see p.127) is the distance to affinity, introduced by Falk and Langer [123]. The method identifies where irreversible plastic rearrangements occur; Falk and Langer proposed to assimilate the plastic micro-rearrangements to the places where molecular displacements are nonaffine, that is, where they deviate substantially from displacements that can be described by a linear strain field.

To this aim, one can compute the closest possible approximation to a local strain tensor in the neighborhood of any particle. So let us consider a

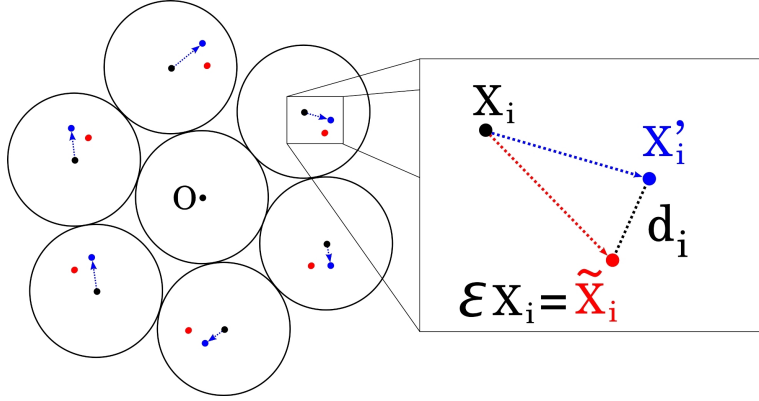


Figure B.5: **Left** Transformation of the neighborhood of the reference particle  $O$  in the coordinate system centered on  $O$ . Blue dots represent the effective transformation of each neighboring particle, while red dots correspond to an affine transformation  $\varepsilon$ . **Right** Zoom on the transformation of one neighbor  $i$ . The position at  $t$  is  $X_i$  (black), the position at  $t + 1$  is  $X_i'$  (blue) and the affine transformation points to  $\tilde{X}_i = \varepsilon X_i$  (red).

reference particle and its neighborhood in the sense of Voronoi<sup>5</sup> (see fig. B.5).

The local strain is then determined by minimizing the mean-square difference between the actual displacements of the neighboring particles relative to the central one and the relative displacements that they would have if they were in a region of uniform strain  $\varepsilon$ . More specifically, given a uniform strain tensor  $\varepsilon$ , one can define the distance  $d_i$  between the real displacement and the displacement induced by  $\varepsilon$ :

$$d_i^2 = \|X_i' - \tilde{X}_i\|^2 = \|X_i' - \varepsilon X_i\|^2 \quad (\text{B.2})$$

$$= [x_i' - \varepsilon_{xx} \cdot x_i - \varepsilon_{xy} \cdot y_i]^2 + [y_i' - \varepsilon_{yx} \cdot x_i - \varepsilon_{yy} \cdot y_i]^2 \quad (\text{B.3})$$

Considering all the neighbors, one would like to find the tensor  $\varepsilon$  that minimizes the following quantity, akin to a “distance to affinity”:

$$D^2(\varepsilon) = \sum_i d_i^2 = \sum_i \left( [x_i' - \varepsilon_{xx} \cdot x_i - \varepsilon_{xy} \cdot y_i]^2 + [y_i' - \varepsilon_{yx} \cdot x_i - \varepsilon_{yy} \cdot y_i]^2 \right)$$

the sum being over the neighbors  $i$ . To find the tensor that minimizes  $D$ , one has to hypothesize that all partial derivatives vanish. For instance, along  $\varepsilon_{xx}$  one has:

$$\frac{\partial D^2(\varepsilon)}{\partial \varepsilon_{xx}} = 2\varepsilon_{xx} \sum_i x_i^2 - 2 \left( \sum_i x_i x_i' - \varepsilon_{xy} \sum_i x_i y_i \right) \quad (\text{B.4})$$

$$\frac{\partial D^2(\varepsilon)}{\partial \varepsilon_{xx}} = 0 \quad \Rightarrow \quad \varepsilon_{xx} \sum_i x_i^2 = \sum_i x_i x_i' - \varepsilon_{xy} \sum_i x_i y_i \quad (\text{B.5})$$

<sup>5</sup>Falk and Langer[123] define the neighborhood by the mean of a sampling radius, which leads to similar results.

One can now introduce the matrices  $\mathcal{M}$  and  $\mathcal{M}'$ :

$$\mathcal{M} = \begin{pmatrix} \sum_i x_i^2 & \sum_i x_i \cdot y_i \\ \sum_i x_i \cdot y_i & \sum_i y_i^2 \end{pmatrix} \quad \text{and} \quad \mathcal{M}' = \begin{pmatrix} \sum_i x_i' \cdot x_i & \sum_i x_i' \cdot y_i \\ \sum_i y_i' \cdot x_i & \sum_i y_i' \cdot y_i \end{pmatrix} \quad (\text{B.6})$$

Hence:

$$\varepsilon_{xx} \cdot \mathcal{M}_{xx} + \varepsilon_{xy} \cdot \mathcal{M}_{yx} = \mathcal{M}_{xx}' \quad (\text{B.7})$$

Applying the same reasoning on  $\varepsilon_{xy}$ ,  $\varepsilon_{yx}$  and  $\varepsilon_{yy}$ , one then gets the following relation:

$$\varepsilon \cdot \mathcal{M} = \mathcal{M}' \quad (\text{B.8})$$

The matrix  $\mathcal{M}$  is always invertible since:

$$\begin{aligned} \det(\mathcal{M}) &= \left( \sum_i x_i^2 \right) \left( \sum_i y_i^2 \right) - \left( \sum_i x_i \cdot y_i \right)^2 \\ &= \sum_{i,j} [x_i^2 y_j^2 - x_i x_j y_i y_j] = \sum_{i<j} [x_i^2 y_j^2 + x_j^2 y_i^2 - 2x_i x_j y_i y_j] \\ &= \sum_{i<j} (x_i y_i - x_j y_j)^2 > 0 \end{aligned}$$

Hence one accesses the tensor  $\varepsilon$  minimizing the distance to affinity  $D$  directly by computing:

$$\varepsilon = \mathcal{M}' \cdot \mathcal{M}^{-1} \quad (\text{B.9})$$

Note that once one has  $\varepsilon$ , the decomposition in rotation, shearing and scaling is easily done by using the decomposition of  $\varepsilon$  in symmetric /antisymmetric matrices. Two definitions can be given, each one having 4 parameters:

- The first definition has 1 parameter for rotation ( $\theta$ ), 1 for shear ( $\sigma_x$ ) and 2 for scaling ( $\lambda_x$  and  $\lambda_y$ ):

$$\varepsilon = \overbrace{\begin{pmatrix} \cos(\theta) & -\sin(\theta) \\ \sin(\theta) & \cos(\theta) \end{pmatrix}}^{\text{Rotation}} \cdot \overbrace{\begin{pmatrix} 1 & \sigma_x \\ 0 & 1 \end{pmatrix}}^{\text{Shear}} \cdot \overbrace{\begin{pmatrix} \lambda_x & 0 \\ 0 & \lambda_y \end{pmatrix}}^{\text{Scaling}} \quad (\text{B.10})$$

and one gets the parameters with, for instance:

$$\theta = \tan^{-1} \left( \frac{\varepsilon_{yx}}{\varepsilon_{xx}} \right), \quad \lambda_x = \frac{\varepsilon_{xx}}{\cos(\theta)}, \quad \lambda_y = \frac{\varepsilon_{yy}}{\sin(\theta)}, \quad \sigma_x = \frac{\varepsilon_{xy}/\lambda_y + \sin(\theta)}{\cos(\theta)}$$

- The second definition has 1 parameter for rotation ( $\theta$ ), 2 for shear ( $\sigma_x$ ,  $\sigma_y$ ) and 1 for scaling ( $\lambda$ ):

$$\varepsilon = \overbrace{\begin{pmatrix} \cos(\theta) & -\sin(\theta) \\ \sin(\theta) & \cos(\theta) \end{pmatrix}}^{\text{Rotation}} \cdot \overbrace{\begin{pmatrix} 1 & \sigma_x \\ \sigma_y & 1 \end{pmatrix}}^{\text{Shear}} \cdot \overbrace{\begin{pmatrix} \lambda & 0 \\ 0 & \lambda \end{pmatrix}}^{\text{Scaling}} \quad (\text{B.11})$$

and one gets the parameters with, for instance:

$$\theta = \tan^{-1} \left( \frac{\varepsilon_{yy} - \varepsilon_{xx}}{\varepsilon_{yx} + \varepsilon_{xy}} \right), \quad \sigma_x = \frac{\varepsilon_{xy} \cos(\theta) + \varepsilon_{yy} \sin(\theta)}{\varepsilon_{yy} \cos(\theta) - \varepsilon_{xy} \sin(\theta)},$$

$$\sigma_y = \frac{\varepsilon_{yx} \cos(\theta) - \varepsilon_{xx} \sin(\theta)}{\varepsilon_{xx} \cos(\theta) + \varepsilon_{yx} \sin(\theta)}, \quad \lambda = \sqrt{\frac{\det(\varepsilon)}{1 - \sigma_x \sigma_y}}$$

### B.1.4 Clustering

One recurrent tool used in this work is *clusterization*. The problem is the following: starting from a given adjacency network, how can one extract the connex clusters in a reasonable computation time? To answer this question, we first define the adjacency matrix  $\mathcal{A}$  as the matrix  $N \times N$  matrix whose element  $a_{ij}$  is 1 if  $i$  is linked to  $j$  and 0 otherwise. Such an example of adjacency matrix for a system of size  $N = 8$  is given in fig B.6-left.

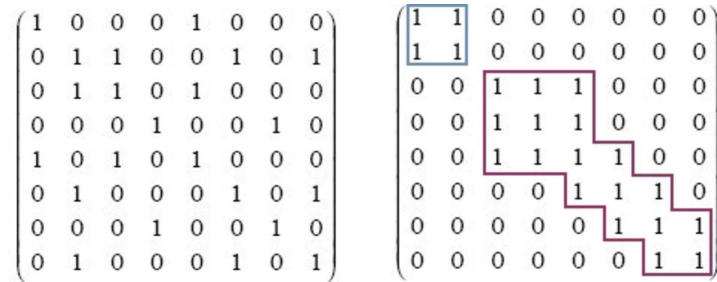


Figure B.6: **Left** Example of adjacency matrix  $\mathcal{A}$  for a system of size  $N = 8$ . **Right** Output of the Cuthill–McKee algorithm: one easily identifies two distinct clusters of 2 and 6 particles.

This raw representation requires a careful examination to extract the connex clusters it contains. The Cuthill–McKee algorithm [144] transforms the input matrix  $\mathcal{A}$  by re-allocating the indexes through successive row and column permutations and produce a very good solution to the *Bandwidth Minimization Problem*<sup>6</sup>, as shown in fig. B.6-right. Within this representation, identifying the clusters is an easy task since one has to look only at the distinct diagonal blocks.

<sup>6</sup>Since the Bandwidth Minimization Problem is NP-complete, the solution returned by the algorithm is not optimal for the BRP problem. It is however far enough to solve the clustering problem.

## B.2 Dynamical recipes

*Sanity is not statistical.*

– George Orwell, Nineteen Eighty-Four (1949)

### B.2.1 Density relaxation statistics

A classical characterization stemming from classical liquid studies is the study of the relaxation properties of the density field  $\rho(\vec{r}) = \sum_i \delta(\vec{r} - \vec{r}_i)$ . The temporal correlation of the density field is given by:

$$\begin{aligned} \langle \delta\rho(\vec{r}, t + \tau) \delta\rho(\vec{r}', t) \rangle_t &= \frac{1}{N} \left\langle \iint d\vec{r} d\vec{r}' \delta\rho(\vec{r}, t + \tau) w(\vec{r} - \vec{r}') \delta\rho(\vec{r}', t) \right\rangle_t \\ &= \frac{1}{N} \left\langle \sum_{i,j} w(\vec{r}_i(t + \tau) - \vec{r}_j(t)) \right\rangle_t - \bar{\rho} \int d\vec{r} w(\vec{r}) \end{aligned}$$

where  $w(\vec{r})$  is a spatial kernel. Note that the second term is often neglectable, and that when  $w(\vec{r}) = \exp(i\vec{k} \cdot \vec{r})$  one recognizes the dynamical structure factor obtained when performing light scattering experiment. Here, following [29, 145], we choose  $w(\vec{r}) = \exp(-\vec{r}^2/2a^2)$ , where  $a$  is a probing length scale akin to the inverse of the light wavenumber for scattering experiments.

In all the data sets presented in this thesis, the displacements are much smaller than the particle diameter even when cumulated on large lag times. As a result, the only significant evolution of the dynamical structure factor comes from its self part, and one can characterize the density field relaxation using:

$$\bar{Q}(a, \tau) = \langle q_i^t(a, \tau) \rangle_{i,t} \quad (\text{B.12})$$

where

$$q_i^t(a, \tau) \equiv e^{-\frac{\|\Delta\vec{r}_i^t(\tau)\|^2}{2a^2}} \quad (\text{B.13})$$

is the local relaxation induced by the displacements  $\Delta\vec{r}_i^t(\tau)$  of the particles on the lag time  $\tau$ .

**Average relaxation** Figure B.7-top left displays  $\bar{Q}(a, \tau)$  for respectable intervals of  $a$  and  $\tau$  in the vibrating experiment. For large values of  $a$  and small time scale  $\tau$ , the particles have not relaxed on average, and  $\bar{Q}$  is close to 1. On the contrary for small values of  $a$  and large time scale all the particles have relaxed on average and  $\bar{Q}$  is close to 0. Three temporal signals of  $\bar{Q}_t(a, \tau) = \langle q_i^t(a, \tau) \rangle_i$  for a fixed value of  $a$  are given as an illustration on fig. B.7-top right.

For a fixed length  $a$ ,  $\bar{Q}(a, \tau)$  decays as the probing time  $\tau$  grows, and the characteristic time scale one can extract obviously depends on the arbitrary choice of  $a$ . One can however notice that  $\bar{Q}(a, \tau) = \mathcal{F}_\tau(\lambda)$ , where  $\mathcal{F}_\tau(\lambda)$

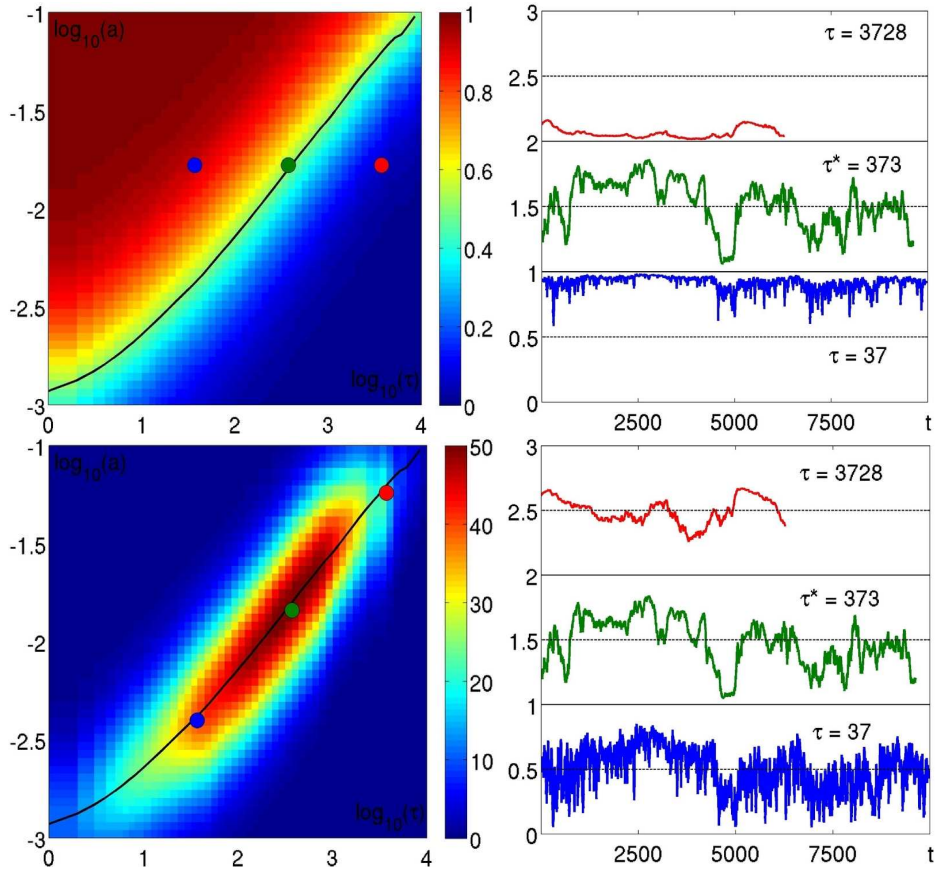


Figure B.7: **Top-left**  $\bar{Q}(a, \tau)$  for several values of  $a$  and  $\tau$ . The colored points correspond to the curves on the right side. The black curve is the  $\zeta(\tau) \simeq \sigma(\tau)$  curve, which corresponds to the isovalue contour for  $\bar{Q} = 0.5$ . **Top-right** Time traces of  $\bar{Q}_t(a^*, \tau)$  for three different lag-times, as defined on the left plot. The curves are shifted to the top by steps of 1 for clarity.  $a^* = 0.017$ . **Bottom-left**  $\chi_4(a, \tau)$  for several values of  $a$  and  $\tau$ . The colored points correspond to the curves on the right side. **Bottom-right** Time traces of  $\bar{Q}_t(a, \tau)$  for three different couples  $(a, \tau)$  on the  $\sigma(\tau)$  line. The curves are shifted to the top by steps of 1 for clarity. All plots stem from the vibrating experiment with  $\phi = 0.8417$  (close to  $\phi_J$ ).

is the generating function introduced in 3.1.2 (p.81) with  $\lambda = 1/2a^2$ ; hence the scaling properties of  $\mathcal{F}_\tau(\lambda)$  can be reformulated in a simple manner:

$$\bar{Q}(a, \tau) = \tilde{Q}(s) \quad \text{with} \quad s = \frac{a}{\zeta_\phi(\tau)}. \quad (\text{B.14})$$

where  $\zeta_\phi(\tau) \simeq \sigma(\tau)$ .

**More on dynamical Heterogeneities** One can also take a look at the fluctuations of  $\bar{Q}_t(a, \tau)$ . The dynamical susceptibility  $\chi_4(a, \tau)$  catches directly the temporal fluctuations of  $\bar{Q}_t(a, \tau)$  since it can be rewritten:

$$\chi_4(a, \tau) = N \cdot \text{Var}_t(\bar{Q}_t(a, \tau)) \quad (\text{B.15})$$

A common misinterpretation of the evolution of the  $\chi_4$  comes from the fact that it feels two effects. The first one corresponds to the fact that the fluctuations are lower when  $\bar{Q}_t$  is close to one of its bounds (either 0 or 1). Therefore for a fixed value of  $a$  the signal feels the bounds when  $\tau$  is very small or very large (see for instance the top and bottom plots of fig. B.7-top right) and as a consequence the fluctuations trivially peak at an intermediate value. The same reasoning can be done when  $\tau$  is fixed and  $a$  varies, leading to the same effect. This predicts the existence of a crest along on the  $\sigma(\tau)$  line.

However, a second effect can be observed. If one plots  $\chi_4$  for several values of  $a$  and  $\tau$  like on fig. B.7-bottom left, one gets the famous “banana plot” and remarks that an absolute maximum jumps out from the banana. Let us call in the following the global maximum  $\chi_4^*(\phi)$ , and let  $\tau^*$  and  $a^* \simeq \sigma_\phi(\tau^*)$  be the values at which the maximum occurs. So, a first conclusion is that at each packing fraction the dynamical heterogeneities are maximal when they are probed on a specific length scale  $a^*$  and a specific time scale  $\tau^*$ , which are “chosen by the system itself”<sup>7</sup>.

Let’s concentrate from now on on the properties of  $\bar{Q}_t(a, \tau)$  along the “crest”  $\zeta_\phi(\tau)$  curve (black solid line on fig. B.7-bottom right), defined as the iso-line  $\bar{Q}(a, \tau) = 0.5$ . A plot of  $\chi_4(\tau, a = \zeta_\phi(\tau))$  is represented on fig. B.8-left for different values of the packing fraction. At each packing fraction, a peak is observed, corresponding to  $\chi_4^*(\phi)$ .

The physical interpretation for these peaks is the following: since all the values are computed on the iso-line  $\bar{Q}(a, \tau) = 0.5$ , the number of decorrelating particles is roughly constant and the fluctuations catch the *spatial* heterogeneity of the  $Q_t(a, \tau)$  field. If the decorrelations are filling homogeneously the space (*e.g.* when randomly distributed) the resulting  $\chi_4$  stays quite low, but the loom of large decorrelation domains makes it grow. Actually the value of  $\chi_4$  *directly* points out a typical lengthscale (in number of particles) of these decorrelation domains.

So the size of the decorrelation patterns can be compared from one run to another. Considering for instance the vibrating experiment, we have represented in fig. B.8-center the maximum value  $\chi_4^*$  as a function of the packing fraction. Yet another peak is found, at  $\phi_J$ , which says that the size of the decorrelation culminates at  $\phi_J$ <sup>8</sup>.

<sup>7</sup>At least they are not chosen by the experimentalist.

<sup>8</sup>We use the word “decorrelation” but one should keep in mind that the probed displacements are marvellously small (of the order of  $a^*$ ) and that they do *not* correspond to a structural relaxation in this experiment.

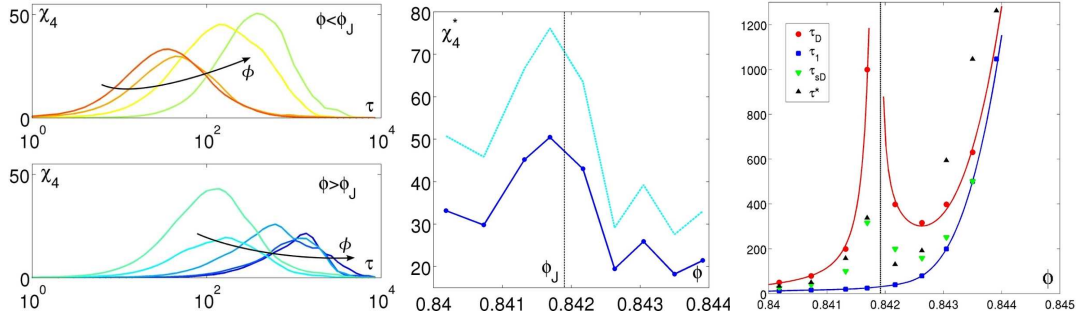


Figure B.8: **Left**  $\chi_4(\tau, a = \zeta(\tau))$  for several packing fraction below (top) and above (bottom)  $\phi_J$ , from  $\phi = 0.8402$  (red) to  $\phi = 0.8439$  (blue). **Middle**  $\chi_4^*$  as a function of the packing fraction (dark blue). The modified  $\tilde{\chi}_4^*$  associated to the heterogeneity fluctuations is also shown (cyan). **Right** Evolution of the timescales  $\tau_1$  (■),  $\tau_{sD}$  (▼),  $\tau_D$  (●) and  $\tau^*$  (▲) as functions of the packing fraction around jamming. All plots stem from the vibrating experiment.

To be perfectly rigorous, one should normalize the  $\chi_4$  by the amplitude of the intensity fluctuations. Indeed, the following relation:

$$\text{Var} \left( \sum_i x_i \right) = \text{Var}(x_i) \cdot \left( 1 + 2 \int \langle \delta x_i \cdot \delta x_j \rangle_{\vec{d}_{i,j} = \vec{r}} \cdot d\vec{r} \right) \quad (\text{B.16})$$

brings to light the role of the variance of the random variable, which is in our case  $\Delta^2(a, \tau) = \langle (q_i^t(a, \tau) - \bar{Q}(a, \tau))^2 \rangle_{i,t}$ . Hence one can define a reduced dynamical susceptibility:

$$\tilde{\chi}_4 = \frac{1}{2} \left( \frac{\chi_4}{\Delta^2} - 1 \right) \quad (\text{B.17})$$

whose maximal value  $\tilde{\chi}_4^*(\phi)$  is plotted in the middle panel of fig. B.8 and has the same behavior than  $\chi_4^*(\phi)$ , indicating that the main contribution to the dynamical susceptibility comes from the heterogeneity of the fluctuations rather than from the intensity of the fluctuations. So in our case the  $\chi_4$  is a powerful tool to unveil the dynamical correlations.

**Time\* and length\* scales.** Let's continue to use the vibrating experiment as an example for our purposes. One can compute the values of  $a^*(\phi)$  and observe that they are roughly constant (of the order of  $10^{-2}$ ).  $\tau^*(\phi)$  has a richer behavior, and one observes a non-monotonous evolution as the packing fraction is increased: it first rises until  $\phi_J$ , falls, and – ultimately – diverges. The timescale  $\tau^*$  of the dynamical heterogeneities can be sub-joined to the timescale plot in fig. 3.3-right (p.77) to complete the picture, as represented of fig. B.8-right.

The strong increase of timescales at  $\phi_J$  altogether with the peak of  $\tilde{\chi}_4^*(\phi)$  suggest the existence of an associated growing lengthscale. As a matter of

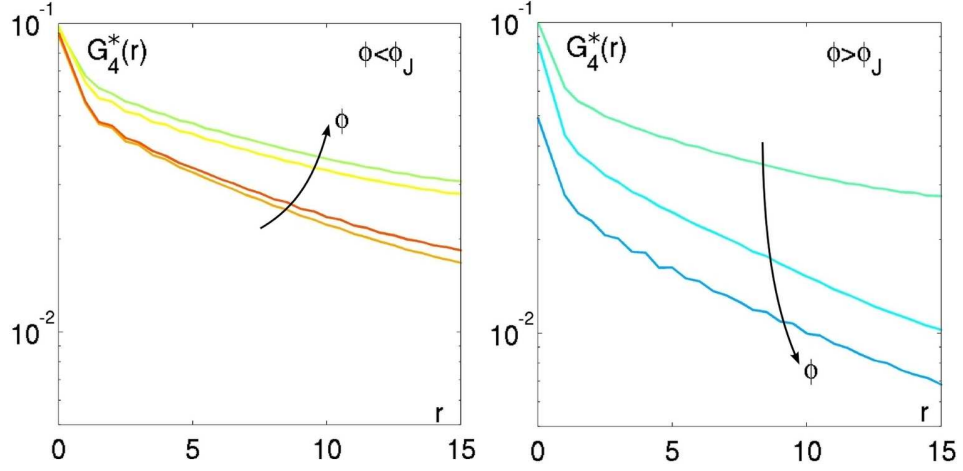


Figure B.9: **Left**  $G_4^*(r)$  for a few values of  $\phi$  below  $\phi_J$ . **Right**  $G_4^*(r)$  for a few values of  $\phi$  above  $\phi_J$ . Both plots stem from the vibrating experiment.

fact, we can indeed introduce the dynamical correlation function  $G_4(\vec{r}; a, \tau)$  (similar to the one defined in eq.(1.8)):

$$G_4(\vec{r}; a, \tau) = \int \langle \delta Q_a^t(\vec{r}; \tau) \cdot \delta Q_a^t(\vec{r} + \vec{r}'; \tau) \rangle_t d\vec{r}' \quad (\text{B.18})$$

where:

$$\delta Q_a^t(\vec{r}; \tau) = Q_a^t(\vec{r}; \tau) - \langle Q_a^t(\vec{r}; \tau) \rangle_t \quad \text{and} \quad (\text{B.19})$$

$$Q_a^t(\vec{r}; \tau) = \frac{1}{N} \sum_i q_i^t(\vec{r}; a, \tau) \quad (\text{B.20})$$

We can assume isotropy and consider only the radial decay of  $G_4(r)$ .

Some examples for various packing fractions below and above  $\phi_J$  at  $a^*(\phi)$  and  $\tau^*(\phi)$  are displayed in fig. B.9. One can see first that the lengthscale grows on approach to jamming, and second that  $G_4^*(r \rightarrow 0^+)$  varies only a few with  $\phi$ , which confirms the fact that the intensity fluctuations weakly drives the behavior of the  $\chi_4$ , which is the spatial integral of the  $G_4$ .

**A simplified model.** For the purpose of clarification, let us introduce a simplified picture of a system of  $N$  particles with a fluctuating number  $M_t$  of mobile regions of size  $n$  and assume that the order parameter is homogeneously  $Q_0$  in all fast regions and  $Q_1$  in slow regions. Then the order parameter is given by a weighted average of these values over the total number  $nM_t$  of grains in the fast regions and the number  $N - nM_t$  of grains in the slow regions:  $Q_t = [f_t Q_0 + (1 - f_t) Q_1]$ , where  $f_t = nM_t/N$  is the fraction of mobile particles. From this one readily obtains the averaged

order parameter and  $\chi_4$ :

$$\bar{Q} = \bar{f}\delta Q + Q_1, \quad (\text{B.21})$$

$$\chi_4 = N \text{var}_t(Q_t) = \frac{n^2\delta Q^2}{N} \cdot \text{var}_t(M_t) = n\delta Q^2 \bar{f} \cdot \frac{\text{var}_t(M_t)}{\bar{M}_t} \quad (\text{B.22})$$

where  $\delta Q = Q_1 - Q_0$  is a measure of how different are fast and slow particles.

If one assumes that there is a large number of mobile regions and that they are decorrelated, then  $\text{var}_t(M_t) \sim \bar{M}_t$  and one can in principle measure the size  $n$  of these regions from the resulting relation:

$$\chi_4 \simeq n\bar{f}\delta Q^2 \quad (\text{B.23})$$

**Finite size effects.** As stated above, it is necessary to have a large enough number of independent mobile regions in order to ensure  $\text{var}_t(M_t) \sim \bar{M}_t$ . Since one also expects large value of  $n^*$  close to the transition of interest, satisfying the above condition requires the use of very large systems, typically of the order of  $N = 100 n^*$ .

In addition, these size effects rapidly become critical since the *relative* error on the measure of  $\text{var}_t(Q_t)$  scales like  $\sqrt{N/T}$ , where  $T$  is the duration of the acquisition. So if one has to take  $N$  large, one has also to take a long acquisition time  $T$  in order to reduce the relative error on the measure of  $\text{var}_t(Q_t)$ .



# Bibliography

- [1] M. Ballerini, N. Cabibbo, R. Candelier, A. Cavagna, E. Cisbani, I. Giardina, V. Lecomte, A. Orlandi, G. Parisi, A. Procaccini, M. Viale, and V. Zdravkovic. Interaction ruling animal collective behaviour depends on topological rather than metric distance: Evidence from a field study. *PNAS*, 105:1232, 2008.
- [2] M. Ballerini, N. Cabibbo, R. Candelier, A. Cavagna, E. Cisbani, I. Giardina, A. Orlandi, G. Parisi, A. Procaccini, M. Viale, and V. Zdravkovic. Empirical investigation of starling flocks: a benchmark study in collective animal behaviour. *Animal Behaviour*, 76(1):201–215, 2008.
- [3] R. W. Cahn. *The Coming of Materials Science*. 2001.
- [4] P. Anderson. *Science*, 267(1615), 1995.
- [5] X. Xia and P. G. Wolynes. Fragilities of liquids predicted from the random first order transition theory of glasses. *PNAS*, 97(7):2990–2994, 2000.
- [6] L. Berthier and G. Biroli. A statistical mechanics perspective on glasses and aging. In *Encyclopedia of Complexity and Systems Science*. Springer, 2009.
- [7] A. Hedler, S. L. Klaumünzer, and W. Wesch. Amorphous silicon exhibits a glass transition. *Nature Materials*, 3:804–809, 2004.
- [8] W. Kauzmann. The Nature of the Glassy State and the Behavior of Liquids at Low Temperatures. *Chem. Rev.*, 43:219, 1948.
- [9] G. Parisi and F. Zamponi. Mean field theory of hard sphere glasses and jamming, 2009. arXiv:0802.2180.
- [10] L. Berthier and T. A. Witten. Compressing nearly hard sphere fluids increases glass fragility. *Europhysics Letters*, 86:10001, 2009.

- [11] D. El Masri, G. Brambilla, M. Pierno, G. Petekidis, A. B. Schofield, L. Berthier, and L. Cipelletti. Dynamic light scattering measurements in the activated regime of dense colloidal hard spheres. *J. of Stat. Mech.: Theory and Experiment*, 2009(07):P07015 (28pp), 2009.
- [12] C. A. Angell. Formation of glasses from liquids and biopolymers. *Science*, 267(5206):1924–1935, 1995.
- [13] P. G. Debenedetti and F. H. Stillinger. Supercooled liquids and the glass transition. *Nature*, 410(6825):259–67, 2001.
- [14] T. Hecksher, A. I. Nielsen, N. B. Olsen, and J. C. Dyre. Little evidence for dynamic divergences in ultraviscous molecular liquids. *Nature Physics*, 4:673, sep 2008.
- [15] Z. Cheng, J. Zhu, P. M. Chaikin, S-E Phan, and W. B. Russel. Nature of the divergence in low shear viscosity of colloidal hard-sphere dispersions. *Phys. Rev. E*, 65(4):041405, Apr 2002.
- [16] G. D’Anna and G. Gremaud. The jamming route to the glass state in weakly perturbed granular media. *Nature*, 413(6854):407–409, 2001.
- [17] J. P. Eckmann and D. Ruelle. Ergodic theory of chaos and strange attractors. *Reviews of Modern Physics*, 57(3):617–656, 1985.
- [18] S. F. Edwards and R. B. S. Oakeshott. Theory of Powders. *Physica A*, 157:1080–1090, 1989.
- [19] P. T. Metzger. Granular contact force density of states and entropy in a modified Edwards ensemble. *Phys. Rev. E*, 70(5):51303, 2004.
- [20] G. Marty. *Comportement vitreux des systèmes athermiques: étude expérimentale d’un matériau granulaire bidimensionnel*. PhD thesis, Université Paris XI, UFR Scientifique d’Orsay, Sep 2005.
- [21] A. Widmer-Cooper. *Structure and Dynamics in Two-Dimensional Glass-Forming Alloys*. PhD thesis, University of Sydney, May 2006.
- [22] D. N. Perera and P. Harrowell. Stability and structure of a supercooled liquid mixture in two dimensions. *Phys. Rev. E*, 59(5):5721–5743, May 1999.
- [23] B. Doliwa and A. Heuer. Energy barriers and activated dynamics in a supercooled lennard-jones liquid. *Phys. Rev. E*, 67(3):031506, Mar 2003.
- [24] F. W. Starr, S. Sastry, J. F. Douglas, and S. C. Glotzer. What do we learn from the local geometry of glass-forming liquids? *Phys. Rev. Lett.*, 89(12):125501, Aug 2002.

- [25] M. D. Ediger. Spatially heterogeneous dynamics in supercooled liquids. *Annu. Rev. Phys. Chem.*, 51:99–128, 2000.
- [26] A. Widmer-Cooper, H. Perry, P. Harrowell, and D. R. Reichman. Irreversible reorganization in a supercooled liquid originates from localized soft modes. *Nature Physics*, 4:711, 2008.
- [27] Gopal E. S. R. Critical opalescence. *Resonance*, (4):37–45, 2000.
- [28] C. Dasgupta, A. V. Indrani, S. Ramaswami, and M. K Phani. Is there a growing correlation length near the glass transition ? *Europhys. Lett. D*, 15:307, 1991.
- [29] C. Donati, S. Franz, S.C. Glotzer, and G. Parisi. Theory of non-linear susceptibility and correlation length in glasses and liquids. *Journal of Non-Crystalline Solids*, 307:215–224, 2002.
- [30] G. Adam and J. H. Gibbs. On the Temperature Dependence of Cooperative Relaxation Properties in Glass-Forming Liquids. *The Journal of Chemical Physics*, 43:139, 2004.
- [31] W. Kob and H. C. Andersen. Testing mode-coupling theory for a supercooled binary lennard-jones mixture i: The van hove correlation function. *Physical Review E*, 51:4626, 1995.
- [32] C. Thibierge. *Etude Expérimentale d'une longueur de corrélation dynamique à la transition vitreuse*. PhD thesis, UPMC, Paris VI, 2009.
- [33] E. R. Weeks, J. C. Crocker, A. C. Levitt, A. Schofield, and D. A. Weitz. Three-Dimensional Direct Imaging of Structural Relaxation Near the Colloidal Glass Transition. *Science*, 287(5453):627–631, 2000.
- [34] O. Pouliquen, M. Belzons, and M. Nicolas. Fluctuating particle motion during shear induced granular compaction. *Phys. Rev. Lett.*, 91:014301, 2003.
- [35] R. Candelier, O. Dauchot, and G. Biroli. Building blocks of dynamical heterogeneities in dense granular media. *Physical Review Letters*, 102(8):088001, 2009.
- [36] W. Kob and J. L. Barrat. Aging Effects in a Lennard-Jones Glass. *Phys. Rev. Lett.*, 78(24):4581–4584, Jun 1997.
- [37] A. Kabla and G. Debrégeas. Contact Dynamics in a Gently Vibrated Granular Pile. *Phys. Rev. Lett.*, 92(3):35501, 2004.
- [38] R. Candelier, A. Widmer-Cooper, J. Kummerfeld, G. Biroli, O. Dauchot, P. Harrowell, and D. Reichman. Avalanches and dynamical correlations in supercooled liquids. *Condmate*, (arXiv.org:0912.0193), 2009.

- [39] C. Brito and M. Wyart. Heterogeneous dynamics, marginal stability and soft modes in hard sphere glasses. *J. Stat. Mech.*, 08:L08003, 2007.
- [40] O. Dauchot, G. Marty, and G. Biroli. Dynamical Heterogeneity Close to the Jamming Transition in a Sheared Granular Material. *Phys. Rev. Lett.*, 95(26):265701, 2005.
- [41] A. Duri and L. Cipelletti. Length scale dependence of dynamical heterogeneity in a colloidal fractal gel. *Europhys. Lett*, 76(5):972, 2006.
- [42] C. Bennemann, C. Donati, J. Baschnagel, and S. C. Glotzer. Growing range of correlated motion in a polymer melt on cooling towards the glass transition. *Nature(London)*, 399(6733):246–249, 1999.
- [43] L. Berthier, G. Biroli, J.-P. Bouchaud, W. Kob, K. Miyazaki, and D. Reichman. Spontaneous and induced dynamic fluctuations in glass-formers I: General results and dependence on ensemble and dynamics. *J.Chem.Phys.*, 126:184503, 2007.
- [44] A.J. Liu and S. R Nagel, editors. *Jamming and rheology: constrained dynamics on microscopic and macroscopic scales*. february 2001.
- [45] C. S. O’Hern, L. E. Silbert, A. J. Liu, and S. R. Nagel. Jamming at zero temperature and zero applied stress: The epitome of disorder. *Phys. Rev. E*, 68(1):11306, 2003.
- [46] W. G. Ellenbroek, E. Somfai, W. van Saarloos, and M. van Hecke. Force Response as a Probe of the Jamming Transition. *Physica A*, 325:19–25, 2003.
- [47] F. Lechenault. *The Jamming transition in a bidimensional granular medium: Statics and dynamics of a model athermal system*. PhD thesis, Unis Paris Sud - Paris XI, September 2007.
- [48] H. M. Jaeger, C. Liu, and S. R. Nagel. Relaxation at the Angle of Repose. *Phys. Rev. Lett.*, 62(1):40–43, 1989.
- [49] D. Bonamy, F. Daviaud, and L. Laurent. Experimental study of granular surface flows via a fast camera: A continuous description. *Physics of fluids(1994)*, 14(5):1666–1673, 2002.
- [50] E. H. Purnomo, D. Van den Ende, J. Mellema, and F. Mugele. Rheological properties of aging thermosensitive suspensions. *Phys. Rev. E*, 76(021404), 2007.
- [51] J. Brujic, P. Wang, G. Marty, C. Song, C. Briscoe, and H.A. Makse. Measuring the Coordination Number and Entropy of a 3D Jammed Emulsion Packing by Confocal Microscopy. *Phys. Rev. Lett.*, 98:248001, 2007.

- [52] S. A. Khan, C. A. Schnepper, and R. C. Armstrong. Foam Rheology: III. Measurement of Shear Flow Properties. *Journal of Rheology*, 32:69, 1988.
- [53] M. Cloitre, R. Borrega, and L. Leibler. Toothpaste Is a Glass. *Phys. Rev. Lett.*, 85(4819):4819, 2000.
- [54] L. S. Young. What Are SRB Measures, and Which Dynamical Systems Have Them? *Journal of Statistical Physics*, 108(5):733–754, 2002.
- [55] M. van Hecke. Jamming of soft particles: Geometry, mechanics, scaling and isostaticity. Preprint.
- [56] J. N. Onuchic, Z. Luthey-Schulten, and P. G. Wolynes. Theory of protein folding: The Energy Landscape Perspective. *Annual Review of Physical Chemistry*, 48(1):545–600, 1997.
- [57] T. Nagatani. Jamming transition in the traffic-flow model with two-level crossings. *Phys. Rev. E*, 48(5):3290–3294, 1993.
- [58] B. Eisenblätter, L. Santen, A. Schadschneider, and M. Schreckenberg. Jamming transition in a cellular automaton model for traffic flow. *Phys. Rev. E*, 57(2):1309–1314, 1998.
- [59] M. Mezard, G. Parisi, and R. Zecchina. Analytic and Algorithmic Solution of Random Satisfiability Problems. *Science*, 297(5582):812–815, 2002.
- [60] Florent Krzakala and Jorge Kurchan. Landscape analysis of constraint satisfaction problems, 2007.
- [61] J. C. Maxwell. On the calculation of the equilibrium and stiffness of frames. *Philosophical Magazine*, 27(294):598–604, 1864.
- [62] C. Kittel. *Introduction to Solid State Physics*. Wiley, 8 edition, November 2004.
- [63] J. B. Marion and S.T. Thornton. *Classical dynamics of particles and systems*. Harcourt Brace, 1988.
- [64] M. Wyart. On the rigidity of amorphous solids. *Ann. Phys. Fr*, 30(3):1–96, 2005.
- [65] S. Alexander. *Phys. Rep.*, 296(65), 1998.
- [66] S. Torquato, T. M. Truskett, and P. G. Debenedetti. Is Random Close Packing of Spheres Well Defined? *Phys. Rev. Lett.*, 84(10):2064–2067, 2000.

- [67] W. G. Ellenbroek, E. Somfai, M. van Hecke, and W. van Saarloos. Critical Scaling in Linear Response of Frictionless Granular Packings near Jamming. *Phys. Rev. Lett.*, 97(25):258001, 2006.
- [68] A. Kasahara and H. Nakanishi. Isostaticity and mechanical response of two-dimensional granular piles. *Phys. Rev. E*, 70(5):051309, Nov 2004.
- [69] H. P. Zhang and H. A. Makse. Jamming transition in emulsions and granular materials. *Phys. Rev. E*, 72(1):011301, Jul 2005.
- [70] E. Somfai, M. van Hecke, W. G. Ellenbroek, K. Shundyak, and W. van Saarloos. Critical and non-critical jamming of frictional grains. *Phys. Rev. E*, 75(2):20301, 2007.
- [71] T. S. Majmudar, M. Sperl, S. Luding, and R. P. Behringer. The Jamming Transition in Granular Systems. *Phys. Rev. Lett.*, 98:058001, 2007.
- [72] K. Shundyak, M. van Hecke, and W. van Saarloos. Force mobilization and generalized isostaticity in jammed packings of frictional grains. *Physical Review E (Statistical, Nonlinear, and Soft Matter Physics)*, 75(1):010301, 2007.
- [73] S. Henkes, M. van Hecke, and W. van Saarloos. Critical jamming of frictional grains in the generalized isostaticity picture. arXiv:0907.3451, Jul 2009.
- [74] M. E. Cates, J. P. Wittmer, J.-P. Bouchaud, and P. Claudin. Jamming, Force Chains, and Fragile Matter. *Phys. Rev. Lett.*, 81(9):1841–1844, Aug 1998.
- [75] A. J. Liu and S. R. Nagel. Jamming is not just cool anymore. *Nature*, 396:21–22, 1998.
- [76] Z. Zhang, N. Xu, D. T. Chen, P. Yunker, A. M. Alsayed, K. B. Aptowicz, P. Habdas, A. J. Liu, S. R. Nagel, and A. G. Yodh. Thermal vestige of the zero-temperature jamming transition. *Nature*, 459(7244):230–233, May 2009.
- [77] L. Santen and W. Krauth. Absence of thermodynamic phase transition in a model glass former. *Nature*, 405(6786):550–551, June 2000.
- [78] M. Tarzia. On the absence of the glass transition in two dimensional hard disks. *Journal of Statistical Mechanics: Theory and Experiment*, 2007(01):P01010, 2007.

- [79] L. Berthier and T. A. Witten. Glass transition of dense fluids of hard and compressible spheres. *Physical Review E (Statistical, Nonlinear, and Soft Matter Physics)*, 80(2):021502+, 2009.
- [80] F. Lechenault, O. Dauchot, G. Biroli, and J.-P. Bouchaud. Critical scaling and heterogeneous superdiffusion across the Jamming transition. *Europhysics Letters*, 83:46003, 2008.
- [81] F. Lechenault, O. Dauchot, G. Biroli, and J.-P. Bouchaud. Lower bound on the four-point dynamical susceptibility: Direct experimental test on a granular packing. *Europhysics Letters*, 83, 2008.
- [82] G. Marty and O. Dauchot. Subdiffusion and Cage Effect in a Sheared Granular Material. *Phys. Rev. Lett.*, 94(1):15701, 2005.
- [83] A. R. Abate and D. J. Durian. Approach to jamming in an air-fluidized granular bed. *Phys. Rev. E*, 74(3):031308, 2006.
- [84] A. S. Keys, A. R. Abate, S. C. Glotzer, and D. J. Durian. Measurement of growing dynamical length scales and prediction of the jamming transition in a granular material. *Nature Physics*, 3(4):260–264, 2007.
- [85] R. Candelier, O. Dauchot, and G. Biroli. Evolution of dynamical facilitation approaching the granular glass transition. *Condmatt*, (arXiv.org:0912.0472), 2009.
- [86] L. Corté, P. M. Chaikin, J. P. Gollub, and D. J. Pine. Random organization in periodically driven systems. *Nature Physics*, 4(5):420–424, 2008.
- [87] G. I. Menon and S. Ramaswamy. Universality Class of the Reversible-Irreversible Transition in Sheared Suspensions. *Arxiv preprint arXiv:0801.3881*, 2008.
- [88] A. R. Abate and D. J. Durian. Topological persistence and dynamical heterogeneities near jamming. *Physical Review E*, 76(2), 2007.
- [89] S. D. Bond, B. J. Leimkuhler, and B. B. Laird. The nosé-poincaré method for constant temperature molecular dynamics. *Journal of Computational Physics*, 151:114–134, 1999.
- [90] J. Sturgeon and B. B. Laird. Symplectic algorithm for constant-pressure molecular dynamics using a Nosé-Poincaré thermostat. *J. Chem. Phys.*, 112:3474–3482, 2000.
- [91] D. N. Perera and P. Harrowell. Relaxation dynamics and their spatial distribution in a two-dimensional glass-forming mixture. *J. Chem. Phys*, 11:5441, 1999.

- [92] P. M. Reis, R. A. Ingale, and M. D. Shattuck. Crystallization of a quasi-two-dimensional granular fluid. *Physical Review Letters*, 96(25):258001, 2006.
- [93] P. M. Reis, R. A. Ingale, and M. D. Shattuck. Caging dynamics in a granular fluid. *Physical Review Letters*, 98(18), 2007.
- [94] J. S. Olafsen and J. S. Urbach. Velocity distributions and density fluctuations in a granular gas. *Phys. Rev. E*, 60(3):R2468–R2471, Sep 1999.
- [95] R. Candelier and O. Dauchot. Creep motion of an intruder within a granular glass close to jamming. *Physical Review Letters*, 103(12):128001, 2009.
- [96] R. Candelier and O. Dauchot. Journey of an intruder through the fluidisation and jamming transitions. *Submitted to Phys. Rev. E*, 2009. ArXiv: 0909.4628.
- [97] E. R. Nowak, J. B. Knight, E. Ben-Naim, H. M. Jaeger, and S. R. Nagel. Density fluctuations in vibrated granular materials. *Phys. Rev. E*, 57(2):1971, 1998.
- [98] M. F. Shlesinger and J. Klafter. Lévy walks versus lévy flights. In H. E. Stanley and N. Ostrowsky, editors, *On Growth and Form: Fractal and Non Fractal Patterns in Physics*, page 306. Kluwer Academic Publishers, 1986. Proceedings of the NATO Advanced Study Institute “On Growth and Form”, Cargèse, France.
- [99] P. Ballesta, A. Duri, and L. Cipelletti. Unexpected drop of dynamical heterogeneities in colloidal suspensions approaching the jamming transition. 2008.
- [100] O. Zik, J. Stavans, and Y. Rabin. Mobility of a Sphere in Vibrated Granular Media. *EPL (Europhysics Letters)*, 17:315–319, 1992.
- [101] R. Albert, M. A. Pfeifer, A.-L. Barabási, and P. Schiffer. Slow drag in a granular medium. *Phys. Rev. Lett.*, 82(1):205–208, Jan 1999.
- [102] B. Dollet, F. Elias, C. Quiliet, C. Raufaste, M. Aubouy, and F. Graner. Two-dimensional flow of foam around an obstacle: Force measurements. *Physical Review E*, 71(3):031403, 2005.
- [103] J. Geng and R. P. Behringer. Slow drag in two-dimensional granular media. *Phys. Rev. E*, 71(1):011302, Jan 2005.
- [104] D. Chehata, R. Zenit, and C. R. Wassgren. Dense granular flow around an immersed cylinder. *Physics of Fluids*, 15:1622, 2003.

- [105] P. Habdas, D. Schaar, A. C. Levitt, and E. R. Weeks. Forced motion of a probe particle near the colloidal glass transition. *Europhysics Letters*, 67(3):477–483, 2004.
- [106] I. Gazuz, A. M. Puertas, and M. Fuchs. Active and nonlinear microrheology in dense colloidal suspensions. *Physical Review Letters*, 102(24):248302+, 2009.
- [107] I. C. Carpen and J. F. Brady. Microrheology of colloidal dispersions by brownian dynamics simulations. *Journal of Rheology*, 49(6):1483–1502, 2005.
- [108] C. J. Olson Reichhardt and C. Reichhardt. Fluctuations, jamming, and yielding for a driven probe particle in disordered disk assemblies, 2009.
- [109] J. A. Drocco, M. B. Hastings, C. J. O. Reichhardt, and C. Reichhardt. Multiscaling at Point J: Jamming is a Critical Phenomenon. *Phys. Rev. Lett.*, 95(8):88001, 2005.
- [110] P. Olsson and S. Teitel. Critical Scaling of Shear Viscosity at the Jamming Transition, 2007.
- [111] D. A. Head. Critical scaling and aging in cooling systems near the jamming transition. *Physical Review Letters*, 102(13):138001, 2009.
- [112] S. Henkes and B. Chakraborty. Jamming as a Critical Phenomenon: A Field Theory of Zero-Temperature Grain Packings. *Phys. Rev. Lett.*, 95(19):198002, 2005.
- [113] M. Wyart, L. E. Silbert, S. R. Nagel, and T. A. Witten. Effects of compression on the vibrational modes of marginally jammed solids. *Phys. Rev. E*, 72(5):051306, Nov 2005.
- [114] M. Goldstein. *J. Chem. Phys.*, 51:3728, 1969.
- [115] G. Biroli and J.-P. Bouchaud. Diverging length scale and upper critical dimension in the Mode-Coupling Theory of the glass transition. *Europhys. Lett*, 67(1):21–27, 2004.
- [116] J.-P. Bouchaud and G. Biroli. Nonlinear susceptibility in glassy systems: A probe for cooperative dynamical length scales. *Phys. Rev. B*, 72(6):064204, Aug 2005.
- [117] M. L. Gardel, M. T. Valentine, and D. A. Weitz. Microrheology. In *Microscale Diagnostic Techniques*. Springer Verlag, 2005.
- [118] T. Aste, M. Saadatfar, and T. J. Senden. Geometrical structure of disordered sphere packings. *Physical Review E*, 71(6):61302, 2005.

- [119] B. Doliwa and A. Heuer. Cage Effect, Local Anisotropies, and Dynamic Heterogeneities at the Glass Transition: A Computer Study of Hard Spheres. *Phys. Rev. Lett.*, 80(22):4915–4918, Jun 1998.
- [120] E. R. Weeks and D. A. Weitz. Properties of Cage Rearrangements Observed near the Colloidal Glass Transition. *Phys. Rev. Lett.*, 89(9):95704, 2002.
- [121] J. P. Garrahan and D. Chandler. Geometrical explanation and scaling of dynamical heterogeneities in glass forming systems. *Physical Review Letters*, 89:035704, 2002.
- [122] G. Biroli, J.-P. Bouchaud, A. Cavagna, T.S. Grigera, and P. Verrocchio. Thermodynamic signature of growing amorphous order in glass-forming liquids. *Nature Physics*, 4:771, 2008.
- [123] M. L. Falk and J. S. Langer. Dynamics of Viscoplastic Deformation in Amorphous Solids. *Phys. Rev. E*, 57:7192, 1998.
- [124] B. A. Berg and R. C. Harris. From data to probability densities without histograms. *Comp. Phys. Commun.*, (179):443–448, 2008.
- [125] H. M. Jaeger, S. R. Nagel, and R. P. Behringer. Granular solids, liquids, and gases. *Reviews of Modern Physics*, 68(4):1259–1273, 1996.
- [126] J. Zhou and A. D. Dinsmore. A statistical model of contacts and forces in random granular media. *J. Stat. Mech.*, (L05001), 2009.
- [127] O. Reynolds. On the dilatancy of media composed of rigid particles in contact. *Phil. Mag. Ser.*, 5(20):469–481, 1885.
- [128] D. Howell, R. P. Behringer, and C. Veje. Stress Fluctuations in a 2D Granular Couette Experiment: A Continuous Transition. *Phys. Rev. Lett.*, 82(26):5241–5244, Jun 1999.
- [129] E. Aharonov, E. Bouchbinder, H. G. E. Hentschel, V. Ilyin, N. Makedonska, I. Procaccia, and N. Schupper. Direct identification of the glass transition: Growing length scale and the onset of plasticity. *EPL*, 77(5):56002, mar 2007.
- [130] T. Kawasaki, T. Araki, and H. Tanaka. Correlation between dynamic heterogeneity and medium-range order in two-dimensional glass-forming liquids. *Physical Review Letters*, 99(21):215701, 2007.
- [131] K. Watanabe and H. Tanaka. Direct observation of medium-range crystalline order in granular liquids near the glass transition. *Physical Review Letters*, 100(15):158002, 2008.

- [132] F. Sausset and G. Tarjus. Comment on “correlation between dynamic heterogeneity and medium-range order in two-dimensional glass-forming liquids”. *Physical Review Letters*, 100(9):099601, 2008.
- [133] T. Kawasaki, T. Araki, and H. Tanaka. Reply to the comment of sausset and tarjus. *Physical Review Letters*, 100(9):099602, 2008.
- [134] M.I. Vogel, S.C. Glotzer, and Y. Gebremichael. Particle dynamics and the development of string-like motion in a simulated monoatomic supercooled liquid. *J. Chem. Phys.*, 120:4415–4427, 2004.
- [135] J. D. Stevenson, J. Schmalian, and P. G. Wolynes. The shapes of cooperatively rearranging regions in glass-forming liquids. *Nature Physics*, 2:268–274, 2006.
- [136] L. Berthier and R. L. Jack. Structure and dynamics of glass formers: Predictability at large length scales. *Physical Review E (Statistical, Nonlinear, and Soft Matter Physics)*, 76(4):041509+, 2007.
- [137] F. Sausset and G. Tarjus. Growing static and dynamic length scales in a glass-forming liquid. ArXiv:0909.0201, 2009.
- [138] F. Sausset and G. Tarjus. Self-diffusion in a monatomic glass-forming liquid embedded in the hyperbolic plane. *Philosophical Magazine*, 88(33):4025–4031, 2008.
- [139] S. Pronk and D. Frenkel. Melting of polydisperse hard disks. *Phys. Rev. E*, 69(6):066123, Jun 2004.
- [140] P. Richard, L. Oger, J. P. Troadec, and A. Gervois. Tessellation of binary assemblies of spheres. *Physica A: Statistical and Theoretical Physics*, 259(1-2):205–221, 1998.
- [141] J. F. Sadoc, R. Jullien, and N. Rivier. The laguerre polyhedral decomposition: application to protein folds. *The European Physical Journal B - Condensed Matter and Complex Systems*, 33:355–363, 2003.
- [142] A. Okabe, B. Boots, K. Sugihara, and S. N. Chi. *Spatial Tessellations: Concepts and Applications of Voronoi Diagrams*. Wiley, Chichester, UK, second edition, 2000.
- [143] P. Richard, L. Oger, J. P. Troadec, and A. Gervois. A model of binary assemblies of spheres. *Eur. Phys. J. E*, 6(4):295–303, 2001.
- [144] E. Cuthill and J. McKee. Reducing the bandwidth of sparse symmetric matrices. In *Proceedings of the 1969 24th national conference*, pages 157–172, New York, NY, USA, 1969. ACM.

- [145] S. Whitelam, L. Berthier, and J. P. Garrahan. Dynamic criticality in glass-forming liquids. *Physical Review Letters*, 92:185705, 2004.